Site U1427[1]

R. Tada, R.W. Murray, C.A. Alvarez Zarikian, W.T. Anderson Jr., M.-A. Bassetti, B.J. Brace, S.C. Clemens, M.H. da Costa Gurgel, G.R. Dickens, A.G. Dunlea, S.J. Gallagher, L. Giosan, A.C.G. Henderson, A.E. Holbourn, K. Ikehara, T. Irino, T. Itaki, A. Karasuda, C.W. Kinsley, Y. Kubota, G.S. Lee, K.E. Lee, J. Lofi, C.I.C.D. Lopes, L.C. Peterson, M. Saavedra-Pellitero, T. Sagawa, R.K. Singh, S. Sugisaki, S. Toucanne, S. Wan, C. Xuan, H. Zheng, and M. Ziegler[2]

Chapter contents

[1] Tada, R., Murray, R.W., Alvarez Zarikian, C.A., Anderson, W.T., Jr., Bassetti, M.-A., Brace, B.J., Clemens, S.C., da Costa Gurgel, M.H., Dickens, G.R., Dunlea, A.G., Gallagher, S.J., Giosan, L., Henderson, A.C.G., Holbourn, A.E., Ikehara, K., Irino, T., Itaki, T., Karasuda, A., Kinsley, C.W., Kubota, Y., Lee, G.S., Lee, K.E., Lofi, J., Lopes, C.I.C.D., Peterson, L.C., Saavedra-Pellitero, M., Sagawa, T., Singh, R.K., Sugisaki, S., Toucanne, S., Wan, S., Xuan, C., Zheng, H., and Ziegler, M., 2015. Site U1427. *In* Tada, R., Murray, R.W., Alvarez Zarikian, C.A., and the Expedition 346 Scientists, *Proc. IODP,* 346: College Station, TX (Integrated Ocean Drilling Program). doi:10.2204/iodp.proc.346.108.2015
[2] **Expedition 346 Scientists' addresses.**

Background and objectives

Integrated Ocean Drilling Program (IODP) Site U1427 is in the Yamato Basin at 35°57.92′N, 134°26.06′E and 330 meters below sea level (mbsl). The site is situated on the outer margin of the southeast-northwest–trending continental shelf ~35 km from the northern coast of Honshu Island and ~110 km south of Site U1426 (Fig. **F1**). Today, this site is under the influence of the first branch of the Tsushima Warm Current (TWC), which is flowing along the outer margin of the continental shelf of Honshu Island (Hase et al., 1999). A piston core obtained during a preexpedition site survey cruise suggests an average sedimentation rate of ~300 m/m.y. (**www.godac.jamstec.go.jp/catalog/data/doc_catalog/media/KR07-12_all.pdf**). This is significantly higher than any other sites drilled in the marginal basin, and coring at this site should provide an extremely high resolution record spanning most of the Pleistocene. In addition, the proximity to the southwestern portion of Honshu Island will provide a rare opportunity to examine the interrelationship between terrestrial climate and oceanography in the southern part of the marginal basin.

Site U1427 is the southernmost site of the IODP Expedition 346 latitudinal transect and is also the shallowest site of the depth transect. The location of Site U1427 was selected to obtain a high-resolution record of changes in the intensity of the influx of the first branch of the TWC during the last 2 m.y. We anticipate that this site will allow high-resolution and continuous reconstruction of the oxygen isotope record because the shallow depth of Site U1427 assures that the site has always been located above the calcium carbonate compensation depth. Accordingly, benthic foraminifers have likely survived burial and resisted corrosion even during glacial maxima climate stages when euxinic deepwater conditions prevailed deeper than 500 mbsl (Ikehara et al., 1994). Together with the results from IODP Sites U1425 and U1426, Site U1427 will enable us to reconstruct sea-surface temperature changes associated with the north–south movement of the Subpolar Front, which is considered to be related to the strength of the TWC (Isoda, 2011).

Operations

Site U1427 (proposed Site YB-1) was occupied at two different times during Expedition 346, first following operations at Site

doi:10.2204/iodp.proc.346.108.2015

U1426 (6 September 2013) and then ~2 weeks later after completing operations at IODP Site U1430 (22 September) to acquire additional material for post-cruise studies, as described below. A return to Site U1427 was possible because all scientific and operations objectives were met ~5 days before the end of the expedition; therefore, the remaining time available was spent reoccupying two sites drilled earlier in the expedition (Sites U1427 and U1425). Preliminary shipboard scientific results from Holes U1427A and U1427B indicated that this site exhibits a continuous Late Pleistocene sedimentary sequence with high sedimentation rates and excellent carbonate preservation, both of which are ideal for high-resolution paleoceanographic studies. Therefore, we drilled Hole U1427C during the revisit.

Three holes were cored at Site U1427 using the full and half advanced piston corer (APC) and the extended core barrel (XCB). Hole U1427A was cored to 548.6 m core depth below seafloor, Method A (CSF-A) (see the **"Methods"** chapter [Tada et al., 2015b]) (81 cores) with a recovery of 542.59 m (98.9%). Hole U1427B was cored to 405.6 m CSF-A (61 cores) with a recovery of 422.41 m (105%). Hole U1427C was cored to 351.1 m (52 cores) with a recovery of 367.77 m (105%) (Table **T1;** see also Fig. **F2** in the "Expedition 346 summary" chapter [Tada et al., 2015a]). Four formation temperature measurements were performed, and downhole wireline log data were obtained to 548.5 m WSF (see the **"Methods"** chapter [Tada et al., 2015b]) in Hole U1427A.

An exciting aspect of operations at Site U1427 included the acquisition of the deepest continuously recovered APC-cored sequence in Deep Sea Drilling Project (DSDP)/Ocean Drilling Program (ODP)/IODP history, in Hole U1427A, as well as the deepest piston core (346-U1427A-81H) from 490.4 m CSF-A.

Transit from Site U1426

The 66 nmi distance to Site U1427 was covered in 6 h at an average speed of 11.1 kt. Sea passage ended at 0542 h on 6 September 2013. The vessel was maneuvered over the location coordinates, a wide-angle positioning beacon was deployed, thrusters were lowered into position, and the vessel was turned over to dynamic positioning control. By 0615 h, the vessel was stabilized, and rig floor operations began.

Hole U1427A

A three-stand APC/XCB bottom-hole assembly (BHA) was assembled, and the drill string was run to the bottom. After picking up the top drive and spacing out the drill string to a depth of 329.4 meters below rig floor (mbrf) (6.0 m shallower than precision depth recorder depth), an APC core barrel was deployed. The first core barrel recovered 1.79 m of core, establishing a seafloor depth of 337.1 mbrf. Oriented APC coring continued using full-length nonmagnetic core barrels through Core 346-U1427A-25H to 228.7 m CSF-A. The base of Core 25H recovered reworked volcanic sand, and the next core contained volcanic ash. At that point, we switched to the half APC system and continued coring through Core 81H to a depth of 490.4 m CSF-A, making this, as mentioned above, the deepest continuously cored sequence ever recovered with the APC coring system in DSDP/ODP/IODP history. An additional 6 XCB cores were cut to a final total depth of 548.6 m CSF-A. The hole was circulated and displaced with 10.5 ppg weighted mud, the top drive was set back, and the pipe was pulled up to logging depth (80 m WSF). Rig-up for wireline logging began at 0630 h on 8 September. Both the paleo combo and Formation MicroScanner (FMS)-sonic tool strings were deployed to 548.5 m WSF, and all wireline logging runs were successful. By 1715 h that same day, the rig floor was rigged down from logging. The pipe was lowered (without the top drive) to 519 m CSF-A, and a 10 bbl (24 m long) 14.5 ppg cement plug was displaced using a circulating head. The drill string was pulled clear of the seafloor at 2020 h on 8 September 2013, ending Hole U1427A and beginning Hole U1427B. Total recovery for this hole was 542.6 m (99%). A total of 56 half APC cores were recovered. Four formation temperature measurements were taken using the advanced piston corer temperature tool (APCT-3) temperature shoe at 30.3, 58.8, 87.3, and 115.8 m CSF-A.

Hole U1427B

Once clear of the seafloor, the drill string was thoroughly flushed to remove any remnant cement, and an XCB was deployed to aid in flushing/cleaning the lockable flow valve. The XCB was recovered and the ship was offset 15 m north of Hole U1427A. The bit was placed at a depth of 332.4 mbrf, and an APC core barrel was deployed. Hole U1427B was spudded at 2220 h on 8 September 2013, and the 4.8 m of core recovered from the mudline core established a seafloor depth of 337.1 mbrf. APC coring with full core barrels continued through Core 346-U1427B-6H to 52.3 m CSF-A before a 1.0 m drilled interval was used to correct the core break offsets. APC coring continued through Core 12H to 100.8 m CSF-A, where a second 1 m advance was made. APC coring resumed, recovering Cores 14H through 28H to 235.8 m CSF-A. This barrel was an incomplete stroke and was very near the interval in Hole U1427A where the APC met refusal. Eight half APC cores

were then recovered (Cores 29H through 36H) to a depth of 273.4 m CSF-A. Because the overpull was zero for the previous six cores, we switched back to full APC barrels beginning with Core 37H. However, this core failed to fully penetrate the formation, and coring resumed at that point using the half APC system once again. A 1.0 m advance was made to properly align the core breaks, and coring then continued recovering half APC Cores 39H through 47H to 325.4 m CSF-A. There, another 3 m "drill ahead" advance was made to realign core breaks, which had drifted close to stacking up with the earlier hole. With the exception of a fourth drill ahead of 2 m after Core 52H, half APC coring continued through Core 65H to a total depth of 405.6 m CSF-A. The hole was displaced with 190 bbl of 10.5 ppg mud, and the drill string was pulled clear of the seafloor by 0605 h on 10 September. The bit cleared the rotary table at 0735 h, the positioning beacon was recovered aboard by 0752 h, and by 0830 h the ship was under way for the next IODP drill site (U1428). Total recovery for Hole U1427B was 422.41 m (105%). Of the 61 cores recovered, 32 were half APC cores.

Return to Site U1427

Nearly 2 weeks later, after completing operations at Site U1430, the ship returned to Site U1427 to drill an additional hole and collect additional data and core material for postcruise studies. The 182 nmi between Sites U1430 and U1427 were covered in 17.2 h at an average speed of 10.6 kt. Sea passage ended at 0830 h on 22 September 2013. The vessel was maneuvered over the location coordinates, and a Falmouth Scientific positioning beacon (model BAP-547; SN1028W, 16 kHz, 206 dB) was deployed at 0958 h. Thrusters were lowered into position, and the vessel was turned over to dynamic positioning control. By 0900 h, the vessel was stabilized and rig floor operations began.

Hole U1427C

The APC/XCB BHA was quickly assembled, and the drill string was run to the bottom. For this hole, the ship was positioned 15 m south of Hole U1427A. The top drive was picked up and the pipe was spaced out, positioning the bit at a depth of 336 mbrf. Hole U1427C was spudded at 1200 h on 22 September. The first core barrel recovered 8.05 m of core, establishing a seafloor depth of 337.5 mbrf. APC coring continued using full-length nonmagnetic core barrels through Core 346-U1427C-10H to 93.5 m CSF-A. A single half APC core was then taken (Core 11H) to adjust the core break offset. APC coring then continued using full barrels through Core 25H to 224.2 m CSF-A. Coring continued from that point using the half APC through Core 52H to a total depth of 351.1 m CSF-A. Two formation temperature measurements were taken using the APCT-3 temperature shoe at 17.5 and 36.5 m CSF-A. The hole was displaced with 140 bbl of 10.5 ppg weighted mud, the top drive was set back, and the drill string was pulled clear of the seafloor at 1710 h on 23 September. The bit was clear of the rotary table by 1815 h. During the pipe trip, the positioning beacon was recovered at 1739 h. The bit and bit sub were removed, and the rig floor was secured for transit by 1845 h. Thrusters and hydrophones were pulled, and the sea voyage to return to Site U1425 was initiated at 1900 h on 23 September. Total recovery for Hole U1427C was 367.77 m (105%). Of the total 52 cores recovered, 25 were full APC cores and 27 were half APC cores. There were no cores cut using the XCB.

Lithostratigraphy

Drilling at Site U1427 penetrated to a maximum subbottom depth of 548.6 m in Hole U1427A, recovering a total of 542.6 m of sediment for a recovery rate of 99% (see **"Operations"**). The shipboard lithostratigraphic program involved detailed visual assessment of sediment composition, color, sedimentary structures, and bioturbation intensity, supplemented by petrographic analysis of smear slides (143 from Hole U1427A and 101 from Hole U1427B) (see Site U1427 smear slides in **"Core descriptions"**) and bulk mineralogic analysis by X-ray diffraction (XRD) (57 samples; Table **T2**). These objective criteria were used to describe the sediment succession and to define facies and facies associations.

The sedimentary sequence recovered at Site U1427 extends from the early Pleistocene to Holocene and is dominated by clayey silt and nannofossil- or biosiliceous-rich clayey silt. Volcaniclastic material represents a minor component throughout the succession, except in tephra (i.e., volcanic ash) layers. Shell fragments of shallow-water origin are observed throughout the recovered section. The character of the sedimentary physical properties, including natural gamma radiation (NGR), magnetic susceptibility, color reflectance parameters, and density, also records the distribution of the various sediment components and lithologies (see **"Physical properties"**). The major characteristics of the sedimentary sequence at Site U1427, together with some of these additional properties, are summarized in Figures **F2, F3,** and **F4.** A hole-to-hole correlation based on the distribution of lithologic units is shown in Figure **F5.**

The lithology at Site U1427 consists of one unit based on the investigation of sediment composition and sedimentary structures. The name "Unit A" is

used for the complete sequence at Site U1427 in order to distinguish it from "Unit I," which was previously used at other sites occupied during Expedition 346. Unit I, as defined by Tada (1994), is recognized in the marginal basin by centimeter- to decimeter-scale alternation of dark and light sediment layers. Because the sediment succession at Site U1427 does not show this characteristic, the name "Unit I" is not used for this site.

Unit A

Intervals: 346-U1427A-1H-1, 0 cm, to 87X-CC, 48 cm; 346-U1427B-1H-1, 0 cm, to 65H-5, 46 cm; 346-U1427C-1H-1, 0 cm, to 52H-CC, 24 cm

Depths: Hole U1427A = 0–547.92 m CSF-A; Hole U1427B = 0–405.95 m CSF-A; Hole U1427C = 0–351.79 m CSF-A

Age: Holocene to early Pleistocene (<1.4 Ma)

Lithology and structures

Unit A consists of clayey silt, silty clay, nannofossil-rich clayey silt, biosiliceous-rich clayey silt, and nannofossil ooze (Figs. **F2, F3, F4**). The sediment is generally heavily bioturbated with a fairly homogeneous, structureless appearance (Fig. **F6**). The major lithologies are interbedded with several centimeter- to decimeter-thick tephra layers. Hole U1427A contains a total of 33 tephra beds >0.5 cm thick (Fig. **F7;** Table **T3**). Unit A is divided into Subunits A1 and A2 based on the difference in minor lithology.

Bulk mineralogy

The results of XRD analyses are listed in Table **T2.** In general, Pleistocene sediment at Site U1427 is composed mainly of quartz, calcite, plagioclase, K-feldspar, and clay minerals (including smectite, illite, and kaolinite and/or chlorite), as well as minor amounts of halite, pyrite, and biogenic opal-A. Hornblende and pyroxene, which were not seen at the previous sites, are also found at this site and show relatively high values in the upper ~200 m CSF-A. Figure **F8** shows the downcore variations in peak intensity of the identified minerals at Site U1427. Quartz and plagioclase contents show a long-term increasing trend toward the top of the hole. In contrast, clay minerals (smectite, illite, and kaolinite and/or chlorite) and opal-A show a long-term decreasing trend toward the top of the hole. Plagioclase and K-feldspar show high values in some intervals.

Tephra

Numerous visible tephra beds were observed in cores from Hole U1427A. Because most of the tephras occurred as small patches or thin discontinuous layers reflecting strong bioturbation throughout the cores and contained high amounts of quartz with volcanic glass shards, it is hard to distinguish between original and reworked beds. Therefore, tephra beds that occurred as small patches or bioturbated thin layers were not counted when documenting tephra abundance except for beds composed of nearly pure volcanogenic materials such as volcanic glass shards and phenocrysts. Tephra beds with a thickness >0.5 cm and thin tephra layers (<0.5 cm) that are probably correlatable between holes are listed in Table **T3.** In this table, tephra layers from the two holes that appear on the same line are thought to be correlative. Thick tephra layers (thickness >10 cm) occur at intervals 346-U1427A-2H-7, 21–31 cm (10.68–10.78 m CSF-A); 5H-7, 55 cm, to 5H-CC, 3 cm (39.25–39.35 m CSF-A); 11H-3, 74–94.5 cm (91.02–91.225 m CSF-A); 25H-6, 14 cm, to 25H-7, 51 cm (226.89–228.71 m CSF-A); and 27H-1, 25.5 cm, to 27H-2, 29 cm (233.655–234.02 m CSF-A). The total thickness of tephra beds shows some peaks at horizons of the thick beds, especially in Cores 23H to 27H, with a small peak in Cores 45H to 49H. However, no clear peak is found in the number of thick tephras with thicknesses >0.5 cm in each core (Fig. **F7**). Several examples of tephra layers recovered at Site U1427 are shown in Figure **F9.**

The thickest tephra layer is >180 cm thick and straddles Sections 346-U1427A-25H-6 to 25H-7. This tephra layer is composed of two parts. The upper 6 cm consists of fine-grained white volcanic glass, and the lower part consists of well-sorted coarse pumice, biotite, and quartz. The lower part of this thick tephra was not recovered in Hole U1427B, and white-colored fine-grained volcanic glass sits directly above clayey silt with an erosional contact. In Hole U1427C, the same tephra consists of 6 cm of fine-grained white glass above 10 cm of a coarse pumiceous layer with a contact that shows no evidence of erosion. Based on these observations, it is concluded that the coarse basal part of this tephra is possibly flow-in in Hole U1427A that is missing in Hole U1427B.

Some tephra beds contained "pumice-type" volcanic glass shards and orthopyroxene, as well as hornblende as phenocrysts. Biotite is also found in some tephras. These characteristics are similar to those of the Daisen and Sanbe Volcanoes located near the site. Therefore, a stronger contribution from local volcanoes to this site relative to the other offshore sites may be expected.

Subunit A1

Intervals: 346-U1427A-1H-1, 0 cm, to 14H-CC, 25 cm; 346-U1427B-1H-1, 0 cm, to 16H-CC, 35 cm; 346-U1427C-1H-1, 0 cm, to 15H-3, 146 cm

Depths: Hole U1427A = 0–125.53 m CSF-A; Hole U1427B = 0–130.95 m CSF-A; Hole U1427C = 0–130.86 m CSF-A
Age: Holocene to Middle Pleistocene (0.5 Ma)

Lithologies and structures

Subunit A1 consists of clayey silt, silty clay, silty sand, nannofossil-rich clayey silt, biosiliceous-rich clayey silt, and nannofossil ooze (Fig. F10). The sediment is characterized by meter- to several tens of meters–scale alternations of biogenic component–rich clayey silt and biogenic component–poor clayey silt (Fig. F6). The biogenic component is mainly composed of nannofossils and secondarily of diatoms and sponge spicules. The biogenic component–rich clayey silt is generally olive-gray or dark greenish gray in color, and the biogenic component–poor clayey silt typically is more grayish green. Although the contrast in color between these lithologies is low and the transition from one to the next is gradual, color variations over depth scales of tens of meters can be observed. These alternations of lithologies are reflected in records of NGR, magnetic susceptibility, and color reflectance. The clayey silt intervals present relatively high NGR and magnetic susceptibility and lower b* values. In contrast, the biogenic component–rich clayey silt intervals are marked by relatively lower NGR and magnetic susceptibility and higher b* values.

As minor lithologies, very dark gray and/or very dark greenish gray clayey silt with heavy bioturbation are observed (Fig. F11). These dark colored intervals occur only in the upper ~120 m CSF-A with ~50–400 cm thickness. They are divided into two types (I and II) based on appearance. Type I dark intervals (e.g., intervals 346-U1427A-5H-1, 20–90 cm [30.5–31.2 m CSF-A]; 7H-1, 0 cm, to 7H-2, 130 cm [49.3–51.26 m CSF-A]; and 9H-1, 0 cm, to 9H-4, 45 cm [68.3–71.94 m CSF-A]) are composed mainly of siliciclastic-rich sediment (i.e., silty clay) and are black to dark greenish gray. Type II dark intervals (e.g., intervals 12H-3, 0 cm, to 12H-5, 20 cm [99.54–102.74 m CSF-A]; and 13H-2, 80 cm, to 13H-4, 10 cm [108.61–110.87 m CSF-A]) are composed of nannofossil-rich clayey silt and nannofossil ooze and are very dark greenish gray to grayish brown.

Composition

The major lithologies of Subunit A1 are dominated by fine- to medium-grained terrigenous materials and biogenic carbonate and biosiliceous components. The relative abundances of terrigenous and biogenic components change alternately (see Site U1427 smear slides in "Core descriptions"). Volcanic glass and pyrite are observed throughout the sediment, and scattered shell fragments and wood fragments can be found in some intervals. Carbonate concretions were observed at intervals 346-U1427A-6H-5, 120–140 cm (45.87–46.07 m CSF-A), and 346-U1427B-6H-2, 90–100 cm (45.20–45.30 m CSF-A), and probably represent the same diagenetic horizon. The dark color intervals contain organic matter and pyrite, although the pyrite contents of these layers are not significantly higher than other intervals.

Subunit A2

Intervals: 346-U1427A-15H-1, 0 cm, to 87X-CC, 48 cm; 346-U1427B-17H-1, 0 cm, to 65H-5, 46 cm; 346-U1427C-15H-4, 0 cm, to 52H-CC, 24 cm
Depths: Hole U1427A = 125.53–547.92 m CSF-A; Hole U1427B = 130.95–405.95 m CSF-A; Hole U1427C = 130.86–351.79 m CSF-A
Age: Middle Pleistocene (0.5 Ma) to early Pleistocene (1.4 Ma)

Lithologies and structures

Subunit A2 is distinguished from Subunit A1 by the lack of dark color intervals and the occurrence of laminated sediment. Subunit A2 consists of clayey silt, silty clay, silt, nannofossil-rich clayey silt, biosiliceous-rich clayey silt, and nannofossil ooze (Fig. F10). The major lithology of Subunit A2 is similar to that of Subunit A1 and is characterized by meter- to several tens of meters–scale alternations of biogenic component–rich clayey silt and biogenic component–poor clayey silt. The biogenic component is mainly composed of nannofossils; however, diatoms are the major component deeper than 449.6 m CSF-A.

As a minor lithology, laminated sediment is observed at three intervals in Hole U1427A: Sections 346-U1427A-17H-6 to 18H-7 (149.8–163.1 m CSF-A), 23H-6 to 24H-6 (208.8–219.8 m CSF-A), and 45H-1 to 49H-CC (318.00–342.19 m CSF-A) and three intervals in Hole U1427B: Sections 346-U1427B-19H-1 to 20H-4 (149.3–163.8 m CSF-A), 25H-1 to 27H-1 (207.5–224.8 m CSF-A), and 47H-1 to 51H-CC (320.7–343.0 m CSF-A). These intervals can be correlated between the two holes. Laminations are generally millimeter-thick and greenish gray in color (Fig. F12) and are composed of silty clay with minor amounts of diatoms.

Composition

The major lithologies of Subunit A2 are dominated by fine- to medium-grained terrigenous materials and biogenic carbonate and biosiliceous components similar to Subunit A1. Calcareous nannofossils are the most dominant of the biogenic components. However, calcareous microfossils, including nannofossils and planktonic and benthic foraminifers, are

rarely observed deeper than ~430 m CSF-A. Dispersed volcanic glass and pyrite are observed throughout the sediment. Shell fragments can also be frequently found, especially from ~370 to 450 m CSF-A.

Summary and discussion

The sedimentary succession at Site U1427 records the paleoceanographic history of the marginal sea from the early Pleistocene to Holocene. The lithostratigraphic characteristics appear to respond sensitively to regional and global climate change.

The lithology of Site U1427 consists of one unit (A), which is characterized by alternation of clayey silt and nannofossil-rich clayey silt over depth scales of meters to tens of meters. Unit A is further divided into two subunits (A1 and A2) based on differences in minor lithology. Sediment appearance at Site U1427 is much different from what is observed at other sites drilled during Expedition 346. Unit I sediment at sites deeper than 900 m are characterized by centimeter- to decimeter-scale alternations of dark and light colored layers. Those dark–light alternations are correlatable in deeper parts of the basin (Tada et al., 1992). Ikehara et al. (1994) showed that the most recent distinct dark layer, deposited during the Last Glacial Maximum (LGM), is observed in all sediment cores except for those shallower than 500 m water depth. The lack of dark–light alternations at Site U1427, which is related to deepwater oxygenation, can be attributed to the shallow setting of this site (~330 m).

The characteristic tens of meters–scale lithologic changes at Site U1427 are reflected in the physical properties. Figure **F13** shows variations in NGR, color reflectance b*, and maximum grain size, which is determined by smear slide observation. Silt/clay-rich sediment has high NGR and low b* values, and nannofossil/biosiliceous-rich sediment has low NGR and high b* values. These data show cyclic changes, in particular in the upper ~350 m CSF-A. Considering the shallow setting of this site, sea level change must have had a strong influence on the sedimentary environment. With an average sedimentation rate of ~40 cm/k.y. (see **"Stratigraphic correlation and sedimentation rates"**), tens of meters–scale changes are probably linked to orbital-scale sea level change.

The maximum grain size variation in Hole U1427A ranges from 50 to 200 µm (Fig. **F13**). Relatively fine grain sizes (<100 µm) are observed at 155, 175, 217–230, 327–352, and 480 m CSF-A. These intervals correspond to the biogenic component–poor silty clay, except for 175 m CSF-A, which is biosiliceous-rich calcareous ooze, and some of them correspond to laminated intervals. The relationship between the maximum grain size and NGR changes with depth. They are well correlated in Subunit A1 (the upper ~130 m CSF-A). Namely, coarser grains are observed in siliciclastic-rich intervals (i.e., high NGR with low b* value). In contrast, the relationship is the opposite in Subunit A2, (~130–480 m CSF-A). In particular, relatively long intervals of siliciclastic-rich sediment (~140–170, 200–250, and 320–350 m CSF-A) consist of fine grain size material. The timing of this change in the relationship between maximum grain size and NGR is consistent with the subunit boundary, and it may be related to the occurrence of dark color intervals and laminated intervals.

The dark color intervals are observed only in Subunit A1, which are the intervals where NGR is positively correlated with maximum grain size. The Type II dark intervals (99.54–102.74 and 108.61–110.87 m CSF-A), which are in nannofossil-rich sediment, are probably related to periods of high productivity in the Late Pleistocene. The Type I dark intervals seem to be transitional from nannofossil-rich to siliciclastic-rich sediment and may be related to perturbations in surface ocean environments during global sea level change. In contrast to dark color intervals, the laminated intervals are observed only in Subunit A2, which are the intervals where NGR is negatively correlated with maximum grain size. Three laminated intervals are composed of siliciclastic-rich and fine-grained sediment (Fig. **F13**). Considering that the pyrite contents, which are based on both smear slide observation and XRD analyses, do not show high values in laminated intervals, these laminations may not be indicative of anoxic environments.

Overall, changes in sedimentation observed at Site U1427 since the early Pleistocene most likely reflect some combination of climate oscillations and eustatic sea level changes. Site U1427 also records the volcanic history of Japan, in particular local volcanoes in western Japan and East Asia. The changes in the relative amount of biogenic components and siliciclastics are plausibly related to the orbital-scale global sea level changes. The high sedimentation rates and good preservation of calcareous fossils at Site U1427 will allow for a suite of high-resolution paleoceanographic studies.

Biostratigraphy

In Hole U1427A, a ~548 m thick succession of Pleistocene sediment was recovered. Throughout the entire succession, nannofossils are generally common to abundant and exhibit moderate to good preservation. Six calcareous nannofossil datums were documented. Planktonic foraminifers are generally abun-

dant, except for a few barren horizons (through 210.7–228.7 m CSF-A) and rare occurrences deeper than 511.8 m CSF-A. Planktonic foraminiferal assemblages are characteristic of temperate to subarctic environments with intermittent incursions of subtropical species. Benthic foraminifers are generally abundant and moderately to well preserved, except for a few samples which are either barren or contain impoverished assemblages. The overall composition of assemblages indicates shelf to upper slope paleodepths. However, downcore changes in assemblage composition reflect changing paleoenvironmental conditions, probably related to distinct phases of Pleistocene climate evolution. In particular, alternating peak abundances of *Cassidulina* and *Uvigerina* in the upper part of the succession (to 308.9 m CSF-A) suggest marked glacial–interglacial changes in surface productivity and bottom water ventilation following inception of high-amplitude 100 k.y. climatic cycles after ~0.9 Ma. Ostracods are present and well preserved throughout the succession and show highest abundance peaks deeper than ~346 m CSF-A in Hole U1427A. Radiolarians are generally rare throughout the section, with the exception of the base of Hole U1427A (547.9 m CSF-A) where they are abundant. Four biostratigraphic markers are documented in Hole U1427A from the *Stylatractus universus* Zone (Middle Pleistocene) and the *Botryostrobus aquilonaris* Zone (Late Pleistocene). Diatoms are generally abundant and exhibit excellent preservation throughout the succession. No biostratigraphically useful marker species were recorded. High abundances of *Chaetoceros* spores and *Paralia sulcata* throughout the succession indicate a productive coastal environment. Freshwater diatom species differing from those at previous sites were also documented. The presence of *Fragilaria* (benthic) and *Cyclotella* (planktonic) specimens indicates running waters and/or lake origin. Phytoliths were also observed in all samples. The radiolarian, calcareous nannofossil, and planktonic foraminifer datums generally agree with only minor inconsistencies. The integrated calcareous and siliceous microfossil biozonation is shown in Figure **F14** with microfossil datums presented in Table **T4.** A biostratigraphic age-depth plot is shown in Figure **F15.** See **"Stratigraphic correlation and sedimentation rates"** for a discussion of sedimentation rates at Site U1427.

Calcareous nannofossils

Calcareous nannofossil biostratigraphy is based on the analysis of 87 core catcher and 26 split-core section samples from Hole U1427A. Nannofossils are present throughout the Pleistocene succession with only minor barren intervals (Table **T5;** Fig. **F16**). Nannofossils are generally common to abundant and preservation is mostly moderate to good (Table **T5**).

Nannofossil diversity at Site U1427 is higher than at IODP Sites U1422–U1426. The nannofossil assemblage consists of 28 taxa, including *Braarudosphaera bigelowii, Calcidiscus leptoporus, Calcidiscus macintyrei, Coccolithus pelagicus, Dictyococcites* spp., *Emiliania huxleyi, Florisphaera profunda, Gephyrocapsa caribbeanica, Gephyrocapsa margerelii/muellerae, Gephyrocapsa oceanica, Gephyrocapsa omega, Gephyrocapsa* spp. (>4 µm), *Gephyrocapsa* spp. large (>5.5 µm), *Gephyrocapsa* spp. (<4 µm), *Helicosphaera carteri, Helicosphaera sellii, Helicosphaera* spp., *Pontosphaera japonica, Pontosphaera* spp., *Pseudoemiliania lacunosa, Reticulofenestra asanoi, Reticulofenestra* "small," *Reticulofenestra* spp., *Rhabdosphaera clavigera, Syracosphaera* spp., and *Umbilicosphaera sibogae*. Specimens of *Reticulofenestra* <5 µm are referred to as *Reticulofenestra* "small." Medium-sized specimens of *Reticulofenestra* (5–7 µm), excluding *R. asanoi*, are referred to as *Reticulofenestra* spp. in Table **T5.** The only specimen of *Coronocyclus nitescens* found in Sample 346-U1427A-51H-5W, 75 cm (351.5 m CSF-A), is documented as a reworked species (last occurrence [LO] at 12.12 Ma). The documented occurrences of *C. macintyrei* are tentative, as individuals were rare, confined to only one sample, and generally <10 µm.

Nannofossil Zones CN15/NN21 through CN14a/NN19 are recognized (Fig. **F14**) based on the first occurrence (FO) of *E. huxleyi*, the LO of *P. lacunosa*, and the presence of *G. oceanica* and *G. caribbeanica*. Additionally, the LO of *R. asanoi* at 347.0 m CSF-A (Sample 346-U1427A-51H-1W, 75 cm), the base common occurrence (Bc) of *R. asanoi* at 426.6 m CSF-A (Sample 67H-CC), the LO of *Gephyrocapsa* spp. large (>5.5 µm) at 482.0 m CSF-A (Sample 80H-1W, 23 cm), and the LO of *H. sellii* at 484.6 m CSF-A (Sample 80H-3W, 80 cm) (Fig. **F17**) provide good age control for the Pleistocene sequence.

Radiolarians

A total of 59 core catcher samples from Hole U1427A were prepared for radiolarian analyses. Radiolarians are generally rare throughout the section (Table **T6;** Fig. **F16**), with the exception of the base of the hole, where radiolarians are abundant (Sample 346-U1427A-87X-CC; 547.9 m CSF-A).

Four biostratigraphic markers were found in Hole U1427A (Table **T4**), including the *S. universus* (Middle Pleistocene) and *B. aquilonaris* (Late Pleistocene) Zones (Fig. **F14**). Sample 346-U1427A-1H-CC (1.7 m CSF-A) is dominated by the *Larcopyle polyacantha* group (including *Larcopyle buetschlii*), belonging to

the *L. buetschlii* Interval Biozone (0.01 Ma to recent) of Itaki and Ikehara (2003) of Holocene age. Pleistocene datums include the LOs of *Lychnocanoma sakaii* (0.05 Ma) at 21.4 m CSF-A (Sample 3H-CC), *Amphimelissa setosa* (0.08 Ma) at 50.0 m CSF-A (Sample 6H-CC), and *Spongodiscus* sp. (0.29 Ma) at 97.0 m CSF-A (Sample 11H-CC). According to Sakai (1980), the FO of *Spongodiscus* sp. is close to the top of the *Eucyrtidium matuyamai* Zone in the North Pacific. Based on the absence of *E. matuyamai* and presence of *Spongodiscus* sp. at 528.1 m CSF-A (Sample 85X-CC), the lower part of Hole U1427A can be placed in the *S. universus* Zone.

In Hole U1427A, the abundance of warm-water taxa such as *Dictyocoryne profunda, Dictyocoryne truncatum, Didymocyrtis tetrathalamus, Euchitonia furcata, Hymeniastrum euclidis*, and the *Octopyle/Tetrapyle* group are much higher compared to Sites U1422–U1426. Because these warm-water radiolarians migrate from the East China Sea to the marginal sea with the TWC, their higher abundances are likely associated with interglacial highstands. In contrast, *Stylochlamydium venustum, Ceratospyris borealis, A. setosa*, and *Spongodiscus* sp. are characteristic cold-water species typical of glacial periods (Itaki et al., 2007). These taxa frequently occur in this hole.

The "Tr" value, which is a simple temperature index based on radiolarians present in the North Pacific Ocean by Nigrini (1970), was calculated in Hole U1427A. In this report, it is defined by

$$Tr = W/(W + C),$$

where W and C are cumulative ranks of abundance for warm- and cold-water species, respectively. Ranks of each species are

5 = abundant (A).
4 = common (C).
3 = few (F).
2 = rare (R).
1 = present (P).
0 = absent (B).

In Hole U1427A, the Tr value fluctuates significantly through the section, with a similar trend to the sediment color index b* (e.g., high Tr values coincide with high b* values) (Fig. **F18**). As Tr is closely related to the interglacial inflow of the TWC, higher b* values most likely correlate with interglacial intervals of the marine isotope curve (Lisiecki and Raymo, 2005). This probable correlation is broadly consistent with biostratigraphic datums in Hole U1427A (Fig. **F15**).

Diatoms

Diatom biostratigraphy was based on smear slides from core catcher samples. A total of 87 core catcher samples were examined. Because no biostratigraphically useful marker species were found, age assignments were not possible. Although rare abundances of *Neodenticula koizumii* (one of the biostratigraphic markers) were found (Table **T7**), these are reworked and were not considered. Rare, reworked specimens from other species were also found throughout the entire succession. However, they represent <0.5% of the assemblage, indicating that the ecological significance of the diatom associations can still be used. Overall, the preservation of the diatoms is excellent, with a considerable amount of specimens still preserving their organic matter (Fig. **F19**).

Overall, diatom abundance is commonly high (20%–60%) through the succession. Abundance >60% is also common (Figs. **F16, F20;** Table **T7**). The high abundances (20%–60%) of *Chaetoceros* spores and *P. sulcata* (Fig. **F20;** Table **T7**) indicate a productive coastal environment. Diatom freshwater species are present in the succession. However, the species found here, benthic specimens from the genus *Fragilaria* and planktonic specimens from the genus *Cyclotella*, were not found at the previous sites. Phytoliths were found, with no particular pattern of distribution, in all observed samples.

Planktonic foraminifers

Planktonic foraminifers were examined in core catcher samples from Hole U1427A (87 samples). Relative abundance of taxa and visual estimates of assemblage preservation are presented in Table **T8.** Planktonic foraminifers are generally abundant, except for a few barren horizons (Samples 346-U1427A-23H-CC through 25H-CC) and rare occurrences deeper than Sample 84X-CC (511.8 m CSF-A) (Fig. **F16**). Planktonic foraminifers are found only in the finer size fraction (63–150 µm) in Sample 19H-CC (172.9 m CSF-A). To assess assemblage composition and variability, all specimens from the >150 µm fraction were picked and transferred to slides for identification and counting. Overall, preservation is moderate to good throughout the succession, becoming poor in samples where planktonic foraminifers are rare.

Planktonic foraminiferal assemblages are characteristic of temperate to subarctic environments with intermittent incursions of subtropical species. The assemblages mainly consist of *Globigerina bulloides, Neogloboquadrina pachyderma* (sinistral and dextral), and the *Neogloboquadrina kagaensis* group (*N. ka-*

gaensis and *Neogloboquadrina inglei*) with rare occurrences of *Globigerina umbilicata, Globigerina quinqueloba, Globigerinita glutinata, Globigerinoides ruber, Globorotalia inflata, Globorotalia praeinflata, Globorotalia menardii, Globoturborotalita woodi, Neogloboquadrina dutertrei* (= *Neogloboquadrina himiensis*), *Neogloboquadrina humerosa*, and *Pulleniatina obliquiloculata*. The subtropical species *G. ruber* and *P. obliquiloculata* are rare (Table T8). *G. ruber* co-occurs with abundant dextral *N. pachyderma* in Sample 346-U1427A-43H-CC (313.1 m CSF-A). The presence of these subtropical species suggests intermittent warm ocean conditions during sea level highstands, when the Tsushima Strait remains open (Fig. F21).

G. bulloides shows a marked increase in abundance from Sample 346-U1427A-51H-CC to the top of the section (Fig. F21) associated with sporadic peaks in *G. quinqueloba* (in Samples 45H-CC, 8H-CC, and 7H-CC) (Fig. F21; Table T8). This pattern may be related to increasing (yet variable) upwelling and cooling conditions from the Middle to Late Pleistocene.

The top of the high abundance interval of *G. inflata* in Sample 346-U1427A-82X-CC (491.9 m CSF-A) indicates an age older than 1.24–1.34 Ma. The coiling direction of *N. pachyderma* changes from dextral to sinistral between Samples 78H-CC (477.4 m CSF-A) and 65H-CC (417.0 m CSF-A). This event marks the Zone PF7/PF8 boundary in the regional zonation for the marginal sea (Maiya, 1978). The LO of the *N. kagaensis* group (0.7 Ma) (Kucera and Kennett, 2000) is in Sample 29H-CC (246.3 m CSF-A). The species *G. ruber* (pink), which ranges from 0.12 to 0.4 Ma in the Pacific and Indian Oceans, is only present in Sample 5H-CC (39.5 m CSF-A).

Benthic foraminifers

Benthic foraminifers were examined in core catcher samples from Hole U1427A (87 samples). Samples with an average volume of ~20 cm^3 were processed from all core catchers to obtain quantitative estimates of benthic foraminiferal distribution patterns downhole. The mudline sample recovered in Hole U1427A was also investigated. To assess assemblage composition and variability, ~100 specimens from the >150 µm fraction were picked and transferred to slides for identification and counting. The presence and distribution of benthic foraminifers was additionally checked in the 63–150 µm fraction to ensure that assemblages in the >150 µm fraction were representative and that small species such as phytodetritus feeders or small infaunal taxa were not overlooked.

Benthic foraminifers are generally abundant and moderately to well preserved throughout the ~548 m thick Pleistocene succession recovered in Hole U1427A (Figs. F16, F22; Table T9). However, Samples 346-U1427A-23H-CC through 25H-CC (210.7–228.7 m CSF-A), which probably correspond to marine isotope Stage (MIS) 16 following a tentative correlation of color reflectance b* data to the benthic $\delta^{18}O$ stack of Lisiecki and Raymo (2005), are barren. Samples 15H-CC (135.2 m CSF-A), 17H-CC (154.1 m CSF-A), and 45H-CC (323.0 m CSF-A) contain only impoverished assemblages (Figs. F16, F22).

A total of 64 benthic foraminiferal taxa were identified. Table T9 summarizes the downcore distribution of benthic foraminifers in core catcher samples from Hole U1427A. Figure F23 illustrates characteristic taxa. The overall composition of assemblages indicates shelf to upper slope paleodepths throughout the Pleistocene. Species commonly recorded through the succession include the calcareous species *Bolivina pacifica, Cassidulina japonica, Cassidulina norcrossi, Cibicidoides lobatulus, Epistominella pulchella, Nonionellina labradoricum, Trifarina angulosa* (= *Angulogerina kokozuraensis* of Kato, 1992), *Uvigerina peregrina*, and *Uvigerina yabei*, which typically indicate enhanced organic flux and/or dysoxic conditions at the seafloor and within the uppermost few centimeters of the sediment (Gooday, 1993; Jorissen et al., 1995, 2007; Jorissen, 1999). High abundance of *Globobulimina pacifica* is also recorded in Samples 346-U1427A-7H-CC through 11H-CC (59.12–97.04 m CSF-A), and *Elphidium* sp. occurs frequently in core catcher samples deeper than ~480 m CSF-A.

Downcore changes in assemblage composition at Site U1427 reflect changes in paleoenvironmental conditions that are probably linked to distinct phases of Pleistocene climate evolution. Alternating peak abundances of *Cassidulina* and *Uvigerina* in the upper part of the succession (Samples 346-U1427A-1H-CC through 42H-CC; 1.74–308.9 m CSF-A) suggests elevated but highly fluctuating food fluxes throughout the Late to Middle Pleistocene (~0.9–0 Ma). *Cassidulina* thrives on pulsed phytodetritus fluxes (Gooday, 1993), whereas *Uvigerina* is a high-productivity indicator tolerant of slightly dysoxic conditions (Jorissen et al., 1995, 2007; Jorissen, 1999). These fluctuations probably relate to major glacial–interglacial changes in surface productivity and bottom water ventilation following inception of high-amplitude climatic cycles after ~0.9 Ma. Higher frequency variability associated with millennial-scale climate events may be identified in higher resolution studies but is not detected in core catcher samples because of the coarse shipboard sampling resolution. In contrast, within the interval ~313–490 m CSF-A (Samples 43H-CC through 81H-CC, early Pleistocene) assemblages are generally dominated by *Uviger-*

ina and contain fewer *Cassidulina*, suggesting more consistent high-productivity conditions. Finally, samples deeper than ~490 m CSF-A (Samples 82H-CC through 87H-CC) contain higher abundances of *Elphidium* and low numbers of planktonic foraminifers, indicating a more marginal shelf environment.

Ostracods

Ostracods were also examined during shipboard preparation of benthic foraminifer samples. The mudline sample recovered in Hole U1427A was also investigated. All specimens present in the >150 µm fraction were picked and transferred to slides for identification and counting. Ostracod abundance varies markedly downhole, ranging from absent to 104 specimens per sample. The highest abundance peaks are observed deeper than ~346 m CSF-A in Hole U1427A. Abundance maxima are observed at 59.1, 271.5, 346.8, 365.7, 384.7, 449.9, and 487.0 m CSF-A (Figs. **F16, F22;** Table **T10**). When compared to the downhole record of the color reflectance parameter b*, which can be used to infer glacial–interglacial intervals (see **"Benthic foraminifers"**), abundance maxima seem to correspond to higher b* values, thus interglacial periods. In contrast, periods of ostracod abundance minima and barren intervals correspond to lowest b* values and presumably glacial conditions (Figs. **F16, F22**). The taxonomic composition of the ostracod assemblage and its distribution throughout the cored interval could not be established on the ship because of time limitations and was deferred to postexpedition studies. However, the main species found at Site U1427 are illustrated in Figure **F24.**

Mudline samples

The mudline sample from Hole U1427A was gently washed in order to preserve fragile, agglutinated foraminifer specimens with extremely low fossilization potential. The mudline sample contains a few organically cemented agglutinated species including *Ammodiscus anguillae, Haplophragmoides sphaeriloculum, Miliammina echigoensis*, and *Reophax scorpiurus* as well as abundant specimens of the calcareous taxa *Bolivina decussata, B. pacifica, C. norcrossi, Epistominella* sp., *Fursenkoina bradyi, G. pacifica, T. angulosa, Triloculina* sp., and *Uvigerina* sp. (Figs. **F25, F26**). The dominance of small (<150 µm) bolivinids and fursenkoinids in the mudline assemblage points to a high organic export flux and strongly dysoxic conditions at the seafloor and upper centimeters of the sediment.

The mudline sample from Hole U1427A also contains abundant and well-preserved diatoms. Calcareous nannofossils found in the mudline sample exhibit moderate to good preservation. Specimens of *C. leptoporus, C. pelagicus, F. profunda, G. oceanica, Gephyrocapsa* spp. (>4 µm), *Gephyrocapsa* spp. large (>5.5 µm), and *Gephyrocapsa* spp. (<4 µm) were identified via light microscope and scanning electron microscope. Presumably in situ large *Gephyrocapsa* spp. with maximum diameters >5.5 µm are present in the mudline sample. This is noteworthy because their last occurrence is documented at 1.24 Ma by Gradstein et al. (2012).

Geochemistry

The geochemistry of sediment and water at Site U1427, within sight of Tottori Prefecture, was completely unknown before drilling. Consequently, after the flying pace at Sites U1422–U1426, the geochemistry group collectively decided that only a few squeezed interstitial water (IW-Sq) samples would be collected in Hole U1427A. By ~26 m CSF-A, interstitial water emerging from the squeezers was obviously yellow, alkalinity had reached 100 mM, and we knew Site U1427 was an extreme example of organic matter decomposition. Being humble guests in Tottori, we felt compelled to collect Rhizon water samples through the upper 10 m and to gather extra volumes of water for future shore-based studies.

Upon completion of Site U1427, the sulfate–methane transition (SMT) was found to lie at ~5 m CSF-A. However, this horizon was not captured in detail with routine sampling in Hole U1427A and was situated within a core gap in Hole U1427B. Sedimentary objectives and time also precluded sampling for the construction of headspace (HS) CH_4 and dissolved hydrogen sulfide (HS^-) profiles across the SMT and NH_4^+ and metal profiles immediately below the seafloor. A return to Site U1427 several weeks later allowed us to fully document this location.

The seafloor at Site U1427 is at 330 m water depth (see **"Operations"**). However, the marginal sea has a very shallow thermocline. Thus, despite the shallow water depth, the position of the seafloor at Site U1427 appears to be bathed in Japan Sea Proper Water (JSPW) with a salinity of 34.06 (Senjyu, 1999).

Sample summary

After initial operations at Site U1427, the geochemistry group had collected and analyzed the following samples (Tables **T11, T12, T13, T14, T15**):

- 2 mudline (ML) samples, representing water poured from inside the liner of Cores 346-U1427A-1H and 346-U1427B-1H.

- 29 interstitial water samples from whole-round squeezing (IW-Sq) of discrete intervals in Hole U1427A.
- 19 interstitial water samples from Rhizons (IW-Rh) of discrete points in Hole U1427B.
- 29 sediment samples from interstitial water squeeze cakes; thus, the distance between samples varies significantly with depth.
- 74 headspace (HS) gas samples from the top of one section of almost every core.
- 6 Vacutainer (VAC) gas samples.

Upon returning to Site U1427 several weeks later, the geochemistry group collected an additional set of samples from Hole U1427C:

- 1 mudline sample, representing water from inside the liner of Core 346-U1427C-1H.
- 20 IW-Rh samples of discrete points in Hole U1427C.
- 12 HS gas samples from the top of each section of Cores 346-U1427C-1H and 2H.

Carbonate and organic carbon

The carbonate, carbon, and nitrogen profiles at Site U1427 (Fig. **F27**) are similar to those of Unit I at Site U1426 (see **"Geochemistry"** in the "Site U1426" chapter [Tada et al., 2015g]). Specific depths for subunits at Site U1427 have not yet been defined. For the purposes of this report, and as advised by the Sedimentology Laboratory, we divide the recovered sedimentary record into an upper unit (0–125.5 m CSF-A) and lower unit (125.5–540.30 m CSF-A).

Sediment at Site U1427 contains modest amounts of carbonate (Fig. **F27**) when compared to material recovered at other sites during Expedition 346. The average carbonate content across all samples analyzed at Site U1427 is 9.4 wt% (Table **T11**). Only Site U1426 had similarly high values. Moreover, carbonate contents vary significantly with depth. For the upper unit, carbonate contents vary between 2.0 and 25.1 wt%. The suite of samples in the upper 50 m of Hole U1427A shows up to 10 wt% differences in carbonate contents between consecutive samples spaced 4 m apart. For the lower unit, carbonate contents average 9.7 wt%, which is very similar to that for the upper unit. Samples with relatively high carbonate contents (>8 wt%) are consistent with intervals containing moderate to high abundances of calcareous microfossil remains, such as coccoliths and foraminifer tests (see **"Biostratigraphy"**). It is likely that higher resolution cycles of carbonate exist at Site U1427, although documenting this full variance will need to wait for shore-based analyses.

The total carbon (TC) content of sediment at Site U1427 ranges between 0.9 and 5.1 wt% (Fig. **F27**). This range represents the variance in mixtures of carbonate carbon (described above) and organic carbon (described below). For example, the high TC value of 5.1 wt% reflects the addition of 3.0 wt% C from carbonate (24 wt% $CaCO_3$) and 2.1 wt% C from organic matter (5.25 wt% CH_2O) (see **"Geochemistry"** in the "Methods" chapter [Tada et al., 2015b]). Of the sites drilled so far during Expedition 346, the relative abundance of carbonate carbon and organic carbon are the most balanced at Site U1427.

The total organic carbon (TOC) contents of samples from Site U1427 range between 0.5 and 2.4 wt% and average 1.2 wt% (Fig. **F27**). Although lower than observed at Site U1426, these values are still fairly high for marine sediment (Müller and Suess, 1979; Emerson and Hedges, 1988). The TOC contents appear to vary more within the upper unit. However, this variability may simply reflect the higher resolution of sampling over the upper 50 m. We could not address the origin and preservation state of the organic matter at Site U1427 because the Source Rock Analyzer (Rock-Eval) remained inoperable, even though continued efforts were made to fix the system while on location. However, we suspect that a significant portion of the organic carbon derives from the adjacent landmass. A more complete understanding of organic carbon, including variations over short time/depth increments and in the origin, will have to await postcruise investigations.

The total nitrogen (TN) contents of sediment at Site U1427 are relatively low. For the upper unit, TN has a mean value of 0.25 wt%, a maximum value of 0.33 wt% (in the topmost sample at 1.56 m CSF-A), and a minimum value of 0.16 wt% (at 2.60 and 7.75 m CSF-A). Compared to Site U1426, TN contents are slightly less at Site U1427. However, the difference is not greater than the error of this analysis (±0.07, 1σ, as determined by repeat analyses of an internal standard, n = 6). At both Sites U1426 and U1427, downhole trends in TN contents generally follow those of TOC. However, there is only a modest correlation (r^2 = 0.51) between the two parameters.

The C:N (atomic) ratio of organic matter is an important parameter for understanding provenance and degradation (Waples, 1985; Meyers, 1997). At Site U1427, this ratio is relatively low, with an average of 5.4. This ratio is partly due to the relatively low values of TC and TN and the limitations on such analyses aboard the R/V *JOIDES Resolution* (see **"Geochemistry"** in the "Methods" chapter [Tada et al., 2015b]). However, there also appears to be a true decrease in C:N with depth. The average C:N for the

upper unit is 6.5, whereas that of the lower unit is 4.5.

Manganese and iron

Dissolved Mn and Fe profiles at Site U1427 (Table T12; Fig. F28) differ somewhat from those at other locations drilled during Expedition 346. As at other sites, some samples from shallow depths have higher concentrations in Mn, Fe, or both. Moreover, IW-Sq and IW-Rh samples from similar depths have different concentrations of Mn, Fe, or both. However, the absolute concentrations and depth intervals of elevated Mn and Fe concentrations are different at Site U1427.

Mn concentration is very low (0.1 µM) in the mudline sample, similar to observations at other sites. Dissolved Mn reaches a maximum of 5 µM at 0.50 m CSF-A (Fig. F29). Deeper than ~2 m CSF-A, Mn concentrations decrease below detection (0.1 µM) in the Rhizon samples. The squeezed samples are also low, remaining <1 µM for the remainder of samples. With either sampling technique, the main finding is that Mn concentrations are very low at Site U1427, especially compared to other sites drilled during Expedition 346.

Low dissolved Mn concentrations at Site U1427 are consistent with previous results and discussions of Mn cycling at other sites during Expedition 346. In shallowly buried sediment, microbes use Mn oxides during consumption of organic carbon, which releases dissolved Mn to interstitial water (e.g., Froelich et al., 1979). Deeper in the sedimentary columns, precipitation of Mn-bearing carbonate phases has been observed, which removes dissolved Mn (e.g., Middelburg et al., 1987). Site U1427 appears different from other sites because the depths of Mn oxide dissolution and Mn carbonate precipitation are much closer to the seafloor and because carbonate precipitation prevents dissolved Mn concentrations from rising to significant concentrations at depth.

Dissolved Fe concentration is below the detection limit (1 µM) in the mudline sample, similar to that observed at previously drilled sites during Expedition 346. For IW-Sq samples, Fe concentrations show high variability between 1 and 30 µM from the seafloor to ~400 m CSF-A (Table T12; Fig. F28). By contrast, Fe concentrations are below the detection limit for all IW-Rh samples (Fig. F29). We are uncertain how to explain the Fe data, especially given previous findings at Sites U1424 and U1425. We expected to find a small maximum in dissolved Fe using Rhizons across the upper 1 m. We may have missed this peak, despite the reasonably close spacing of samples. We anticipated low dissolved Fe concentrations in the IW-Sq samples, perhaps caused by fine-grained magnetite (see "Geochemistry" in the "Site U1425" chapter [Tada et al., 2015f]). However, we did not expect measurable Fe concentrations at 400 m below the seafloor.

Alkalinity, ammonium, and phosphate

The alkalinity, NH_4^+, and PO_4^{3-} profiles at Site U1427 (Table T12; Fig. F30) are exceptional given their concentration changes over depth. Concentrations of all three are relatively low in the mudline sample, being 2.4 mM, 14 µM, and 2.7 µM, respectively. Below the seafloor, concentrations rise very quickly. At ~26 m CSF-A, alkalinity is 99.5 mM, NH_4^+ is 11.9 mM, and PO_4^{3-} is 625 µM. The maximum values are 132.3 mM alkalinity at 352.3 m CSF-A, 39.6 mM NH_4^+ at 446.5 m CSF-A, and 625 µM PO_4^{3-} at 26.5 m CSF-A.

Over the past four decades of scientific drilling, extreme profiles of alkalinity, NH_4^+, and PO_4^{3-} have been generated at several locations. Examples of drill sites where alkalinity exceeds 100 mM in the upper 200 m below the seafloor include DSDP Site 496/568 (Middle America Trench, Legs 67/84 [Harrison et al., 1982; Hesse et al., 1985]) and ODP Sites 685/1230 (Peru margin, Legs 112/201 [Suess, von Huene, et al., 1988; D'Hondt, Jørgensen, Miller, et al., 2003]), 997 (Blake Ridge, Leg 164 [Paull, Matsumoto, Wallace, et al., 1996]), 1019 (California margin, Leg 167 [Lyle, Koizumi, Richter, et al., 1997]), 1084 (Namibia margin, Leg 175 [Wefer, Berger, Richter, et al., 1998; Murray et al., 1998]), and 1251 (Oregon margin, Leg 204 [Tréhu, Bohrmann, Rack, Torres, et al., 2003]). These sites span a wide range of latitude, longitude, bottom water chemistry, and water depth (Site U1427 = 321 m; Sites 685/1230 = 5086 m). There is, however, a common theme: at each of these sites, organic matter has accumulated along a continental margin with very high linear sedimentation rates (>30 cm/k.y.) over the last 1 m.y. or so.

Sediment buried beneath the seafloor at Site U1427 averages ~3.0 wt% CH_2O with a C:N ratio of 6.5 (above). More crucially, because of high terrigenous input from the adjacent continent ("Lithostratigraphy"), the mean sedimentation rate is ~40 cm/k.y. ("Biostratigraphy"). An enormous quantity of organic carbon and nitrogen are entering the sediment column at Site U1427 and fueling fermentation and methanogenesis. As discussed in previous chapters of this volume and elsewhere (e.g., Sayles and Manheim, 1975; Gieskes, 1975; Harrison et al., 1982; Murray et al., 1998), these processes release alkalinity (as HCO_3^-), NH_4^+, and PO_4^{3-} to pore space at depth, but much of the PO_4^{3-} precipitates into phosphate-bearing minerals.

When shown over the entire depth of the cored site (~550 m CSF-A), both the alkalinity and NH_4^+ profiles at Site U1427 appear concave downward between the seafloor and 100 m CSF-A (Fig. F30). This is true for all "high alkalinity" sites listed above. However, such broad-scale presentation overlooks an essential aspect of the geochemistry, as documented at Site U1427 (Fig. F31). High-resolution Rhizon sampling over the uppermost 10 m shows a significant inflection in the alkalinity profile at ~5 m CSF-A. Shallower than this inflection, alkalinity changes nearly linearly by ~9 mM/m; below the inflection, it changes nearly linearly by ~3 mM/m. This implies an approximate threefold increase in the net flux of alkalinity added to interstitial water of Site U1427 at ~5 m CSF-A. Moreover, the source of this excess alkalinity does not involve solid organic matter because organic matter contains nitrogen, and no inflection in NH_4^+ is found at ~5 m CSF-A.

Therefore, we suggest that the very high alkalinity and NH_4^+ concentrations at Site U1427 have a root cause similar to other high alkalinity sites along continental margins: they mostly reflect the decomposition of considerable organic matter over time, especially through fermentation and methanogenesis. This leads to some testable predictions. Previously drilled locations with very high alkalinity and NH_4^+ concentrations have unusually high Br^- concentrations, yellow water, and considerable biogenic CH_4 (as cited previously). Note, however, that Br^- and color are rarely measured, and CH_4 concentrations are rarely determined at in situ pressure.

Bromide

Site U1427 is the first drilling location during Expedition 346 with a Br^- profile worthy of highlighting (Table T12; Fig. F32). The dissolved Br^- concentration is 0.83 mM in the mudline sample, which is the same as inferred for JSPW (Table T10 in the "Methods" chapter [Tada et al., 2015b]). Below the seafloor, Br^- systematically increases with a concave downward profile. Bromide concentrations are ~1.0 mM at 20 m CSF-A, ~2.0 mM at 400 m CSF-A, and 2.18 mM at 522 m CSF-A. Thus, the shape of the Br^- profile resembles those of alkalinity and especially NH_4^+.

Similar to alkalinity and dissolved NH_4^+, interstitial water has extreme Br^- concentrations at depth at Site U1427. Indeed, after a cursory shipboard review, afforded by the relatively luxurious pace of operations, after acknowledging that Br^- is not routinely measured on interstitial water and after excluding sites with evaporative brines at depth, we found only two sites with higher dissolved Br^- concentrations: Site 685/1230 on the Peru slope (2.49 mM at 491 meters below seafloor [mbsf]) (Martin et al., 1993) and Site 997 on Blake Ridge (3.3 mM at 500 mbsf) (Egeberg and Barth, 1998). As noted above, and similar to Site U1427, Sites 685/1230 and 997 have very high alkalinity and NH_4^+ concentrations.

Bromide is usually considered a highly conservative ion in water chemistry, where concentration changes only with variations in salinity. The reason for exceptionally high dissolved Br^- levels in certain pore waters lies in an understanding of marine halogen cycling (Gieskes and Mahn, 2007). Organic matter landing on the seafloor incorporates Br from seawater. During burial of organic matter and its subsequent decomposition, this Br is released to interstitial water as Br^-. Bromide concentrations thus reflect the integrated accumulation of organic matter over long time frames and generally track NH_4^+ profiles. For locations with high levels of fermentation and methanogenesis at depth, Br^- concentrations typically exceed 1.5 mM (Martin et al., 1993; Egeberg and Barth, 1998; Gieskes and Mahn, 2007). The very high Br^- concentrations at Site U1427 are consistent with other indicators for extreme organic diagenesis at this location. Moreover, the fact that Br^- and NH_4^+ concentrations are still rising with depth at 550 m CSF-A (Fig. F32) indicates this diagenesis extends well beyond the upper 100 m of sediment, and most likely continues deeper than 550 m CSF-A.

Absorbance/Yellowness

Interstitial water samples at Site U1427 are visibly yellow. This phenomenon has been observed previously at several scientific drill sites, although only formally documented at a few locations (e.g., ODP Site 808, Nankai Trough [You et al., 1993]; Site 685/1230, Peru margin [D'Hondt, Jørgensen, Miller, et al., 2003]; and ODP Site 1244, Hydrate Ridge [Tréhu, Bohrmann, Rack, Torres, et al., 2003]).

A total of 51 interstitial water samples collected at Site U1427 were analyzed for their "yellowness" by measuring absorbance at three wavelengths: 375, 325, and 227 nm (Table T14). Examination of nine randomly selected samples showed that absorbance at 325 nm exceeded 1.0 for several samples. Consequently, 1 mL aliquots of all 51 samples, including the initial 9 analyzed, were placed into a vial and diluted with 2 mL of deionized water for analyses.

Absorbance measured for all three wavelengths shows obvious trends with depth (Fig. F33). The mudline sample has very low absorbance. Below the seafloor, absorbance rises rapidly. At the broad scale, absorbance reaches maxima for all three wavelengths between 100 and 300 m CSF-A and declines

at deeper depths. However, a prominent peak in absorbance for 227 nm at ~6 m CSF-A is not seen at other wavelengths. Similar to observations at Sites U1425 and U1426 (see "Geochemistry" in the "Site U1425" chapter and "Geochemistry" in the "Site U1426" chapter [Tada et al., 2015f, 2015g]), the absorbance at longer wavelengths also decreases more rapidly with depth.

The absorbance of interstitial water samples from Site U1427 has been measured in batches with the JWBL standard (see "Geochemistry" in the "Methods" chapter [Tada et al., 2015b]). This is important because it lessens ambiguities in reported measurements between studies, which can arise from different equipment and configurations (e.g., cell length). Interstitial water at Sites 1230 and 1244 have also been determined for absorbance at 325 nm with the JWBL standard (D'Hondt, Jørgensen, Miller, et al., 2003; Tréhu, Bohrmann, Rack, Torres, et al., 2003). The average yellowness of these sites, both characterized by very high CH_4 concentrations, brackets that at Site U1427.

The yellowness of marine water has been ascribed to dissolved organic carbon in general (Briucaud et al., 1981) and fulvic acid more specifically (Krom and Sholkovitz, 1977). At Sites 808 and 1230, the absorbance of water at 325 nm correlates fairly well with independent measurements of dissolved organic carbon (You et al., 1993; Smith, 2005). Considering the degree of yellowness and that Site 808 also has high amounts of CH_4, considerable fermentation and methanogenesis may necessarily occur within the sediment column of Site U1427.

Volatile hydrocarbons

Similar to Site U1426, significant gas expansion occurred during recovery of sediment at Site U1427. Indeed, visible gas cracks and gas voids began appearing inside of core liners within 15 m CSF-A of the seafloor. In theory, these gas release features should first appear when gas concentrations at in situ pressure and temperature conditions surpass those of solubility for interstitial water at shipboard pressure and temperature conditions. At even relatively low in situ gas concentrations, recovery of sediment cores from depth results in gas escaping from interstitial water (Paull et al., 2000).

Methane is the dominant hydrocarbon gas (>99.9%) in HS samples from Site U1427 (Table T13), and the HS CH_4 profile (Fig. F34) appears to exhibit a pattern observed at many other locations (Paull et al., 2000). Methane concentrations in headspace are very low (<50 ppmv) in the first two samples from the upper 3.3 m CSF-A. CH_4 concentration in the next sample, at 12.8 m CSF-A, is 44,000 ppmv. Below this apparent maximum, CH_4 values rapidly decrease to 10,000 ppmv at ~32 m CSF-A and then gradually decrease further to the bottom of the cored hole.

Methane profiles such as found at Site U1427 are mostly an artifact of degassing (Paull et al., 2000). At sites with very high in situ CH_4 concentrations, headspace CH_4 values are low above a shallow SMT. Below the SMT, CH_4 concentrations rise abruptly with depth and shortly cross the CH_4 solubility curve at 1 atm pressure. Within several meters after this crossover depth, gas begins escaping from interstitial water. Once gas voids start occurring, headspace values decrease significantly such that they approximate those on the solubility curve at 1 atm. However, values on this curve decrease with sedimentary depth because core temperatures, even after recovery, are warmer, and the solubility of CH_4 decreases with increasing temperature (Rettich et al., 1981).

Headspace ethane concentrations range between 0 and 9 ppmv in Hole U1427A and generally increase with depth. As a consequence, the downhole CH_4 to C_2H_6 (C1:C2) ratio exceeds 1000 shallower than 260 m CSF-A but gradually decreases, reaching 250 at the bottom of the site. Similar to the CH_4 concentration profile, the C1:C2 profile partly reflects the effect of degassing (Paull et al., 2000) and the different gas solubility of CH_4 and C_2H_6 (Rettich et al., 1981). In general, the C1:C2 ratio increases with depth simply because of differential degassing (Paull et al., 2000). However, a thermogenic origin for some of the CH_4 and other gases at depth cannot be excluded. Small amounts of propane and propene (<26 ppmv) occur in the headspace samples.

Several gas samples were taken from gas voids (Table T15). For these VAC samples, CH_4 concentrations range from 800,000 to 900,000 ppmv, whereas C_2H_6 concentrations range between 50 and 80 ppmv. Importantly, higher molecular weight hydrocarbon gases are absent, presumably because they are diluted by the extremely high CH_4 concentrations. VAC gas samples have been shown to more accurately represent the relative abundance of gases at in situ conditions (Paull et al., 2000).

Overall, the gas concentration profiles at Site U1427 are very similar to those found at other scientific drill sites, notably the same ones with very high interstitial water alkalinity and NH_4^+ concentrations, such as Sites 997, 1230, and 1251 (cited previously). The singular unusual aspect of the gas profiles at Site U1427 is the rapid increase in CH_4 between samples at 3.3 and 12.8 m CSF-A. We contend this is an artifact of sample resolution and that analyses of detailed headspace gas sampling would show a steep

CH_4 concentration gradient rising between 5 and 12 m CSF-A.

All drilling locations discussed in the above paragraphs, with the exception of Site 1084, have gas hydrate within sediment at depth. However, at 330 m water depth, the gas hydrate stability zone is very thin at Site U1427, and in situ CH_4 concentrations probably do not cross the gas hydrate solubility curve.

Sulfate, sulfide, and barium

Almost universally, when examined in detail, drill sites with extreme alkalinity, NH_4^+, and CH_4 concentrations at depth are characterized by a near-linear dissolved SO_4^{2-} profile and a maximum in dissolved HS^- in the upper 0–20 m of sediment. We now return to the prominent alkalinity inflection at ~5 m CSF-A and present the interstitial water SO_4^{2-} (Fig. **F35**) and HS^- (Fig. **F31**) profiles at Site U1427 (Table **T12**).

Sulfate concentration is 28.5 mM in the mudline sample, which is slightly higher than the 28.2 mM inferred for JSPW (Table **T10** in the "Methods" chapter [Tada et al., 2015b]). Below the seafloor, dissolved SO_4^{2-} decreases to 0.0 mM at ~5 m CSF-A. This drop is nearly linear (r^2 = 0.998). Beneath 5 m CSF-A, concentrations remain at 0.0 mM. Sulfide concentration is below the detection limit (~5 µM) at the seafloor, but starting at ~0.4 m CSF-A, HS^- concentrations rapidly increase, reaching a maximum value of 4498 µM at ~5 m CSF-A. Deeper than ~5 m CSF-A, HS^- concentrations decrease to below the detection limit by ~17 m CSF-A.

The linearity of the SO_4^{2-} profile strongly suggests that net SO_4^{2-} removal from sediment at Site U1247 occurs over a thin horizon at 5 m CSF-A rather than over a significant thickness beneath the seafloor. The maximum in dissolved HS^- strongly indicates production of HS^- over the same horizon. The most likely explanation is that a significant upward flux of CH_4 reacts with downward diffusing SO_4^{2-} via anaerobic oxidation of methane (AOM) (Reeburgh, 1976; Borowski et al., 1996):

$$CH_{4(aq)} + SO_4^{2-}{}_{(aq)} \rightarrow HCO_3^-{}_{(aq)} + HS^-{}_{(aq)} + H_2O.$$

As clear from this equation and as discussed previously (see **"Geochemistry"** in the "Site U1422" chapter [Tada et al., 2015c]), removal of SO_4^{2-} across a thin horizon by AOM should generate significant HCO_3^- and HS^-, which must necessarily cause a sharp inflection in alkalinity. The total impact of AOM upon shallow carbon chemistry can be determined through flux calculations that include the loss of SO_4^{2-} and CH_4, the change in alkalinity, and authigenic carbonate precipitation (below). Such calculations have been made for piston cores northeast of Site U1427 and show that AOM consumes almost all SO_4^{2-} in shallow sediment (Snyder et al., 2007). We therefore maintain that methane generation and consumption most likely underlies much of the geochemistry at Site U1427.

A similar theme has emerged in our presentation of dissolved SO_4^{2-} and Ba profiles at sites within the marginal sea (see "Geochemistry" in the "Site U1422" through "Site U1426" chapters [Tada et al., 2015c, 2015d, 2015e, 2015f, 2015g]). Sulfate reduction through oxidation of solid organic carbon, AOM, or some combination of both decreases SO_4^{2-} concentrations to low values. Over time and with sediment burial, barite grains pass into the low-SO_4^{2-} fluids and dissolve (von Breymann et al., 1992; Dickens, 2001). Consequently, interstitial water Ba concentrations are high at depth. The SO_4^{2-} and Ba profiles at Site U1427 (Fig. **F36**) bring a twist to this discussion.

Dissolved Ba concentration is below the detection limit (1 µM) in the mudline sample. Below this depth, Ba concentrations remain very low until ~2 m CSF-A and then begin to rise. As found at previous sites, the increase in dissolved Ba begins above the SMT, and Ba concentrations are higher in IW-Sq samples compared to IW-Rh samples. These aspects have been discussed in previous site chapters. The new consideration is the magnitude of the rise in dissolved Ba concentrations. Within 5 m below the SMT, dissolved Ba concentrations are <80 µM, at least for IW-Rh samples. Indeed, interstitial water Ba values do not rise higher than 250 µM for any sample across the entire sediment column.

Dissolved Ba concentrations below the SMT are much lower at Site U1427 than at other sites drilled during Expedition 346 (von Breymann et al., 1992). We offer two possible explanations. First, the very high sedimentation rate at Site U1427 adds a significant downward burial flux of dissolved Ba below the SMT. This would counter the upward diffusion of dissolved Ba and diminish the expected recycling of Ba across the SMT (Dickens, 2001). Second, the amount of Ba entering the sediment column as barite may be much less at Site U1427 than at sites drilled in deeper water. Much of the barite incorporated into deep-sea sediment forms within the water column in association with sinking organic matter (Bishop, 1988). However, the actual process appears to occur over a depth range, such that barite contents increase significantly with greater water depth

(Ganeshram et al., 2003; van Beek et al., 2007; Dehairs et al., 2008).

Calcium, magnesium, and strontium

Calcium concentration is 9.9 mM at the mudline and decreases to 3.6 mM at 4.3 m CSF-A, where there is an inflection point in the profile and the rate of decrease is reduced (Table T12; Fig. F37, F38). This lower rate of decrease is maintained until a minimum of 1.06 mM is reached at 31.75 m CSF-A, where at this deeper, second inflection point, concentrations begin generally increasing with depth to 5 mM at 540.3 m CSF-A. The increased sample resolution of the upper 10 m CSF-A shows a linear decreasing trend in values from 10 mM, with an inflection point deeper than 4 m CSF-A (Fig. F38).

At the mudline, strontium concentration is 88 µM and decreases fairly linearly to 32 µM at 31.75 m CSF-A (Fig. F37, F38). At deeper depths, concentrations generally begin to increase to a maximum of 138 µM at 540.3 m CSF-A.

Magnesium concentration is 50 mM at the seafloor and remains constant until 10 m CSF-A (Fig. F38), where a maximum of ~65 mM is observed between 40 and 70 m CSF-A. Deeper than 70 m CSF-A, concentrations begin to decline, reaching a minimum of 16.2 mM at 540.3 m CSF-A (Fig. F37).

The decline in calcium and strontium concentrations from 0 to 31.75 m CSF-A suggests that calcite formation is removing both of these elements from interstitial water (Snyder et al., 2007). The relatively constant magnesium concentrations over the same depth interval exclude the possibility of dolomite formation and lends support to the calcite hypothesis. Calcium and strontium both show similar downcore peaks and troughs in their concentration profiles; these elements were analyzed in different analytical runs with different dilutions and standards, indicating that these features are likely real and indicative of changes in authigenic carbonate phases.

Chlorinity and sodium

At Site U1427, Cl^- concentrations with depth yield a profile (Table T12; Fig. F39) somewhat similar to those at other locations drilled during Expedition 346. The mudline sample has a Cl^- concentration of 545 mM, which is the same as the 545 mM expected for JSPW (Table T10 in the "Methods" chapter [Tada et al., 2015b]). Immediately below the seafloor, Cl^- concentrations begin to decrease. The values show considerable scatter when examined in detail (Fig. F39), which probably reflects the relatively low precision of the shipboard automated Cl^- titration system. Nonetheless, Cl^- concentrations clearly decrease to a minimum of between 510 and 520 mM between ~10 and 40 m CSF-A. Deeper than 40 m CSF-A, Cl^- concentrations vary between ~520 and 540 mM.

The decrease in dissolved Cl^- within the upper 50 m of the sediment column is now a robust finding at every site drilled so far during Expedition 346. As discussed previously in this volume, less saline "deep water" probably existed within this basin during the recent past. The significance of the result at Site U1427 concerns the magnitude of the Cl^- minimum and water depth. This location appears to have the lowest Cl^- values, perhaps because it was at ~200 m water depth and within the thermocline during the LGM. A fresher mixed layer in the marginal sea during the LGM with a nominal salinity (*S*) of 31 would explain the Cl^- minima at Site U1427 and foraminifer assemblages and stable isotopes in piston cores (Oba et al., 1991). The Cl^- concentrations of deeper fluids at Site U1427 may represent the long-term average salinity of the thermocline in the marginal sea. Sodium concentrations range from 450 to 470 mM from the mudline to ~3 m CSF-A. From 3 to 60 m CSF-A, concentrations range from 430 to 450 mM. Deeper than 60 m CSF-A, concentrations increase gradually with depth to the bottom of the hole, ranging from 475 to 500 mM.

Potassium

Potassium concentration is 10.4 mM at the mudline and quickly increases to ~12 mM at 0.5 m CSF-A (Table T12; Fig. F40). Potassium increases to a maximum of 16 mM at 70 m CSF-A before decreasing slightly to between 13 and 14 mM for the remainder of the sampled depths.

Boron and lithium

The dissolved boron profile at Site U1427 (Table T12; Fig. F41) exhibits a different pattern than those found at previously drilled sites during Expedition 346. B concentration is 423 µM in the mudline sample, which is similar to the ~420 µM expected for JSPW (Table T10 in the "Methods" chapter [Tada et al., 2015b]). Concentrations then rapidly increase with depth to a distinct peak of ~760 µM at ~40 m CSF-A. This rise is consistent across both IW-Sq and IW-Rh samples, at least over the uppermost 10 m where overlap occurs, and has a concave downward shape. Deeper than 40 m CSF-A, B concentrations become less coherent and more scattered, varying between 430 and 710 µM.

At the coarse depth scale (Fig. F41), dissolved Li increases gradually downhole from a mudline value of

25 µM to a value of 38 µM at 70 m CSF-A. Concentrations then rise more rapidly, such that Li reaches ~680 µM at ~540 m CSF-A. This is the highest Li concentration measured in interstitial water thus far during Expedition 346.

However, the full Li profile at Site U1427 (Fig. **F41**) shows the power of supplementing conventional IW-Sq samples with detailed IW-Rh samples where the sediment characteristics allow (Fig. **F42**). Over the upper 15 m, Li concentrations decrease from 25 µM at the seafloor to ~15 µm at 5 m CSF-A. Li then rises back to ~27 µM at 18 m CSF-A. The gradual coarse-scale rise in Li with depth has a significant trough precisely at the SMT. Similar decreases in Li across the SMT have been found at other high-alkalinity sites (D'Hondt, Jørgensen, Miller, et al., 2003; Tréhu, Bohrmann, Rack, Torres, et al., 2003).

Silica

Comparing water samples analyzed with dual measurements, dissolved Si concentrations (by inductively coupled plasma–atomic emission spectroscopy) and dissolved H_4SiO_4 concentrations (by spectrophotometry) agree well (r^2 = 0.97). Typically, the Si values are slightly less than the H_4SiO_4 values, but this is not considered significant, and we discuss the H_4SiO_4 specifically.

The dissolved H_4SiO_4 profile at Site U1427 (Table **T12;** Fig. **F41**) resembles those at other sites drilled in the marginal basin (Murray et al., 1992), with one main exception. The mudline sample has a concentration of 145 µM. Below this bottom water value, there is a characteristic rapid increase in H_4SiO_4 concentrations to 652 µM at ~1.6 m CSF-A. However, at Site U1427, H_4SiO_4 concentrations change much less with depth compared to other locations. Dissolved concentration is only ~1250 µM at ~540 m CSF-A.

Similar to previously discussed sites, the H_4SiO_4 profile has a fairly straightforward explanation (e.g., Kastner et al., 1977). Within the uppermost meter or so below the seafloor, H_4SiO_4 concentrations increase significantly. This could be caused by temperature, as noted for K^+ (Sayles and Manheim, 1975). More likely, it is caused by rapid dissolution of siliceous microfossils (Schink et al., 1974). The increase in dissolved H_4SiO_4 with depth relates to higher solubility at greater temperature and changes in mineralogy (**"Lithostratigraphy"**). In any case, the rise in H_4SiO_4 concentrations is slower at Site U1427 because the geothermal gradient is much more gradual than at previously drilled sites (**"Downhole measurements"**).

Rhizon commentary

A zone of exceptional interest—the SMT—was hypothesized to exist between 3.0 and 7.5 m CSF-A, based on alkalinity and SO_4^{2-} measurements of routine IW-Sq samples in Hole U1427A. Multiple IW-Rh samples were spread across the depth horizon in Hole U1427B. Other than the unfortunate coincidence of the SMT with a gap between Cores 346-U1427B-1H and 2H, analyses of the Rhizon samples captured the expected kink in alkalinity and inflection in SO_4^{2-} (Fig. **F31**).

Preliminary conclusions

In their now classic review of interstitial water chemistry, Sayles and Manheim (1975) stated: "The most complex pattern of interstitial water diagenesis is found in rapidly deposited, organic-rich, sediments containing a large proportion of terrigenous silts and clays in addition to variable amounts of biogenic carbonate. These sediments are typical of continental margin areas …" Site U1427 exemplifies this type of location. Following early literature (Gieskes, 1975; Sayles and Manheim, 1975), the geochemistry at Site U1427 is explained by the rapid burial of organic carbon driving a series of microbial reactions, including oxic respiration, metal oxide reduction, and sulfate reduction (fermentation and methanogenesis).

Here, we diverge from most previous work to make two summary comments. First, at the broad scale, the overall pattern of diagenesis and interstitial water chemistry at Site U1427 is remarkably predictable. Second, this chemistry cannot be understood or appreciated without a return flux of CH_4 that drives AOM at an SMT. We suggest that basic aspects of geochemistry at Site U1427 are representative of many continental margins.

Paleomagnetism

Paleomagnetic samples and measurements

Paleomagnetic investigations at Site U1427 included measurement of magnetic susceptibility of whole-core and archive-half split-core sections, and natural remanent magnetization (NRM) of archive-half sections. NRM was measured before and after alternating field (AF) demagnetization with a 20 mT peak field for all archive-half sections from Hole U1427A at 5 cm intervals. Because of increased core flow and limited measurement time available at the paleomagnetism station, NRM of archive-half sections from Hole U1427B was measured only after 20 mT AF demagnetization at 5 cm intervals. The FlexIT

core orientation tool (see **"Paleomagnetism"** in the "Methods" chapter [Tada et al., 2015b]) was used to orient Cores 346-U1427A-2H through 25H. The APC-collected core orientation data for Hole U1427A are reported in Table **T16.**

We collected one paleomagnetic discrete cube sample (see **"Paleomagnetism"** in the "Methods" chapter [Tada et al., 2015b]) from the first section of Cores 346-U1427A-1H through 81H, 85X, and 87X (triangles in Fig. **F43A, F43B**). Stepwise AF demagnetization on all discrete samples collected from Hole U1427A was performed at successive peak fields of 0, 5, 10, 15, 20, 25, 30, 40, 50, and 60 mT to verify the reliability of the split-core measurements and to determine the demagnetization behavior of the recovered sediment. Following each demagnetization step, NRM of the discrete samples was measured with the samples placed in the "top-toward" or "+*z*-axis toward magnetometer" orientation (see **"Paleomagnetism"** in the "Methods" chapter [Tada et al., 2015b]) on the discrete sample tray.

We processed data extracted from the shipboard Laboratory Information Management System (LIMS) database by removing all measurements collected from disturbed and void intervals and all measurements that were made within 10 cm of the section ends, which are slightly biased by measurement edge effects. The XCB-cored archive-half sections of Hole U1427A frequently contain drilling "biscuits" surrounded by as much disturbed material as intact material, strongly compromising the quality of the resulting paleomagnetic data. We removed data collected during the disturbed intervals in core sections of the four measured XCB cores. For declination data from cores in Hole U1427A where FlexIT tool data are available, we corrected the declination values for each core using the estimated orientation angles. A modified version of the UPmag software (Xuan and Channell, 2009) was used to analyze the NRM data of both the split-core section and the discrete cube samples. The disturbed and void intervals used in this process are reported in Table **T17.** The processed NRM inclination, declination, and intensity data after 20 mT AF demagnetization are reported in Table **T18** and shown in Figure **F43.**

Natural remanent magnetization and magnetic susceptibility

NRM intensity after 20 mT AF demagnetization in the two measured holes at Site U1427 is similar in magnitude for overlapping intervals, mostly ranging between ~10^{-4} and 10^{-3} A/m. For the uppermost ~280 m of the recovered sediment, NRM intensity of the measured core sections after 20 mT AF demagnetization is mostly on the order of 10^{-3} A/m. Deeper than ~280 m CSF-A until the bottom of the holes, NRM intensity drops to the order of 10^{-4} A/m and appears to be noisier than that of sediment from shallower than ~280 m CSF-A. The noisier NRM intensity data deeper than ~280 m CSF-A until the bottom of the holes is accompanied by large scatter in paleomagnetic direction data.

The upper ~120 m of the holes contain intervals of heavily bioturbated deep dark gray and deep dark greenish gray sediment with thicknesses between ~0.5 and 4.0 m. These dark intervals are divided into two types: Type I intervals (Sections 346-U1427A-5H-1, 7H-1~7H-2, and 9H-1~9H-2) are composed of mainly siliciclastics with black to dark greenish gray color, and Type II intervals (Sections 346-U1427A-12H-3~12H-5 and 13H-2~13H-4) are composed of nannofossil-rich clayey silt and nannofossil ooze with dark greenish gray to grayish brown (see **"Lithostratigraphy"**).

The color of sediment from the two interval types changed quickly after the cores were split. We monitored NRM after 20 mT AF demagnetization for selected core sections from the two interval types through time. NRM after 20 mT AF demagnetization of archive-half core Sections 346-U1427A-7H-1 through 7H-4 (~49–53.5 m CSF-A, Type I interval) and 12H-1 through 12H-5 (~97–104 m CSF-A, Type II interval) were measured as soon as the cores were split and then remeasured after ~2–6 h, after 1 day, and finally after 3 days. The results indicate that core sections from both interval types show some decay in NRM intensity through time, and NRM decay in Type II sediment appears larger than that in Type I sediment (Fig. **F44**). The decay in NRM intensity could be related to magnetic mineral alternation because of oxidation after the core was split.

The AF demagnetization behavior of the 12 measured discrete samples is illustrated in Figure **F45.** Declination and inclination values acquired from the discrete sample measurement generally agree well with the split-core measurement after 20 mT AF demagnetization. All samples exhibit a steep, normal overprint that was generally removed after AF demagnetization at peak fields of ~15–20 mT, demonstrating that the 20 mT AF demagnetization is, in general, sufficient to eliminate the drilling overprint. Compared with the two discrete samples from 174.73 and 221.55 m CSF-A, measured discrete samples from deeper depth levels appear to have lower coercivity. NRM measurement of discrete samples from the deep depth with weak intensity often ap-

pears to be affected by acquisition of an anhysteretic remanent magnetization, possibly due to bias caused by ambient magnetic field during demagnetization.

Magnetic susceptibility measurements were taken on whole cores from all holes as part of the Whole-Round Multisensor Logger (WRMSL) analysis and on archive-half sections using the Section Half Multisensor Logger (SHMSL) (see **"Physical properties"**). The WRMSL acquired susceptibility was stored in the database in raw meter units. These were multiplied by a factor of 0.68×10^{-5} to convert to the dimensionless volume SI unit (Blum, 1997). A factor of $(67/80) \times 10^{-5}$ was multiplied by the SHMSL acquired susceptibility stored in the database. Magnetic susceptibility measurement is consistent between the two instruments and across the different holes for overlapping intervals, and varies mostly between 5×10^{-5} and 20×10^{-5} SI (Fig. **F43,** fourth panel). Magnetic susceptibility of sediment in both holes, in general, mimics NRM intensity, suggesting that the magnetic minerals that carry NRM are the same or at least coexist with those that dominate magnetic susceptibility.

Magnetostratigraphy

Paleomagnetic inclination and declination data of the holes show patterns that allow for the determination of magnetic polarity for the uppermost ~280 m of recovered sediment. Both magnetic declination and inclination after 20 mT AF demagnetization were used when possible for the magnetostratigraphic interpretation at Site U1427. The geomagnetic field at the latitude of Site U1427 (35.965°N) has an expected inclination of 55.43°, assuming a geocentric axial dipole field model, which is sufficiently steep to determine magnetic polarity in APC cores that lack horizontal orientation. We identified the Brunhes/Matuyama boundary (0.781 Ma) at ~295.3 m CSF-A in Hole U1427A and at ~293.7 m CSF-A in Hole U1427B (Table **T19**).

Above the identified Brunhes/Matuyama boundary, inclinations after 20 mT AF demagnetization from both holes vary closely around the expected normal polarity inclination at Site U1427. In Hole U1427A, the FlexIT-corrected declinations (green dots in Fig. **F43A**) are mostly stable and vary around 0°. Right below the Brunhes/Matuyama boundary, inclinations from both holes are apparently dominated by shallow and negative values. The interpreted Brunhes/Matuyama boundary is consistent with the stepwise demagnetization data from the measured discrete samples. Discrete samples from above the boundary (Fig. **F45A–F45D**) show well-defined characteristic remanence with positive inclinations, whereas discrete samples from right below the Brunhes/Matuyama boundary (Fig. **F45E, F45F**) apparently have negative inclinations at high demagnetization steps. The depth level of the Brunhes/Matuyama boundary in Hole U1427A agrees well with the LO of planktonic foraminifer *N. kagaensis* (~0.70 Ma) at 242.86 m CSF-A (Section 346-U1427A-28H-CC) as well as the LO of calcareous nannofossil *R. asanoi* (~0.91 Ma) at 346.95 m CSF-A (Section 346-U1427A-51H-1W, 75 cm) (see **"Biostratigraphy"**).

Below the Brunhes/Matuyama boundary, NRM inclinations after 20 mT AF demagnetization show mostly positive values that are apparently steeper than the expected normal polarity dipole inclination at the site location and scattered intervals with shallow and negative inclinations. Increased coring disturbance, strong drill string overprint, the lack of core orientation, and the large scatter in paleomagnetic declinations makes magnetostratigraphic interpretations difficult for the deep part of sediment recovered at Site U1427.

Physical properties

Physical properties measurements at Site U1427 were conducted to provide high-resolution data on the bulk physical properties and their downhole variations in Holes U1427A, U1427B, and U1427C. After the sections reached thermal equilibrium with the ambient room temperature of ~20°C, thermal conductivity (one per core) and NGR measurements (eight per full section) completed the suite of whole-core measurements. One half of the split core was reserved for archiving and the other half was for analysis and sampling (working half). Shear stress measurements were performed (most commonly two per core) from 0 to 200 m CSF-A on the working halves of Hole U1427A. Moisture and density measurements were performed on discrete core samples (most commonly one or two per core) collected from the working halves of Hole U1427A. Color reflectance (most commonly at 5 cm intervals) and point magnetic susceptibility (most commonly at 5 cm intervals) were measured using the SHMSL on the archive halves. Physical properties measurements are presented synthetically in Figures **F46, F47, F48,** and **F49.**

Thermal conductivity

Thermal conductivity was measured once per core using the full-space probe, usually near the middle of Section 4. Thermal conductivity values range from ~0.8 to ~1.2 W/(m·K) without any clear trend downhole. The relatively large scatter of data suggests a

wide variety of sediment properties controlled by the relative abundances of detrital and biogenic materials.

Moisture and density

Although measurement errors exist in gamma ray attenuation (GRA) bulk density data because of the presence of air between a core and a core liner, in general the GRA bulk density reflects the core's lithologic characteristic (Fig. F46; see "Lithostratigraphy"). GRA bulk density ranges from 1.11 g/cm^3 to values >1.90 g/cm^3 and generally increases with depth. A minimum value was determined at ~228 m CSF-A, and a maximum value was measured at ~478 m CSF-A. GRA bulk density at Site U1427 differs significantly from previous sites. The higher GRA bulk density values continue to the bottom of the hole with high variability. The mean GRA bulk densities at previous Sites U1422–U1426 were 1.37, 1.42, 1.40, 1.41, and 1.49 g/cm^3, respectively, whereas the mean GRA bulk density at Site U1427 is 1.62 g/cm^3. This mean higher bulk density may be related to relatively higher abundance of coarse terrigenous material supplied from the nearby continental shelf and upper continental slope. Although GRA bulk density at previous sites reflected well the lithologic unit boundaries, GRA bulk density at this site shows a strong relationship with the lithologic changes alternating between heavier clay-rich and lighter biogenic components (mainly nannofossil- and diatom-rich sediment) (see "Lithostratigraphy"). Although GRA bulk density generally increases with depth because of sediment compaction, higher bulk density values (ranging from 1.55 to 1.99 g/cm^3) occur in intervals corresponding to clayey silt and silty clay sediment, whereas relatively lower bulk density values (ranging from 1.31 to 1.66 g/cm^3) dominate in biogenic component–rich sediment layers. This relationship between GRA bulk density and lithologic change becomes more evident when comparing with color reflectance b* values (yellow-blue ratio, Fig. F47). Higher GRA bulk density values are matched with blueish compounds of b*, with high NGR values. In long term trend, GRA bulk density generally increases between 0 and ~220 m CSF-A. At ~228 m CSF-A a minimum value of GRA bulk density (1.11 g/cm^3) appears to correlate with to a thick tephra/ash layer. GRA bulk density slightly decreases to ~400 m CSF-A and then increases again to ~480 m CSF-A. The low density values recorded deeper than ~482 m CSF-A may result from drilling disturbance caused by the change from the APC to XCB coring system. The above GRA bulk density trends at Site U1427 correlate well with density log acquired in open Hole U1427A (see Fig. F47 and "Downhole measurements").

Although discrete wet bulk density and grain density are relatively constant for the entire core interval, ranging from 1.42 to 1.84 g/cm^3 and from 2.50 to 2.77 g/cm^3, respectively, the primary trends agree well with GRA bulk density (Fig. F48). Porosity and water content show generally reversed trends when compared to density, ranging from 51.4% to 73.8% and from 29.3% to 53.4%, respectively. Discrete bulk density and grain density generally increase with depth where porosity and water content of the sediment decrease. Although Site U1427 has relatively higher discrete bulk density and lower porosity (and derived water content) throughout its entire depth than at previous sites, the trends also reflect well the lithologic changes alternating between clay-rich and biogenic component–rich sediment.

Magnetic susceptibility

Whole-core magnetic susceptibility at Site U1427 shows consistently low values downhole, typically <15 × 10^{-5} SI (Fig. F46). Point magnetic susceptibility from the SHMSL closely tracks whole-core magnetic susceptibility. Although the mean values stay between 10 × 10^{-5} and 15 × 10^{-5} SI for this site, high magnetic susceptibility maxima (up to 50 × 10^{-5} SI) occur at 7, 205, 228, 291, and 458 m CSF-A. A magnetic susceptibility maximum occurs between 227 and 228 m CSF-A, where values as high as 370 × 10^{-5} SI were measured. These occurrences of high magnetic susceptibility are due to highly magnetic authigenic minerals within tephra/ash layers (see "Lithostratigraphy"). Although magnetic susceptibility at Site U1427 shows low variability, the downhole trend agrees well with GRA bulk density and varies with lithologic changes alternating between clay-rich and biogenic component–rich sediment.

Natural gamma radiation

The NGR trends at Site U1427 correlate well with the gamma ray log acquired in open Hole U1427A (see Fig. F50 and "Downhole measurements"). Total NGR counts range from 7 to 65 cps and generally increase with depth (Fig. F46). A minimum value was determined at ~228 m CSF-A, coinciding with a thick tephra/ash layer, and a maximum value was measured at ~478 m CSF-A. NGR shows strong cyclicity similar to the GRA bulk density cyclicity. As these conformable variation patterns with GRA bulk density suggest that their controls are closely related, NGR also shows the trend pattern related to the lithologic changes alternating between clay-rich (higher

NGR values) and biogenic component–rich sediment (lower NGR values) (see also **"Downhole measurements"**). Total NGR counts increase with blueish compounds of b* and decrease with yellowish compounds of b* (Fig. **F47**). This correlation between NGR and color reflectance b* is more clear than the relationship to GRA bulk density.

Compressional wave velocity

Compressional *P*-wave velocity was measured with the WRMSL in Sections 1, 2, and 3 of each core for Holes U1427A and U1427B. Although compressional *P*-wave velocities were only measured in the upper 6.7 m CSF-A at this site because of degassing cracks, meter-scale cyclicity is evident, with a range of velocities between 1493 and 1564 m/s following cycles in GRA bulk density (Fig. **F46**).

Vane shear stress

Shear stress measurements were performed (generally two per core) from 0 to 200 m CSF-A on the working halves of Hole U1427A using an analog vane shear device. Deeper than 200 m CSF-A, the high sediment strength did not allow measurements. Shear strength ranges from 12.8 to 115.4 kPa and generally increases with depth (Fig. **F48**). Between 0 and ~36 m CSF-A, shear strength gradually increases from 12.8 to 36.4 kPa, and shear strength values are highly scattered in the deeper sediment. This scattering shear strength may be related to the highly diatomaceous layers or degassing sediment fractures.

Diffuse reflectance spectroscopy

Color reflectance data measured on the split archive-half sections at Site U1427 is distinctly different from the previously drilled sites. At previous sites, L*, a*, and b* show high variability caused by the alternating dark organic-rich and greenish organic-poor lithologic packages in the upper part of the stratigraphic sequence, whereas this site shows relatively low variability of color reflectance except b* (Fig. **F49**). This can be observed in the range of L* that only extends between values of 24 and 43, compared to Site U1425 where L* in Unit I extended between values of 17 and 53 (Fig. **F51**). Parameters a* and b* combined indicate the variable presence of primarily yellowish-blueish compounds. In contrast, Site U1425 showed a larger dynamic range for a*, leading to a more diverse hue spectrum (Fig. **F51**). The lithologic changes alternating between clay-rich and biogenic component–rich sediment are responsible for this high variability of b*. Although color reflectance L* and a* show relatively low variation, the trends agree well with the lithologic change as well as with b*.

Summary

Physical properties measured at Site U1427 generally show trends that follow the sediment lithology alternating between dense clay-rich and less dense biogenic component–rich sediment (see also **"Downhole measurements"**). Bulk density, NGR, and magnetic susceptibility show higher values in the clay-rich sediment interval, whereas lower values occur in the biogenic component–rich sediment interval. Porosity and water content show a trend opposite to bulk density and NGR. Color reflectance also reflects well these lithologic changes. At this site, color reflectance b*, representing the yellow-blue ratio, is a good indicator to identify the clay-rich and biogenic component–rich sediment and correlates well with the trends of bulk density and NGR.

Downhole measurements

Logging operations

Downhole logging measurements at Site U1427 were conducted in Hole U1427A after completion of APC/XCB coring to a total depth of 548.6 m CSF-A. The hole was reported to be in good condition. In preparation for logging, the hole was flushed with a 220 bbl sweep of high-viscosity mud, and the bit was pulled up to 80 mbsf. The paleo combo and FMS-sonic tool strings were deployed in Hole U1427A (Fig. **F52**) (see **"Downhole measurements"** in the "Methods" chapter [Tada et al., 2015b], see also Table **T12** in the "Methods" chapter [Tada et al., 2015b] for tool acronyms). The Hostile Environment Natural Gamma Ray Sonde (HNGS) was included in the FMS-sonic tool string to increase precise depth match processing between logging strings and passes.

On 7 September 2013 at 2315 h (UTC), the paleo combo tool string (comprising resistivity, density, natural and spectral gamma radiation, and magnetic susceptibility tools) descended from the rig floor into the pipe. A downlog was taken at ~600 m/h to the bottom of the hole at 550.5 m WSF. The hole was logged up to ~463 m WSF at 540 m/h (Pass 1). The tool string returned for the main pass from the bottom of the hole to the seafloor.

The FMS-sonic tool string was rigged at ~0315 h on 8 September. A downlog was taken at 850 m/h. The tool string reached the bottom of Hole U1427A at ~548.5 m WSF. Two uphole passes of the FMS-sonic tool string were run, the first pass to ~461 m WSF

and the main pass to the seafloor, both at 550 m/h. Rig down was completed at 0810 h.

The seafloor depth was indicated by the step in the gamma logs. The paleo combo tool string uplog (main pass) found the seafloor at 339.5 mbrf (see the "Methods" chapter [Tada et al., 2015b]), and the main pass of the FMS-sonic tool string found the seafloor at 338 mbrf. Heave was very low (<0.3 m peak-to-peak) during operations and the wireline heave compensator was not used (see "Downhole measurements" in the "Methods" chapter [Tada et al., 2015b]).

Logging data quality

Tool calibration was performed both before and after the logging runs to ensure quality control. In Hole U1427A, borehole conditions were very good with a baseline diameter (11.5–12.5 inches) close to the bit size (~11 inches) and few washouts (225, ~236, 316–340, and 474–478 mbsf). The borehole is slightly larger from the pipe entrance to 187 mbsf, although it does not exceed 14 inches in diameter (Fig. F53, Column 1). Because of good borehole conditions and negligible heave during downhole logging data acquisition, log data quality is generally very good.

There is good agreement between physical properties and logging data for the NGR and density logs along almost the entire borehole depth (Fig. F50, Columns 2 and 3). As a result of caliper closure (see "Downhole measurements" in the "Site U1423" chapter [Tada et al., 2015d]), from ~103 mbsf to the pipe entrance, the uplog gamma ray deviates from the core NGR data to lower values and no longer overlaps the downlog (Fig. F50, Column 2). For the same reason, the density log shows lower values than the core data over the same interval. Natural and spectral gamma ray data recorded shallower than 80 mbsf should only be used qualitatively because of the attenuation of the signal through the pipe (Figs. F50, F53). The resistivity curves are good, except for some high-frequency noise starting from ~157 mbsf to the pipe entrance and increasing uphole. Preprocessing has been applied to correct the logs of the Magnetic Susceptibility Sonde (MSS) from temperature drift (see "Downhole measurements" in the "Site U1423" chapter [Tada et al., 2015d]). The corrected deep-reading and high-resolution logs do not show any clear evidence for correlations with the magnetic susceptibility measurements on cores (Fig. F50, Column 5). This may reflect the very low magnetic susceptibility signal in the sediment, which may be lower than the detection limits of the tool. The step in the high-resolution MSS log observed at ~180 m probably reflects the borehole diameter enlargement, as the high-resolution response is affected by borehole size and borehole wall rugosity. The velocity log correlates relatively well with the density log and has a steadily increasing downhole trend. The FMS resistivity images were of very good quality, except for some short intervals where the borehole diameter was enlarged (225, ~236, 316–340, and 474–478 mbsf), resulting in very conductive intervals (Fig. F53, Column 6).

Logging unit

The Hole U1427A logs do not show major steps in the base levels. The entire logged interval was thus assigned to one logging unit (LI, Fig. F50) correlating with lithologic Unit A (see "Lithostratigraphy"). Logging Unit LI is characterized by moderate-amplitude variability in NGR (and its U, Th, and K components) on a decameter to submeter scale (Fig. F53). The HNGS signal ranges on average from 40 to 80 gAPI and most likely tracks clay content. The K and Th curves are generally well correlated. Uranium behaves differently and often shows inverse correlation to K and Th. The U content varies from 1 to 3.5 ppm. The gamma ray signal correlates well with the bulk density log, which shows high-amplitude variations ranging from 1.60 to 1.9 g/cm^3 (Fig. F50, Column 2) with a very slight increasing trend downhole. Resistivity logs have a negative trend downhole, reflecting compaction, and show pronounced oscillations of varied amplitude and frequency, which are well correlated with the density logs. Sonic velocity ranges from 1.5 to 2.0 km/s, with an increasing downhole trend reflecting downhole compaction.

Terrigenous clays have high K and Th contents and have relatively higher density and lower porosity than diatom-rich sediment. As a consequence, intervals with high gamma ray values, high density, and high resistivity generally reflect an increase in terrigenous clay content relative to diatom-rich intervals. Such intervals likely correspond to glacial stages characterized by lowered productivity (see "Lithostratigraphy"). Inversely, the intervals with gamma ray, density, and resistivity low values correlate in cores with diatom-rich intervals (e.g., 246–256 mbsf, diatom ooze, Cores 346-U1427B-31H through 33H, see "Lithostratigraphy").

FMS images

In Hole U1427A, the FMS resistivity data quality was very good, allowing the borehole formation resistivity to be interpreted at several scales. The FMS images reveal numerous resistive and conductive intervals, with thicknesses ranging from several tens of centimeters to a few meters. At the scale of the borehole, the interval shallower than ~200 mbsf is characterized by medium to high conductivity (orange

and dark colors in the FMS image in Fig. F53). Higher resistivity (light colors in the FMS image) are observed at deeper depths, from ~200 to ~340 mbsf. The interval deeper than ~340 mbsf is dominated by medium conductivity with intercalated higher resistivity intervals.

Conductive intervals (dark color in the FMS image in Figs. F53, F54) generally correlate with diatomaceous-rich intervals characterized by low gamma ray, low density, and low resistivity logs. Conversely, more resistive intervals (light colors in the FMS images) generally correlate with clay-rich intervals with higher values in the gamma ray, bulk density, and resistivity logs. This is particularly clear for three, several meters thick, very conductive intervals from 388 to 433 mbsf (Fig. F54) and consisting of diatomaceous ooze (see "Lithostratigraphy").

In situ temperature and heat flow

APCT-3 downhole temperature measurements were performed in Hole U1427A at five depths, including the mudline. Additional APCT-3 measurements were performed in Hole U1427C at three depths, including the mudline. In situ temperatures range from 3.13°C at 27.0 m CSF-A to 9.10°C at 115.8 m CSF-A (Table T20). Deeper than 30.3 mbsf, temperatures increase linearly with depth. A linear fit of temperature versus depth gives a geothermal gradient of 69°C/km, which is much lower than was measured at previous Expedition 346 sites by tens of degrees. A heat flow of 71 mW/m^2 was obtained from the slope of the linear fit between in situ temperature and calculated in situ thermal resistance (Fig. F55) (Pribnow et al., 2000). These very low values, compared to other sites, reflect the location of Site U1427 above continental crust, rather than in the open, deep marginal basin.

The trend line of the in situ temperature measurements intersects the seafloor at 1.08°C (Fig. F55A). This is much lower than the average mudline temperature in the four APCT-3 measurements (7.31°C). In a stable area, a temperature-depth plot should converge with the average annual seafloor temperature. The bottom water temperature was difficult to determine accurately from the Hole U1427A APCT-3 temperature profiles, as the measured temperature trend did not stabilize when the APCT-3 was held at the mudline. In Hole U1427C, the measurement duration at the mudline was increased from 5 to 10 min, but the bottom water temperature measurement remained inaccurate. The seafloor temperature at Site U1427 was expected to be slightly warmer than at previous sites because of the shallower water depth and the presence of the warm Tsushima Current. However, the hole was drilled below the thermocline (which is at ~200 m water depth), and it is likely that the temperature estimate from the mudline measurements was overestimated. A measurement performed into the pipe at 30 mbsf in Hole U1427C before running Core 346-U1427C-5H yielded a temperature of 7.5°C, which is essentially the same value as when the mudline temperature was measured (7.31°C, also through the pipe). The measurement at 30 mbsf in Hole U1427C is ~4.4°C warmer than the in situ temperature measured in Hole U1427A at approximately the same depth. We suggest that because of the shallow water depth, the drill pipe may not have time to fully equilibrate with the ambient bottom water and borehole temperatures compared to the very warm air temperature, which lead to overestimated in-pipe measurements.

Stratigraphic correlation and sedimentation rates

A composite section and splice "Stratigraphic correlation and sedimentation rates" in the "Methods" chapter [Tada et al., 2015b]) were constructed for Site U1427 to establish a continuous sediment sequence using Holes U1427A, U1427B, and U1427C, which were cored to 548.6, 405.6, and 351.79 m CSF-A, respectively. Splicing among these three holes enabled us to construct a continuous stratigraphic sequence for the interval from the seafloor to the bottom of Core 346-U1427A-63H (407.3 m CSF-A). From that depth downhole, only sediment from Hole U1427A was recovered.

Construction of CCSF-A scale

Definition of top (0 m CCSF-A)

Holes U1427A–U1427C all recovered the mudline. We selected the longer Core 346-U1427C-1H, where no whole-round sampling was conducted, as the anchor core and defined the top as 0 m core composite depth below seafloor, Method A (CCSF-A) (as defined in "Stratigraphic correlation and sedimentation rates" in the "Methods" chapter [Tada et al., 2015b]).

Compositing of cores

The CCSF-A scale for Site U1427 is based on correlation of magnetic susceptibility and GRA density data from the WRMSL and the Special Task Multisensor Logger (STMSL), as well as RGB blue (B) data extracted from images acquired by the Section Half Imaging Logger (SHIL) (see "Physical properties" in the "Methods" chapter [Tada et al., 2015b] for de-

tails). Magnetic susceptibility and GRA density were measured at 5 cm intervals for Hole U1427A and at 10 cm intervals for Holes U1427B and U1427C, whereas B was recovered at 0.5 cm intervals.

Correlative horizons were primarily identified using the B data, and confirmed with magnetic susceptibility data. The cores at Site U1427 were frequently fractured because of gas expansion; therefore, GRA density data were difficult to use for precise pattern matching. The typical spatial scale of the pattern matching of B data was several tens of centimeters because of a relatively homogeneous lithology. Fine tuning of correlation was possible using ash-bearing horizons and ash layers correlative among Holes U1427A–U1427C (see Table T3).

All the cores to 407.3 m CSF-A (bottom of Core 346-U1427A-63H) were well aligned and prepared to construct a splice record (Fig. F56A, F56B, F56C). Because only Hole U1427A was drilled deeper than 407.3 m CSF-A, the CCSF-A depth scale was provided to Cores 346-U1427A-64H through 87X, applying a constant offset of 22.45 m. The vertical depth offsets used to create the CCSF-A scale are given in the affine table (Table T21).

Construction of CCSF-D scale

A combination of Holes U1427A–U1427C cover the complete stratigraphic section to 407.3 m CSF-A (430.34 m CCSF-A). We constructed a splice primarily using Holes U1427B and U1427C, avoiding whole-round sampling in Hole U1427A intervals and minimizing inclusion of disturbed intervals as much as possible. Because Hole U1427C was only recovered to 365.41 m CSF-A (370.80 m CCSF-A), Holes U1427A and U1427B were used for splicing from 364.33 to 430.34 m CCSF-A. Selected splice intervals are listed in Table T22, and a sample splice of NGR data is shown in Figure F56A, F56B, and F56C.

Although the cores deeper than Core 346-U1427A-63H were not included in the splice, the NGR profiles from Cores 346-U1427A-64H through 87X were compared to the total spectral gamma ray (HSGR) profile from paleo combo logging (Fig. F56D; see "Downhole measurements"). Even the fine fluctuation patterns are well correlated downhole to 512.88 m CCSF-A (bottom of Core 346-U1427A-81H). We infer that no significant core gaps exist beyond the general size of gaps identified in the spliced section above (Fig. F56D).

Age model and sedimentation rates

A preliminary age model was established on the basis of all available biostratigraphic and paleomagnetic age control points. All the identified age datums were plotted on Figure F57A and listed in Table T23. The Brunhes/Matuyama (B/M) boundary is situated nearly in the middle of the whole sequence, helping to define the average sedimentation rate. Above the B/M boundary, age-depth lines are set between the constraints defined by the LOs of *G. ruber* (pink) and *N. kagaensis* group and the FO of *E. huxleyi*. In order to minimize the number of inflection points within a lithologic subunit, we defined the age of Subunit A1/A2 boundary as 0.5 Ma. Although this age-depth relationship might violate the constraint given by the LO of *P. lacunosa*, this event was regarded as reworked and could be set at a deeper horizon (see "Biostratigraphy"). Below the B/M boundary, the Bc of *R. asanoi* and the LO of *Gephyrocapsa* (>5.5 µm) narrowed a possible depth-age line. Although the LO of *H. sellii* was an apparent outlier, the age of disappearance of this species was diachronous and might be younger by ~1.2 Ma in this marginal sea (Muza, 1992). The resulting age of the bottom of the hole is 1.4 Ma (Table T23).

Sedimentation rates at Site U1427 range from 264 to 630 m/m.y. and are lower in Subunit A1, moderate in lower Subunit A2, and higher in upper Subunit A2 (Fig. F57B). Higher sedimentation rates tend to be associated with higher GRA density, which suggests the higher detrital flux made the sedimentation rate and GRA density increase.

References

Bishop, J.K.B., 1988. The barite-opal-organic carbon association in oceanic particulate matter. *Nature (London, U. K.),* 332(6162):341–343. doi:10.1038/332341a0

Blum, P., 1997. Physical properties handbook: a guide to the shipboard measurement of physical properties of deep-sea cores. *ODP Tech. Note,* 26. doi:10.2973/odp.tn.26.1997

Borowski, W.S., Paull, C.K., and Ussler, W., III, 1996. Marine pore-water sulfate profiles indicate in situ methane flux from underlying gas hydrate. *Geology,* 24(7):655–658. doi:10.1130/0091-7613(1996)024<0655:MPWSPI>2.3.CO;2

Briucaud, A., Morel, A., and Prieur, L., 1981. Absorption by dissolved organic matter of the sea (yellow substance) in the UV and visible domains. *Limnol. Oceanogr.,* 26(1):43–53. doi:10.4319/lo.1981.26.1.0043

Dehairs, F., Jacquet, S., Savoye, N., Van Mooy, B.A.S., Buesseler, K.O., Bishop, J.K.B., Lamborg, C.H., Elskens, M., Baeyens, W., Boyd, P.W., Casciotti, K.L., and Monnin, C., 2008. Barium in twilight zone suspended matter as a potential proxy for particulate organic carbon remineralization: results for the North Pacific. *Deep-Sea Res., Part II,* 55(14–15):1673–1683. doi:10.1016/j.dsr2.2008.04.020

D'Hondt, S.L., Jørgensen, B.B., Miller, D.J., et al., 2003. *Proc. ODP, Init. Repts.,* 201: College Station, TX (Ocean Drilling Program). **doi:10.2973/odp.proc.ir.201.2003**

Dickens, G.R., 2001. Sulfate profiles and barium fronts in sediment on the Blake Ridge: present and past methane fluxes through a large gas hydrate reservoir. *Geochim. Cosmochim. Acta,* 65(4):529–543. **doi:10.1016/S0016-7037(00)00556-1**

Egeberg, P.K., and Barth, T., 1998. Contribution of dissolved organic species to the carbon and energy budgets of hydrate bearing deep sea sediments (Ocean Drilling Program Site 997 Blake Ridge). *Chem. Geol.,* 149:25–35. **doi:10.1016/S0009-2541(98)00033-3**

Emerson, S., and Hedges, J.I., 1988. Processes controlling the organic carbon content of open ocean sediments. *Paleoceanography,* 3(5):621–634. **doi:10.1029/PA003i005p00621**

Froelich, P.N., Klinkhammer, G.P., Bender, M.L., Luedtke, N.A., Heath, G.R., Cullen, D., Dauphin, P., Hammond, D., Hartman, B., and Maynard, V., 1979. Early oxidation of organic matter in pelagic sediments of the eastern equatorial Atlantic: suboxic diagenesis. *Geochim. Cosmochim. Acta,* 43(7):1075–1090. **doi:10.1016/0016-7037(79)90095-4**

Ganeshram, R.S., François, R., Commeau, J., and Brown-Leger, S.L., 2003. An experimental investigation of barite formation in seawater. *Geochim. Cosmochim. Acta,* 67(14):2599–2605. **doi:10.1016/S0016-7037(03)00164-9**

Gieskes, J.M., 1975. Chemistry of interstitial waters of marine sediments. *Annu. Rev. Earth Planet. Sci.,* 3:433–453. **doi:10.1146/annurev.ea.03.050175.002245**

Gieskes, J.M., and Mahn, C., 2007. Halide systematics in interstitial waters of ocean drilling sediment cores. *Appl. Geochem.,* 22(3):515–533. **doi:10.1016/j.apgeochem.2006.12.003**

Gooday, A.J., 1993. Deep-sea benthic foraminiferal species which exploit phytodetritus: characteristic features and controls on distribution. *Mar. Micropaleontol.,* 22(3):187–205. **doi:10.1016/0377-8398(93)90043-W**

Gradstein, F.M., Ogg, J.G., Schmitz, M.D., and Ogg, G.M. (Eds.), 2012. *The Geological Time Scale 2012:* Amsterdam (Elsevier).

Hase, H., Yoon, J.-H., and Koterayama, W., 1999. The current structure of the Tsushima Warm Current along the Japan coast. *J. Oceanogr.,* 55(2):217–235. **doi:10.1023/A:1007894030095**

Harrison, W.E., Hesse, R., and Gieskes, J.M., 1982. Relationship between sedimentary facies and interstitial water chemistry of slope, trench, and Cocos plate sites from the Middle America Trench transect, active margin off Guatemala, Deep Sea Drilling Project Leg 67. *In* Aubouin, J., von Huene, R., et al., *Init. Repts. DSDP,* 67: Washington, DC (U.S. Govt. Printing Office), 603–614. **doi:10.2973/dsdp.proc.67.129.1982**

Hesse, R., Lebel, J., and Gieskes, J.M., 1985. Interstitial water chemistry of gas hydrate–bearing sections on the Middle America Trench slope, Deep-Sea Drilling Project Leg 84. *In* von Huene, R., Aubouin, J., et al., *Init. Repts. DSDP,* 84: Washington, DC (U.S. Govt. Printing Office), 727–737. **doi:10.2973/dsdp.proc.84.130.1985**

Ikehara, K., Kikawa, K., Katayama, H., and Seto, K., 1994. Late Quaternary paleoceanography of the Sea of Japan; a tephrochronological and sedimentological study. *In* Juvigne, E.H. (Ed.), *Quaternary Environmental Changes.* Proc. Int. Geol. Congr., 29th (Part B), 229–235.

Isoda, Y., 2011. Climate change and physical process associated with the Tsushima Warm Current. *Mem. Fac. Fish. Sci., Hokkaido Univ.,* 53(2):2–12. **http://hdl.handle.net/2115/47547**

Itaki, T., and Ikehara, K., 2003. Radiolarian biozonation for the upper Quaternary in the Japan Sea. *J. Geol. Soc. Jpn.,* 109(2):96–105. **doi:10.5575/geosoc.109.96**

Itaki, T., Komatsu, N., and Motoyama, I., 2007. Orbital- and millennial-scale changes of radiolarian assemblages during the last 220 kyrs in the Japan Sea. *Palaeogeogr., Palaeoclimatol., Palaeoecol.,* 247(1–2):115–130. **doi:10.1016/j.palaeo.2006.11.025**

Jorissen, F.J., 1999. Benthic foraminiferal microhabitats below the sediment-water interface. *In* Sen Gupta, B.K. (Ed.), *Modern Foraminifera:* Dordrecht (Kluwer), 161–179. **doi:10.1007/0-306-48104-9_10**

Jorissen, F.J., de Stigter, H.C., and Widmark, J.G.V., 1995. A conceptual model explaining benthic foraminiferal microhabitats. *Mar. Micropaleontol.,* 26(1–4):3–15. **doi:10.1016/0377-8398(95)00047-X**

Jorissen, F.J., Fontanier, C., and Thomas, E., 2007. Paleoceanographical proxies based on deep-sea benthic foraminiferal assemblage characteristics. *In* Hillaire-Marcel, C. and De Vernal, A. (Eds.), *Proxies in Late Cenozoic Paleoceanography.* Dev. Mar. Geol., 263–325. **doi:10.1016/S1572-5480(07)01012-3**

Kastner, M., Keene, J.B., and Gieskes, J.M., 1977. Diagenesis of siliceous oozes, I. Chemical controls on the rate of opal-A to opal-CT transformation—an experimental study. *Geochim. Cosmochim. Acta,* 41(8):1041–1051. **doi:10.1016/0016-7037(77)90099-0**

Kato, M., 1992. Benthic foraminifers from the Japan Sea: Leg 128. *In* Pisciotto, K.A., Ingle, J.C., Jr., von Breymann, M.T., Barron, J., et al., *Proc. ODP, Sci. Results,* 127/128 (Pt. 1): College Station, TX (Ocean Drilling Program), 365–392. **doi:10.2973/odp.proc.sr.127128-1.142.1992**

Krom, M.D., and Sholkovitz, E.R., 1977. Nature and reactions of dissolved organic matter in the interstitial waters of marine sediments. *Geochim. Cosmochim. Acta,* 41(11):1565–1574. **doi:10.1016/0016-7037(77)90168-5**

Kucera, M., and Kennett, J.P., 2000. Biochronology and evolutionary implications of late Neogene California margin planktonic foraminiferal events. *Mar. Micropaleontol.,* 40(1–2):67–81. **doi:10.1016/S0377-8398(00)00029-3**

Lisiecki, L.E., and Raymo, M.E., 2005. A Pliocene–Pleistocene stack of 57 globally distributed benthic $\delta^{18}O$ records. *Paleoceanography,* 20(1):PA1003. **doi:10.1029/2004PA001071**

Lyle, M., Koizumi, I., Richter, C., et al., 1997. *Proc. ODP, Init. Repts.,* 167: College Station, TX (Ocean Drilling Program). doi:10.2973/odp.proc.ir.167.1997

Maiya, S., 1978. Late Cenozoic planktonic foraminiferal biostratigraphy of the oil-field region of Northeast Japan. *In* Fujita, K., Ichikawa, K., Ichihara, M., Chiji, M., Unabara, K., Fujita, T., and Takayanagi, Y. (Eds.), *Cenozoic Geology of Japan:* Osaka (Osaka City Univ.), 35–60.

Martin, J.B., Gieskes, J.M., Torres, M., and Kastner, M., 1993. Bromide and iodine in Peru margin sediments and pore fluids: implication for fluid origins. *Geochim. Cosmochim. Acta,* 57(18):4377–4389. doi:10.1016/0016-7037(93)90489-J

Meyers, P.A., 1997. Organic geochemical proxies of paleoceanographic, paleolimnologic, and paleoclimatic processes. *Org. Geochem.,* 27(5–6):213–250. doi:10.1016/S0146-6380(97)00049-1

Middelburg, J.J., de Lange, G.J., and van der Weijden, C.H., 1987. Manganese solubility control in marine pore waters. *Geochim. Cosmochim. Acta,* 51(3):759–763. doi:10.1016/0016-7037(87)90086-X

Müller, P.J., and Suess, E., 1979. Productivity, sedimentation rate, and sedimentary organic matter in the oceans—I. Organic carbon preservation. *Deep-Sea Res., Part A,* 26(12):1347–1362. doi:10.1016/0198-0149(79)90003-7

Murray, R.W., Brumsack, H.J., von Breymann, M.T., Sturz, A.A., Dunbar, R.B., and Gieskes, J.M., 1992. Diagenetic reactions in deeply buried sediments of the Japan Sea: a synthesis of interstitial-water chemistry results from Legs 127 and 128. *In* Tamaki, K., Suyehiro, K., Allan, J., McWilliams, M., et al., *Proc. ODP, Sci. Results,* 127/128 (Pt. 2): College Station, TX (Ocean Drilling Program), 1261–1274. doi:10.2973/odp.proc.sr.127128-2.177.1992

Murray, R.W., Wigley, R., and Shipboard Scientific Party, 1998. Interstitial water chemistry of deeply buried sediments from the southwest African margin: a preliminary synthesis of results from Leg 175. *In* Wefer, G., Berger, W.H., and Richter, C., et al., *Proc. ODP, Init. Repts.,* 175: College Station, TX (Ocean Drilling Program), 547–553. doi:10.2973/odp.proc.ir.175.120.1998

Muza, J.P., 1992. Calcareous nannofossil biostratigraphy from the Japan Sea, Sites 798 and 799: evidence for an oscillating Pleistocene oceanographic frontal boundary. *In* Pisciotto, K.A., Ingle, J.C., Jr., von Breymann, M.T., Barron, J., et al., *Proc. ODP, Sci. Results,* 127/128 (Pt. 1): College Station, TX (Ocean Drilling Program), 155–169. doi:10.2973/odp.proc.sr.127128-1.122.1992

Nigrini, C., 1970. Radiolarian assemblages in the North Pacific and their application to a study of Quaternary sediments in core V20-130. *In* Hays, J.D. (Ed.), *Geological Investigations of the North Pacific*. Mem.—Geol. Soc. Am., 126:139–183. doi:10.1130/MEM126-p139

Oba, T., Kato, M., Kitazato, H., Koizumi, I., Omura, A., Sakai, T., and Takayama, T., 1991. Paleoenvironmental changes in the Japan Sea during the last 85,000 years. *Paleoceanography,* 6(4):499–518. doi:10.1029/91PA00560

Paull, C.K., Lorenson, T.D., Dickens, G., Borowski, W.S., Ussler, W., III, and Kvenvolden, K., 2000. Comparisons of in situ and core gas measurements in ODP Leg 164 bore holes. *Ann. New York Acad. Sci.,* 912:23–31. doi:10.1111/j.1749-6632.2000.tb06756.x

Paull, C.K., Matsumoto, R., Wallace, P.J., et al., 1996. *Proc. ODP, Init. Repts.,* 164: College Station, TX (Ocean Drilling Program). doi:10.2973/odp.proc.ir.164.1996

Pribnow, D., Kinoshita, M., and Stein, C., 2000. *Thermal Data Collection and Heat Flow Recalculations for Ocean Drilling Program Legs 101–180:* Hanover, Germany (Inst. Joint Geosci. Res., Inst. Geowiss. Gemeinschaftsauf. [GGA]). http://www-odp.tamu.edu/publications/heatflow/ODPReprt.pdf

Reeburgh, W.S., 1976. Methane consumption in Cariaco Trench waters and sediments. *Earth Planet. Sci. Lett.,* 28(3):337–344. doi:10.1016/0012-821X(76)90195-3

Rettich, T.R., Handa, Y.P., Battino, R., and Wilhelm, E., 1981. Solubility of gases in liquids. 13. High-precision determination of Henry's constants for methane and ethane in liquid water at 275 to 328 K. *J. Phy. Chem.,* 85(22):3230–3237. doi:10.1021/j150622a006

Sakai, T., 1980. Radiolarians from Sites 434, 435, and 436, northwest Pacific, Leg 56, Deep Sea Drilling Project. *In* von Huene, R., Nasu, N., et al., *Init. Repts. DSDP,* 56, 57: Washington, DC (U.S. Govt. Printing Office), 695–733. doi:10.2973/dsdp.proc.5657.119.1980

Sayles, F.L., and Manheim, F., 1975. Interstitial solutions and diagenesis in deeply buried marine sediments: results from the Deep Sea Drilling Project. *Geochim. Cosmochim. Acta,* 39(2):103–127. doi:10.1016/0016-7037(75)90165-9

Schink, D.R., Fanning, K.A., and Pilson, M.E.Q., 1974. Dissolved silica in the upper pore waters of the Atlantic Ocean floor. *J. Geophys. Res.,* 79(15):2243–2250. doi:10.1029/JC079i015p02243

Senjyu, T., 1999. The Japan Sea Intermediate Water; its characteristics and circulation. *J. Oceanogr.,* 55(2):111–122. doi:10.1023/A:1007825609622

Smith, D.C., 2005. Data report: dissolved organic carbon in interstitial waters, equatorial Pacific and Peru margin, ODP Leg 201. *In* Jørgensen, B.B., D'Hondt, S.L., and Miller, D.J. (Eds.), *Proc. ODP, Sci. Results,* 201: College Station, TX (Ocean Drilling Program), 1–10. doi:10.2973/odp.proc.sr.201.111.2005

Snyder, G.T., Hiruta, A., Matsumoto, R., Dickens, G.R., Tomaru, H., Takeuchi, R., Komatsubara, J., Ishida, Y., and Yu, H., 2007. Pore water profiles and authigenic mineralization in shallow marine sediments above the methane-charged system on Umitaka Spur, Japan Sea. *Deep-Sea Res., Part II,* 54(11–13):1216–1239. doi:10.1016/j.dsr2.2007.04.001

Suess, E., von Huene, R., et al., 1988. *Proc. ODP, Init. Repts.,* 112: College Station, TX (Ocean Drilling Program). doi:10.2973/odp.proc.ir.112.1988

Tada, R., 1994. Paleoceanographic evolution of the Japan Sea. *Palaeogeogr., Palaeoclimatol., Palaeoecol.,* 108(3–4):487–508. **doi:10.1016/0031-0182(94)90248-8**

Tada, R., Koizumi, I., Cramp, A., and Rahman, A., 1992. Correlation of dark and light layers, and the origin of their cyclicity in the Quaternary sediments from the Japan Sea. *In* Pisciotto, K.A., Ingle, J.C., Jr., von Breymann, M.T., Barron, J., et al., *Proc. ODP, Sci. Results,* 127/128 (Pt. 1): College Station, TX (Ocean Drilling Program), 577–601. **doi:10.2973/odp.proc.sr.127128-1.160.1992**

Tada, R., Murray, R.W., Alvarez Zarikian, C.A., Anderson, W.T., Jr., Bassetti, M.-A., Brace, B.J., Clemens, S.C., da Costa Gurgel, M.H., Dickens, G.R., Dunlea, A.G., Gallagher, S.J., Giosan, L., Henderson, A.C.G., Holbourn, A.E., Ikehara, K., Irino, T., Itaki, T., Karasuda, A., Kinsley, C.W., Kubota, Y., Lee, G.S., Lee, K.E., Lofi, J., Lopes, C.I.C.D., Peterson, L.C., Saavedra-Pellitero, M., Sagawa, T., Singh, R.K., Sugisaki, S., Toucanne, S., Wan, S., Xuan, C., Zheng, H., and Ziegler, M., 2015a. Expedition 346 summary. *In* Tada, R., Murray, R.W., Alvarez Zarikian, C.A., and the Expedition 346 Scientists, *Proc. IODP,* 346: College Station, TX (Integrated Ocean Drilling Program). **doi:10.2204/iodp.proc.346.101.2015**

Tada, R., Murray, R.W., Alvarez Zarikian, C.A., Anderson, W.T., Jr, Bassetti, M.-A., Brace, B.J., Clemens, S.C., Dickens, G.R., Dunlea, A.G., Gallagher, S.J., Giosan, L., da Costa Gurgel, M.H., Henderson, A.C.G., Holbourn, A.E., Ikehara, K., Irino, T., Itaki, T., Karasuda, A., Kinsley, C.W., Kubota, Y., Lee, G.S., Lee, K.E., Lofi, J., Lopes, C.I.C.D., Peterson, L.C., Saavedra-Pellitero, M., Sagawa, T., Singh, R.K., Sugisaki, S., Toucanne, S., Wan, S., Xuan, C., Zheng, H., and Ziegler, M., 2015b. Methods. *In* Tada, R., Murray, R.W., Alvarez Zarikian, C.A., and the Expedition 346 Scientists, *Proc. IODP,* 346: College Station, TX (Integrated Ocean Drilling Program). **doi:10.2204/iodp.proc.346.102.2015**

Tada, R., Murray, R.W., Alvarez Zarikian, C.A., Anderson, W.T., Jr., Bassetti, M.-A., Brace, B.J., Clemens, S.C., da Costa Gurgel, M.H., Dickens, G.R., Dunlea, A.G., Gallagher, S.J., Giosan, L., Henderson, A.C.G., Holbourn, A.E., Ikehara, K., Irino, T., Itaki, T., Karasuda, A., Kinsley, C.W., Kubota, Y., Lee, G.S., Lee, K.E., Lofi, J., Lopes, C.I.C.D., Peterson, L.C., Saavedra-Pellitero, M., Sagawa, T., Singh, R.K., Sugisaki, S., Toucanne, S., Wan, S., Xuan, C., Zheng, H., and Ziegler, M., 2015c. Site U1422. *In* Tada, R., Murray, R.W., Alvarez Zarikian, C.A., and the Expedition 346 Scientists, *Proc. IODP,* 346: College Station, TX (Integrated Ocean Drilling Program). **doi:10.2204/iodp.proc.346.103.2015**

Tada, R., Murray, R.W., Alvarez Zarikian, C.A., Anderson, W.T., Jr, Bassetti, M.-A., Brace, B.J., Clemens, S.C., Dickens, G.R., Dunlea, A.G., Gallagher, S.J., Giosan, L., da Costa Gurgel, M.H., Henderson, A.C.G., Holbourn, A.E., Ikehara, K., Irino, T., Itaki, T., Karasuda, A., Kinsley, C.W., Kubota, Y., Lee, G.S., Lee, K.E., Lofi, J., Lopes, C.I.C.D., Peterson, L.C., Saavedra-Pellitero, M., Sagawa, T., Singh, R.K., Sugisaki, S., Toucanne, S., Wan, S., Xuan, C., Zheng, H., and Ziegler, M., 2015d. Site U1423. *In* Tada, R., Murray, R.W., Alvarez Zarikian, C.A., and the Expedition 346 Scientists, *Proc. IODP,* 346: College Station, TX (Integrated Ocean Drilling Program). **doi:10.2204/iodp.proc.346.104.2015**

Tada, R., Murray, R.W., Alvarez Zarikian, C.A., Anderson, W.T., Jr., Bassetti, M.-A., Brace, B.J., Clemens, S.C., da Costa Gurgel, M.H., Dickens, G.R., Dunlea, A.G., Gallagher, S.J., Giosan, L., Henderson, A.C.G., Holbourn, A.E., Ikehara, K., Irino, T., Itaki, T., Karasuda, A., Kinsley, C.W., Kubota, Y., Lee, G.S., Lee, K.E., Lofi, J., Lopes, C.I.C.D., Peterson, L.C., Saavedra-Pellitero, M., Sagawa, T., Singh, R.K., Sugisaki, S., Toucanne, S., Wan, S., Xuan, C., Zheng, H., and Ziegler, M., 2015e. Site U1424. *In* Tada, R., Murray, R.W., Alvarez Zarikian, C.A., and the Expedition 346 Scientists, *Proc. IODP,* 346: College Station, TX (Integrated Ocean Drilling Program). **doi:10.2204/iodp.proc.346.105.2015**

Tada, R., Murray, R.W., Alvarez Zarikian, C.A., Anderson, W.T., Jr., Bassetti, M.-A., Brace, B.J., Clemens, S.C., da Costa Gurgel, M.H., Dickens, G.R., Dunlea, A.G., Gallagher, S.J., Giosan, L., Henderson, A.C.G., Holbourn, A.E., Ikehara, K., Irino, T., Itaki, T., Karasuda, A., Kinsley, C.W., Kubota, Y., Lee, G.S., Lee, K.E., Lofi, J., Lopes, C.I.C.D., Peterson, L.C., Saavedra-Pellitero, M., Sagawa, T., Singh, R.K., Sugisaki, S., Toucanne, S., Wan, S., Xuan, C., Zheng, H., and Ziegler, M., 2015f. Site U1425. *In* Tada, R., Murray, R.W., Alvarez Zarikian, C.A., and the Expedition 346 Scientists, *Proc. IODP,* 346: College Station, TX (Integrated Ocean Drilling Program). **doi:10.2204/iodp.proc.346.106.2015**

Tada, R., Murray, R.W., Alvarez Zarikian, C.A., Anderson, W.T., Jr., Bassetti, M.-A., Brace, B.J., Clemens, S.C., da Costa Gurgel, M.H., Dickens, G.R., Dunlea, A.G., Gallagher, S.J., Giosan, L., Henderson, A.C.G., Holbourn, A.E., Ikehara, K., Irino, T., Itaki, T., Karasuda, A., Kinsley, C.W., Kubota, Y., Lee, G.S., Lee, K.E., Lofi, J., Lopes, C.I.C.D., Peterson, L.C., Saavedra-Pellitero, M., Sagawa, T., Singh, R.K., Sugisaki, S., Toucanne, S., Wan, S., Xuan, C., Zheng, H., and Ziegler, M., 2015g. Site U1426. *In* Tada, R., Murray, R.W., Alvarez Zarikian, C.A., and the Expedition 346 Scientists, *Proc. IODP,* 346: College Station, TX (Integrated Ocean Drilling Program). **doi:10.2204/iodp.proc.346.107.2015**

Tréhu, A.M., Bohrmann, G., Rack, F.R., Torres, M.E., et al., 2003. *Proc. ODP, Init. Repts.,* 204: College Station, TX (Ocean Drilling Program). **doi:10.2973/odp.proc.ir.204.2003**

van Beek, P., François, R., Conte, M., Reyss, J.-L., Souhaut, M., and Charette, M., 2007. $^{228}Ra/^{226}Ra$ and $^{226}Ra/Ba$ ratios to track barite formation and transport in the water column. *Geochim. Cosmochim. Acta,* 71(1):71–86. **doi:10.1016/j.gca.2006.07.041**

von Breymann, M.T., Brumsack, H., and Emeis, K.C., 1992. Depositional and diagenetic behavior of barium in the Japan Sea. *In* Pisciotto, K.A., Ingle, J.C., Jr., von Breymann, M.T., Barron, J., et al., *Proc. ODP, Sci. Results,* 127/128 (Pt. 1): College Station, TX (Ocean Drilling Pro-

gram), 651–665. doi:10.2973/odp.proc.sr.127128-1.168.1992

Waples, D.W., 1985. Organic and inorganic nitrogen in sediments from Leg 80, Deep Sea Drilling Project. *In* de Graciansky, P.C., Poag, C.W., et al., *Init. Repts. DSDP,* 80 (Pt. 2): Washington (U.S. Govt. Printing Office), 993–997. doi:10.2973/dsdp.proc.80.146.1985

Wefer, G., Berger, W.H., and Richter, C., et al., 1998. *Proc. ODP, Init. Repts.,* 175: College Station, TX (Ocean Drilling Program). doi:10.2973/odp.proc.ir.175.1998

Xuan, C., and Channell, J.E.T., 2009. UPmag: MATLAB software for viewing and processing U channel or other pass-through paleomagnetic data. *Geochem., Geophys., Geosyst.,* 10(10):Q10Y07. doi:10.1029/2009GC002584

You, C.-F., Gieskes, J.M., Chen, R.F., Spivack, A., and Gamo, T., 1993. Iodide, bromide, manganese, boron, and dissolved organic carbon in interstitial waters of the organic carbon–rich marine sediments: observations in the Nankai accretionary prism. *In* Hill, I.A., Taira, A., Firth, J.V., et al., *Proc. ODP, Sci. Results,* 131: College Station, TX (Ocean Drilling Program), 165–174. doi:10.2973/odp.proc.sr.131.116.1993

Publication: 28 March 2015
MS 346-108

Figure F1. Bathymetric map of Expedition 346 sites (red circles). Sites previously drilled by the Deep Sea Drilling Project (DSDP) and Ocean Drilling Program (ODP) (white circles) are also shown. Also illustrated are surface current systems.

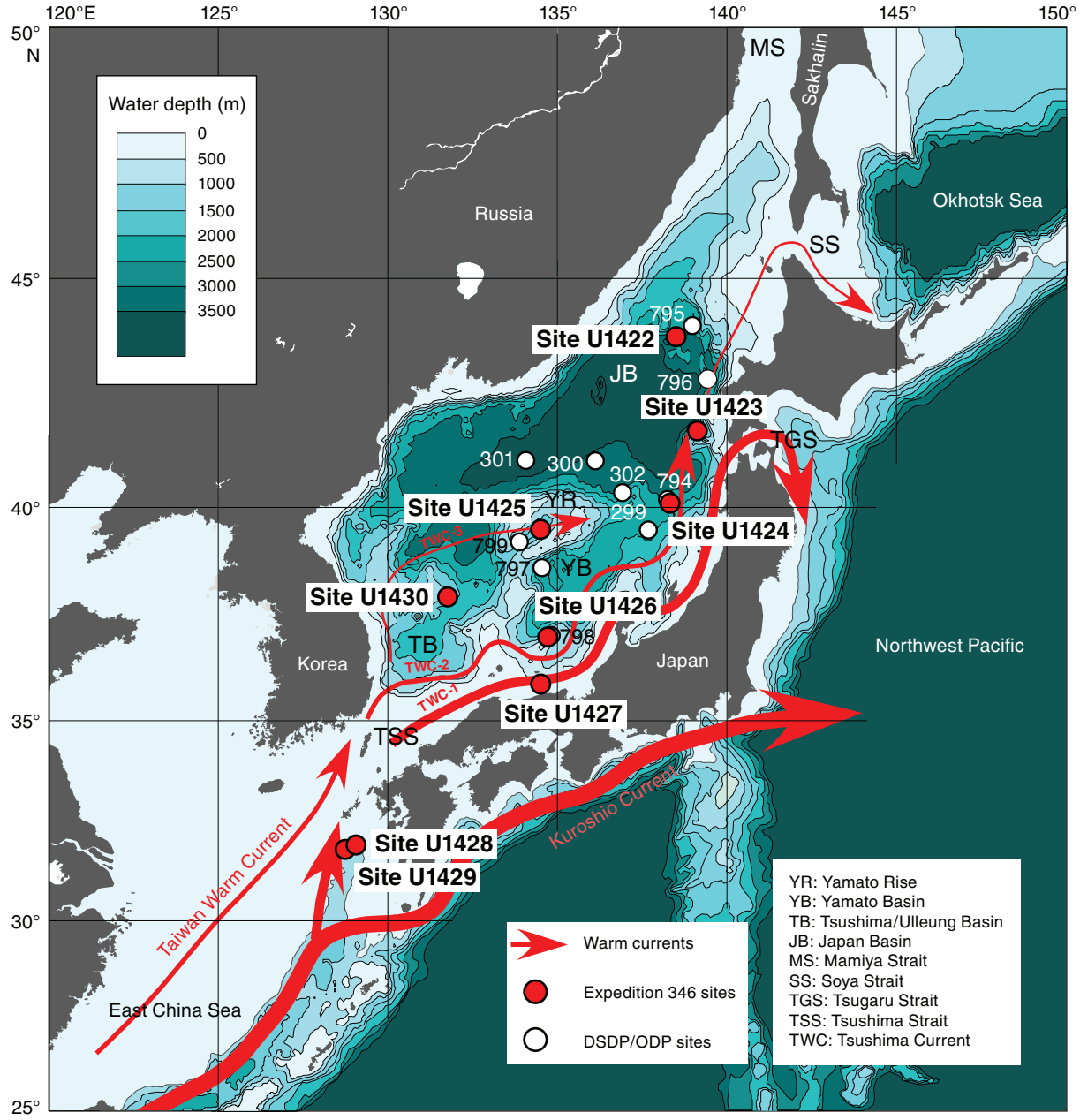

Figure F2. Lithologic summary, Hole U1427A. GRA = gamma ray attenuation.

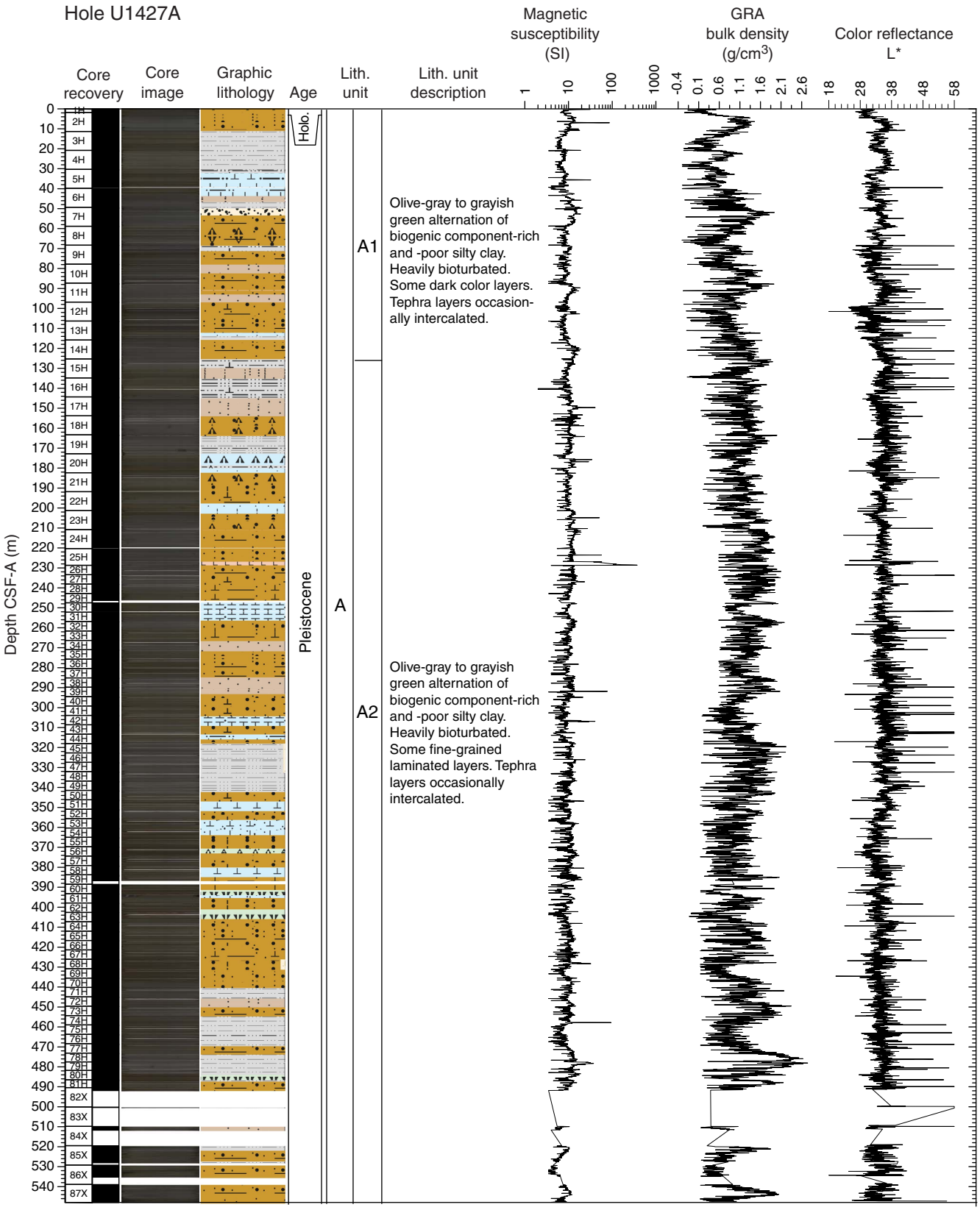

Figure F3. Lithologic summary, Hole U1427B. GRA = gamma ray attenuation.

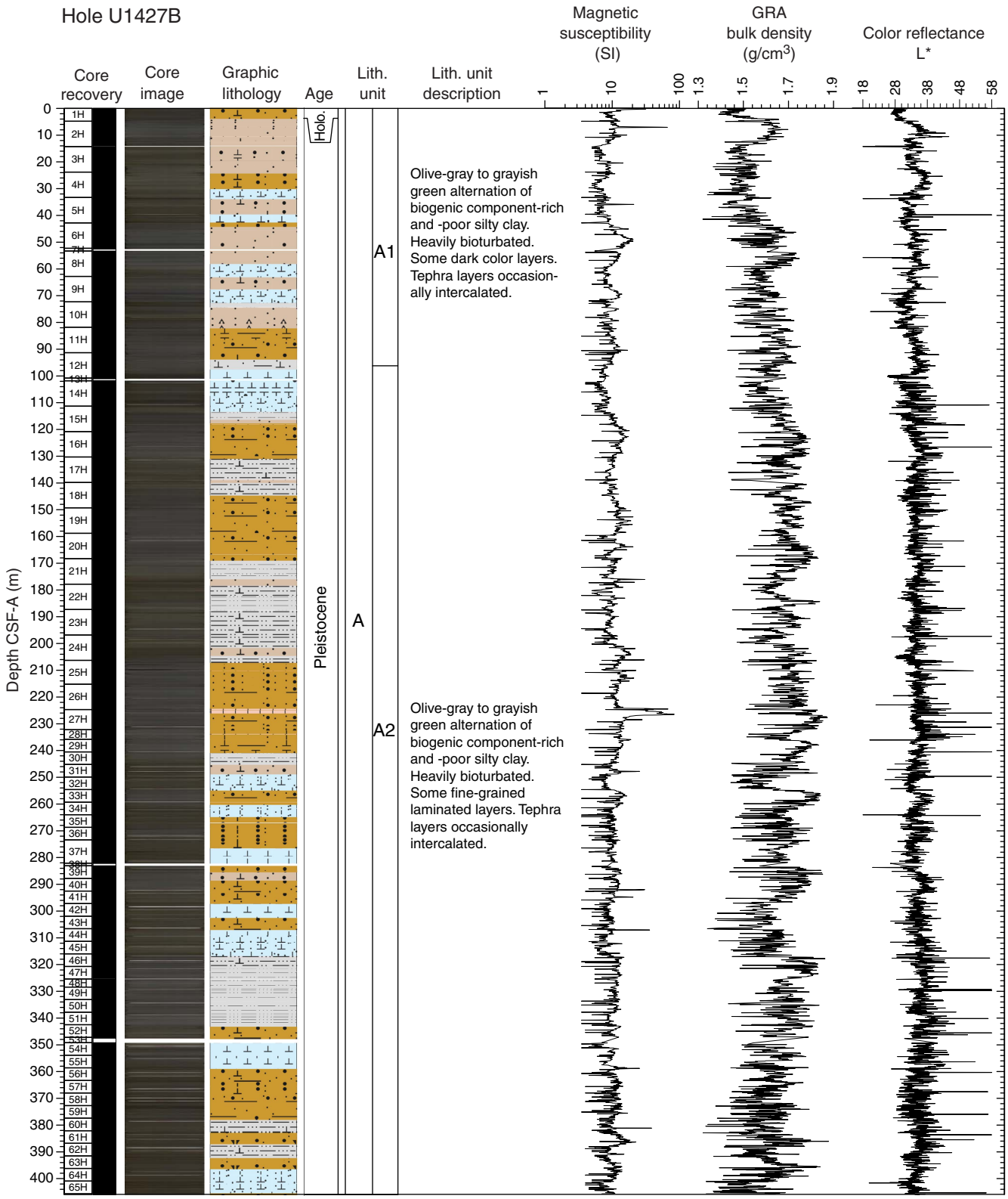

Figure F4. Lithologic summary, Hole U1427C. GRA = gamma ray attenuation.

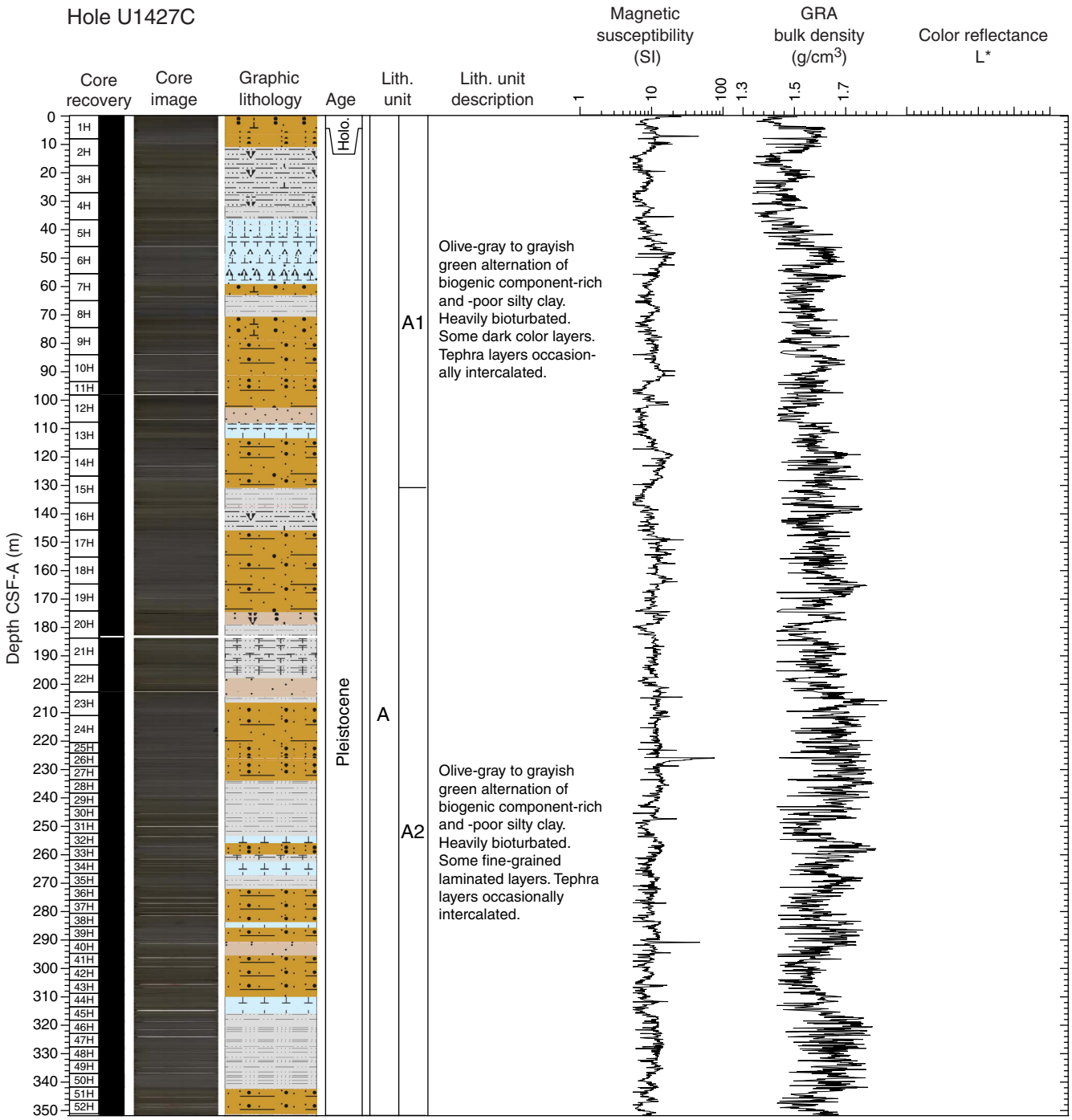

Figure F5. Hole-to-hole lithostratigraphic correlation, Site U1427.

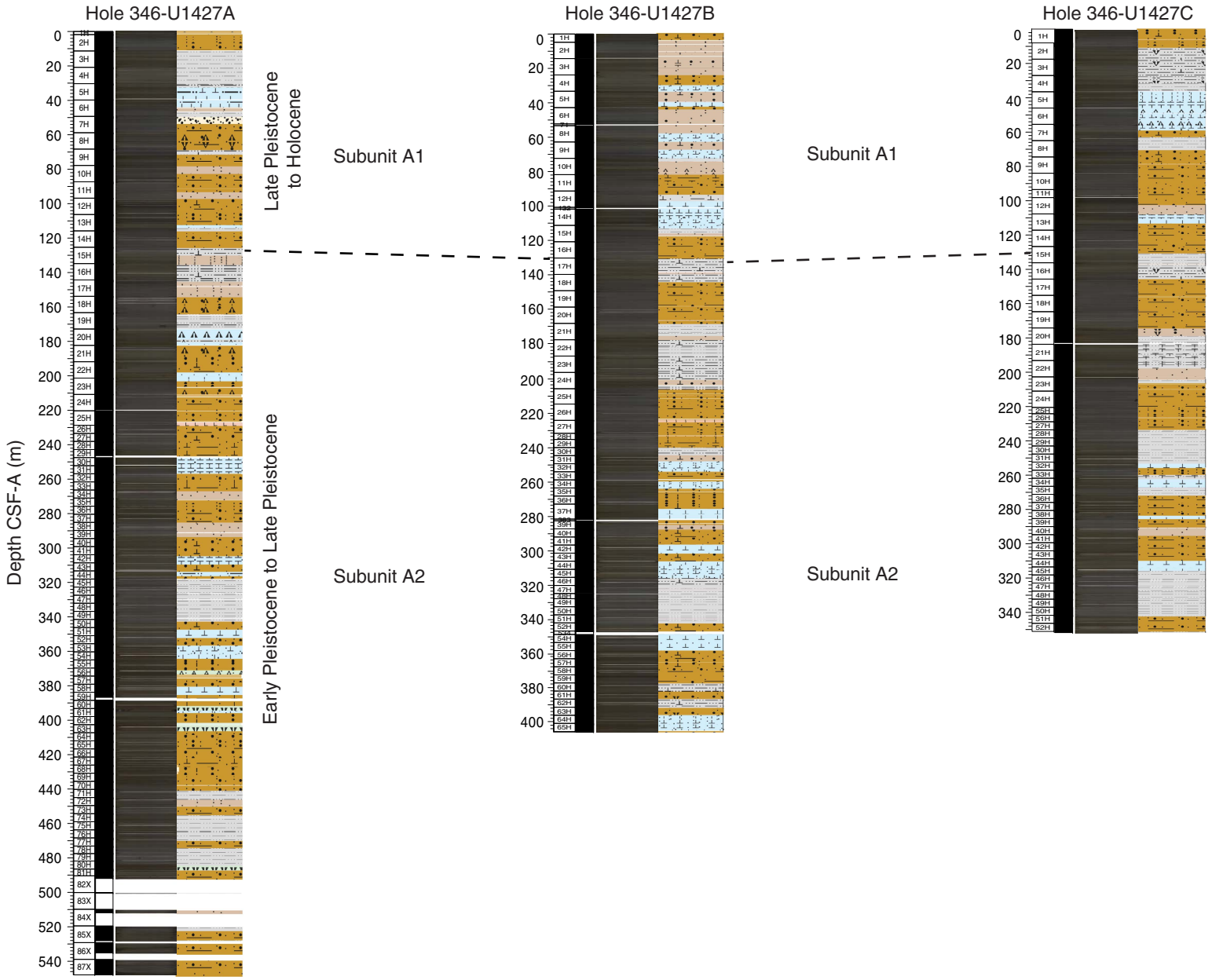

Figure F6. Photographs representative of Unit A, Hole U1427A. Note enhanced color contrast to highlight sedimentary structures.

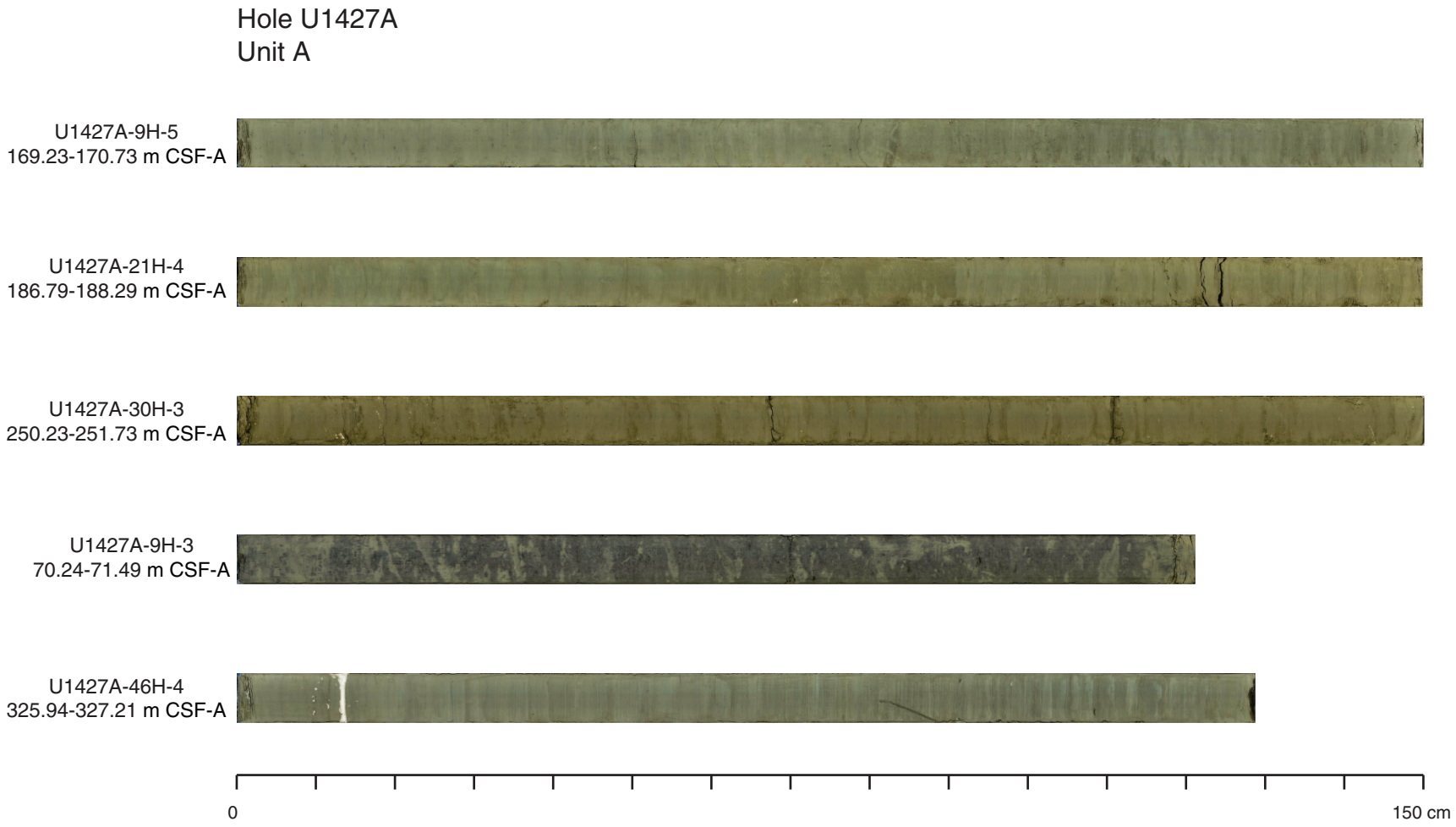

Figure F7. Distribution of the number of tephra layers and total thickness of tephra in each core, Hole U1427A.

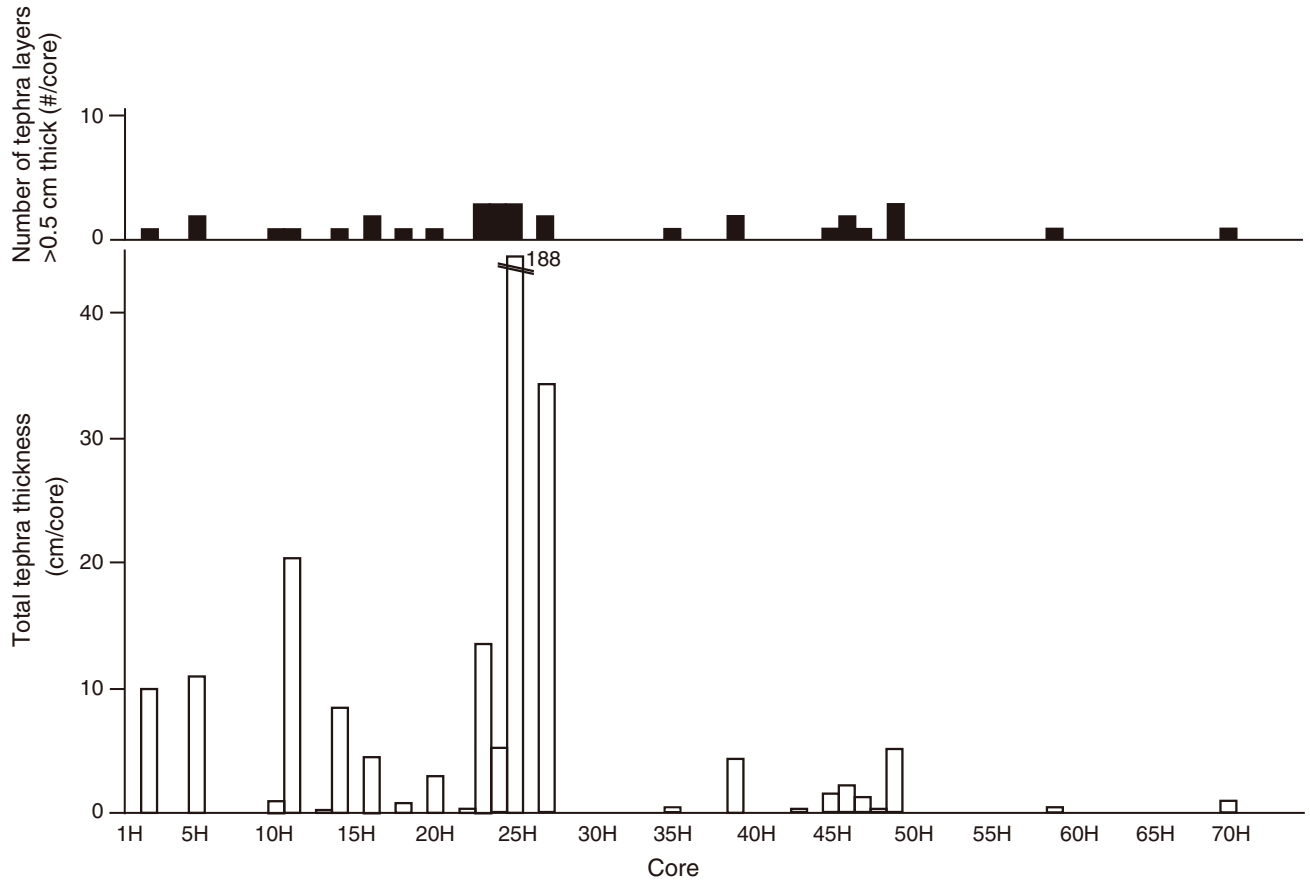

Figure F8. Variation of bulk sediment sample XRD peak intensity of identified minerals with depth, Hole U1427A.

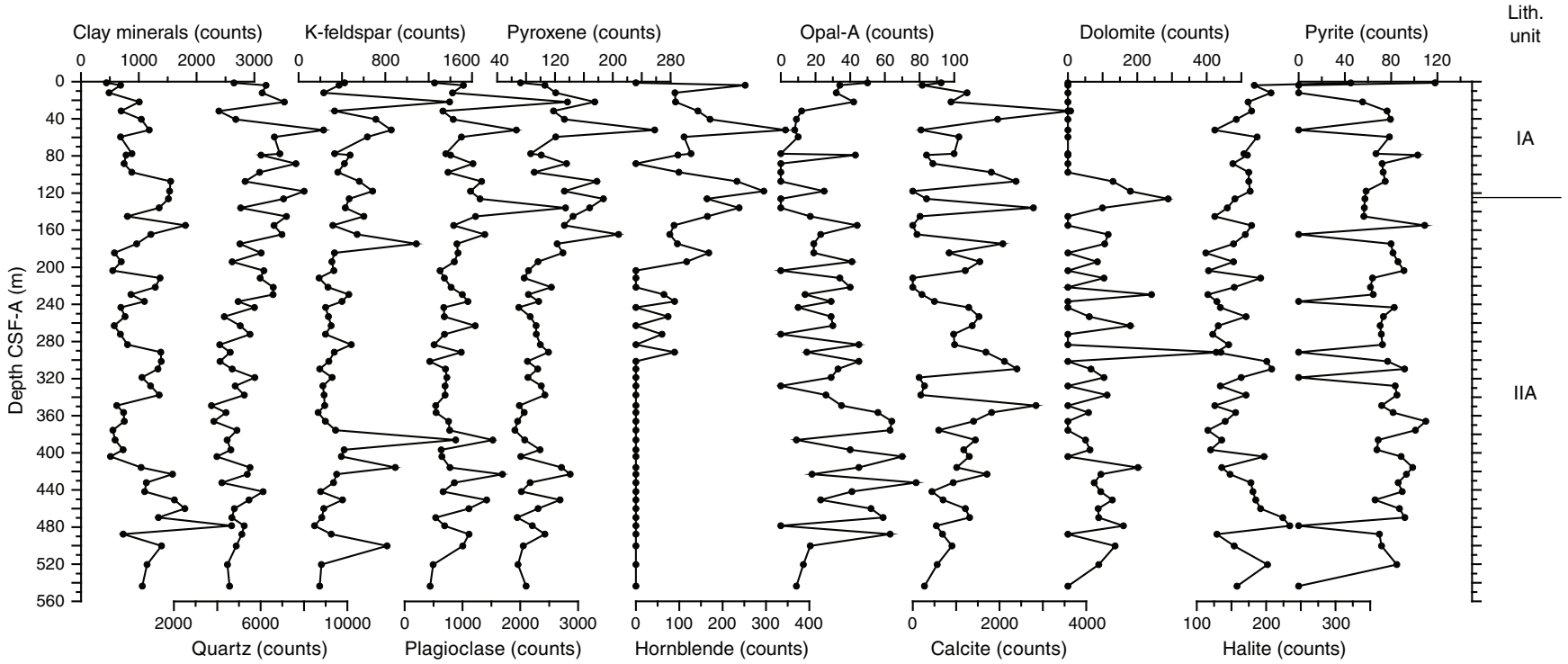

Figure F9. Photographs of typical vitric tephra layers.

U1427A-25H-6, 4-34 cm
226.79-227.09 m CSF-A

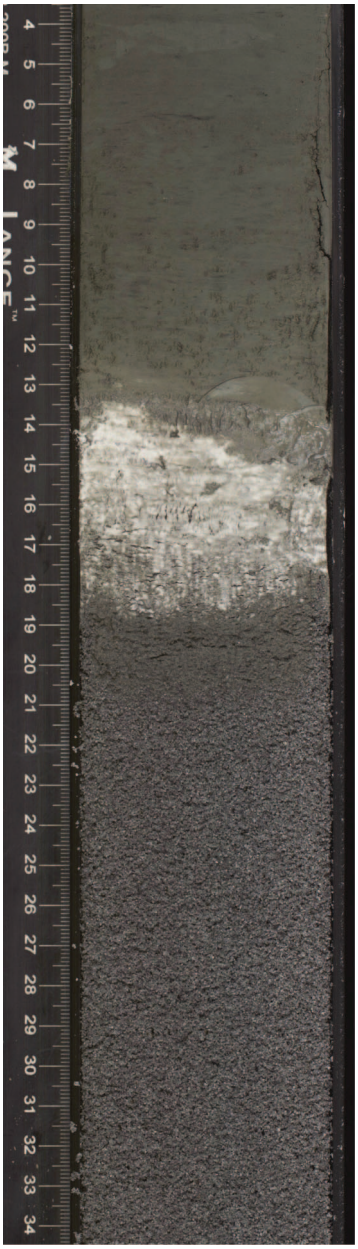

U1427B-27H-1, 108-138 cm
224.78-225.08 m CSF-A

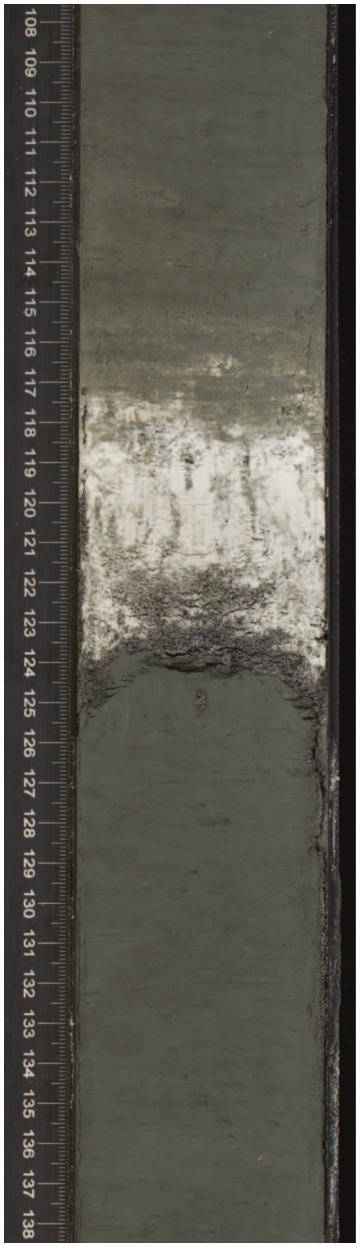

U1427C-26H-3, 1-31 cm
224.21-224.51 m CSF-A

Figure F10. Photomicrographs showing detail of (**A**) nannofossil ooze (Section 346-U1427A-51H-4, 40 cm) and (**B**) clayey silty sand (Section 346-U1427A-7H-2, 75 cm).

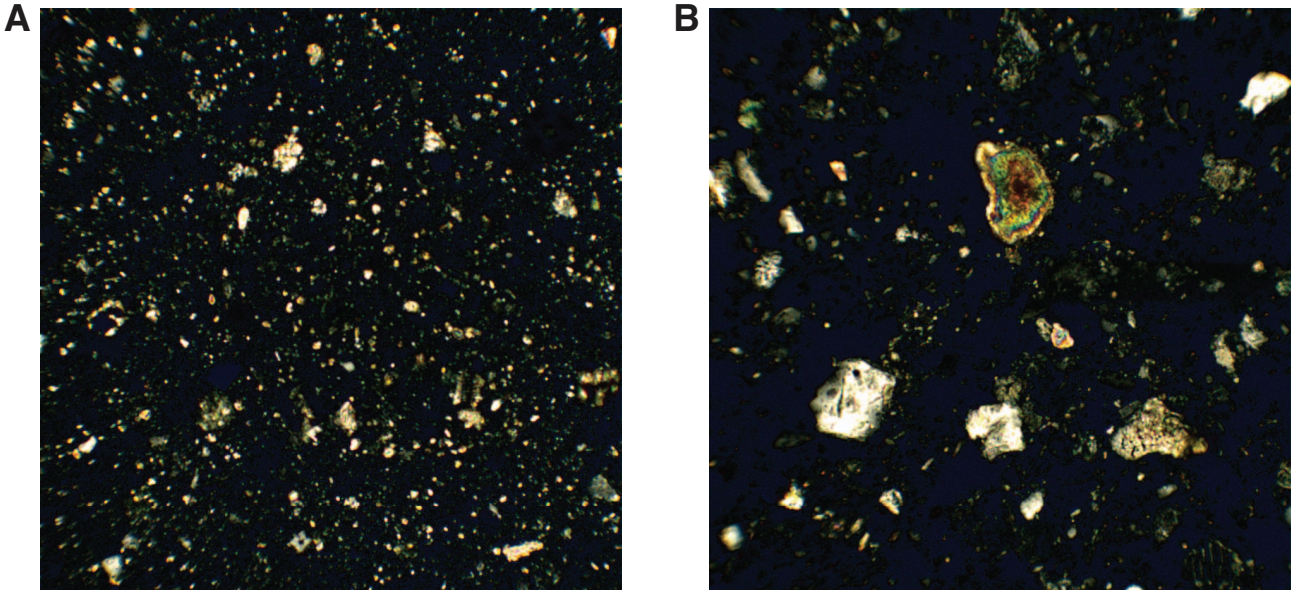

Figure F11. Photographs of black bioturbated clayey sandy silt. **A.** Interval 346-U1427A-9H-3, 10–40 cm (70.34–70.74 m CSF-A). **B.** Interval 346-U1427A-12H-7, 30–60 cm (99.41–99.71 m CSF-A). Note enhanced color contrast to highlight sedimentary structures.

Figure F12. Photographs showing laminations preserved in clayey silt.

U1427B-19H-6, 30-60 cm
156.95-157.55 m CSF-A

U1427B-26H-3, 5-35 cm
217.52-217.82 m CSF-A

U1427A-46H-4, 30-60 cm
326.54-326.84 m CSF-A

Figure F13. Downcore variations of maximum grain size, natural gamma radiation (NGR), and color reflectance parameter b* for Hole U1427A. Shaded areas indicate siliciclastic-rich sediment intervals. Blue and brown bars on upper axis show dark color intervals and laminated intervals, respectively.

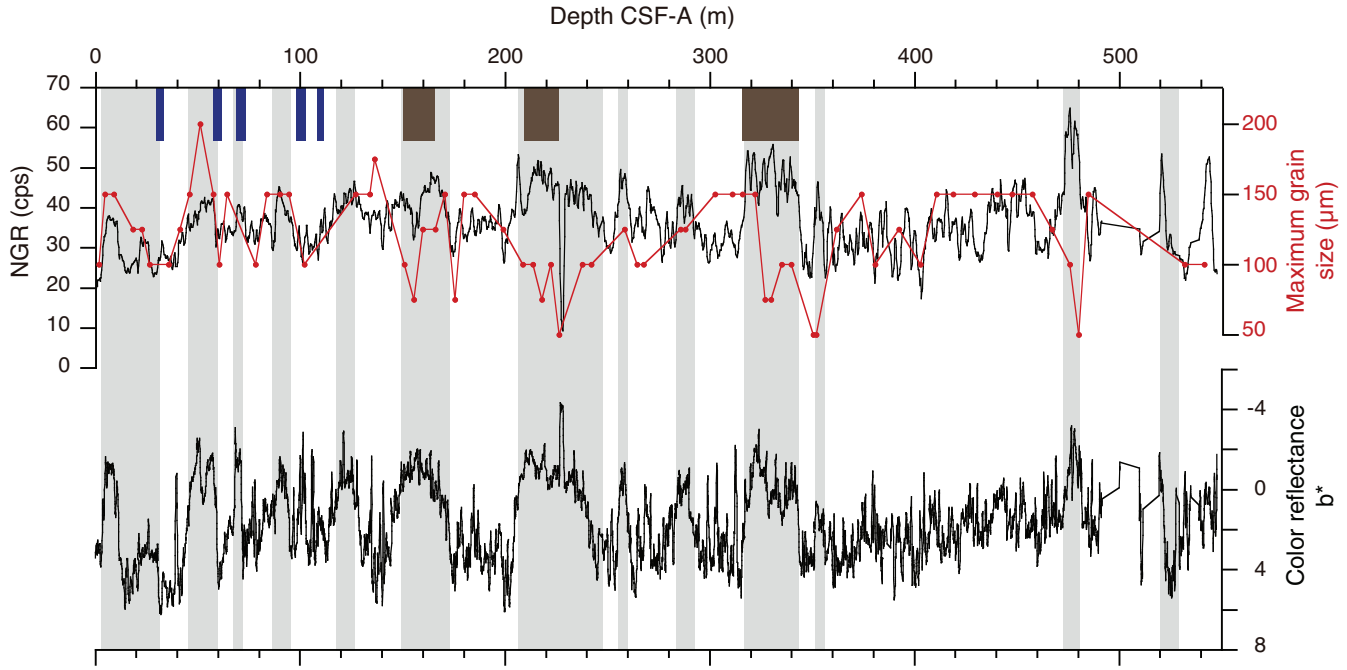

Figure F14. Integrated calcareous and siliceous microfossil biozonation, Site U1427. Barren = sample intervals barren of calcareous microfossils.

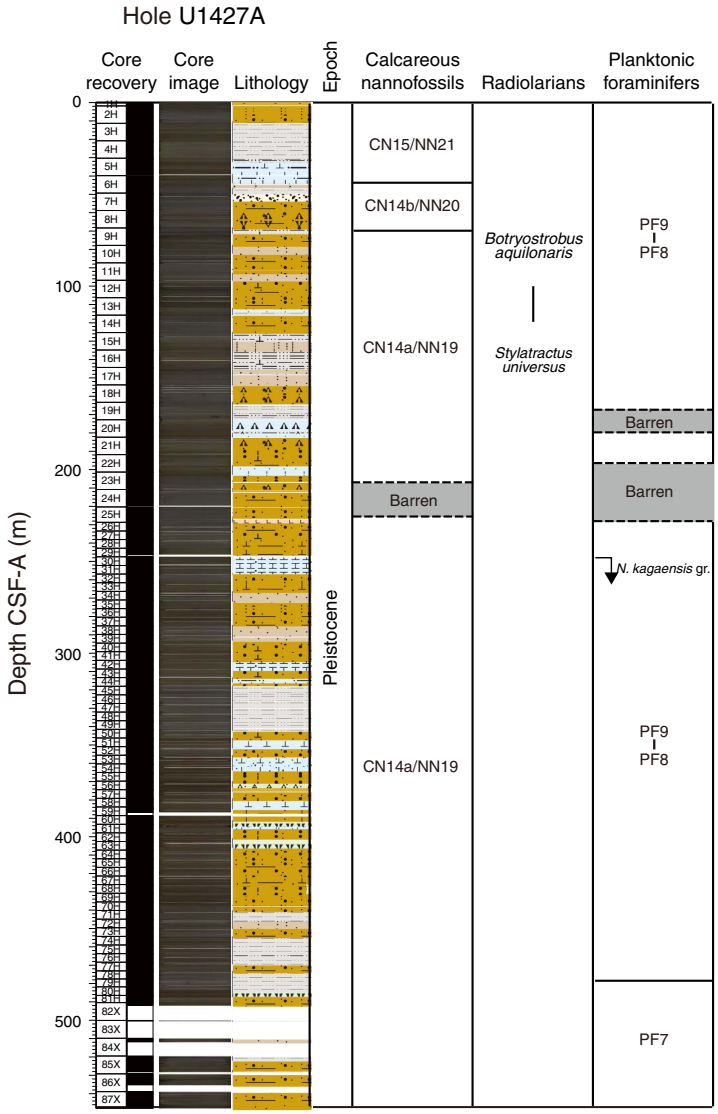

Figure F15. Age-depth profile, Site U1427. LO = last occurrence, D/S = dextral/sinistral crossover, FO = first occurrence, FCO = first common occurrence.

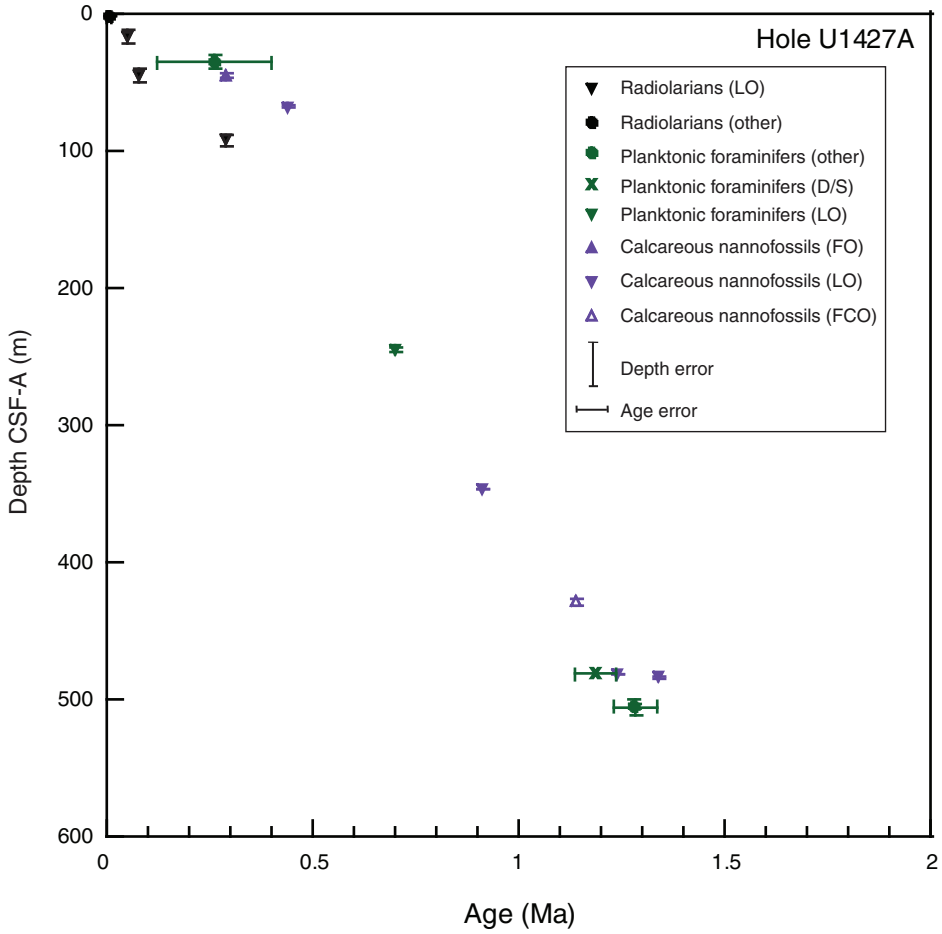

Figure F16. Distribution of siliceous and calcareous microfossils, Site U1427. B = barren, R = rare, F = few, C = common, A = abundant, D = dominant.

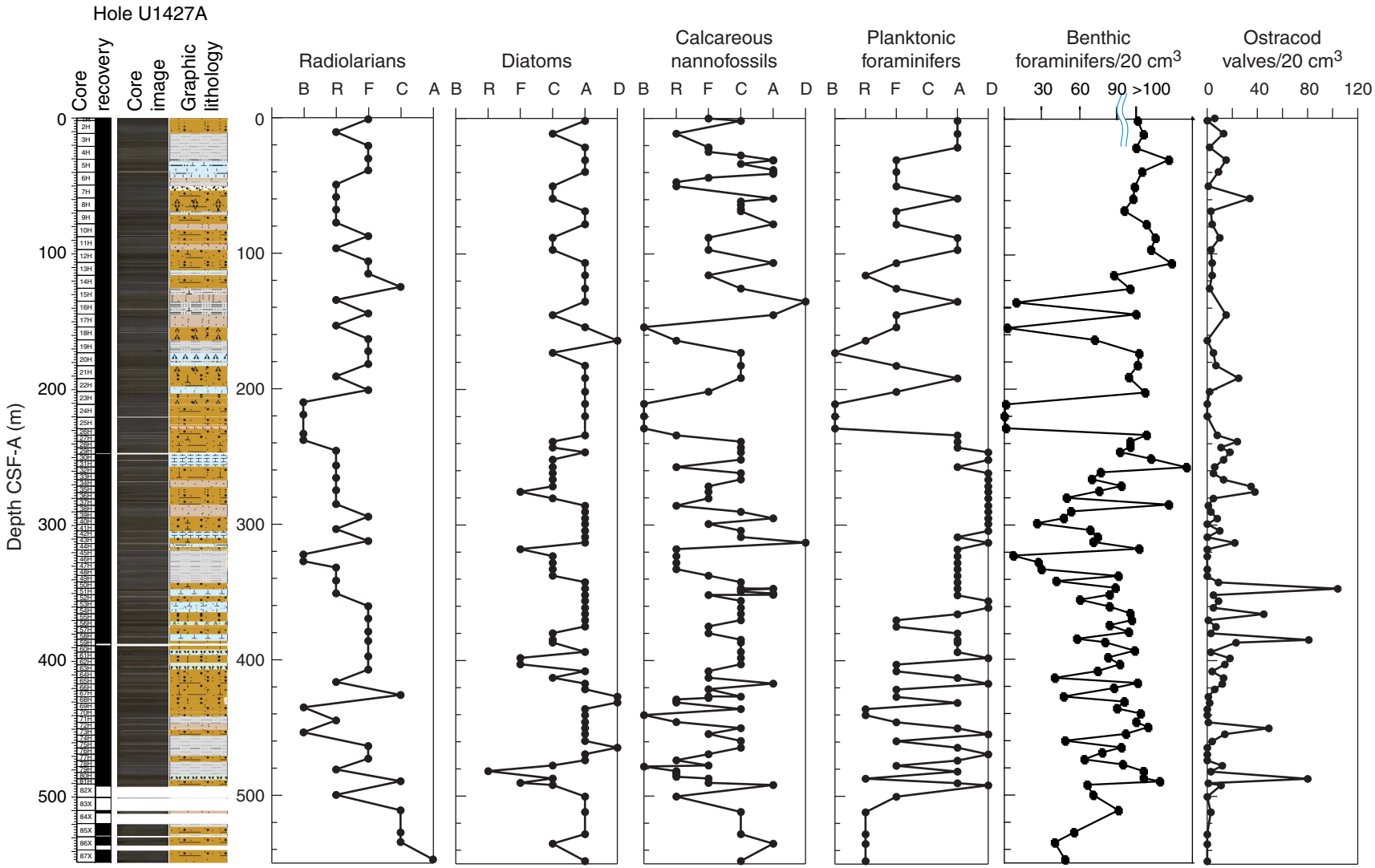

Figure F17. Calcareous nannofossils. Scale bars = 2 µm. **1.** *Coccolithus pelagicus* (proximal view) (Sample 346-U1427B-1H-1 mudline). **2.** *Gephyrocapsa oceanica* (Sample 346-U1427A-36H-2, 75 cm). **3.** *Gephyrocapsa* spp. large (>5.5 µm) (Sample 346-U1427B-1H-1 mudline). **4, 5.** Small *Gephyrocapsa* (<4 µm) (Sample 346-U1427B-1H-1 mudline). **6.** *Reticulofenestra* spp. (Sample 346-U1427A-36H-2, 75 cm). **7.** *Pseudoemiliania lacunosa* (Sample 346-U1427A-67H-3, 75 cm). **8, 9.** *Reticulofenestra* spp. (Sample 346-U1427A-67H-3, 75 cm). **10, 11.** *Emiliania huxleyi* (Sample 346-U1427A-1H-CC). **12, 13.** *Reticulofenestra asanoi* (Sample 346-U1427A-51H-2, 75 cm). **14, 15.** *Gephyrocapsa* spp. large (>5.5 µm); (14) Sample 346-U1427A-80H-2, 80 cm; (15) Sample 346-U1427A-80H-3, 80 cm. **16, 17.** *Helicosphaera sellii* (Sample 346-U1427A-80H-3, 80 cm). **18, 19.** *Calcidiscus macintyrei* (Sample 346-U1427A-85X-CC). 1–9: scanning electron microscope, 10–19: light microscope (cross-polarized light).

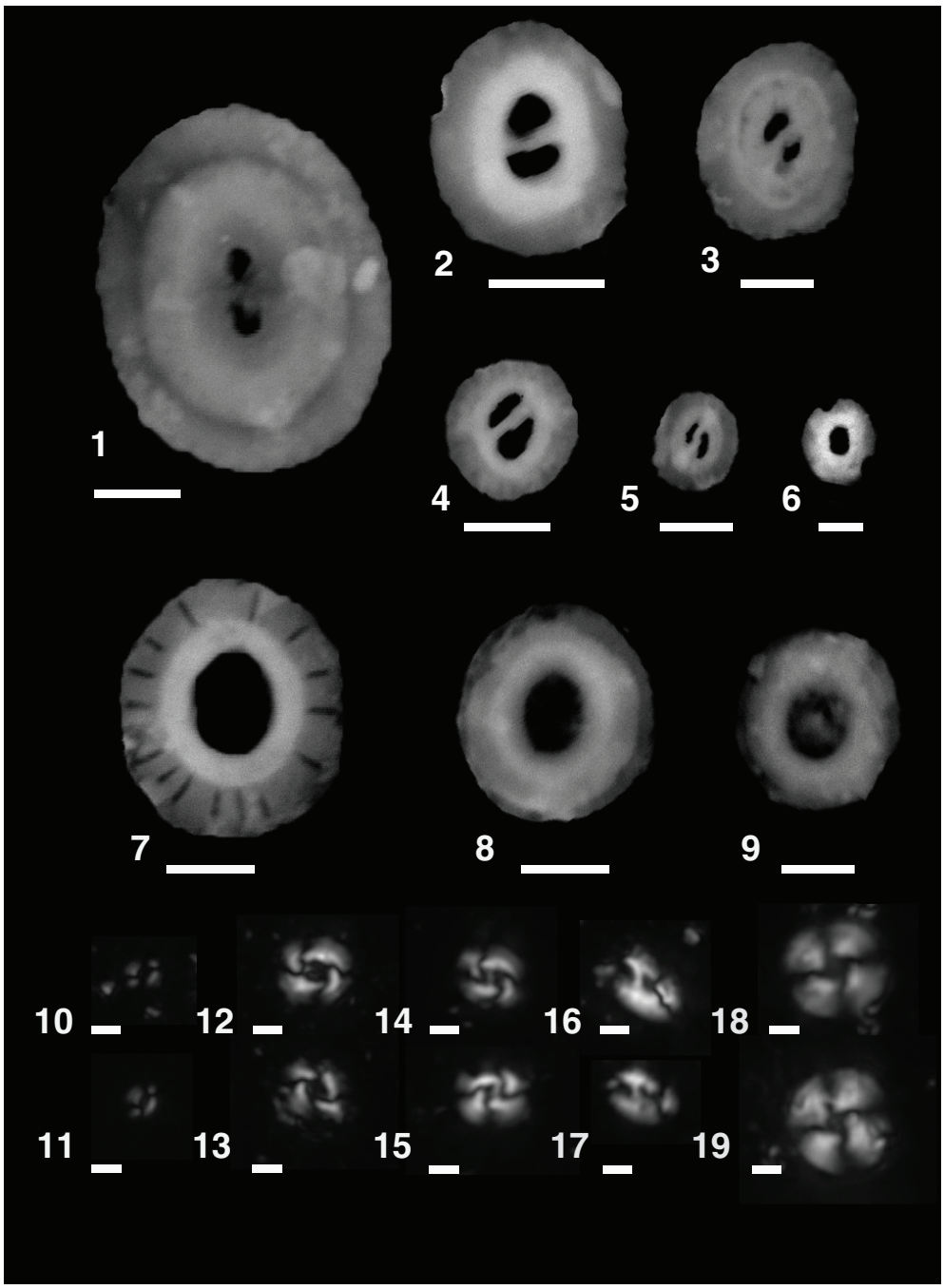

Figure F18. Variations of b* (blue line) and Tr value (red line) with positions of biostratigraphic datums (triangles under the depth scale, see Table T4), Site U1427. Marine isotope curve of LR04 (Lisiecki and Raymo, 2005) is also shown (gray line). Yellow hatches indicate intervals of high Tr values. Probable correlations between Tr peaks and corresponding interglacial periods are shown by pink dashed lines.

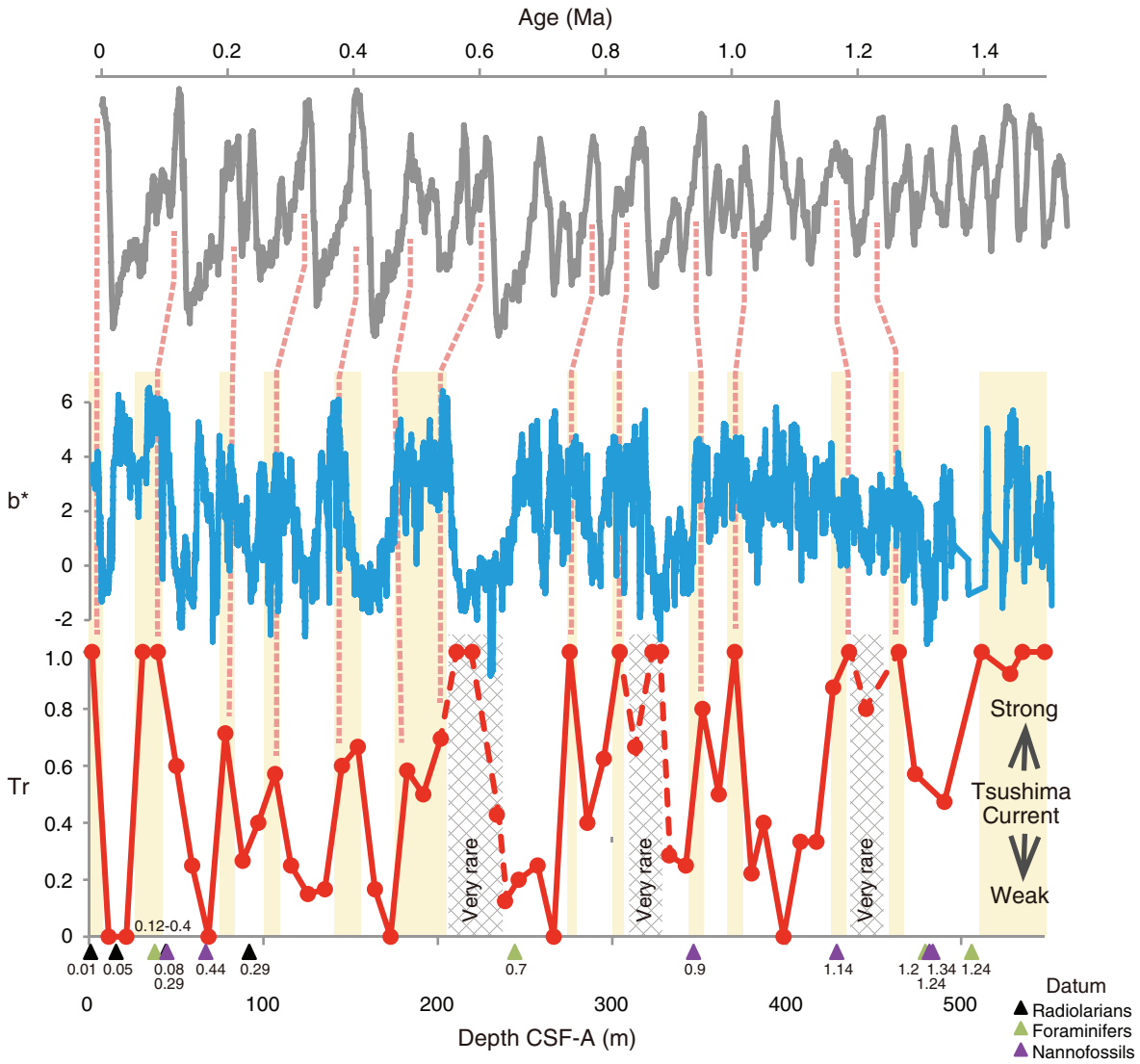

Figure F19. A. Living specimens of *Thalassionema nitzschioides* showing their chloroplasts. **B.** Same species found in Sample 346-U1427A-40H-CC with organic matter preserved inside the frustule.

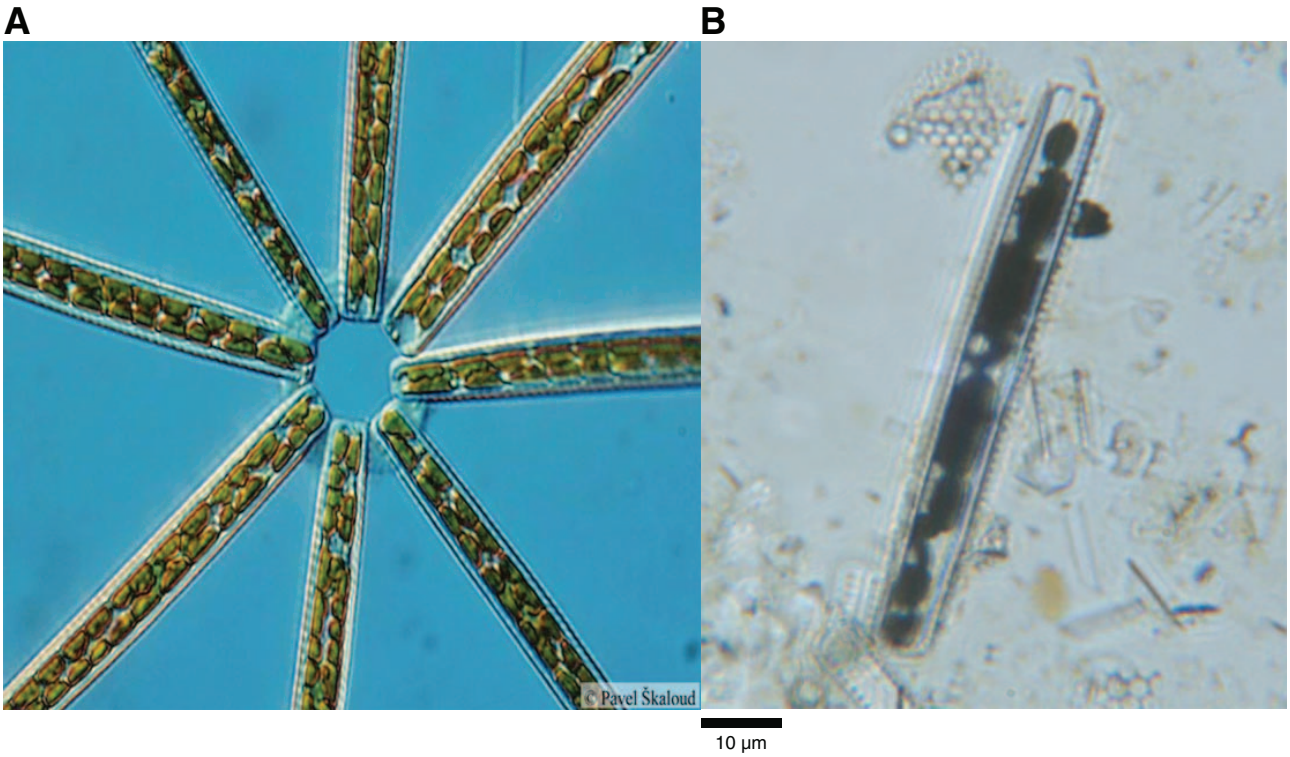

Figure F20. Relative abundances of diatoms, *Chaetoceros* spores, *Paralia sulcata,* and freshwater species, Site U1427. B = barren, R = rare, F = few, C = common, A = abundant, D = dominant.

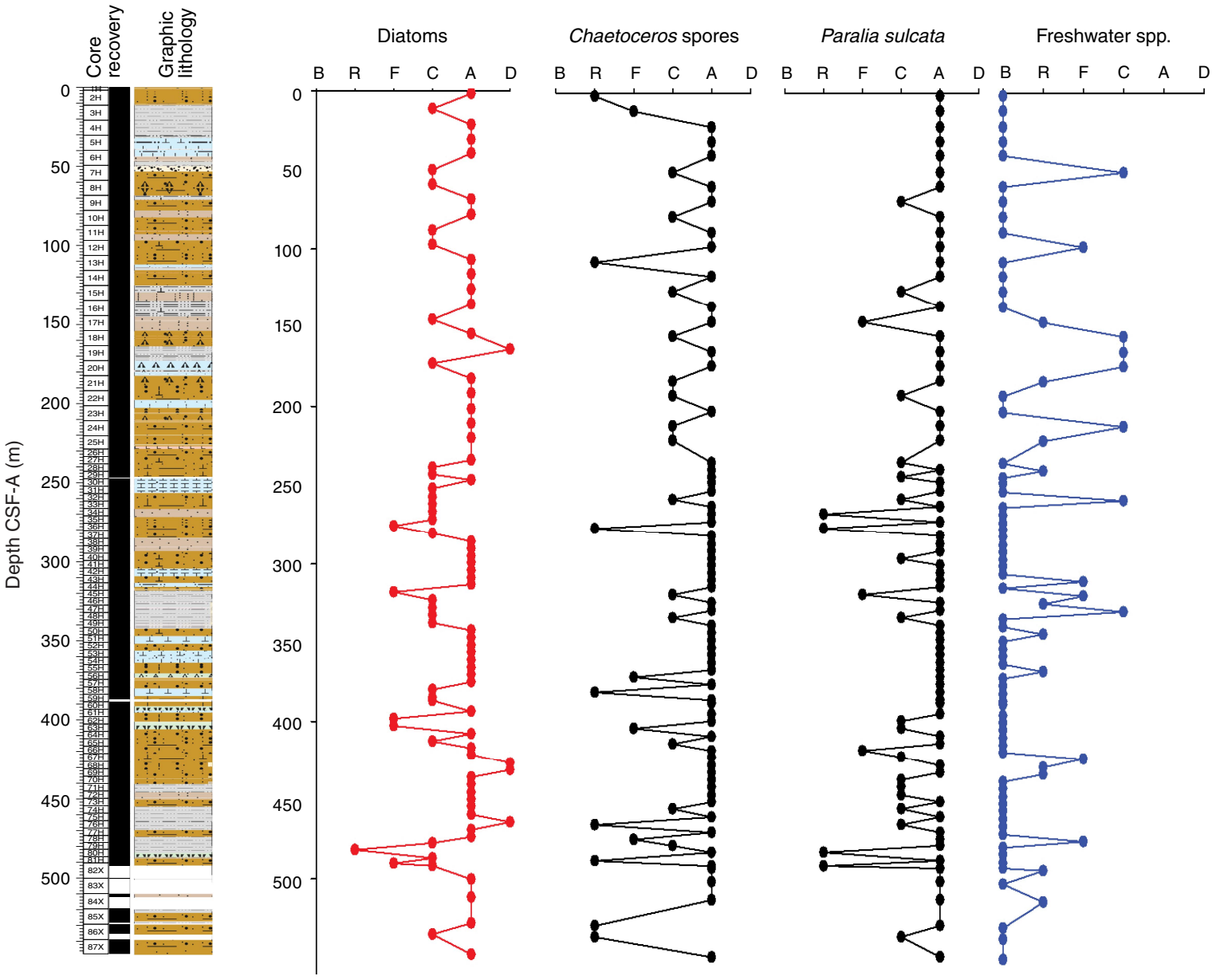

Figure F21. Comparison of color reflectance b* and planktonic foraminiferal distribution data, Hole U1427A. The percentage of planktonics refers to the total foraminiferal assemblage. The percentage of various species is expressed as a percentage of the total planktonic assemblage. Red arrows = *G. ruber*, purple arrows = *P. obliquiloculata*. Black down and up arrows indicate LO and FO, respectively, of each species. Barren = sample intervals barren of calcareous microfossils, rare = intervals where calcareous microfossils are present in very low numbers.

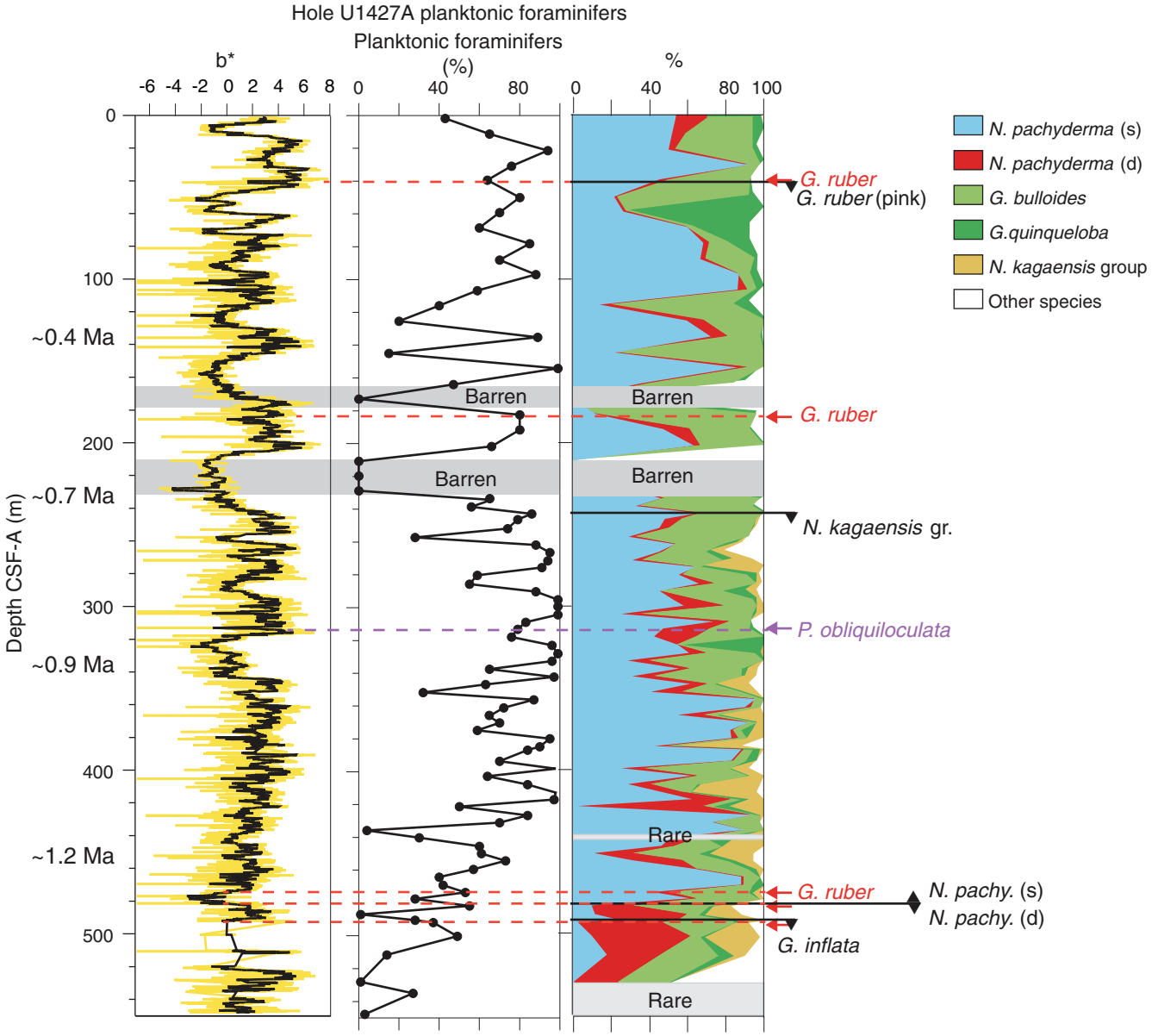

Figure F22. Comparison of color reflectance b*, benthic foraminiferal, and ostracod distribution data, Hole U1427A. The percentage of benthics refers to the total foraminiferal assemblage. The percentage of various species is expressed as a percentage of the total benthic assemblage.

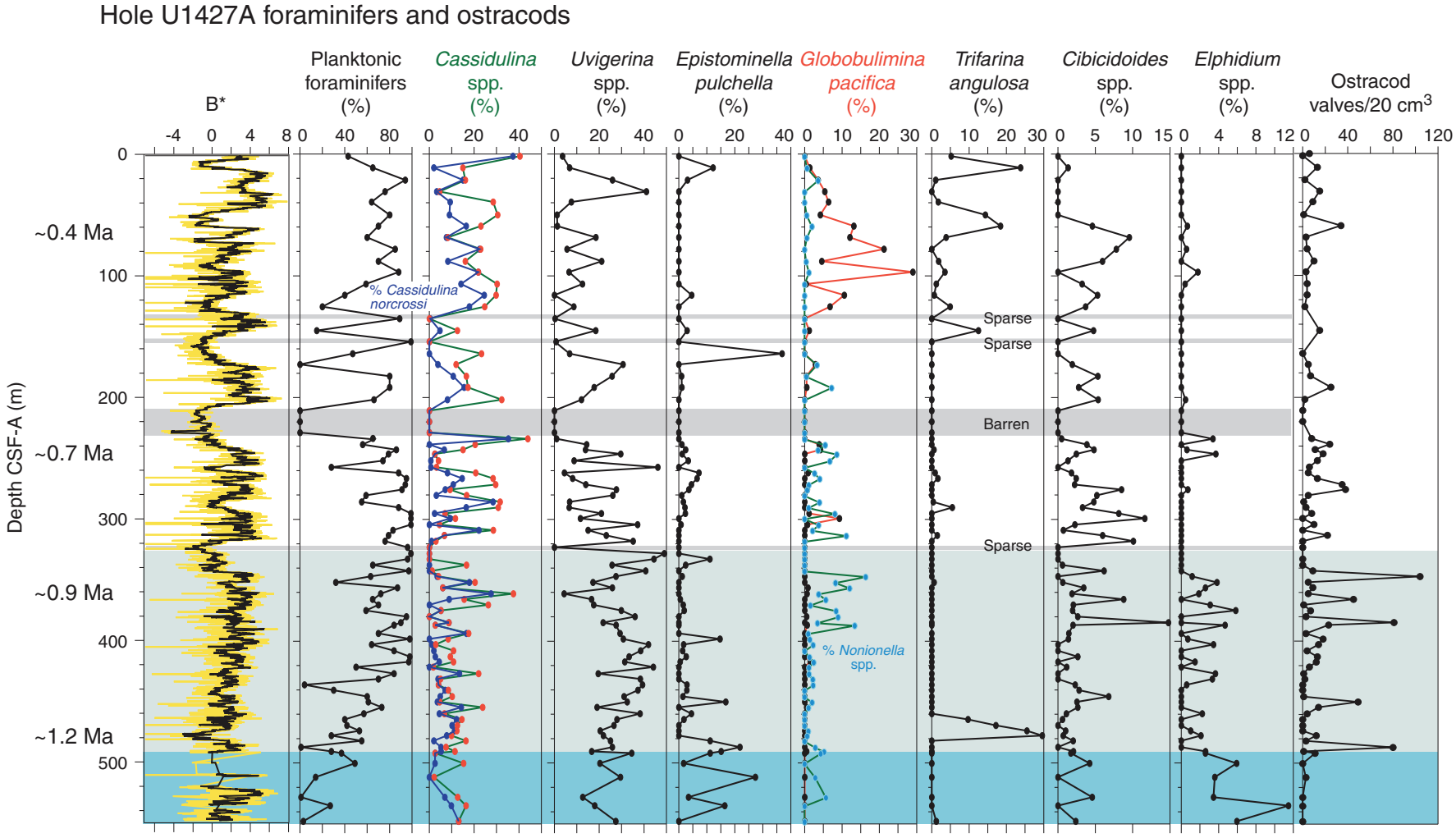

Figure F23. Benthic foraminifers. Scale bars = 50 µm. **1.** *Cassidulina japonica* (Sample 346-U1427A-37H-CC). **2.** *Cassidulina norcrossi* (Sample 346-U1427A-37H-CC). **3, 4.** *Cibicidoides lobatulus* (Sample 346-U1427A-37H-CC). **5.** *Cassidulina* sp. (Sample 346-U1427A-37H-CC). **6, 7.** *Pullenia* sp. (Sample 346-U1427A-5H-CC). **8.** *Grigelis* sp. (Sample 346-U1427A-37H-CC). **9, 10.** *Nonionellina labradorica* (Sample 346-U1427A-37H-CC). **11, 12.** *Fursenkoina* sp. (Sample 346-U1427A-56H-CC). **13.** *Quinqueloculina* sp. (Sample 346-U1427A-37H-CC). **14.** *Uvigerina yabei* (Sample 346-U1427A-37H-CC). **15, 16.** *Elphidium* sp. (Sample 346-U1427A-56H-CC).

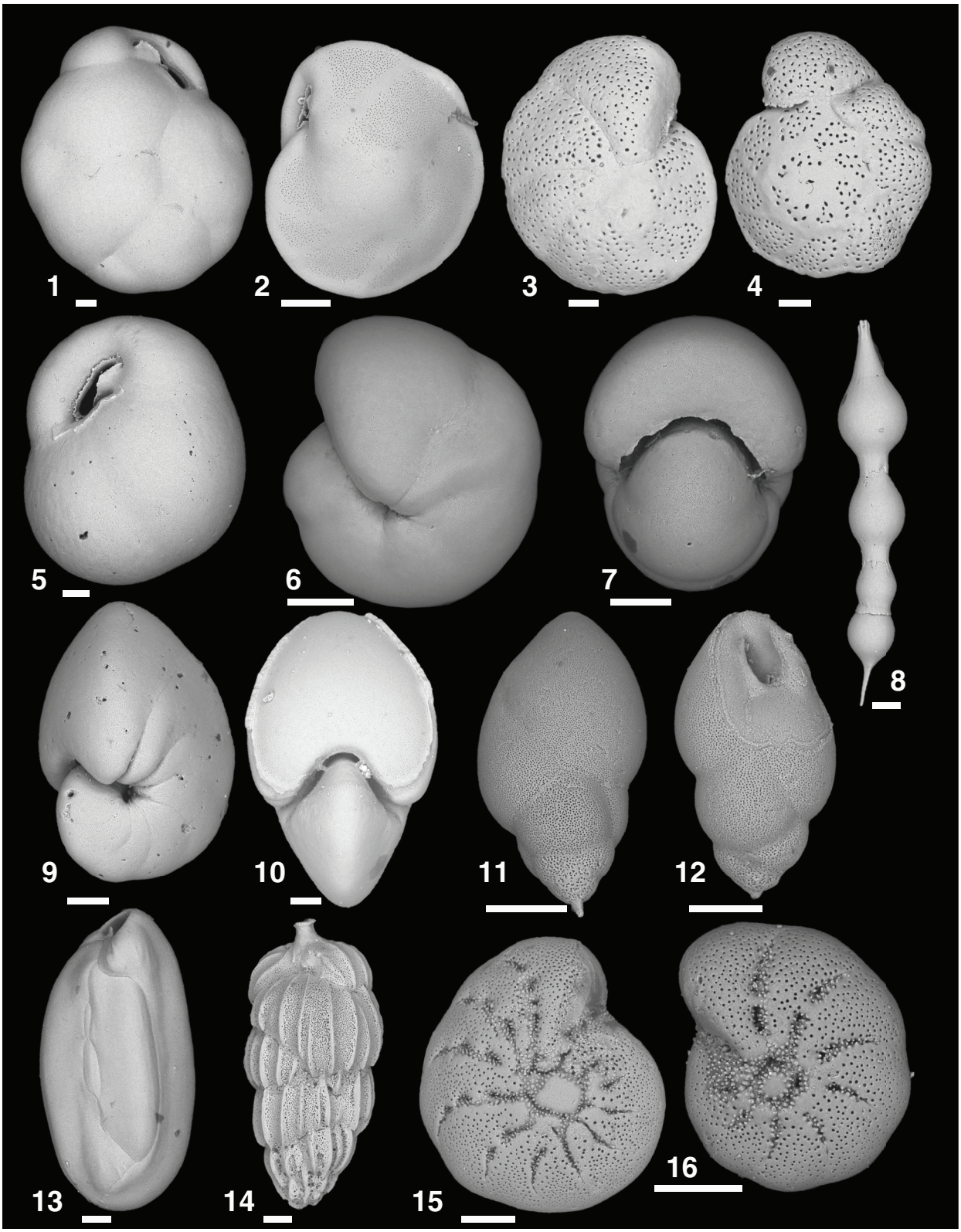

Figure F24. Scanning electron microscope illustrations of representative ostracods in Hole U1427A. **1.** *Pterigocythereis* sp. (left valve, Sample 346-U1247A-2H-CC). **2, 3.** *Cytheropteron* cf. *C. syntomalatum* Whatley and Coles, 1987: (2) right valve, (3) left valve; Sample 4H-CC. **4.** *Krithe sawanensis* Hanai, 1959 (left valve, Sample 2H-CC). **5.** *Acanthocythereis dunelmensis* (Norman, 1865) (left valve, Sample 20H-CC). **6.** *Propontocypris* sp. (left valve, Sample 4H-CC). **7.** *Robertsonites* cf. *R. hanaii* Tabuki, 1986 (left valve, Sample 35H-CC). **8.** *Loxoconcha parapontica* Zhou, 1995 (left valve, Sample 20H-CC). **9.** *Loxoconcha* sp. B (right valve, Sample 35H-CC). **10.** *Cytheropteron* sp. B (left valve, Sample 33H-CC). **11.** *Falsobuntonia* sp. (right valve, Sample 7H-CC). **12.** *Kyphocythere limicola* (Norman, 1865) (right valve, Sample 34H-CC). **13, 14.** *Legitimocythere* sp.: (13) left valve, Sample 4H-CC, (14) right valve, Sample 28H-CC. **15.** *Munseyella* sp. (left valve, Sample 28H-CC).

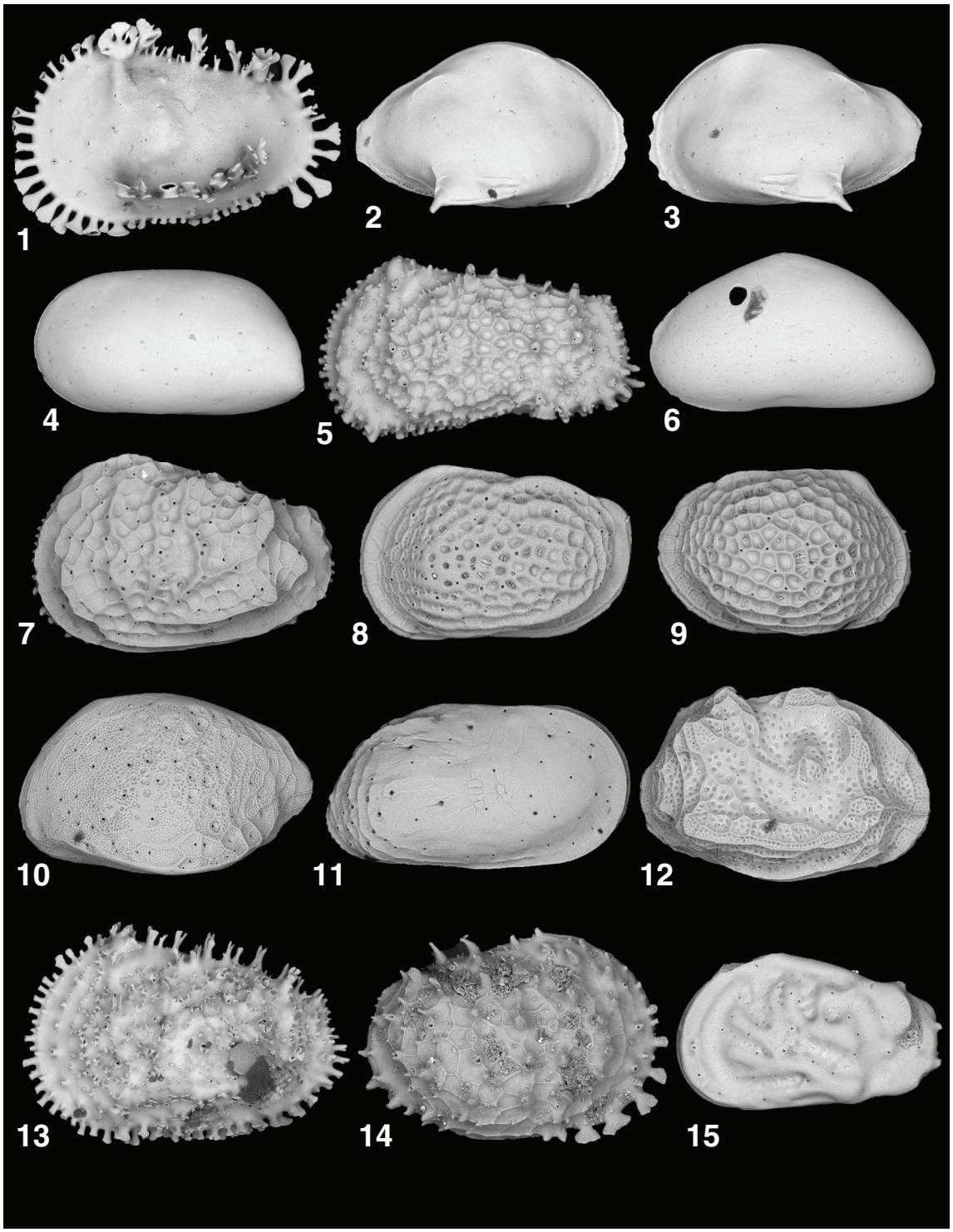

Figure F25. Calcareous and organically cemented, agglutinated foraminifers from Hole U1427A mudline sample. Scale bars = 50 µm. **1.** *Bolivina pacifica*. **2, 3.** *Bolivina decussata*. **4, 5.** *Fursenkoina bradyi*. **6.** *Trifarina angulosa*. **7.** *Procerolagena gracillima*. **8, 9.** *Ammodiscus anguillae*. **10–14.** *Epistominella* spp. **15.** *Nonionella labradorica*. **16.** *Triloculina* sp. **17.** *Haplopharagmoides sphaeriloculum*. **18.** *Valvulineria sadonica*. **19.** *Lagena multilatera*.

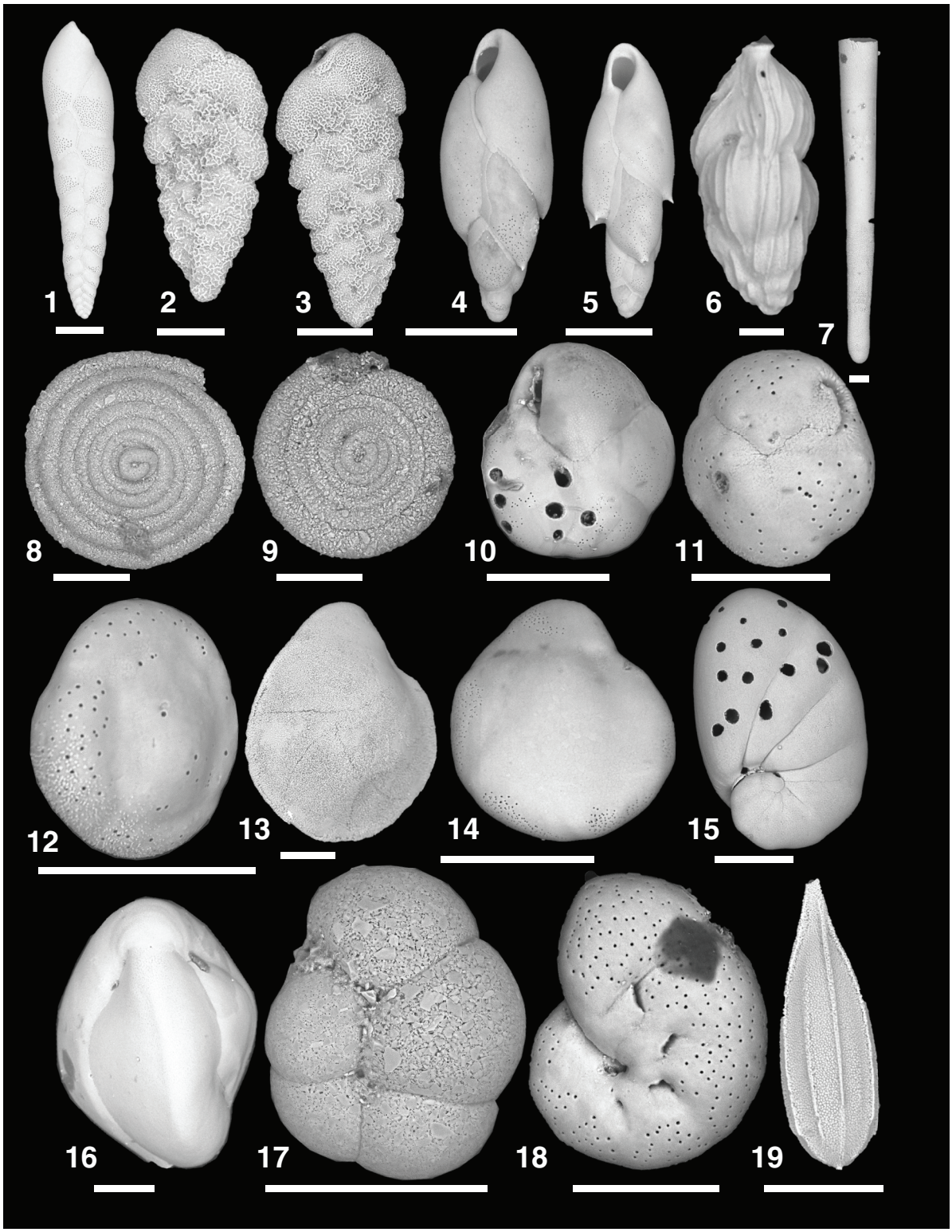

Figure F26. Overview of mudline benthic foraminiferal assemblage in slide, Site U1427. Live specimens are stained red with rose bengal.

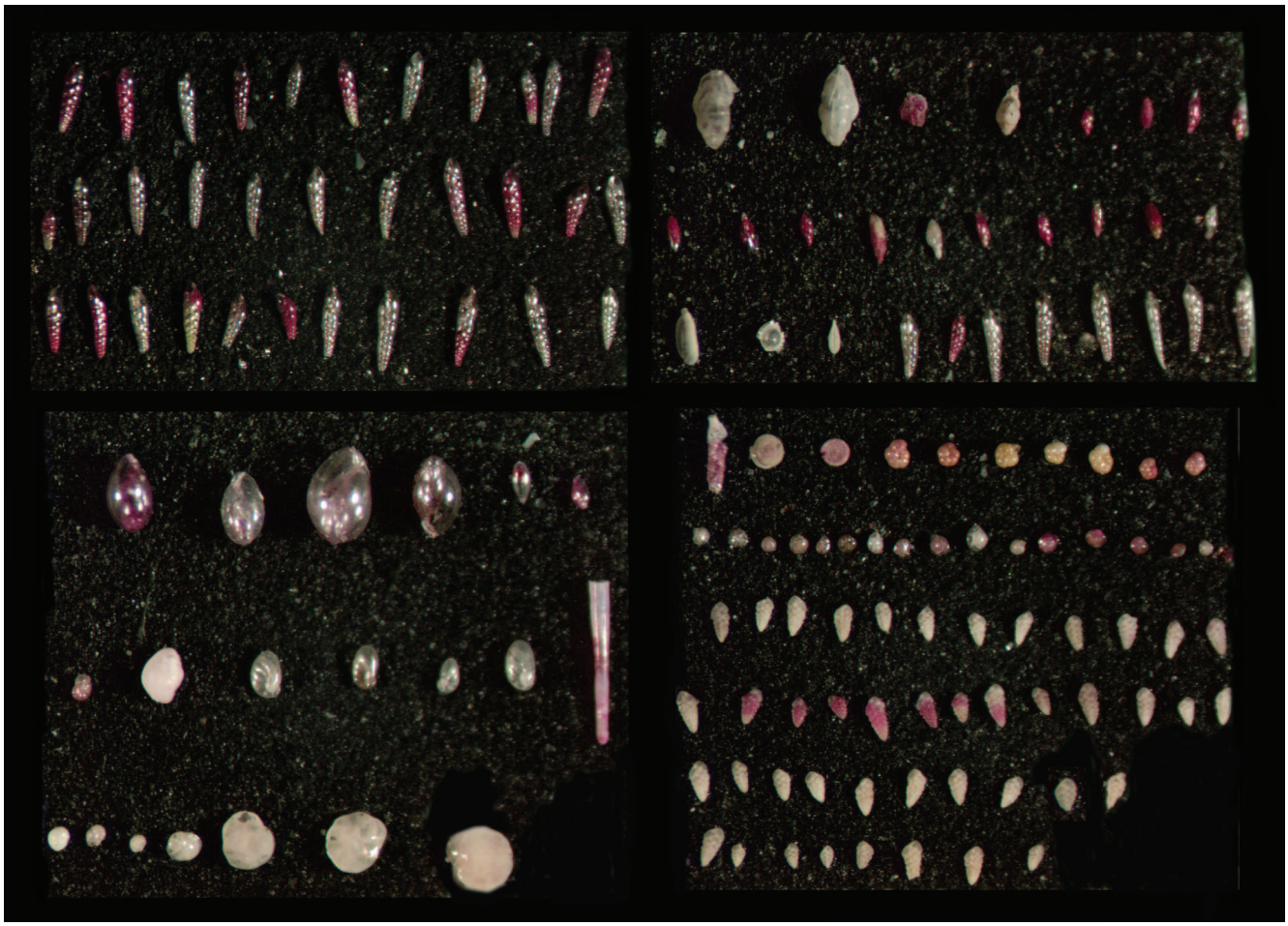

Figure F27. Solid-phase contents of discrete sediment samples, Site U1427. TC = total carbon, TOC = total organic carbon, TN = total nitrogen.

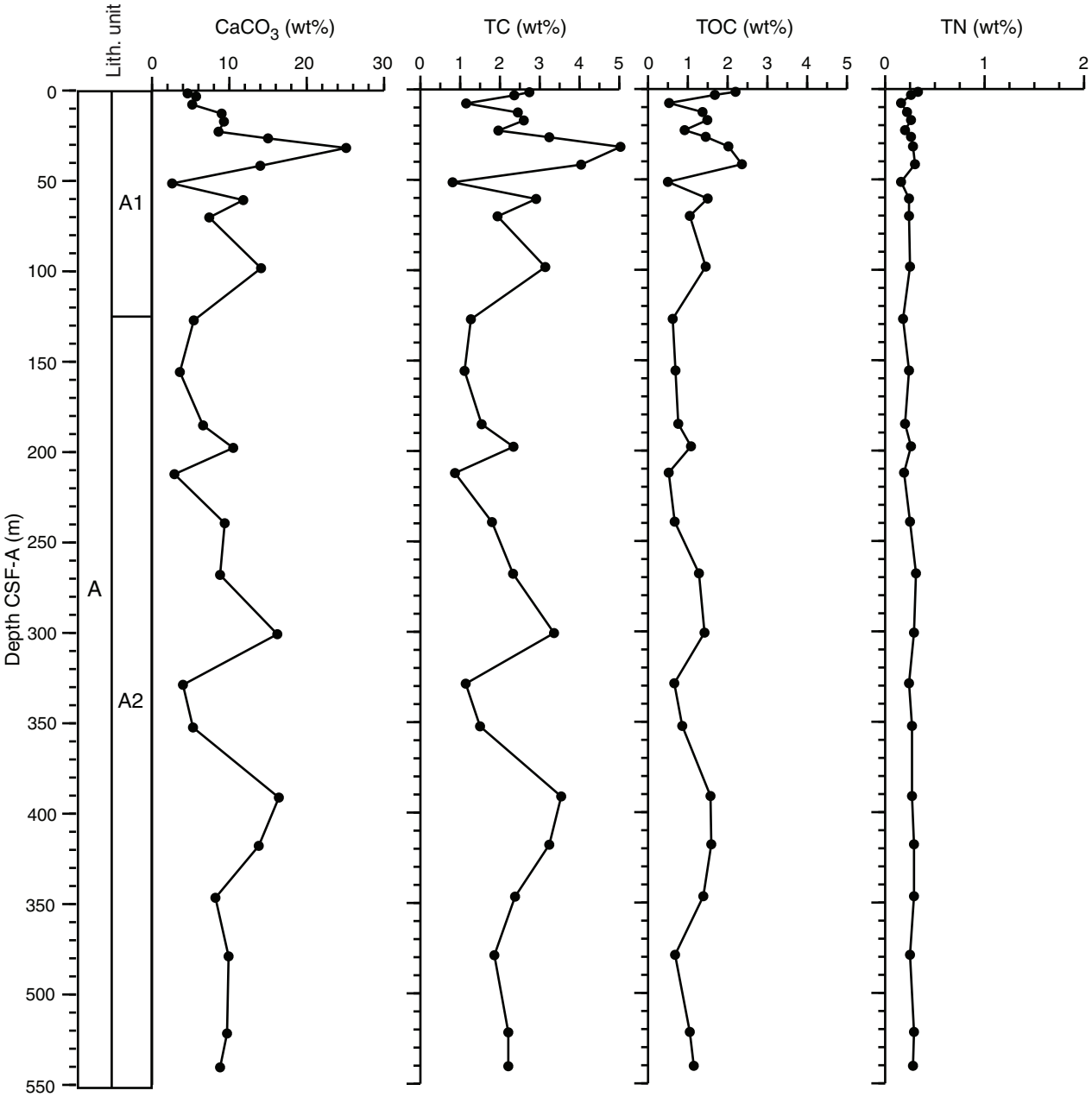

Figure F28. Dissolved manganese and iron profiles over the entire depth, Site U1427.

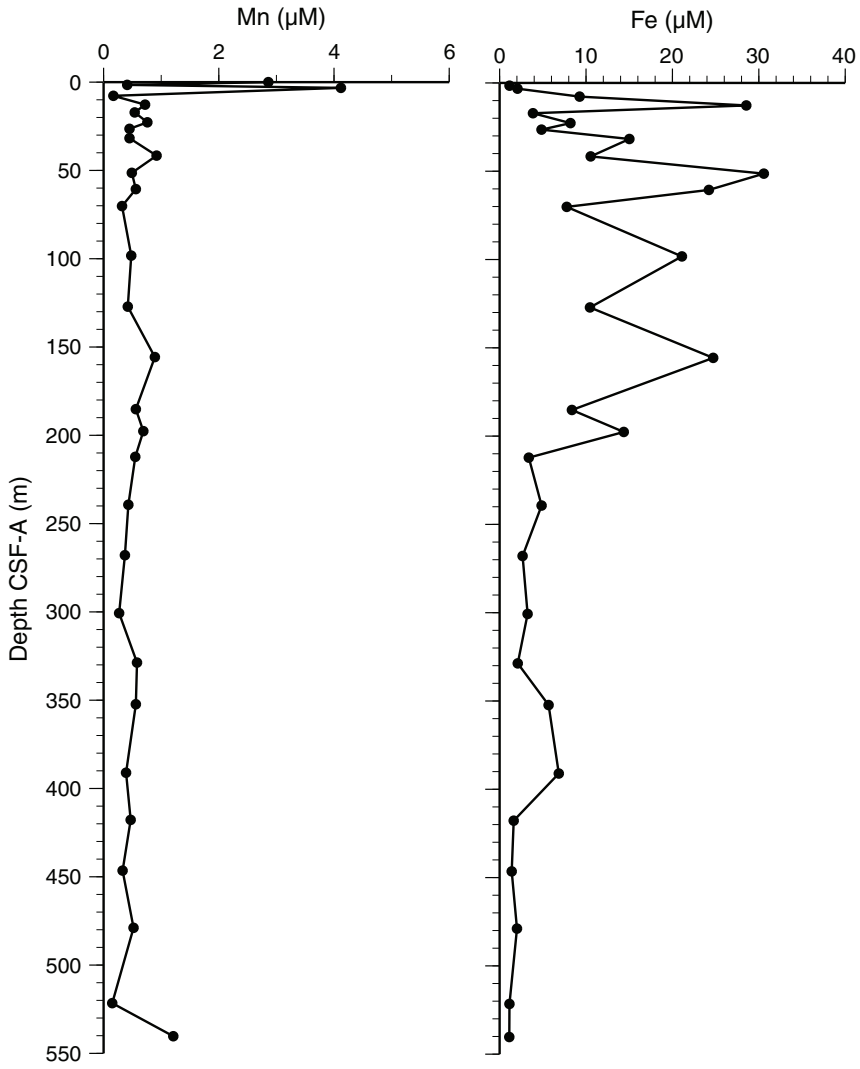

Figure F29. Dissolved manganese and iron profiles over the uppermost 9 m below the seafloor, Site U1427. IW-sq = squeezed interstitial water.

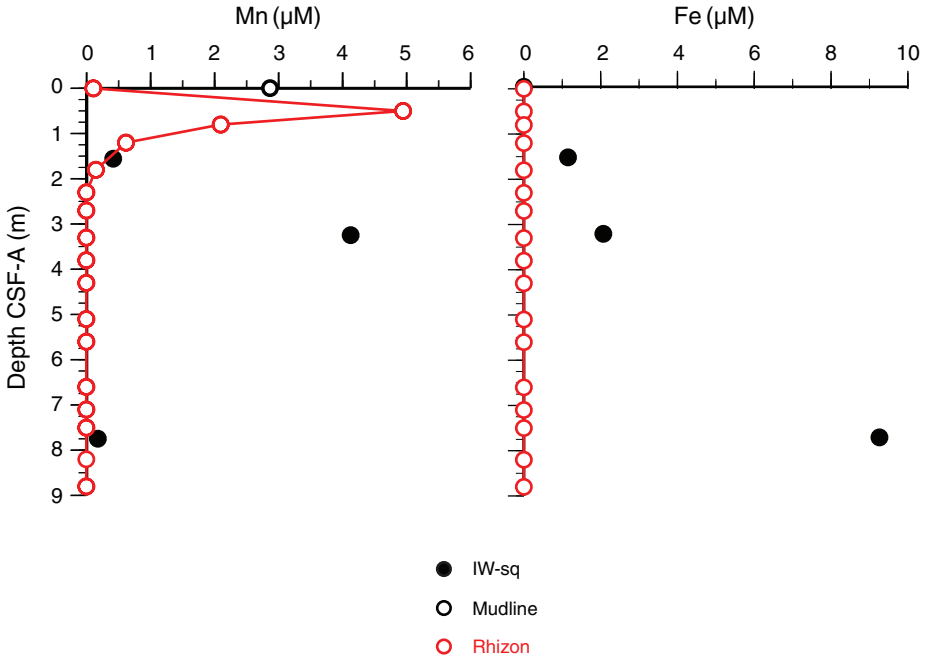

Figure F30. Dissolved alkalinity, ammonium, and phosphate profiles over the full depth, Site U1427. IW-sq = squeezed interstitial water.

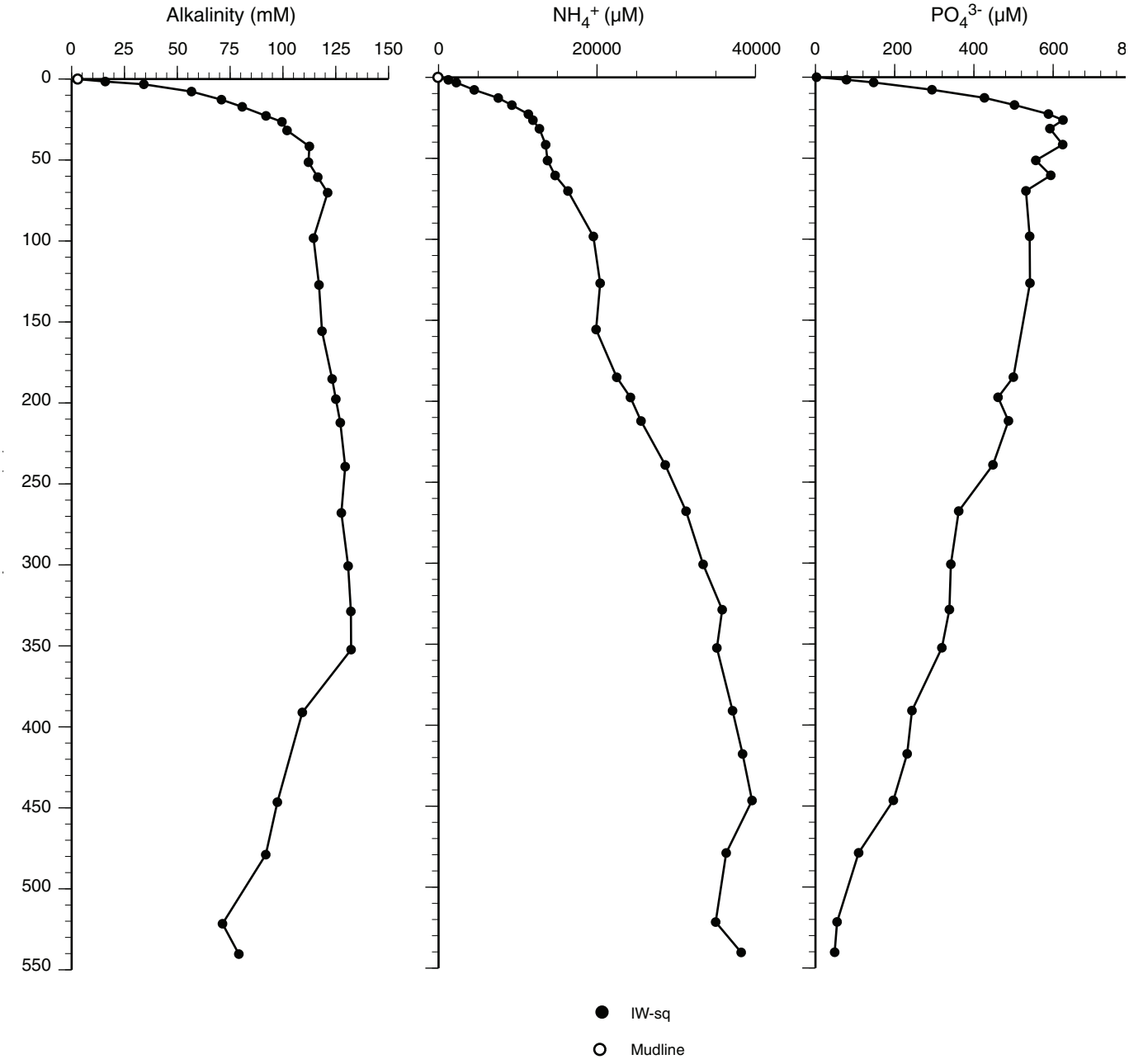

Figure F31. Dissolved alkalinity, ammonium, sulfide, methane, and sulfate profiles over the upper 10 m, Site U1427. The sulfate–methane transition (SMT) occurs at ~5 m CSF-A. IW-sq = squeezed interstitial water.

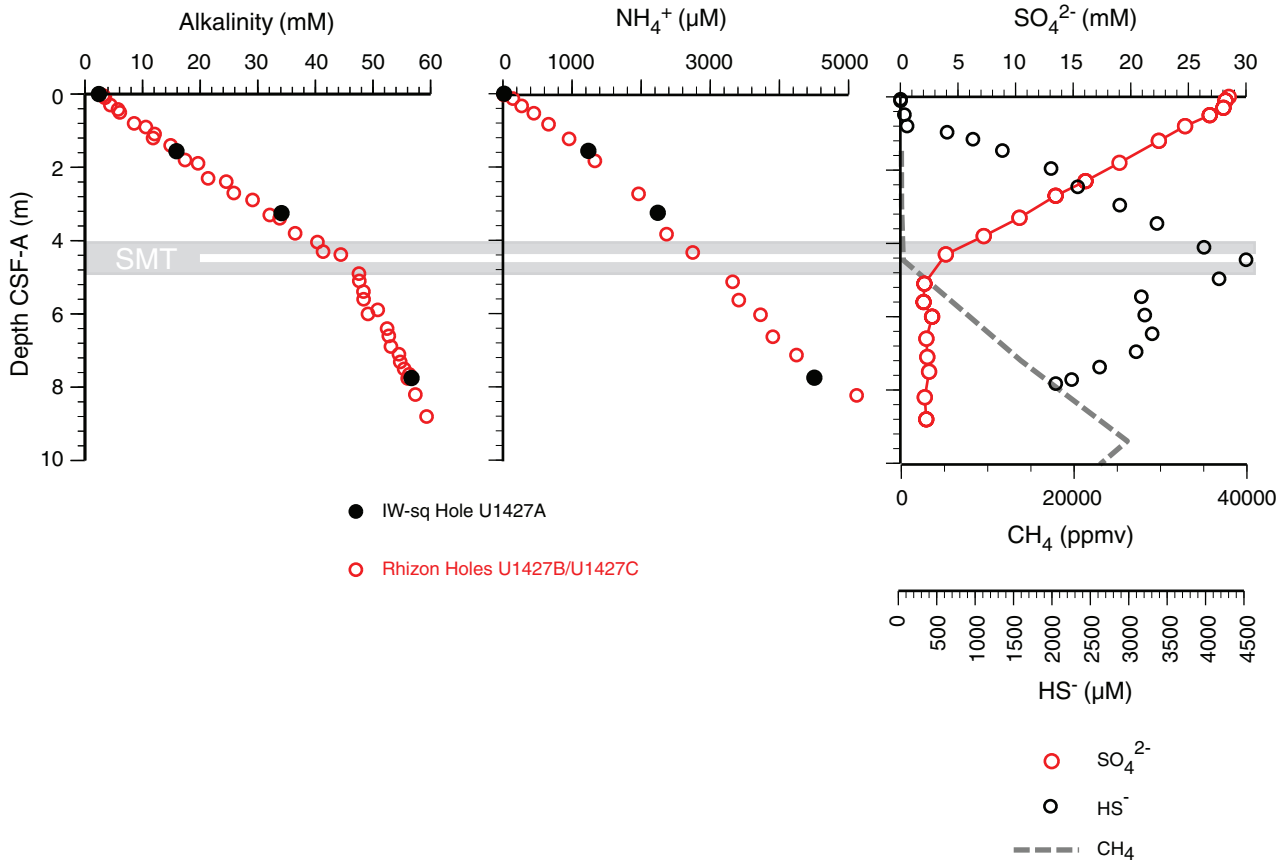

Figure F32. Dissolved bromide concentrations over the entire depth, Site U1427.

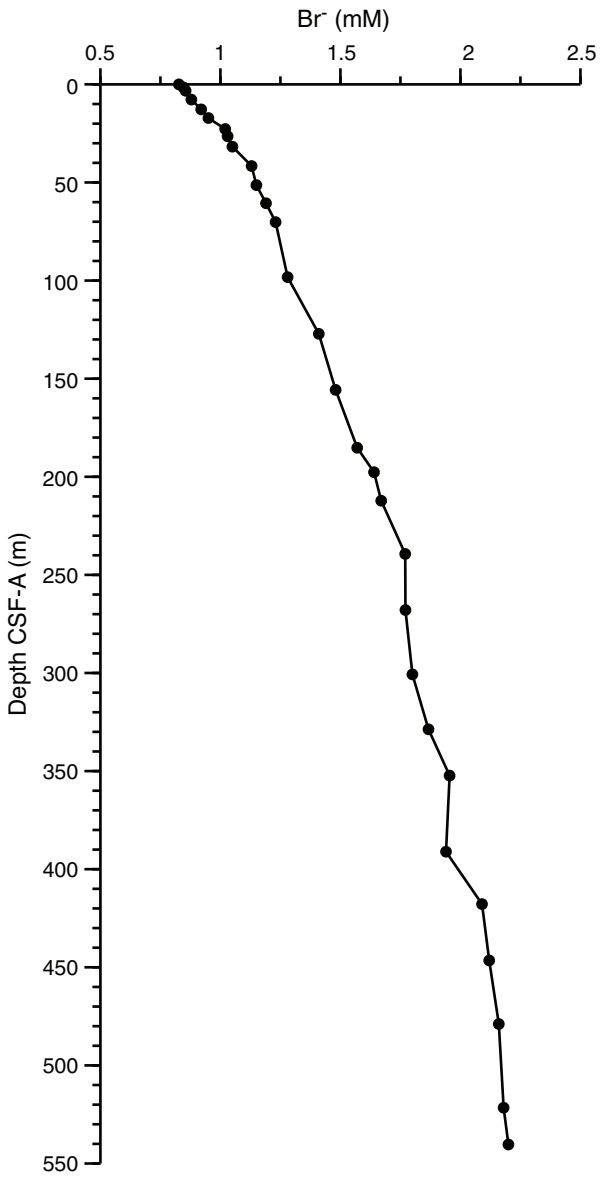

Figure F33. Absorbances of interstitial water at Site U1427 at three different wavelengths. Table T14 shows the reproducibility of measurements between different batches. IW-sq = squeezed interstitial water.

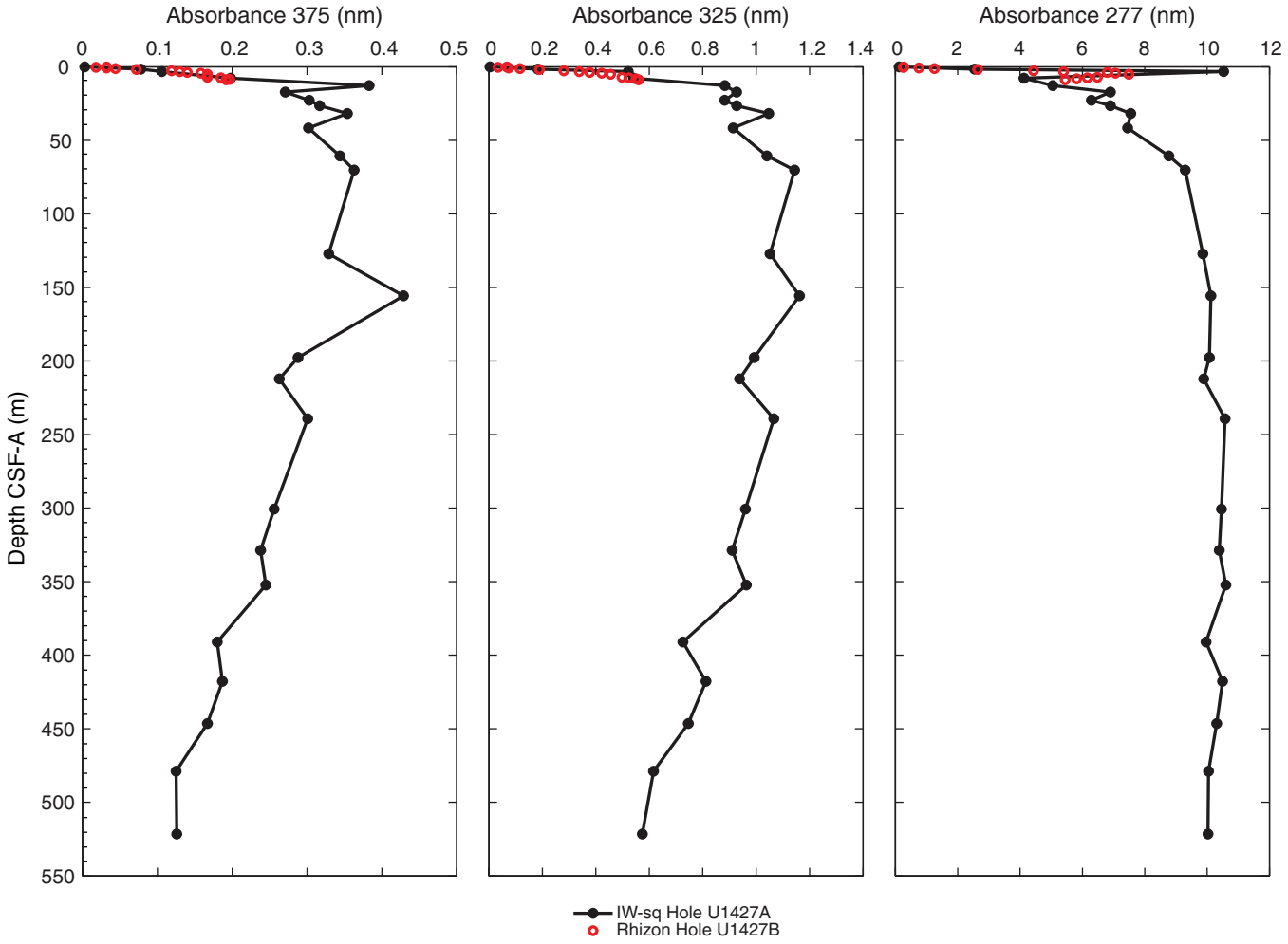

Figure F34. Headspace CH_4 concentrations (other sites plotted for comparison) and methane to ethane ratio with depth, Site U1427. Note that concentration values are not meaningful at depths where CH_4 surpasses saturation at 1 atm pressure (~10,000 ppm at ~20 m CSF-A). Also note that measured concentrations and ratios decrease with depth because of differential gas solubility with temperature.

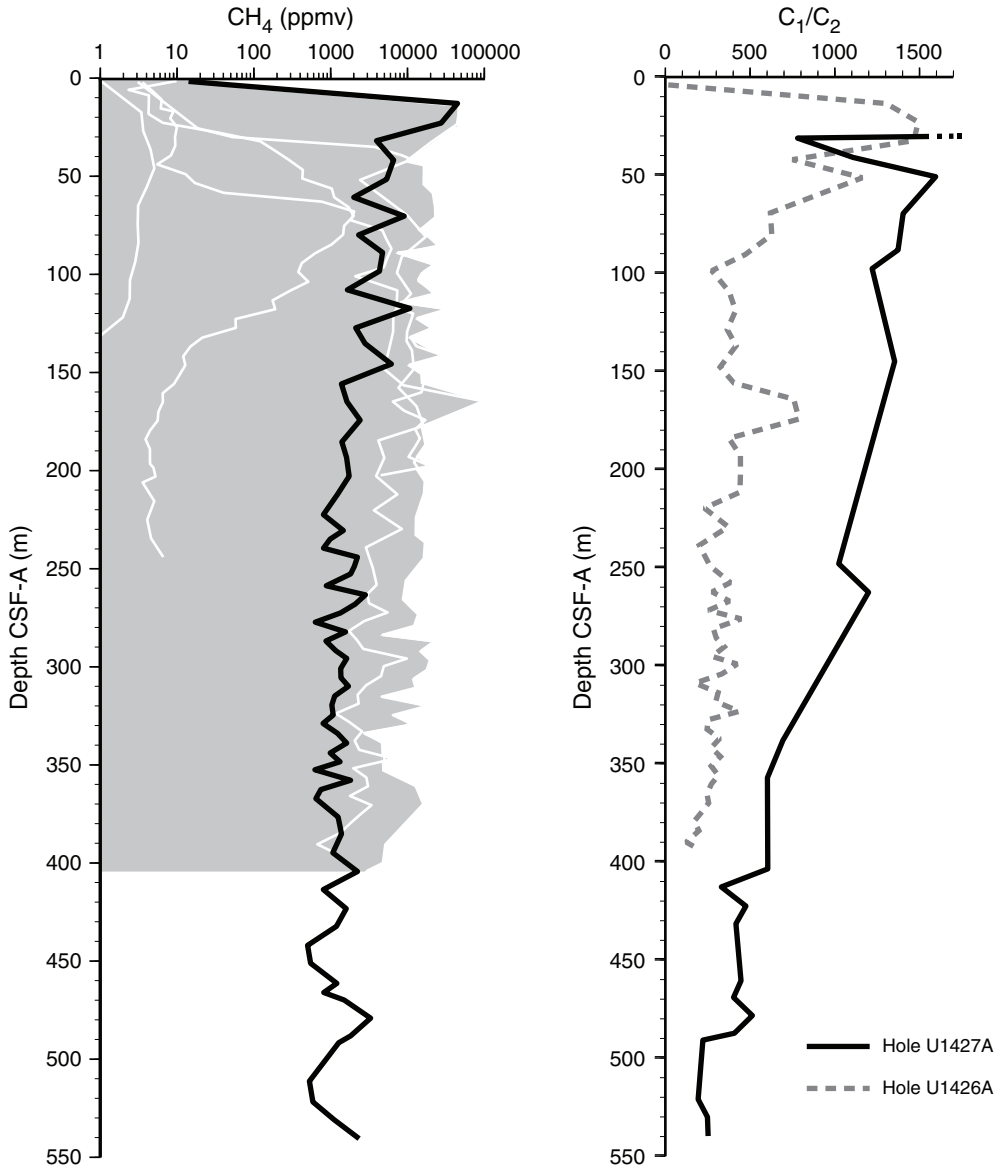

Figure F35. Dissolved sulfate concentrations over the full depth, Site U1427. Also shown is headspace CH_4 concentration (on a linear scale).

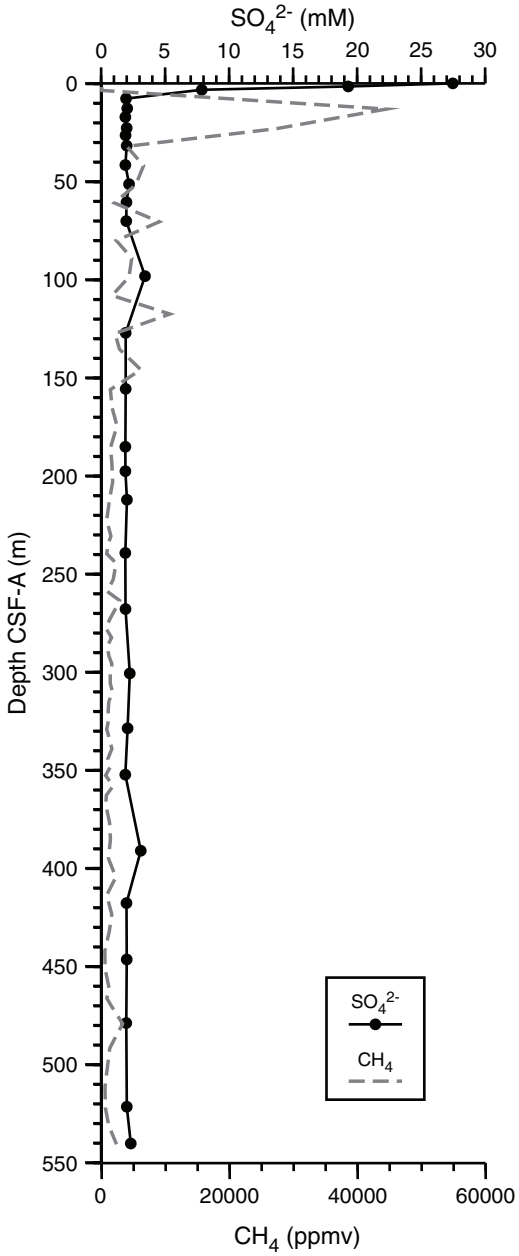

Figure F36. Dissolved barium profiles with depth, Site U1427. **A.** Full depth. **B.** The uppermost 10 m below the seafloor. IW-sq = squeezed interstitial water.

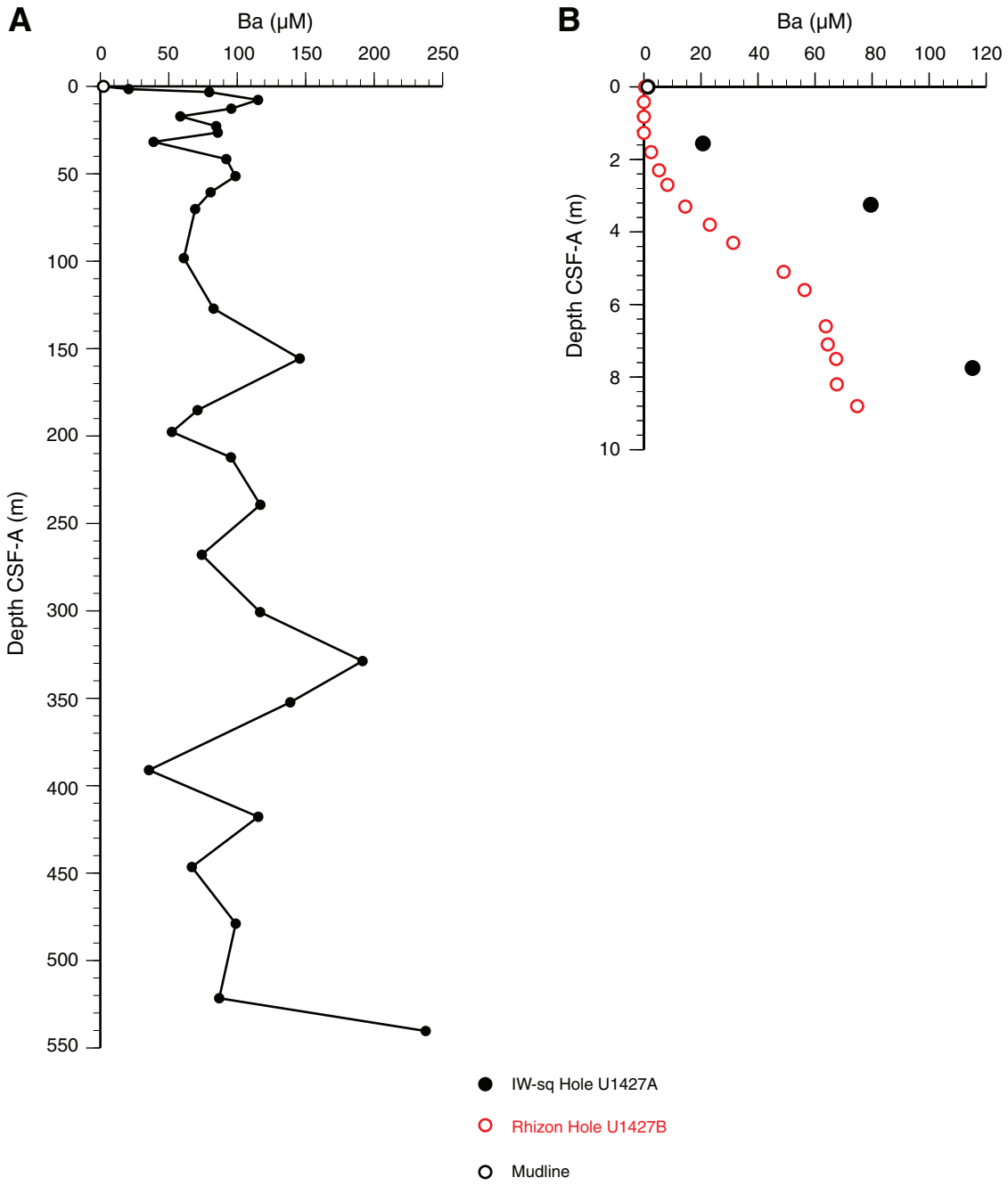

Figure F37. Dissolved calcium, magnesium, and strontium profiles across the full depth, Site U1427.

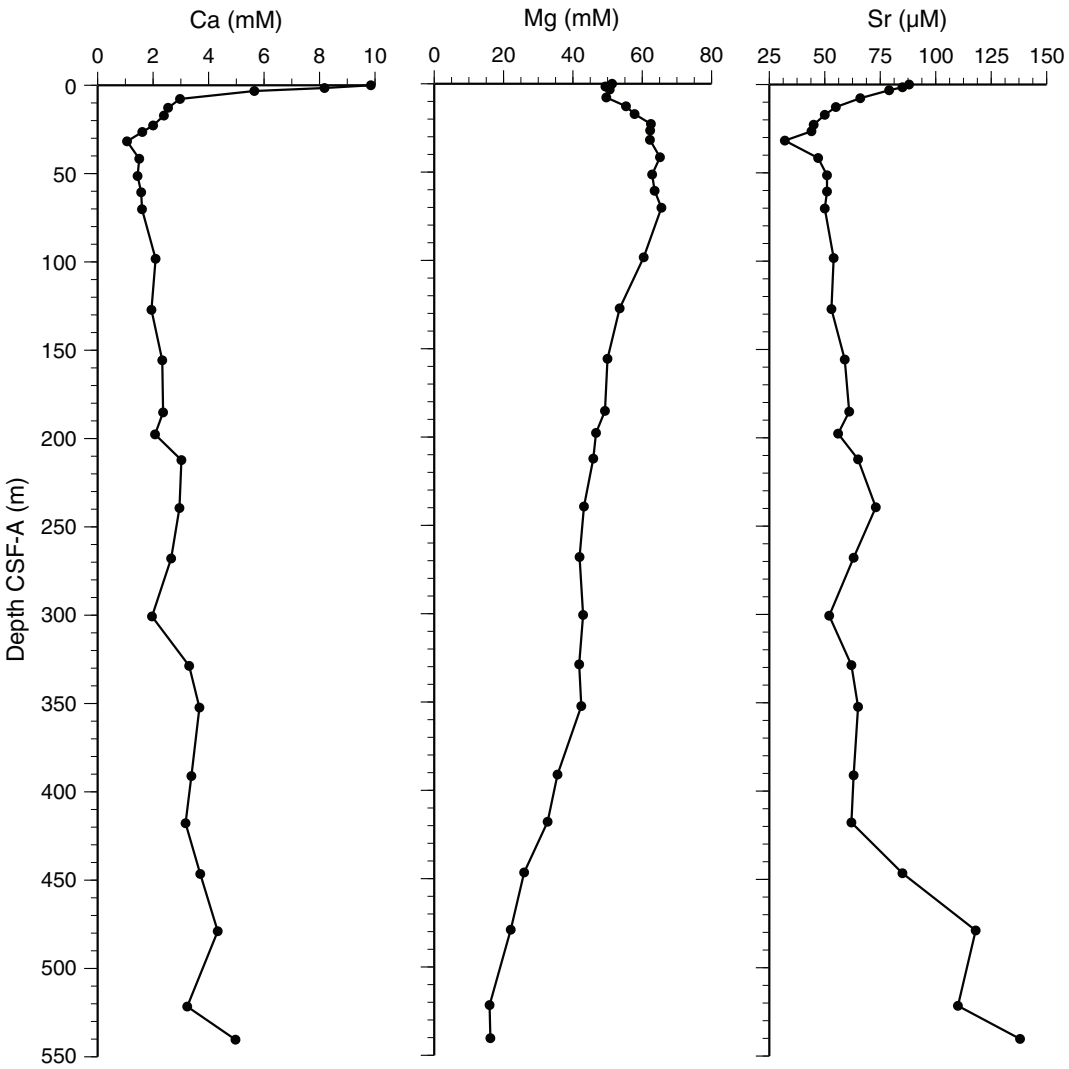

Figure F38. Dissolved calcium, magnesium, and strontium profiles across the uppermost 10 m, Site U1427. IW-sq = squeezed interstitial water.

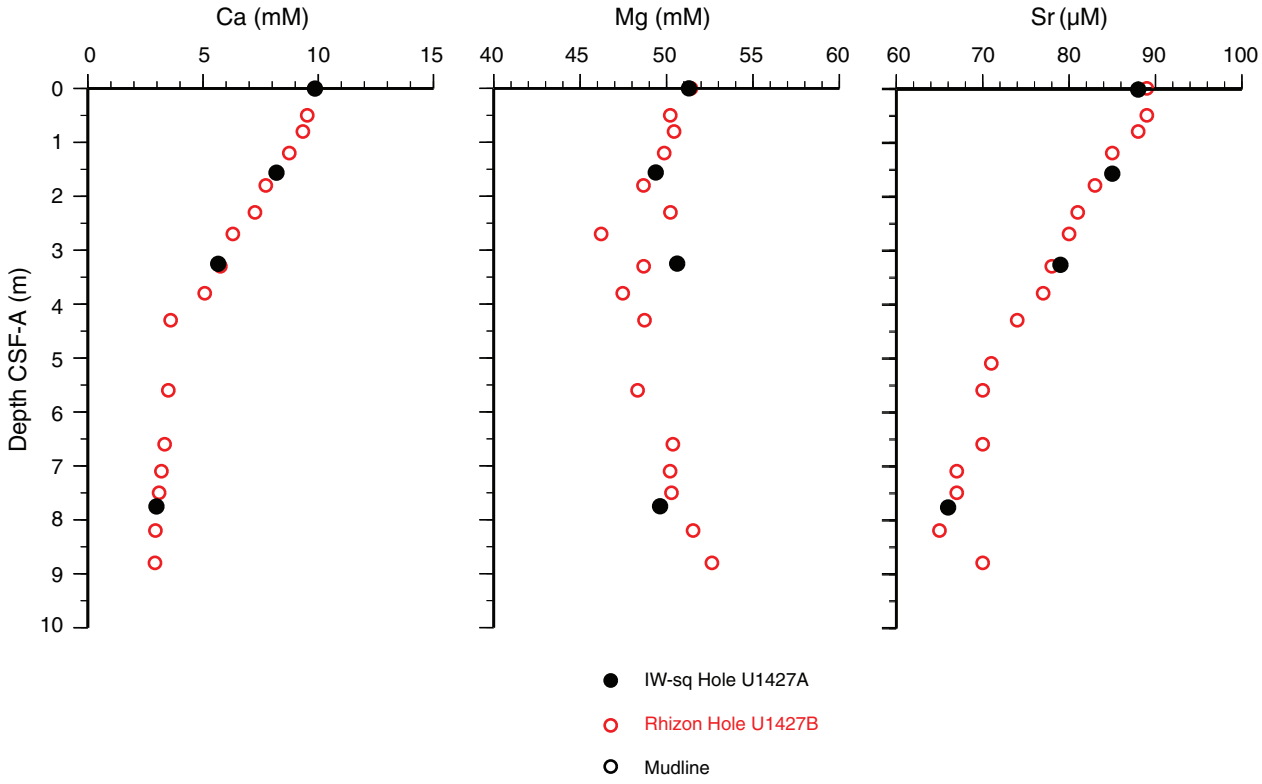

Figure F39. Dissolved chloride and sodium profiles with depth, Site U1427. **A.** Full depth. **B.** Chloride across the uppermost 10 m below the seafloor. **C.** Sodium across the uppermost 10 m below the seafloor. IW-sq = squeezed interstitial water.

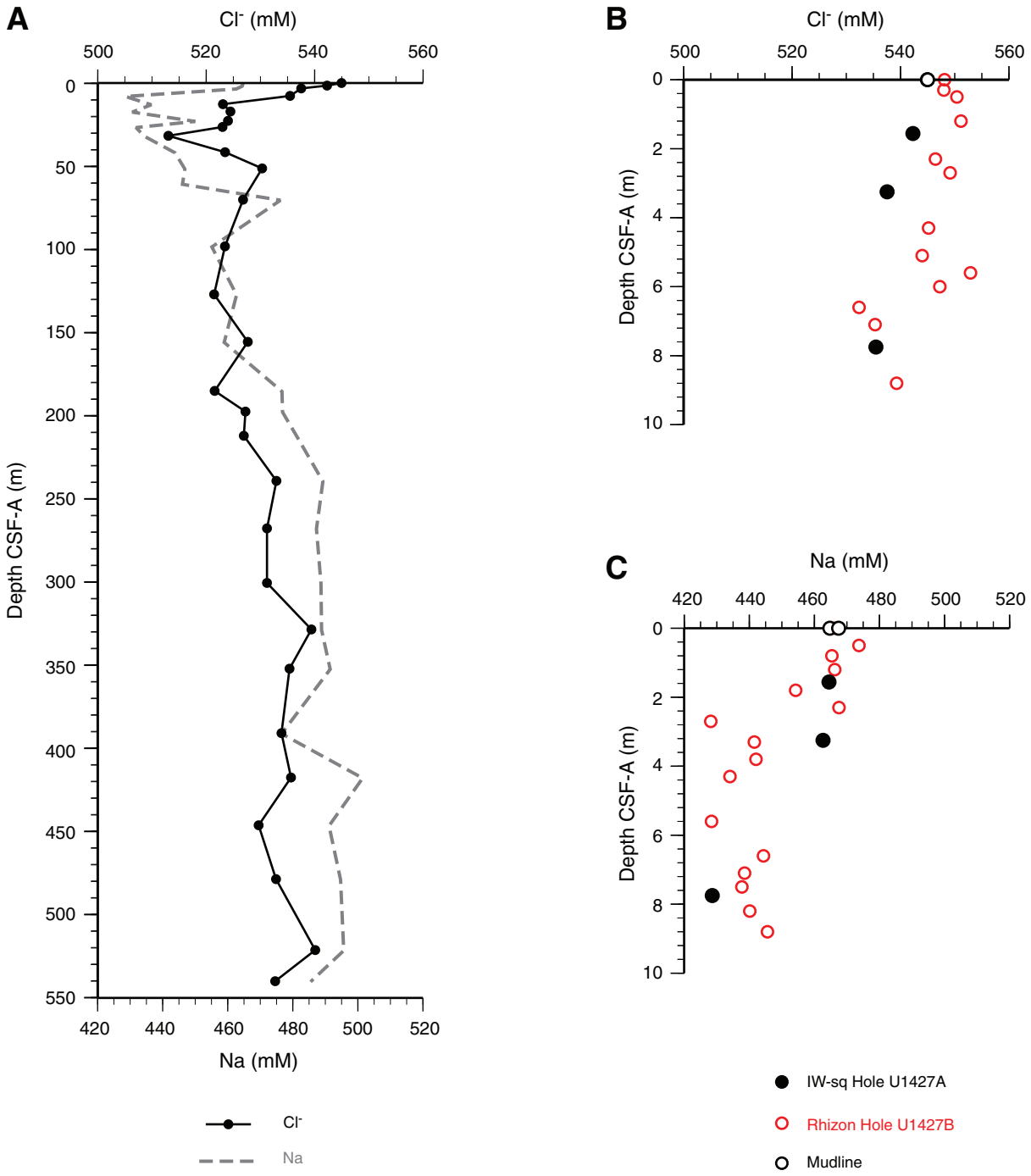

Figure F40. Dissolved potassium profiles with depth, Site U1427. **A.** Full depth. **B.** Uppermost 10 m below the seafloor. IW-sq = squeezed interstitial water.

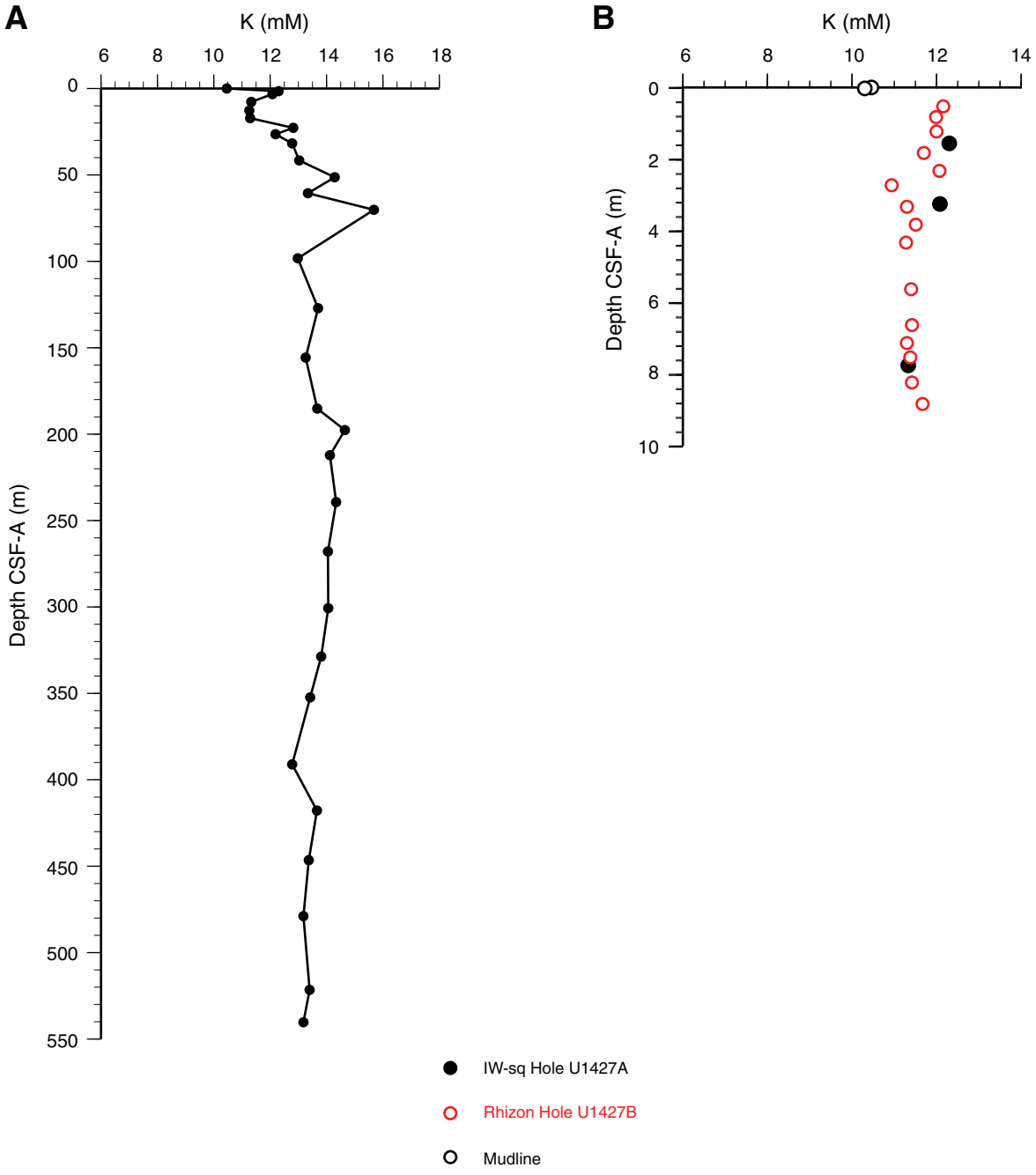

Figure F41. Dissolved boron, lithium, and silica profiles across the full depth, Site U1427.

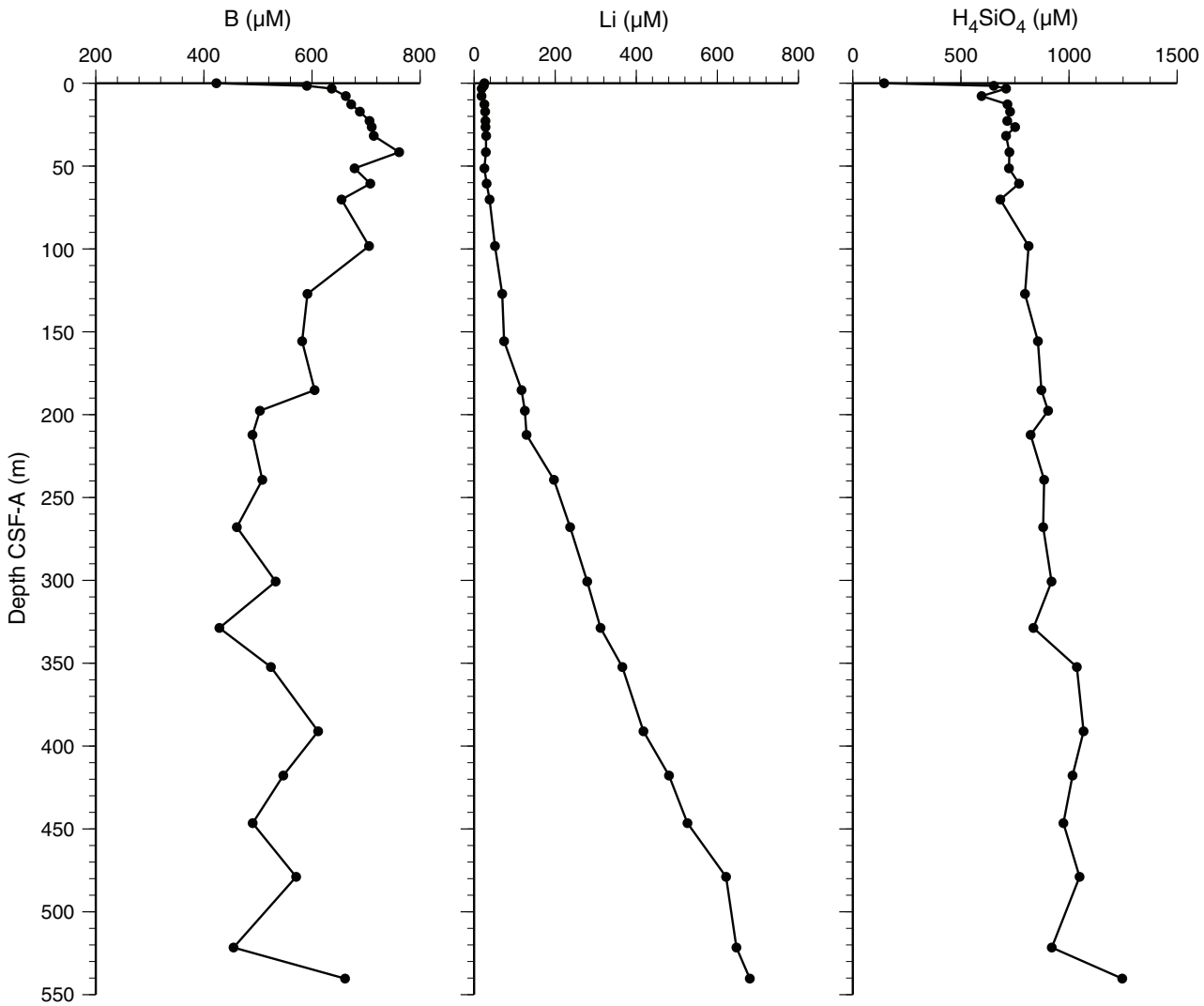

Figure F42. Dissolved lithium profile across the upper 25 m, Site U1427. IW-sq = squeezed interstitial water.

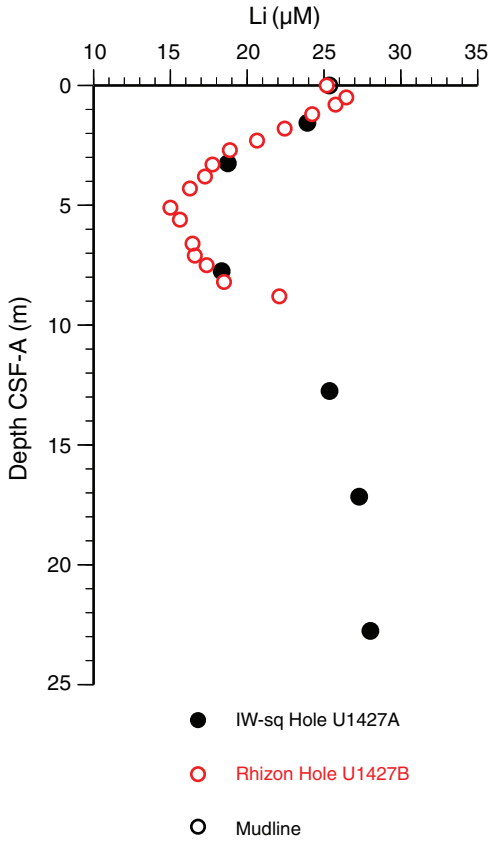

Figure F43. Paleomagnetism after 20 mT AF demagnetization, Site U1427. Chron column: black = normal polarity, white = reversed polarity, gray = zones or polarity boundaries without clear magnetostratigraphic interpretation. Inclination column: thin black dashed lines = expected geocentric axial dipole inclinations at the site latitude during reversed (left) and normal (right) polarities, triangles along the left side mark depths where discrete paleomagnetic cube samples were collected (orange = discrete samples measured during the expedition). Declination column: gray dots = measured declination values, green dots = declination values corrected using core orientation data collected by the FlexIT tool. Susceptibility column: SHMSL and WRMSL measured values are shown in magenta and gray dots, respectively. **A.** Hole U1427A shallower than 250 m CSF-A. (Continued on next three pages.)

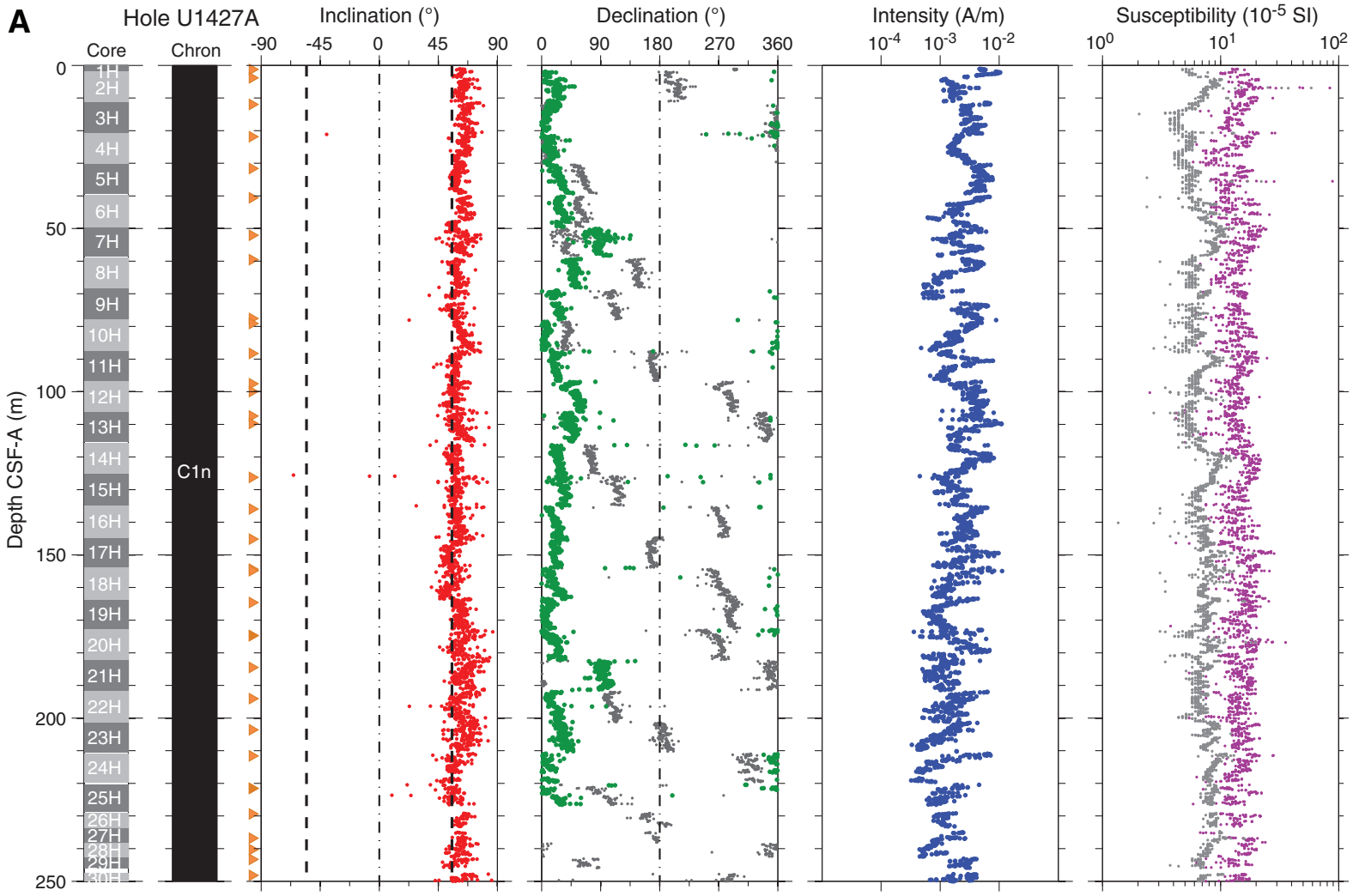

Figure F43 (continued). B. Hole U1427A deeper than 250 m CSF-A. (Continued on next page.)

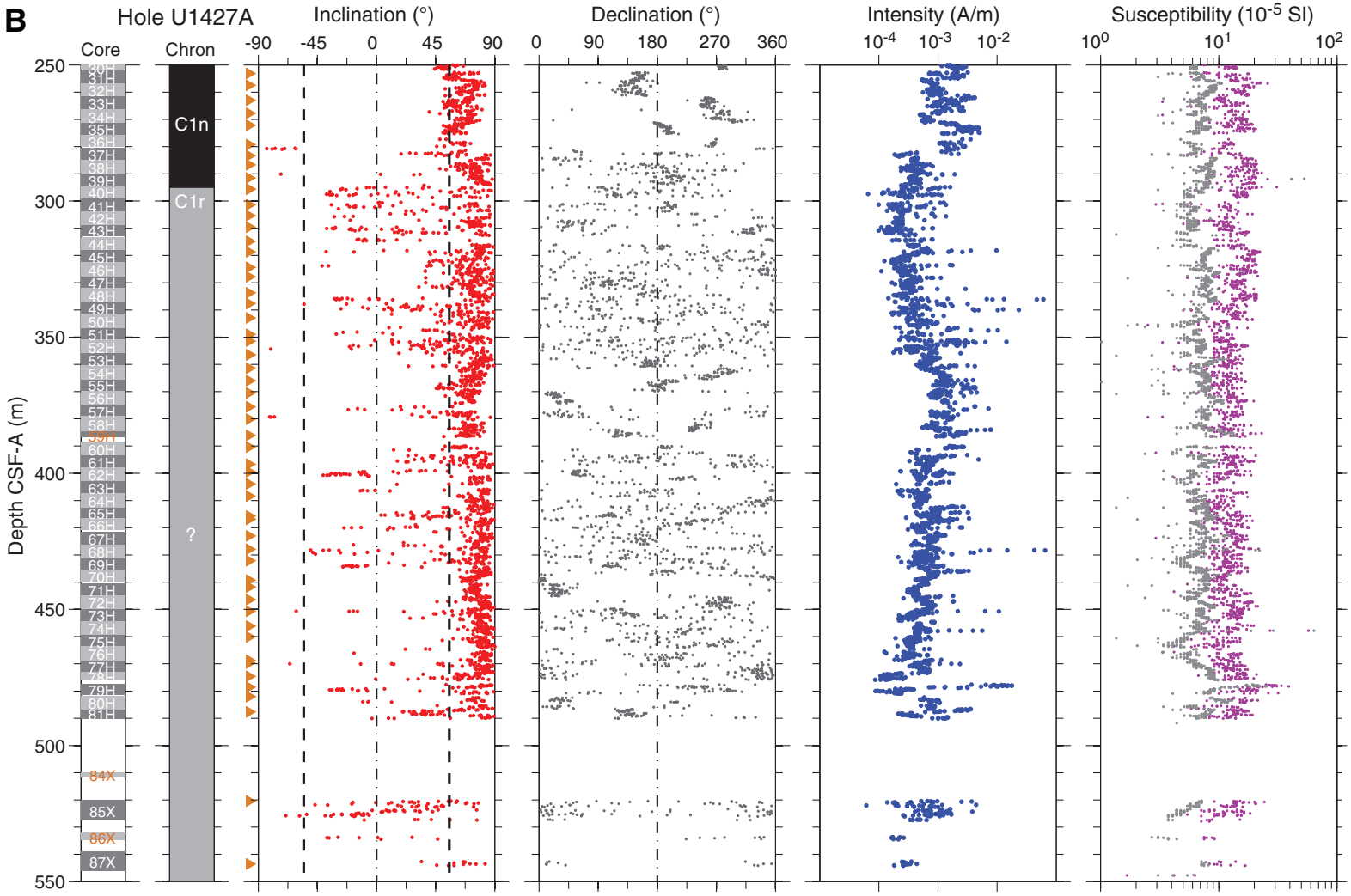

Figure F43 (continued). C. Hole U1427B shallower than 250 m CSF-A. (Continued on next page.)

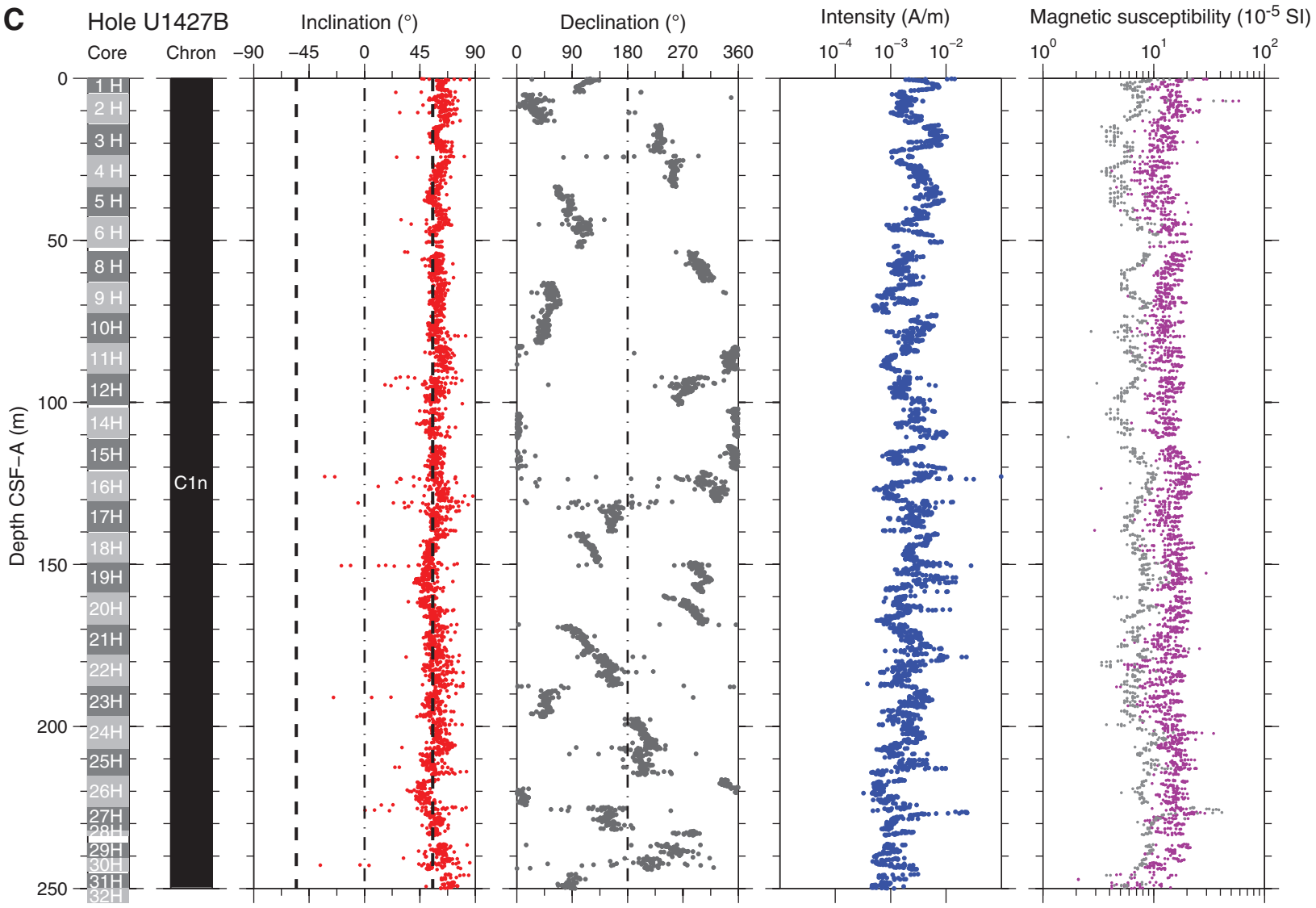

Figure F43 (continued). D. Hole U1427B deeper than 250 m CSF-A.

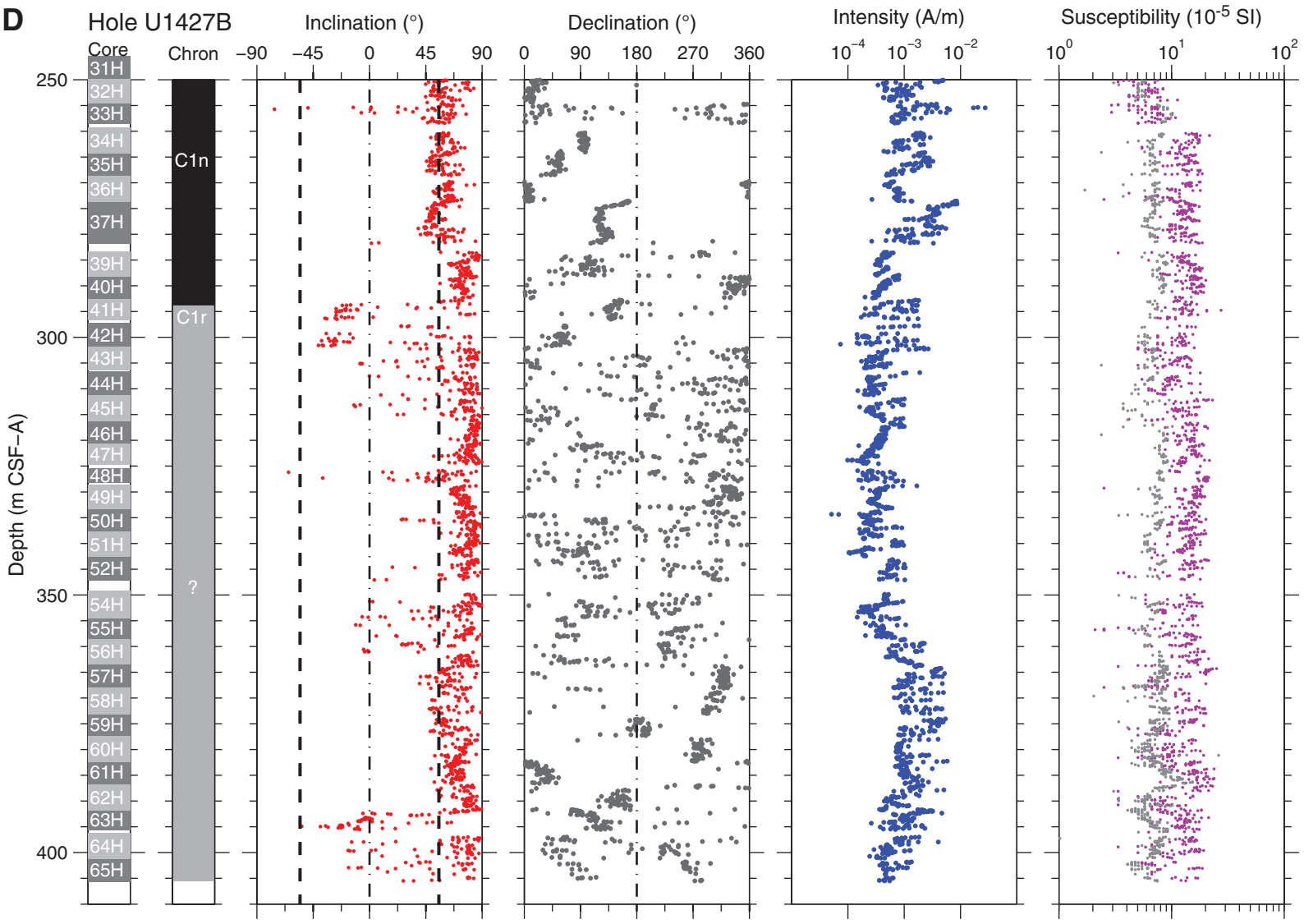

Figure F44. NRM intensity after 20 mT AF demagnetization monitored for Sections 346-U1427A-7H-1~4 and 12H-1~5 as soon as the cores were split, after ~2–6 h, after 1 day, and after 3 days. Note the core photo brightness and contrast was enhanced to make black interval visible. Void intervals are shown in white.

Type I :
Core 346-U1427A-7H

Siliciclastics with black to dark greenish gray color

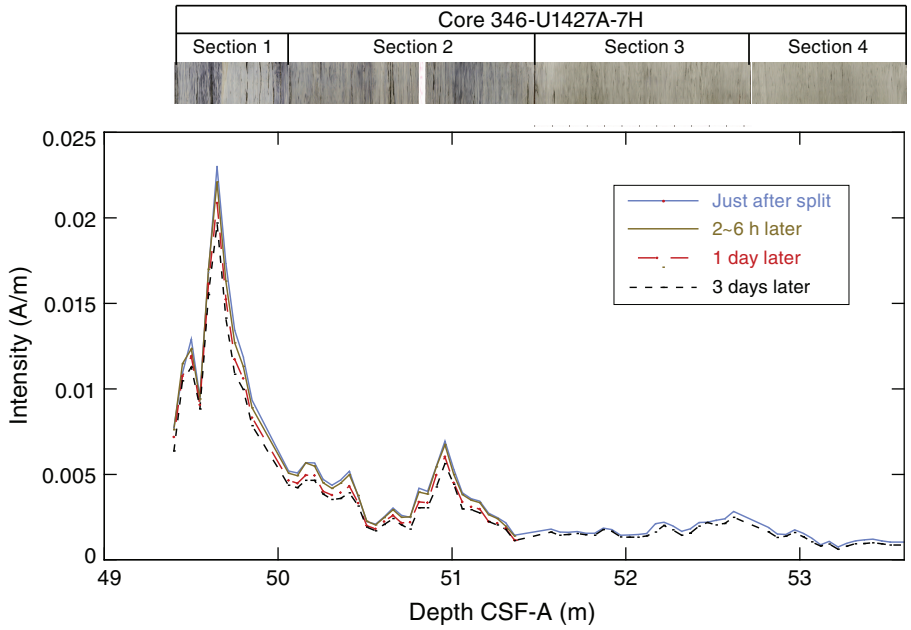

Type II :
Core 346-U1427A-12H

Nannofossil-rich clayey silt and nannofossil ooze with dark greenish gray to grayish brown

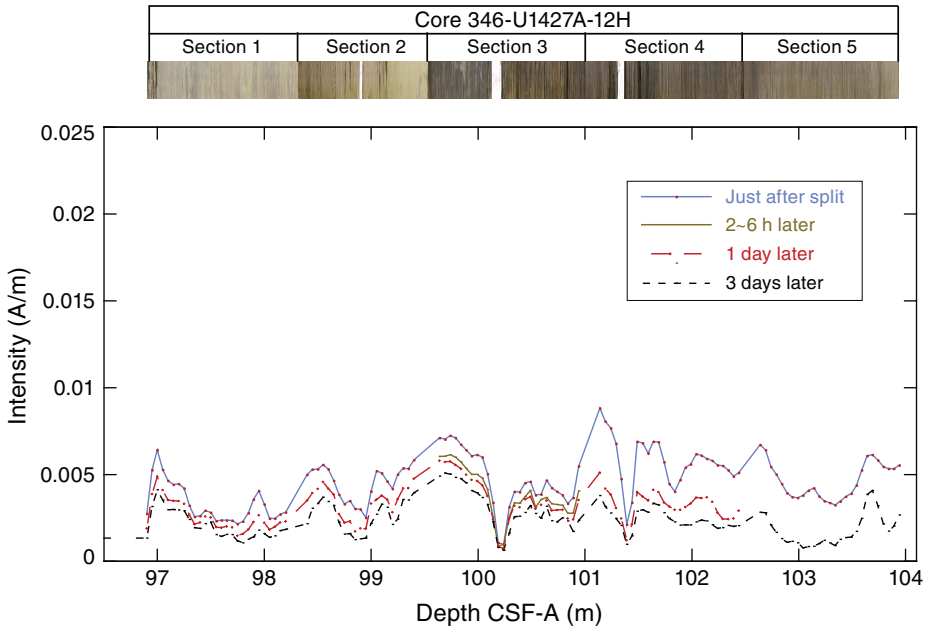

Figure F45. AF demagnetization results for discrete samples, Site U1427. For each sample, the left plot shows the intensity variation with progressive demagnetization. The middle and right plots show the NRM vector measured after each demagnetization treatment on an orthogonal projection (Zijderveld) and on an equal area projection respectively. In the orthogonal projection plot, squares = horizontal projections, circles = vertical projections. In the equal area projection plot, closed circles = projection data with positive inclinations, open circles = projection data with negative inclinations. Note that on the orthogonal projection (Zijderveld) plot, NRM data before demagnetization have been removed to better display the demagnetized data. **A–H.** Hole U1427A discrete cube samples from 356.51 m CSF-A and shallower. (Continued on next page.)

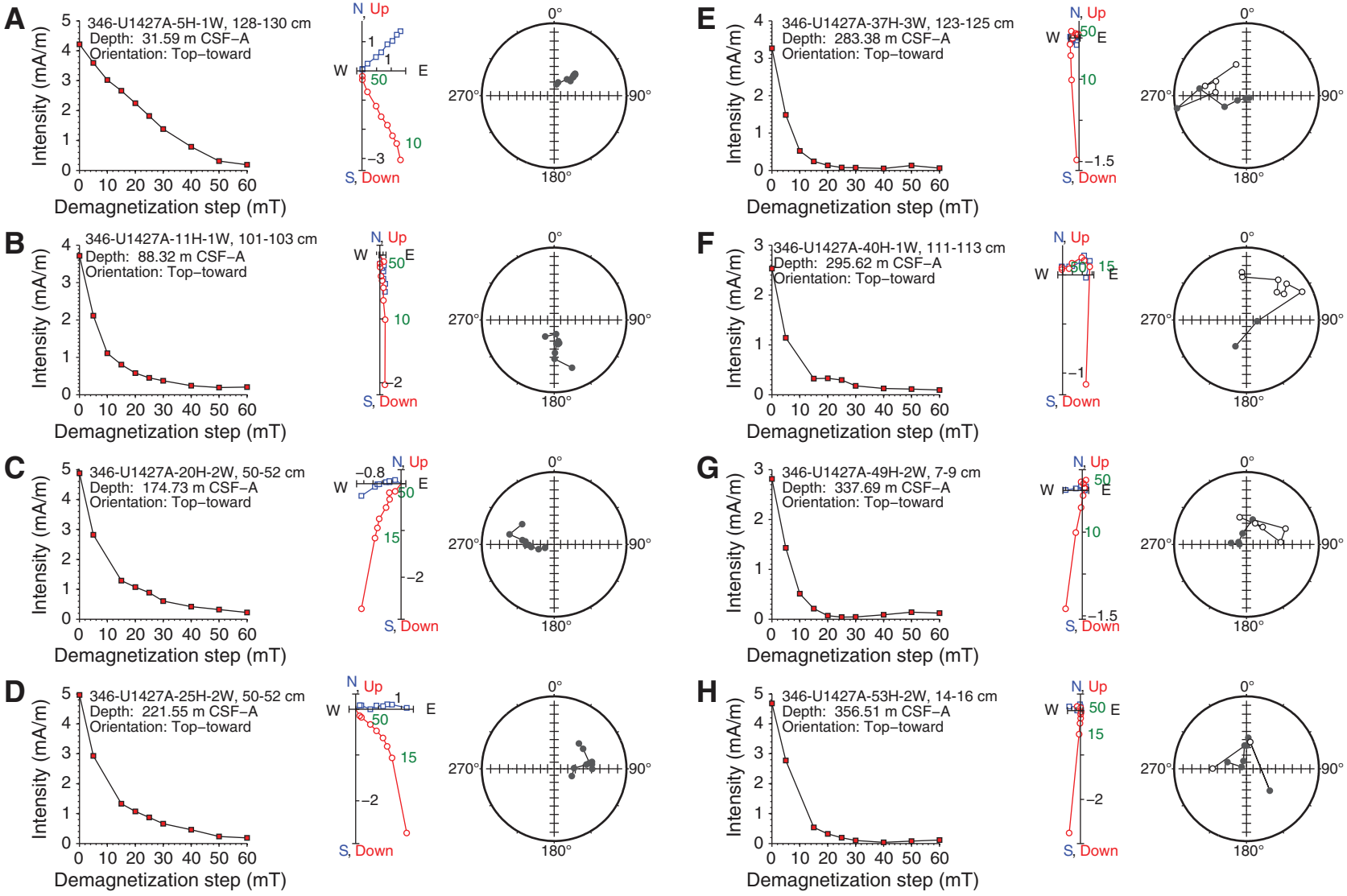

Figure F45 (continued). I–L. Hole U1427A discrete cube samples from 365.99 m CSF-A and deeper.

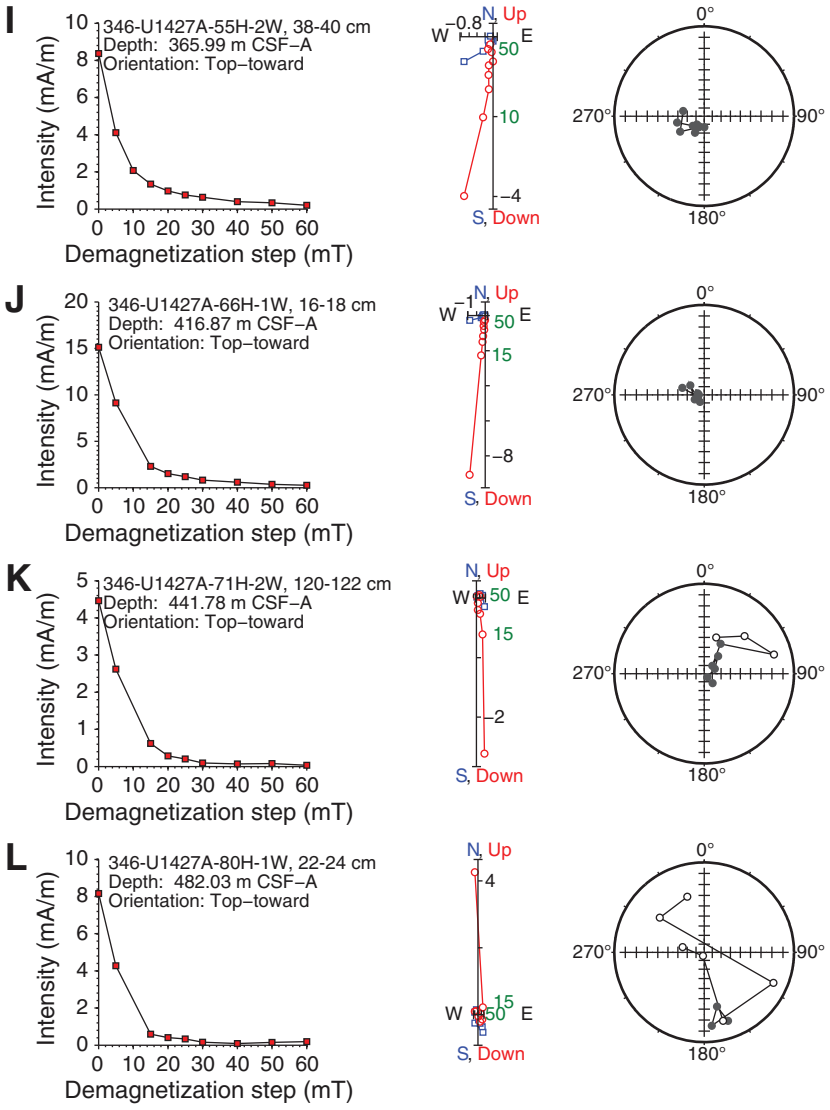

Figure F46. Suite of physical properties measured in Holes U1427A and U1427B. The first magnetic susceptibility panel shows WRMSL data of Hole U1427A (black) and U1427B (red), whereas the second panel shows point SHMSL susceptibility data of Hole U1427A. Gamma ray attenuation (GRA) bulk density is from Hole U1427A. Natural gamma radiation (NGR) counts are from Hole U1427A. *P*-wave velocity panel shows combined data from WRMSL of Holes U1427A and U1427B. Shaded blue areas indicate clay-rich sediment interval and remains are biogenic component–rich sediment intervals.

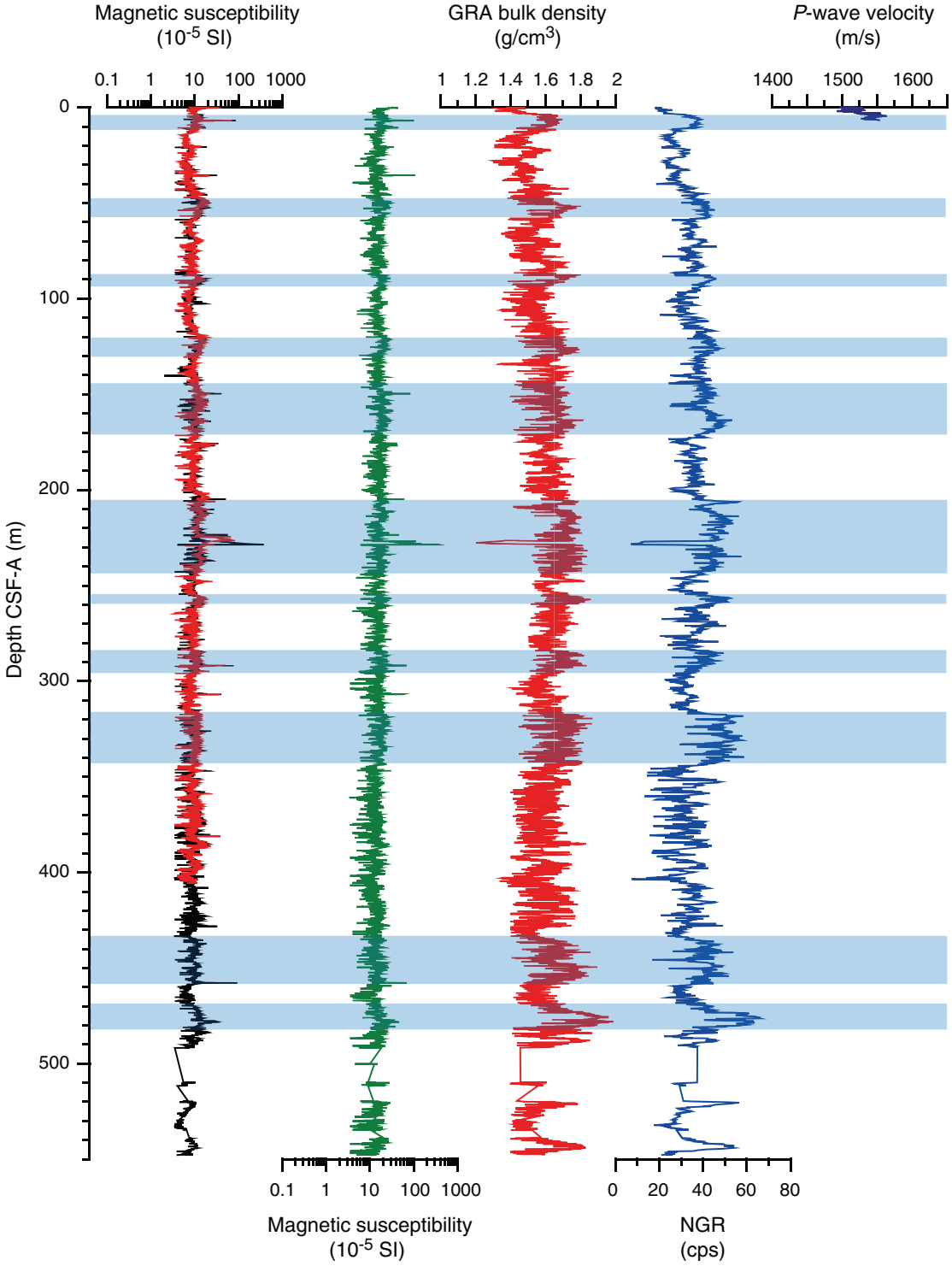

Figure F47. Relationship between color reflectance b* as a proxy for lithology, natural gamma radiation (NGR), and gamma ray attenuation (GRA) bulk density. Shaded blue areas indicate clay-rich sediment interval and remains are biogenic component–rich sediment intervals.

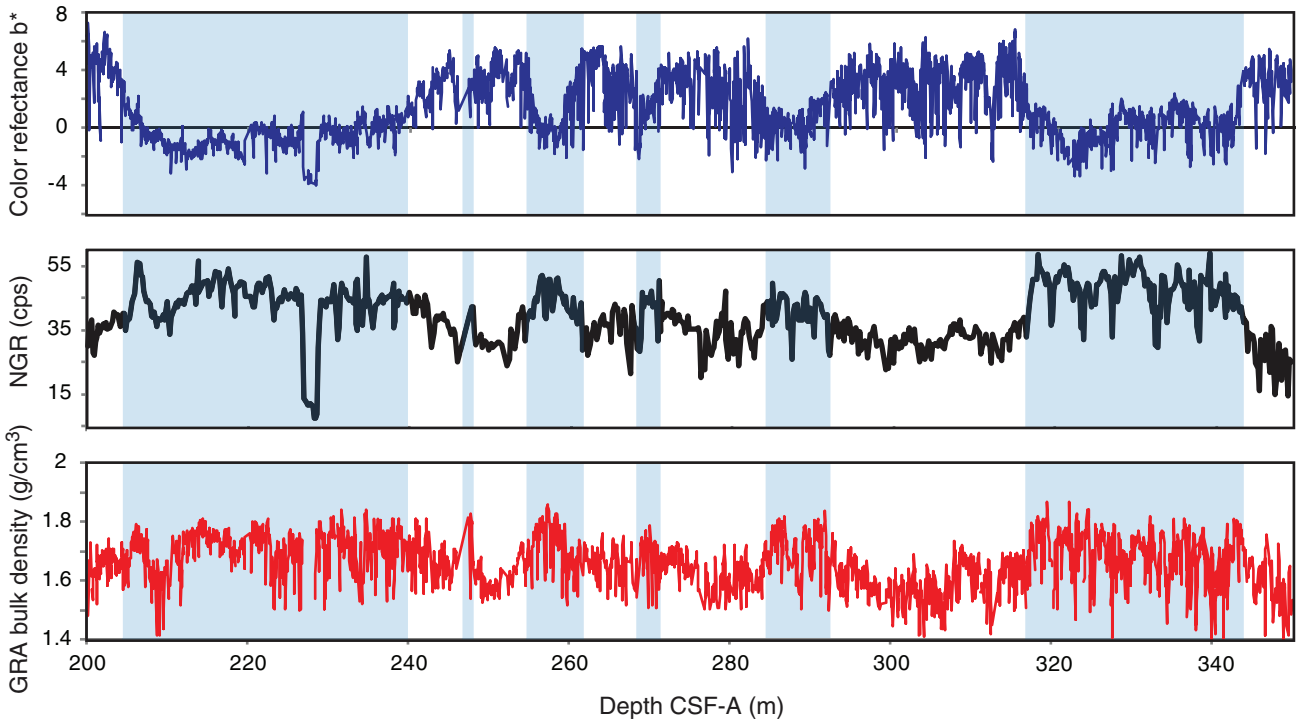

Figure F48. Discrete bulk density, grain density, porosity, water content, and shear strength, Hole U1427A. Shaded blue areas indicate clay-rich sediment interval and remains are biogenic component–rich sediment intervals.

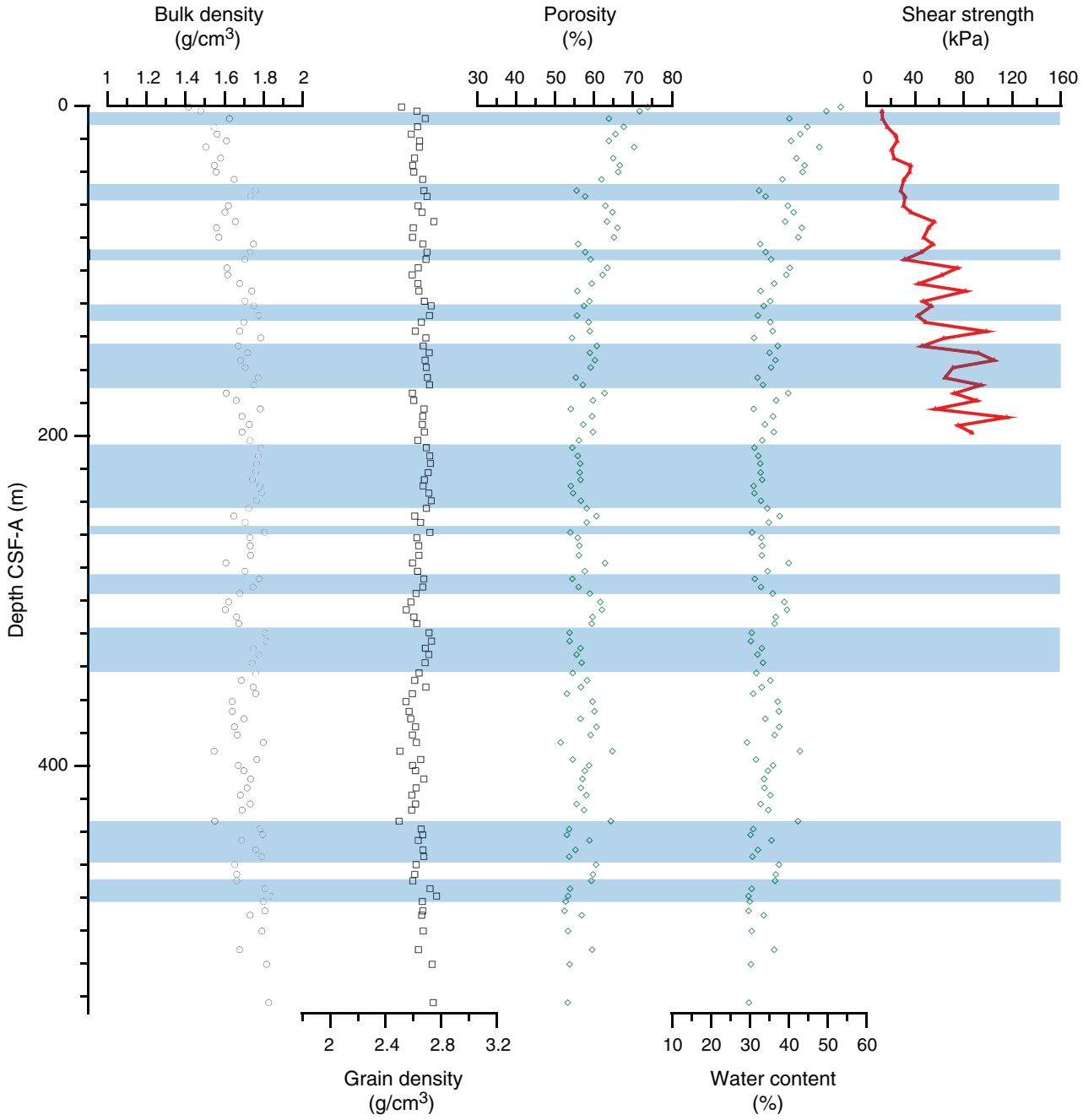

Figure F49. Color reflectance (L*, a*, and b*) in Hole U1427A. Shaded blue areas indicate clay-rich sediment interval and remains are biogenic component–rich sediment intervals.

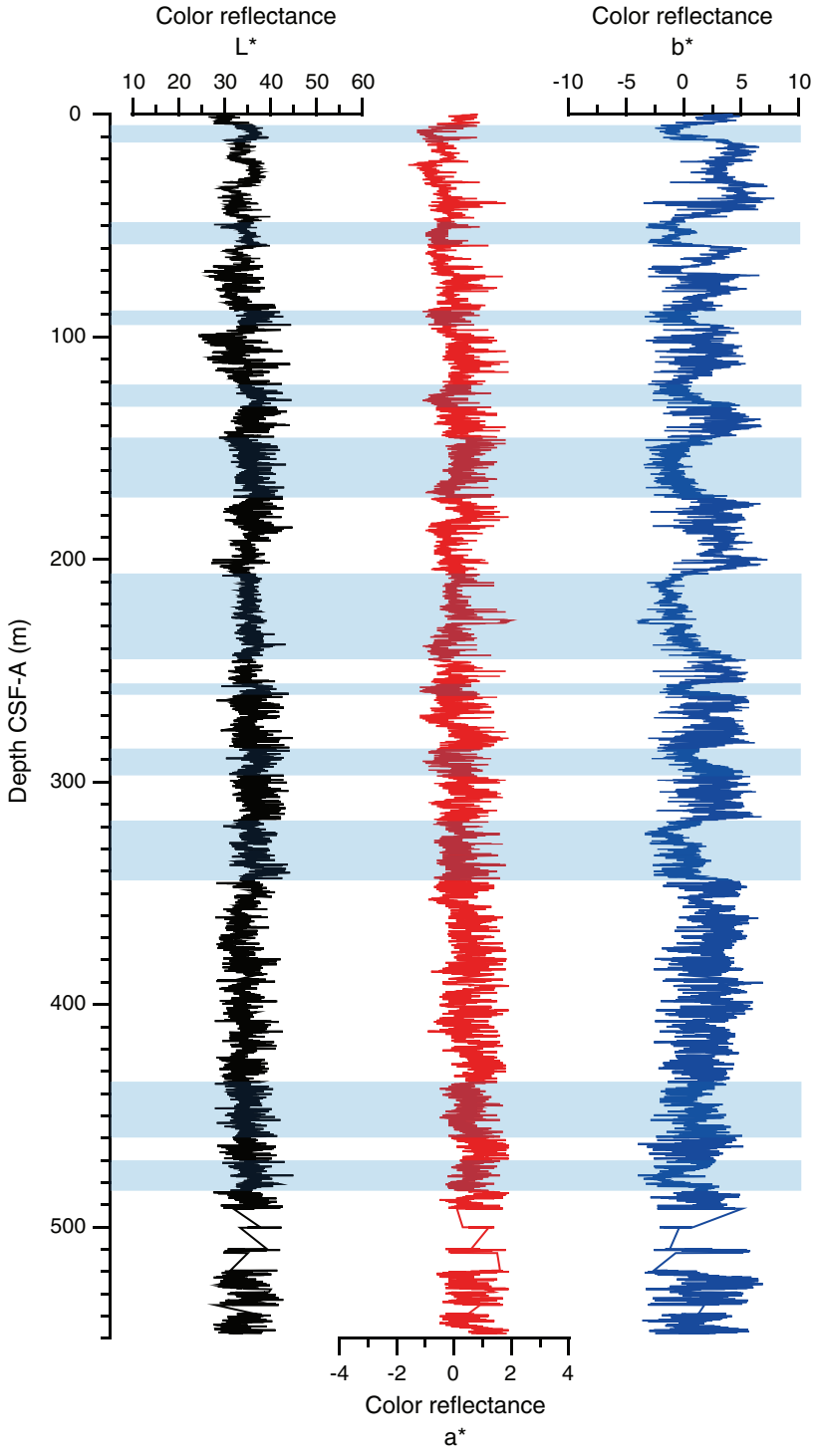

Figure F50. Downhole logs and logging units, Hole U1427A. HSGR = standard (total) gamma radiation, NGR = natural gamma radiation, RHOM = bulk density, GRA= gamma ray attenuation measured on core, RLA1 = shallow apparent resistivity, RLA5 = deep apparent resistivity, MSS = Magnetic Susceptibility Sonde, LMSS = low-resolution MSS, HMSS = high-resolution MSS.

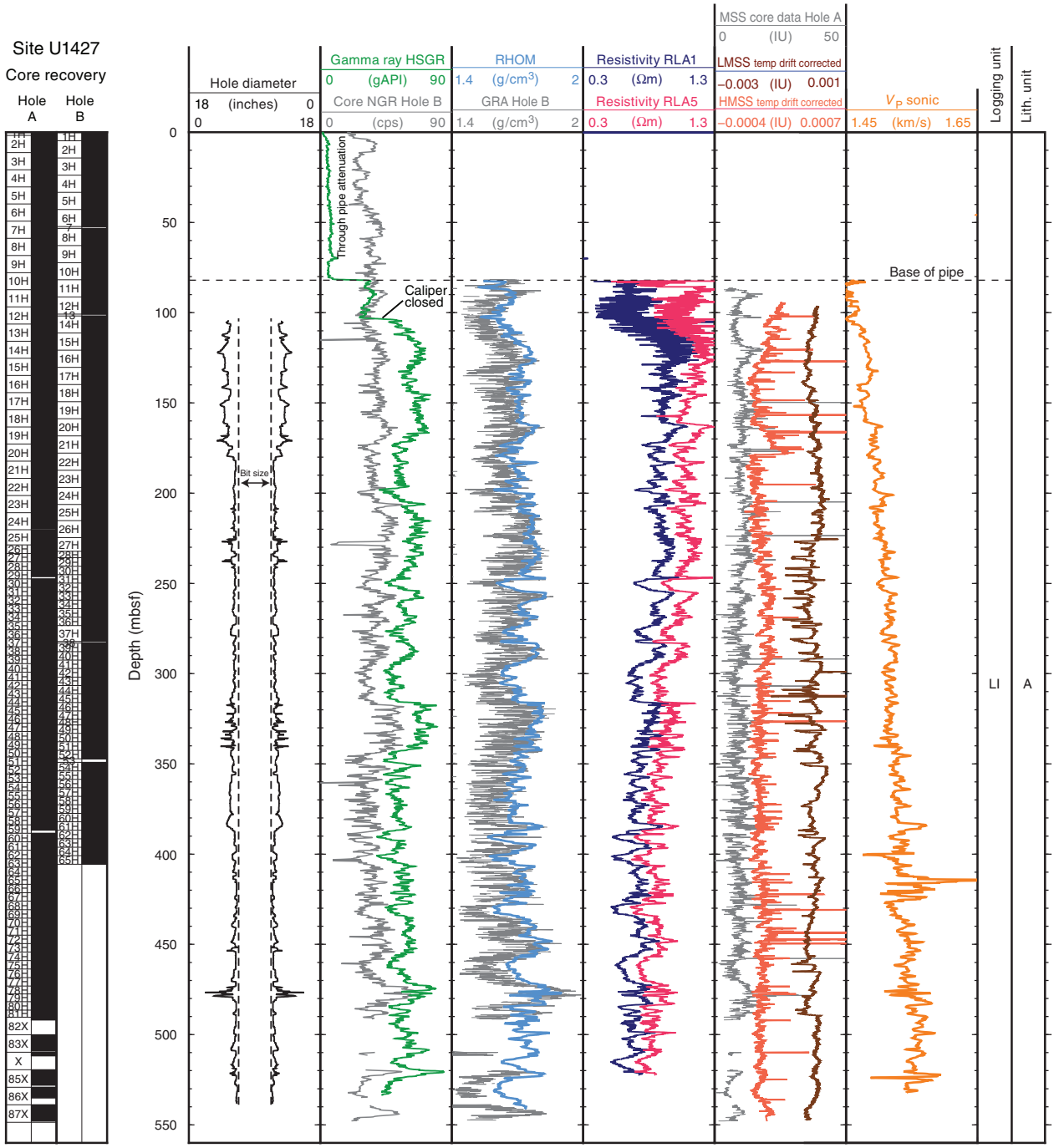

Figure F51. Diffuse reflectance data comparison between Sites U1425 (deeper) and U1427 in L*-a* and a*-b* color spaces. Average L* for each site is depicted by lines in upper panels.

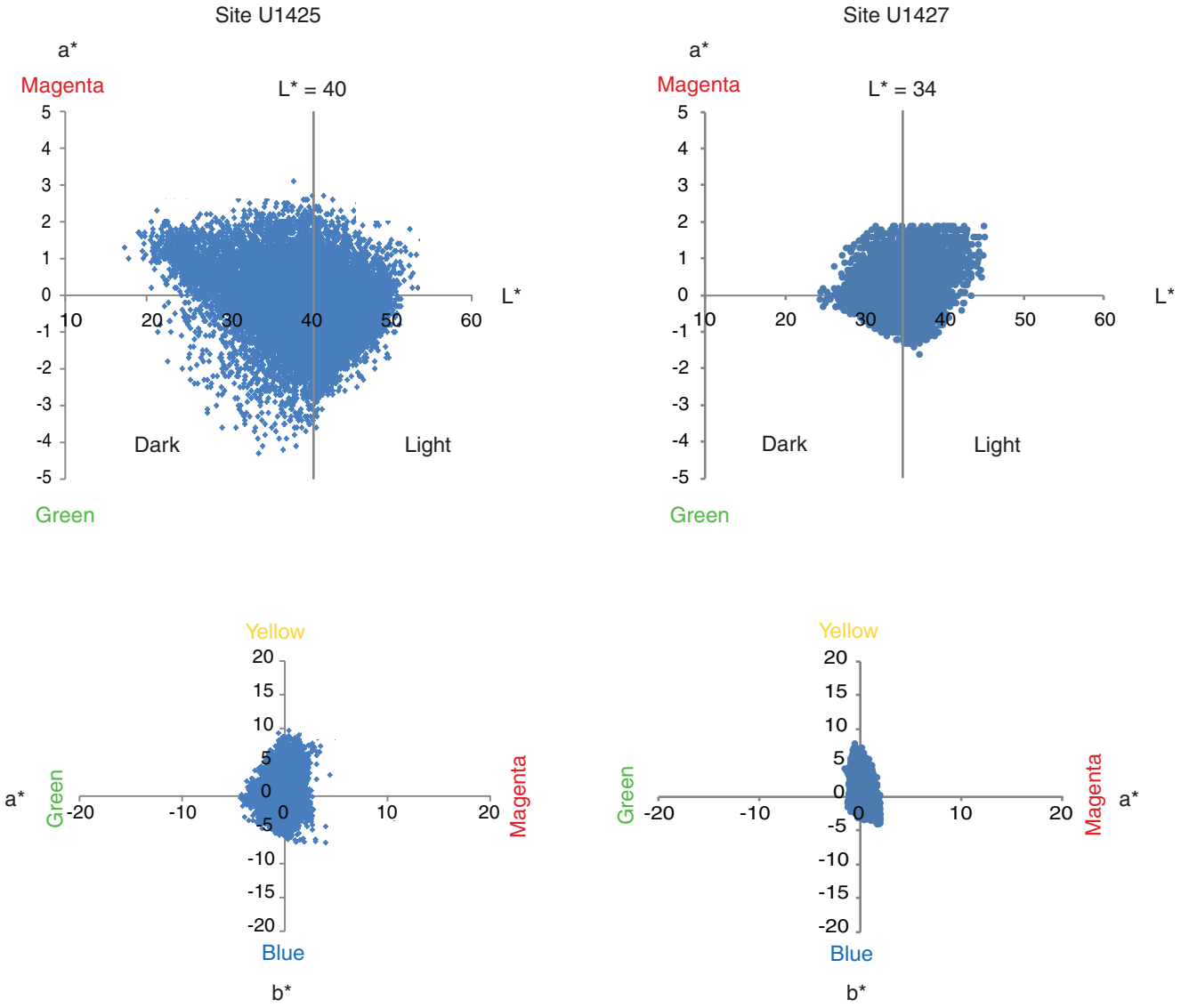

Figure F52. Logging operations summary diagram, Site U1427. FMS = Formation MicroScanner.

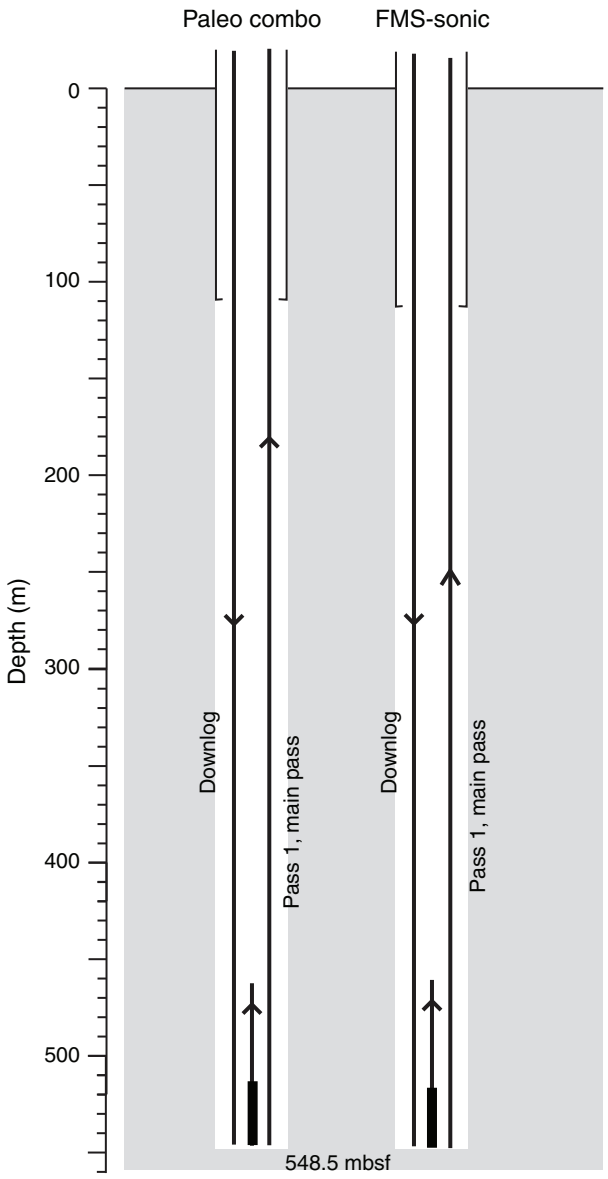

Figure F53. Natural gamma radiation logs, straight (non-oriented) Formation MicroScanner (FMS) images and logging units, Hole U1427A. HSGR = standard (total) gamma radiation, HCGR = computed gamma radiation.

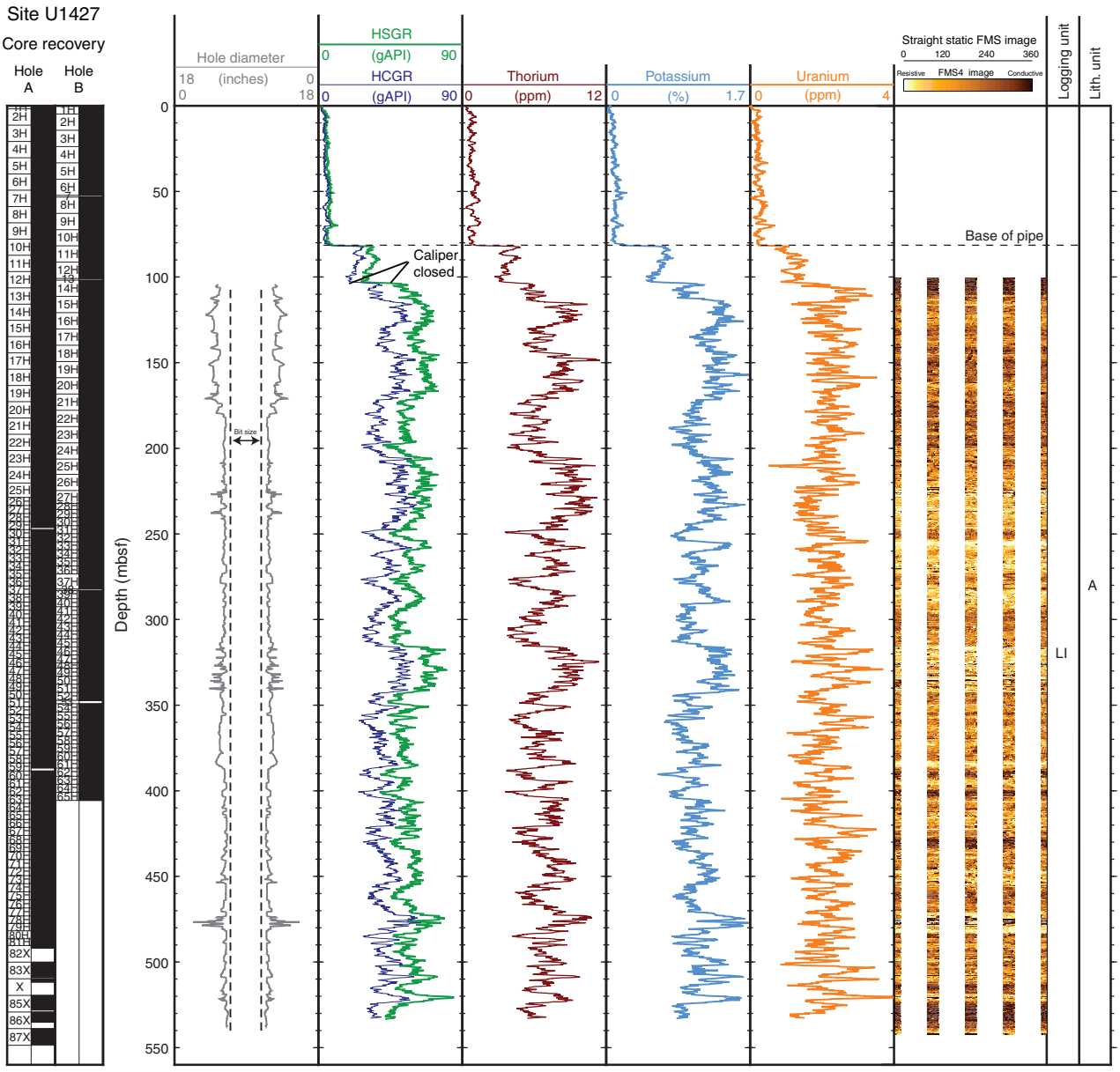

Figure F54. Correlation of downhole logs and straight (non-oriented) Formation MicroScanner (FMS) images (290–323 mbsf) in Hole U1427A, illustrating the cyclic nature of the sediment record at intervals of ~8–15 m. NGR = natural gamma radiation, HSGR = standard (total) natural gamma radiation, RA5 = deep apparent resistivity.

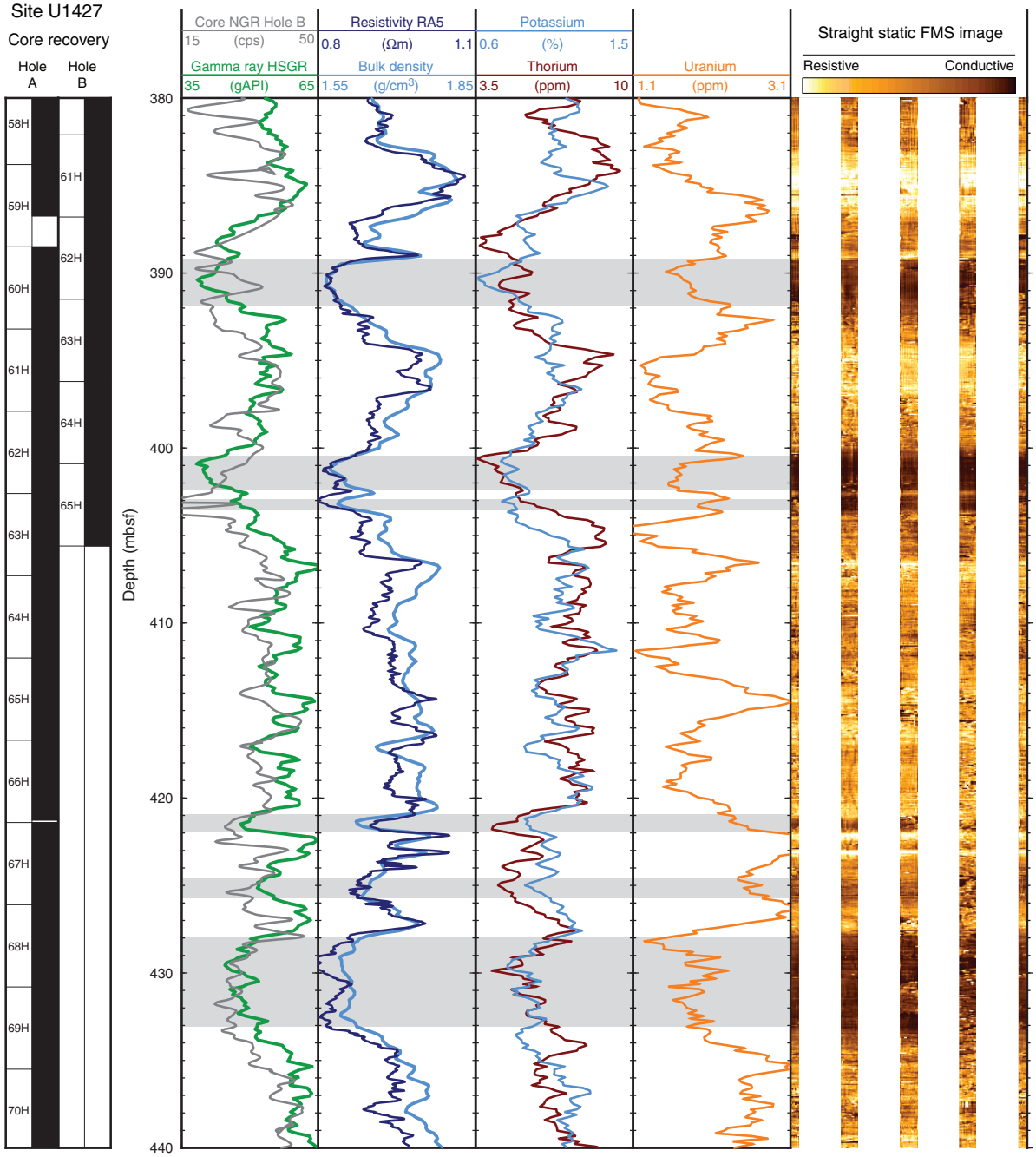

Figure F55. Plots of heat flow calculations, Holes U1427A and U1427C. **A.** In situ sediment temperatures from advanced piston corer temperature tool (APCT-3) measurements with average values for mudline (star), Cores 346-U1427A-4H, 7H, 10H, and 13H (circles) and 346-U1427C-3H and 5H (squares), and linear fit (excluding the mudline). **B.** In situ thermal conductivity data (squares) with calculated thermal resistance (solid line). **C.** Bullard plot of heat flow calculated from a linear fit of temperature vs. thermal resistance data.

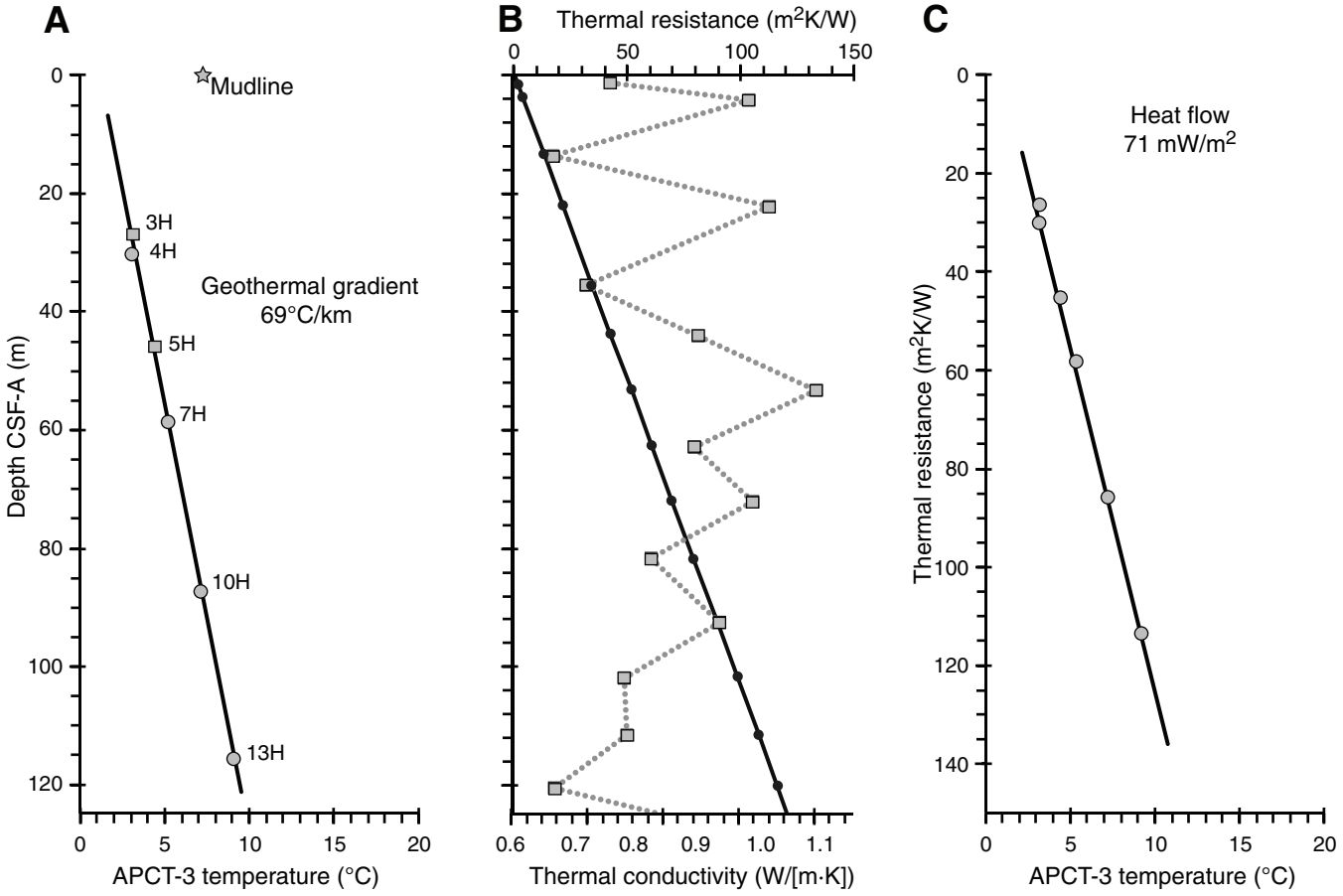

Figure F56. A–C. Alignment of all the cores from Holes U1427A (red), U1427B (blue), and U1427C (orange) illustrated using natural gamma radiation (NGR) profiles. The spliced profile is also shown (black). Splice tie points are indicated by red solid triangles. **D.** For the interval deeper than 430.34 m CCSF-A, NGR from Hole U1427A (red) is compared with total spectral gamma ray (HSGR) from paleo combo log (black).

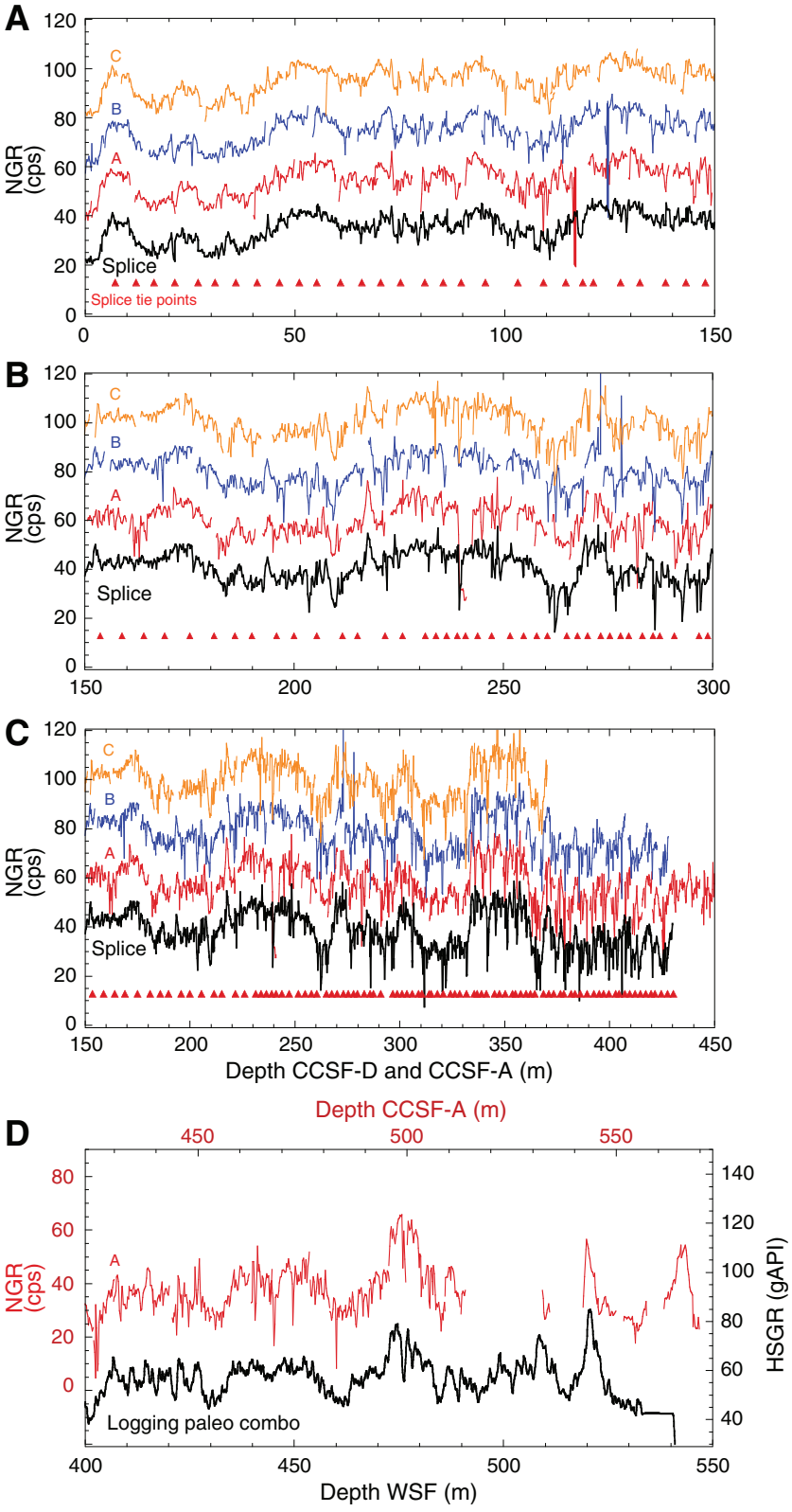

Figure F57. Age model and sedimentation rates, Site U1427. **A.** Synthesis of biostratigraphic and paleomagnetic age control points with most likely depth-age relationship lines, establishing a preliminary age model. **B.** Average sedimentation rates between age control points plotted with gamma ray attenuation (GRA) density.

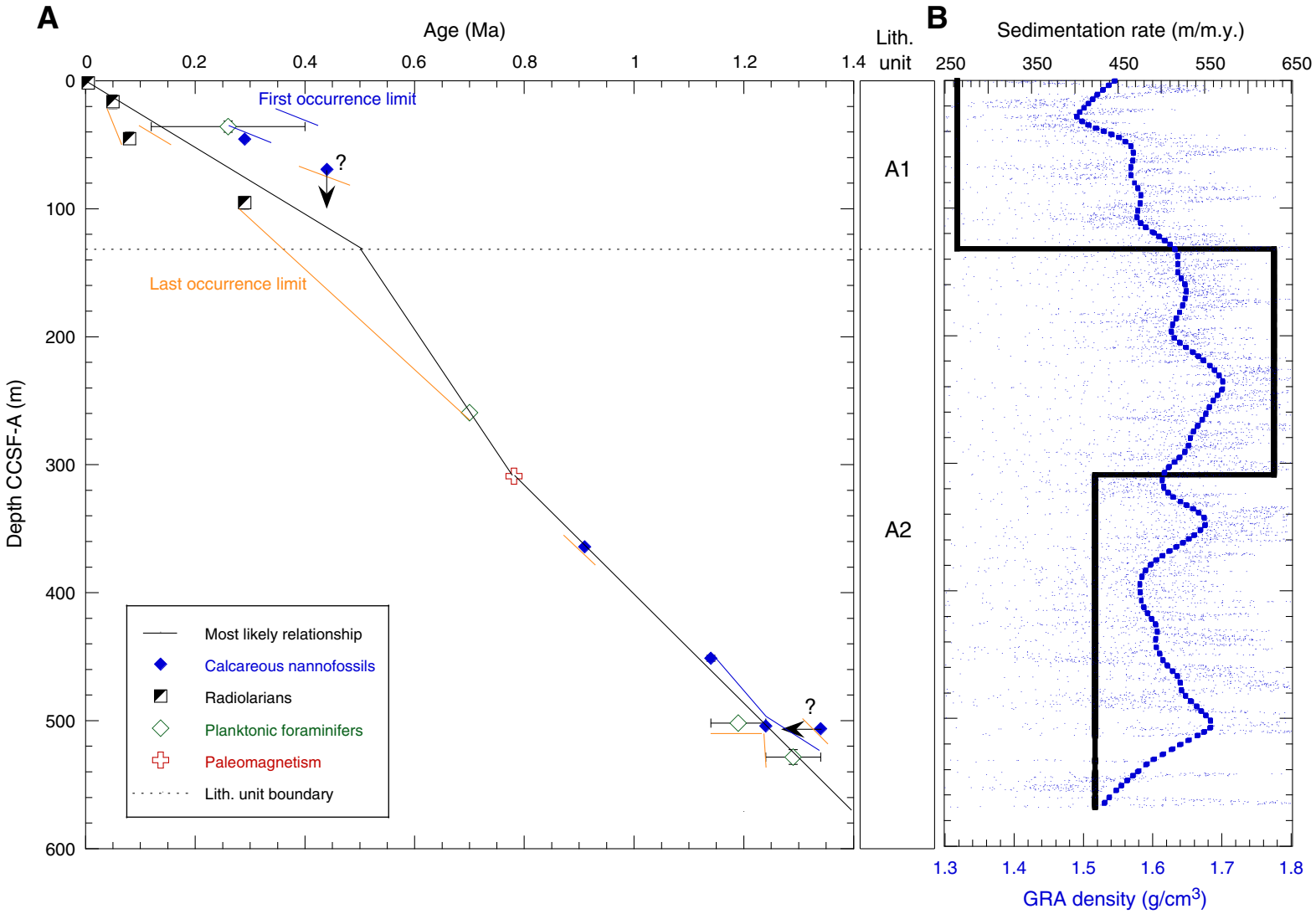

Table T1. Coring summary, Site U1427. (Continued on next four pages.)

Hole U1427A
Latitude: 35°57.9200′N
Longitude: 134°26.0604′E
Water depth (m): 339.36
Date started (UTC): 2042 h 5 September 2013
Date finished (UTC): 0520 h 9 September 2013
Time on hole (days): 3.36
Seafloor depth (drill pipe measurement below rig floor, m DRF): 337.1
Rig floor to sea level (m): 11.52
Penetration DSF (m): 548.6
Cored interval (m): 548.6
Recovered length (m): 542.59
Recovery (%): 99
Drilled interval (m): NA
Drilled interval: 0
Total cores: 87
APC cores: 81
XCB cores: 6
RCB cores: 0
Other cores: 0

Hole U1427B
Latitude: 35°57.9276′N
Longitude: 134°26.0600′E
Water depth (m): 325.58
Date started (UTC): 0520 h 9 September 2013
Date finished (UTC): 1730 h 10 September 2013
Time on hole (days): 1.51
Seafloor depth DRF (m): 337.1
Rig floor to sea level (m): 11.52
Penetration DSF (m): 405.6
Cored interval (m): 400.6
Recovered length (m): 422.41
Recovery (%): 105
Drilled interval (m): 5
Drilled interval: 4
Total cores: 61
APC cores: 61
XCB cores: 0
RCB cores: 0
Other cores: 0

Hole U1427C
Latitude: 35°57.9109′N
Longitude: 134°26.0600′E
Water depth (m): 325.89
Date started (UTC): 2330 h 21 September 2013
Date finished (UTC): 1000 h 23 September 2013
Time on hole (days): 1.44
Seafloor depth DRF (m): 337.5
Rig floor to sea level (m): 11.61
Penetration DSF (m): 351.1
Cored interval (m): 351.1
Recovered length (m): 367.77
Recovery (%): 105
Drilled interval (m): NA
Drilled interval: 0
Total cores: 52
APC cores: 52
XCB cores: 0
RCB cores: 0
Other cores: 0

Site U1427 totals
Number of cores: 200
Penetration (m): 1305.3
Cored (m): 1300.3
Recovered (m): 1332.77 (102.5%)

Table T1 (continued). (Continued on next page.)

Core	Date (Sep 2013)	Time (h)	Top depth of cored interval DSF (m)	Bottom depth of cored interval DSF (m)	Interval advanced (m)	Top depth of recovered core CSF (m)	Bottom depth of recovered core CSF (m)	Length of core recovered (m)	Curated length (m)	Recovery (%)
346-U1427A-										
1H	6	0030	0.0	1.8	1.8	0.0	1.79	1.79	1.79	99
2H	6	0110	1.8	11.3	9.5	1.8	11.34	9.48	9.54	100
3H	6	0130	11.3	20.8	9.5	11.3	21.44	10.14	10.14	107
4H	6	0205	20.8	30.3	9.5	20.8	30.84	10.04	10.04	106
5H	6	0225	30.3	39.8	9.5	30.3	39.51	9.21	9.21	97
6H	6	0250	39.8	49.3	9.5	39.8	50.08	10.28	10.28	108
7H	6	0325	49.3	58.8	9.5	49.3	59.17	9.87	9.87	104
8H	6	0345	58.8	68.3	9.5	58.8	68.57	9.77	9.77	103
9H	6	0405	68.3	77.8	9.5	68.3	78.19	9.89	9.89	104
10H	6	0435	77.8	87.3	9.5	77.8	88.12	10.32	10.32	109
11H	6	0500	87.3	96.8	9.5	87.3	97.09	9.79	9.79	103
12H	6	0515	96.8	106.3	9.5	96.8	106.76	9.96	9.96	105
13H	6	0545	106.3	115.8	9.5	106.3	115.85	9.55	9.55	101
14H	6	0610	115.8	125.3	9.5	115.8	125.53	9.73	9.73	102
15H	6	0635	125.3	134.8	9.5	125.3	135.27	9.97	9.97	105
16H	6	0700	134.8	144.3	9.5	134.8	145.04	10.24	10.24	108
17H	6	0720	144.3	153.8	9.5	144.3	154.14	9.84	9.84	104
18H	6	0745	153.8	163.3	9.5	153.8	163.96	10.16	10.16	107
19H	6	0820	163.3	172.8	9.5	163.3	172.92	9.62	9.62	101
20H	6	0845	172.8	182.3	9.5	172.8	182.43	9.63	9.63	101
21H	6	0910	182.3	191.8	9.5	182.3	191.67	9.37	9.37	99
22H	6	0940	191.8	201.3	9.5	191.8	201.72	9.92	9.92	104
23H	6	1010	201.3	210.8	9.5	201.3	210.73	9.43	9.43	99
24H	6	1035	210.8	220.3	9.5	210.8	219.80	9.00	9.00	95
25H	6	1100	220.3	228.7	8.4	220.3	228.73	8.43	8.43	100
26H	6	1145	228.7	233.4	4.7	228.7	233.85	5.15	5.15	110
27H	6	1205	233.4	238.1	4.7	233.4	238.54	5.14	5.14	109
28H	6	1300	238.1	242.8	4.7	238.1	242.91	4.81	4.81	102
29H	6	1320	242.8	247.5	4.7	242.8	246.35	3.55	3.55	76
30H	6	1340	247.5	252.2	4.7	247.5	251.87	4.37	4.37	93
31H	6	1400	252.2	256.9	4.7	252.2	257.23	5.03	5.03	107
32H	6	1420	256.9	261.6	4.7	256.9	261.75	4.85	4.85	103
33H	6	1440	261.6	266.3	4.7	261.6	266.46	4.86	4.86	103
34H	6	1500	266.3	271.0	4.7	266.3	271.54	5.24	5.24	111
35H	6	1520	271.0	275.7	4.7	271.0	275.63	4.63	4.63	99
36H	6	1540	275.7	280.4	4.7	275.7	280.38	4.68	4.68	100
37H	6	1600	280.4	285.1	4.7	280.4	285.74	5.34	5.34	114
38H	6	1615	285.1	289.8	4.7	285.1	290.25	5.15	5.15	110
39H	6	1635	289.8	294.5	4.7	289.8	295.15	5.35	5.35	114
40H	6	1655	294.5	299.2	4.7	294.5	299.26	4.76	4.76	101
41H	6	1715	299.2	303.9	4.7	299.2	304.28	5.08	5.08	108
42H	6	1735	303.9	308.6	4.7	303.9	308.92	5.02	5.02	107
43H	6	1755	308.6	313.3	4.7	308.6	313.13	4.53	4.53	96
44H	6	1820	313.3	318.0	4.7	313.3	317.96	4.66	4.66	99
45H	6	1900	318.0	322.7	4.7	318.0	323.07	5.07	5.07	108
46H	6	1920	322.7	327.4	4.7	322.7	328.00	5.30	5.30	113
47H	6	1950	327.4	332.1	4.7	327.4	332.63	5.23	5.23	111
48H	6	2015	332.1	336.8	4.7	332.1	337.53	5.43	5.43	116
49H	6	2040	336.8	341.5	4.7	336.8	342.19	5.39	5.39	115
50H	6	2100	341.5	346.2	4.7	341.5	346.87	5.37	5.37	114
51H	6	2130	346.2	350.9	4.7	346.2	351.73	5.53	5.53	118
52H	6	2155	350.9	355.6	4.7	350.9	356.08	5.18	5.18	110
53H	6	2215	355.6	360.3	4.7	355.6	361.07	5.47	5.47	116
54H	6	2235	360.3	365.0	4.7	360.3	365.75	5.45	5.45	116
55H	6	2300	365.0	369.7	4.7	365.0	370.25	5.25	5.25	112
56H	6	2320	369.7	374.4	4.7	369.7	374.93	5.23	5.23	111
57H	6	2350	374.4	379.1	4.7	374.4	379.88	5.48	5.48	117
58H	7	0010	379.1	383.8	4.7	379.1	384.76	5.66	5.66	120
59H	7	0030	383.8	388.5	4.7	383.8	386.75	2.95	2.95	63
60H	7	0125	388.5	393.2	4.7	388.5	393.61	5.11	5.11	109
61H	7	0145	393.2	397.9	4.7	393.2	398.20	5.00	5.00	106
62H	7	0240	397.9	402.6	4.7	397.9	402.81	4.91	4.91	104
63H	7	0300	402.6	407.3	4.7	402.6	407.89	5.29	5.29	113
64H	7	0315	407.3	412.0	4.7	407.3	412.68	5.38	5.38	114
65H	7	0335	412.0	416.7	4.7	412.0	417.06	5.06	5.06	108
66H	7	0415	416.7	421.4	4.7	416.7	421.27	4.57	4.57	97

Table T1 (continued). (Continued on next page.)

Core	Date (Sep 2013)	Time (h)	Top depth of cored interval DSF (m)	Bottom depth of cored interval DSF (m)	Interval advanced (m)	Top depth of recovered core CSF (m)	Bottom depth of recovered core CSF (m)	Length of core recovered (m)	Curated length (m)	Recovery (%)
67H	7	0435	421.4	426.1	4.7	421.4	426.67	5.27	5.27	112
68H	7	0515	426.1	430.8	4.7	426.1	431.13	5.03	5.03	107
69H	7	0535	430.8	435.5	4.7	430.8	435.80	5.00	5.00	106
70H	7	0605	435.5	440.2	4.7	435.5	440.26	4.76	4.76	101
71H	7	0645	440.2	444.9	4.7	440.2	445.52	5.32	5.32	113
72H	7	0720	444.9	449.6	4.7	444.9	449.94	5.04	5.04	107
73H	7	0745	449.6	454.3	4.7	449.6	454.32	4.72	4.72	100
74H	7	0810	454.3	459.0	4.7	454.3	459.45	5.15	5.15	110
75H	7	0900	459.0	463.7	4.7	459.0	464.29	5.29	5.29	113
76H	7	0945	463.7	468.4	4.7	463.7	469.19	5.49	5.49	117
77H	7	1010	468.4	473.1	4.7	468.4	473.63	5.23	5.23	111
78H	7	1035	473.1	477.5	4.4	473.1	477.47	4.37	4.37	99
79H	7	1110	477.5	481.8	4.3	477.5	481.78	4.28	4.28	100
80H	7	1200	481.8	486.5	4.7	481.8	487.09	5.29	5.29	113
81H	7	1235	486.5	490.4	3.9	486.5	490.43	3.93	3.93	101
82X	7	1340	490.4	500.1	9.7	490.4	491.94	1.54	1.54	16
83X	7	1430	500.1	509.8	9.7	500.1	500.42	0.32	0.32	3
84X	7	1510	509.8	519.5	9.7	509.8	511.80	2.00	2.00	21
85X	7	1610	519.5	529.2	9.7	519.5	528.11	8.61	8.61	89
86X	7	1730	529.2	538.9	9.7	529.2	535.19	5.99	5.99	62
87X	7	1835	538.9	548.6	9.7	538.9	547.92	9.02	9.02	93
				Total advanced (m):	548.6		Total recovered (m):	542.59		
346-U1427B-										
1H	8	1325	0.0	4.8	4.8	0.0	4.80	4.80	4.80	100
2H	8	1350	4.8	14.3	9.5	4.8	14.05	9.25	9.25	97
3H	8	1415	14.3	23.8	9.5	14.3	24.27	9.97	9.97	105
4H	8	1435	23.8	33.3	9.5	23.8	33.85	10.05	10.05	106
5H	8	1455	33.3	42.8	9.5	33.3	42.74	9.44	9.44	99
6H	8	1515	42.8	52.3	9.5	42.8	52.59	9.79	9.79	103
71	8	1530			*****Drilled from 52.3 to 53.3 mbsf*****					
8H	8	1540	53.3	62.8	9.5	53.3	63.02	9.72	9.72	102
9H	8	1600	62.8	72.3	9.5	62.8	72.71	9.91	9.91	104
10H	8	1620	72.3	81.8	9.5	72.3	82.25	9.95	9.95	105
11H	8	1640	81.8	91.3	9.5	81.8	91.52	9.72	9.72	102
12H	8	1705	91.3	100.8	9.5	91.3	101.08	9.78	9.78	103
132	8	1720			*****Drilled from 100.8 to 101.8 mbsf*****					
14H	8	1730	101.8	111.3	9.5	101.8	111.58	9.78	9.78	103
15H	8	1755	111.3	120.8	9.5	111.3	121.03	9.73	9.73	102
16H	8	1820	120.8	130.3	9.5	120.8	130.95	10.15	10.15	107
17H	8	1900	130.3	139.8	9.5	130.3	139.97	9.67	9.67	102
18H	8	1930	139.8	149.3	9.5	139.8	149.82	10.02	10.02	105
19H	8	1955	149.3	158.8	9.5	149.3	158.88	9.58	9.58	101
20H	8	2035	158.8	168.3	9.5	158.8	168.97	10.17	10.17	107
21H	8	2100	168.3	177.8	9.5	168.3	178.32	10.02	10.02	105
22H	8	2125	177.8	187.3	9.5	177.8	187.79	9.99	9.99	105
23H	8	2200	187.3	196.8	9.5	187.3	197.43	10.13	10.13	107
24H	8	2225	196.8	206.3	9.5	196.8	207.14	10.34	10.34	109
25H	8	2250	206.3	215.2	8.9	206.3	215.23	8.93	8.93	100
26H	8	2325	215.2	224.7	9.5	215.2	224.99	9.79	9.79	103
27H	9	0000	224.7	232.2	7.5	224.7	232.26	7.56	7.56	101
28H	9	0100	232.2	235.8	3.6	232.2	235.78	3.58	3.58	99
29H	9	0145	235.8	240.5	4.7	235.8	240.83	5.03	5.03	107
30H	9	0215	240.5	245.2	4.7	240.5	245.23	4.73	4.73	101
31H	9	0240	245.2	249.9	4.7	245.2	250.41	5.21	5.21	111
32H	9	0255	249.9	254.6	4.7	249.9	254.83	4.93	4.93	105
33H	9	0315	254.6	259.3	4.7	254.6	259.17	4.57	4.57	97
34H	9	0335	259.3	264.0	4.7	259.3	264.71	5.41	5.41	115
35H	9	0350	264.0	268.7	4.7	264.0	269.04	5.04	5.04	107
36H	9	0410	268.7	273.4	4.7	268.7	274.09	5.39	5.39	115
37H	9	0430	273.4	282.1	8.7	273.4	282.11	8.71	8.71	100
383	9	0505			*****Drilled from 282.1 to 283.1 mbsf*****					
39H	9	0515	283.1	287.8	4.7	283.1	288.51	5.41	5.41	115
40H	9	0535	287.8	292.5	4.7	287.8	292.95	5.15	5.15	110
41H	9	0600	292.5	297.2	4.7	292.5	297.16	4.66	4.66	99
42H	9	0620	297.2	301.9	4.7	297.2	302.30	5.10	5.10	109
43H	9	0640	301.9	306.6	4.7	301.9	306.92	5.02	5.02	107
44H	9	0655	306.6	311.3	4.7	306.6	311.64	5.04	5.04	107

Table T1 (continued). (Continued on next page.)

Core	Date (Sep 2013)	Time (h)	Top depth of cored interval DSF (m)	Bottom depth of cored interval DSF (m)	Interval advanced (m)	Top depth of recovered core CSF (m)	Bottom depth of recovered core CSF (m)	Length of core recovered (m)	Curated length (m)	Recovery (%)
45H	9	0715	311.3	316.0	4.7	311.3	316.64	5.34	5.34	114
46H	9	0735	316.0	320.7	4.7	316.0	321.26	5.26	5.26	112
47H	9	0755	320.7	325.4	4.7	320.7	325.21	4.51	4.51	96
48H	9	0825	325.4	328.4	3.0	325.4	328.44	3.04	3.04	101
49H	9	0910	328.4	333.1	4.7	328.4	333.68	5.28	5.28	112
50H	9	0955	333.1	337.8	4.7	333.1	338.44	5.34	5.34	114
51H	9	1020	337.8	342.5	4.7	337.8	343.03	5.23	5.23	111
52H	9	1045	342.5	347.2	4.7	342.5	347.53	5.03	5.03	107
534	9	1100			*****Drilled from 347.2 to 349.2 mbsf*****					
54H	9	1115	349.2	353.9	4.7	349.2	354.77	5.57	5.57	119
55H	9	1150	353.9	358.6	4.7	353.9	359.25	5.35	5.35	114
56H	9	1250	358.6	363.3	4.7	358.6	363.57	4.97	4.97	106
57H	9	1315	363.3	368.0	4.7	363.3	368.51	5.21	5.21	111
58H	9	1340	368.0	372.7	4.7	368.0	373.40	5.40	5.40	115
59H	9	1405	372.7	377.4	4.7	372.7	377.71	5.01	5.01	107
60H	9	1430	377.4	382.1	4.7	377.4	382.78	5.38	5.38	114
61H	9	1455	382.1	386.8	4.7	382.1	386.93	4.83	4.83	103
62H	9	1530	386.8	391.5	4.7	386.8	392.14	5.34	5.34	114
63H	9	1725	391.5	396.2	4.7	391.5	396.23	4.73	4.73	101
64H	9	1750	396.2	400.9	4.7	396.2	401.52	5.32	5.32	113
65H	9	1850	400.9	405.6	4.7	400.9	405.95	5.05	5.05	107
				Total advanced (m):	405.6		Total recovered (m):	422.41		
346-U1427C-										
1H	22	0310	0.0	8.0	8.0	0.0	8.05	8.05	8.05	101
2H	22	0335	8.0	17.5	9.5	8.0	18.19	10.19	10.19	107
3H	22	0425	17.5	27.0	9.5	17.5	27.78	10.28	10.28	108
4H	22	0455	27.0	36.5	9.5	27.0	36.40	9.40	9.40	99
5H	22	0555	36.5	46.0	9.5	36.5	45.88	9.38	9.38	99
6H	22	0620	46.0	55.5	9.5	46.0	56.23	10.23	10.23	108
7H	22	0650	55.5	65.0	9.5	55.5	65.68	10.18	10.18	107
8H	22	0715	65.0	74.5	9.5	65.0	74.62	9.62	9.62	101
9H	22	0740	74.5	84.0	9.5	74.5	83.88	9.38	9.38	99
10H	22	0805	84.0	93.5	9.5	84.0	93.58	9.58	9.58	101
11H	22	0830	93.5	98.2	4.7	93.5	97.94	4.44	4.44	94
12H	22	0855	98.2	107.7	9.5	98.2	107.94	9.74	9.74	103
13H	22	0920	107.7	117.2	9.5	107.7	117.50	9.80	9.80	103
14H	22	0950	117.2	126.7	9.5	117.2	127.06	9.86	9.86	104
15H	22	1020	126.7	136.2	9.5	126.7	136.16	9.46	9.46	100
16H	22	1045	136.2	145.7	9.5	136.2	145.79	9.59	9.59	101
17H	22	1115	145.7	155.2	9.5	145.7	155.51	9.81	9.81	103
18H	22	1150	155.2	164.7	9.5	155.2	164.94	9.74	9.74	103
19H	22	1220	164.7	174.2	9.5	164.7	174.30	9.60	9.60	101
20H	22	1255	174.2	183.7	9.5	174.2	182.75	8.55	8.55	90
21H	22	1335	183.7	193.2	9.5	183.7	193.45	9.75	9.75	103
22H	22	1400	193.2	202.7	9.5	193.2	202.52	9.32	9.32	98
23H	22	1435	202.7	211.0	8.3	202.7	211.08	8.31	8.38	100
24H	22	1515	211.0	220.5	9.5	211.0	220.88	9.88	9.88	104
25H	22	1615	220.5	224.2	3.7	220.5	224.97	4.47	4.47	121
26H	22	1640	224.2	228.9	4.7	224.2	229.27	5.07	5.07	108
27H	22	1740	228.9	233.6	4.7	228.9	233.81	4.91	4.91	104
28H	22	1810	233.6	238.3	4.7	233.6	238.64	5.04	5.04	107
29H	22	1840	238.3	243.0	4.7	238.3	243.53	5.23	5.23	111
30H	22	1940	243.0	247.7	4.7	243.0	247.71	4.71	4.71	100
31H	22	2005	247.7	252.4	4.7	247.7	253.17	5.47	5.47	116
32H	22	2030	252.4	257.1	4.7	252.4	257.65	5.25	5.25	112
33H	22	2055	257.1	261.8	4.7	257.1	262.20	5.10	5.10	109
34H	22	2120	261.8	266.5	4.7	261.8	266.97	5.17	5.17	110
35H	22	2150	266.5	271.2	4.7	266.5	271.77	5.27	5.27	112
36H	22	2220	271.2	275.9	4.7	271.2	276.37	5.17	5.17	110
37H	22	2250	275.9	280.6	4.7	275.9	281.20	5.30	5.30	113
38H	22	2320	280.6	285.3	4.7	280.6	285.38	4.78	4.78	102
39H	22	2350	285.3	290.0	4.7	285.3	290.32	5.02	5.02	107
40H	23	0020	290.0	294.7	4.7	290.0	295.19	5.19	5.19	110
41H	23	0050	294.7	299.4	4.7	294.7	300.00	5.30	5.30	113
42H	23	0120	299.4	304.1	4.7	299.4	304.45	5.05	5.05	107
43H	23	0150	304.1	308.8	4.7	304.1	309.57	5.47	5.47	116
44H	23	0220	308.8	313.5	4.7	308.8	313.68	4.88	4.88	104

Table T1 (continued).

Core	Date (Sep 2013)	Time (h)	Top depth of cored interval DSF (m)	Bottom depth of cored interval DSF (m)	Interval advanced (m)	Top depth of recovered core CSF (m)	Bottom depth of recovered core CSF (m)	Length of core recovered (m)	Curated length (m)	Recovery (%)
45H	23	0250	313.5	318.2	4.7	313.5	319.26	5.76	5.76	123
46H	23	0320	318.2	322.9	4.7	318.2	323.31	5.11	5.11	109
47H	23	0350	322.9	327.6	4.7	322.9	328.49	5.59	5.59	119
48H	23	0420	327.6	332.3	4.7	327.6	332.54	4.94	4.94	105
49H	23	0450	332.3	337.0	4.7	332.3	342.13	5.01	9.83	107
50H	23	0520	337.0	341.7	4.7	337.0	342.12	5.12	5.12	109
51H	23	0550	341.7	346.4	4.7	341.7	346.56	4.86	4.86	103
52H	23	0610	346.4	351.1	4.7	346.4	351.79	5.39	5.39	115
				Total advanced (m):	351.1		Total recovered (m):	367.77		

DRF = drilling depth below rig floor, DSF = drilling depth below seafloor, CSF = core depth below seafloor. APC = advanced piston corer, XCB = extended core barrel, RCB = rotary core barrel. H = APC system, X = XCB system, numeric core type = drilled interval. NA = not applicable.

Table T2. XRD analysis of bulk samples, Site U1427. (Continued on next page.)

Core section, interval (cm)	Top depth CSF-A (m)	Smectite (counts)	Illite (counts)	Hornblende (counts)	Kaolinite + chlorite (counts)	Pyroxene (counts)	Opal-A (counts)	Quartz (counts)	K-feldspar (counts)	Plagioclase (counts)	Calcite (counts)	Dolomite (counts)	Halite (counts)	Pyrite (counts)
346-U1427A-														
1H-2, 35.0–36.0	1.26	138	172	0	130	72.3	50	4770	424	517	653	0	322	118
2H-2, 54.0–55.0	3.84	214	219	252	252	106	34	6248	373	1016	218	0	183	0
3H-1, 69.0–70.0	11.99	163	222	89.9	101	121	32	6072	232	828	1252	0	207	0
4H-2, 52.0–53.0	21.83	290	407	91.4	311	175	42	7094	1393	2817	882	0	174	55.3
5H-1, 127.0–128.0	31.57	215	257	143	223	118	12	4076	332	662	3640	0	179	76.5
6H-2, 41.0–42.0	40.56	249	545	171	250	133	9	4853	712	841	1957	0	157	79.4
7H-3, 59.0–60.0	52.06	334	546	345	301	258	8	8902	855	1932	189	0	126	0
8H-2, 32.0–33.0	59.52	188	261	111	236	121	10	6634	634	982	1063	0	187	78.5
9H-8, 56.0–57.0	77.59	169	427	127	285	86.4	0	6885	332	711	952	0	168	66.9
10H-2, 81.0–82.0	79.12	158	368	96.9	254	101	43	6019	475	794	317	0	173	103
11H-1, 99.0–100.0	88.29	151	306	0	289	136	0	7628	423	1181	463	0	152	72.2
12H-1, 79.0–80.0	97.59	223	369	99.1	287	91.3	0	5952	362	750	1811	0	175	73.1
13H-1, 111.0–112.0	107.41	346	805	233	400	178	0	5284	560	1331	2380	130	175	74.9
14H-2, 72.0–73.0	117.98	282	837	295	414	133	25	8006	683	1139	0	180	177	58.3
15H-2, 48.0–49.0	126.22	336	751	164	425	187	0	7056	466	1304	317	289	155	57.3
16H-2, 78.0–79.0	135.94	284	697	238	371	168	0	5082	431	2783	2783	99.5	144	56.8
17H-2, 69.0–70.0	145.15	145	408	165	251	145	17	7191	602	1226	168	0	126	56.4
18H-2, 59.0–60.0	154.84	315	1003	88	489	133	44	6617	316	848	0	0	179	109
19H-1, 131.0–132.0	164.61	249	625	78.2	335	208	23	6981	540	1387	96.7	116	170	0
20H-2, 49.0–50.0	174.71	166	542	95.7	256	123	19	5045	1086	904	2077	106	153	79.9
21H-2, 69.0–70.0	184.49	145	275	168	159	131	19	6024	331	923	838	0	113	81.6
22H-2, 83.0–84.0	194.03	103	409	117	185	96.5	41	4688	307	859	1545	85	153	85.9
23H-2, 79.0–80.0	203.6	125	275	0	150	83.4	0	6150	325	612	1210	0	117	91.1
24H-1, 79.0–80.0	211.59	191	715	0	462	77.4	34	5979	189	688	0	104	192	63.9
25H-2, 49.0–50.0	221.53	244	653	0	388	115	40	6582	271	803	0	0	154	62.1
26H-2, 34.0–35.0	229.35	136	424	64.6	305	83.2	14	6572	463	998	211	241	116	64.5
27H-4, 45.0–46.0	236.81	171	618	89.2	309	97.4	29	4963	400	1094	499	0	129	0
29H-1, 49.0–50.0	243.29	89.3	400	0	201	69.9	10	5715	249	677	1290	0	134	82.7
31H-2, 57.0–58.0	253.15	125	422	74.1	216	85.7	29	4323	275	686	1527	61.6	171	73.3
33H-2, 108.0–109.0	262.94	137	302	0	136	93.8	30	5058	300	1220	1371	180	131	70.5
35H-1, 115.0–116.0	272.15	107	357	60.1	218	94.1	0	5509	248	689	942	0	123	71.5
37H-3, 125.0–126.0	283.39	120	465	0	220	99.7	45	4113	486	509	964	0	146	72.5
39H-2, 100.0–101.0	291.54	220	747	89.1	414	111	15	4597	329	979	1686	441	128	0
41H-3, 59.0–60.0	301.4	205	592	0	592	81.9	45	4127	279	434	2114	0	201	77
43H-1, 100.0–101.0	309.6	246	704	0	381	96.1	33	4689	195	706	2402	66.4	208	91.6
45H-1, 73.0–74.0	318.73	170	568	0	317	82.5	29	5730	309	730	146	104	164	0
47H-2, 10.0–11.0	327.85	202	667	0	335	101	0	4827	224	700	270	0	134	83.5
49H-2, 5.0–6.0	337.66	243	703	0	407	106	26	5247	235	700	185	113	171	85
51H-3, 69.0–70.0	349.02	144	306	0	169	70.7	35	3732	241	537	2841	0	126	71.8
53H-2, 13.0–14.0	356.49	116	385	0	236	77.4	56	4401	180	544	1817	59.3	156	81.7
55H-2, 37.0–38.0	365.97	116	479	0	155	68.3	64	3842	247	760	1401	0	141	110
57H-2, 27.0–28.0	375.6	103	320	0	129	64.5	63	4906	341	779	599	0	116	101
59H-3, 22.0–23.0	386.11	127	322	0	141	78.1	9	4456	1449	1525	1443	50.8	136	68.8
61H-3, 47.0–48.0	396.68	116	442	0	171	99.3	40	4625	420	632	1175	63.6	120	67.7
63H-2, 85.0–86.0	403.9	115	250	0	146	72.7	70	3983	394	644	1303	0	197	88.6
65H-3, 79.0–80.0	415.74	164	625	0	251	129	45	5511	892	784	1012	202	136	99
67H-2, 104.0–105.0	423.02	260	922	0	402	141	18	5384	351	1691	1711	95	148	93
69H-1, 132.0–133.0	432.12	169	620	0	342	86	78	4212	322	860	932	76	178	86
71H-2, 119.0–120.0	441.76	151	573	0	378	74	41	6114	203	665	442	95	181	90

Table T2 (continued).

Core section, interval (cm)	Top depth CSF-A (m)	Smectite (counts)	Illite (counts)	Hornblende (counts)	Kaolinite + chlorite (counts)	Pyroxene (counts)	Opal-A (counts)	Quartz (counts)	K-feldspar (counts)	Plagioclase (counts)	Calcite (counts)	Dolomite (counts)	Halite (counts)	Pyrite (counts)
73H-1, 108.0–109.0	450.68	279	842	0	495	127	23	5461	405	1418	699	128	185	66
75H-2, 12.0–13.0	460.06	256	1033	0	508	97	52	4786	232	1111	1213	87	192	87
77H-1, 130.0–131.0	469.7	187	735	0	418	68	59	4673	214	537	1311	89	224	92
79H-1, 102.0–103.0	478.52	451	1340	0	815	89	0	5243	147	692	543	160	234	0
81H-1, 112.0–113.0	487.62	107	380	0	243	106	63	5133	301	1113	685	0	129	70
83X-CC, 15.0–16.0	500.25	183	764	0	446	76	17	4875	816	1005	904	136	154	72
85X-2, 19.0–20.0	520.37	144	628	0	371	69	13	4469	210	493	563	89	202	85
87X-4, 22.0–23.0	543.58	132	598	0	331	80	9	4568	194	441	269	0	158	0

Table T3. List of visible tephra layers thicker than 0.5 cm, Holes U1427A and U1427B.

Core, section, interval (cm)	Top depth CSF-A (m)	Bottom depth CSF-A (m)	Thickness (cm)	Color	Occurrence	Core, section, interval (cm)	Top depth CSF-A (m)	Bottom depth CSF-A (m)	Thickness (cm)	Color	Occurrence
346-U1427A-						346-U1427B-					
2H-7, 21–31	10.68	10.78	10.0	Gray	Layered	2H-4, 120–133	10.5	10.63	13.0	Gray	Layered
5H-5, 44.5–45.5	36.575	36.585	1.0	Dark gray	Layered	2H-4					
5H-7, 55	39.25		10.0	White	Layered	5H-5, 62–72	39.57	39.67	10	White	Layered
5H-CC, 3		39.42									
5H-CC						6H-5, 145–147	51.59	51.61	1	Gray	Patched
10H-2, 117–120	79.48	79.51	1.0	Light gray	Patched	6H-5					
11H-3, 74–94.5	91.02	91.225	20.5	Light gray	Layered	6H-5					
14H-1, 142.5	117.225		8.5	Light gray	Layered	15H-6, 38–45.8	118.1	118.178	7.8	Light gray	Layered
14H-2, 5.5		117.315									
16H-3, 122–125	137.89	137.92	3.0	Light gray	Layered	17H-6, 114–121.5	138.61	138.685	7.5	Light gray	Layered
16H-4, 7–8.5	138.09	138.105	1.5	White	Layered	17H-6, 139–145	138.86	138.92	6	White	Layered
18H-4, 18–18.3	157.34	157.343	0.3	White	Layered	19H-6, 74.7–75	157.397	157.4	0.3	White	Layered
18H-5, 9.4–9.9	158.754	158.759	0.5	Black	Layered	19H-CC, 6.5–6.7	158.705	158.707	0.2	Black	Layered
20H-6, 85–88	180.99	181.02	3.0	Light gray	Patched	22H-2, 110–112.5	180.4	180.425	2	Pink	Layered
23H-3, 54–60	204.85	204.91	6.0	Dark gray	Layered	24H-8, 6.5–8.5	206.115	206.135	2	Light gray	Layered
3H-3						24H-8, 10–13.5	206.15	206.185	3.5	Black	Layered
3H-4, 102.5–103.5	206.835	206.845	1.0	Light gray	Layered	25H-1, 49–50.2	206.79	206.802	1.2	Light gray	Layered
3H-7, 24–30	210.24	210.3	6.0	Light gray	Layered	25H-3, 76–82.5	210.08	210.145	6.5	Light gray	Layered
24H-1, 35–36	211.15	211.16	1.0	Gray	Layered	25H-5, 24.5–28.5	212.585	212.625	4	Gray	Layered
24H-1, 100–103.5	211.8	211.835	3.5	Light gray	Layered	25H-5					
24H-1, 130–130.5	212.1	212.105	0.5	Gray	Layered	25H-5					
25H-3, 114–115	223.48	223.51	1.0	Gray	Layered	26H-8, 23–25	224.27	224.29	2	Gray	Layered
25H-3, 118–120	223.54	223.56	2.0	Light gray	Layered	26H-8					
25H-6, 14–20	226.89	226.95	6.0	White	Layered	27H-1, 115–124.5	225.85	225.945	9.5	White	Layered
25H-6, 20	226.95		>180.0	White	Layered	27H-1					
25H-7, 51		228.67				27H-1					
27H-1, 11–11.5	233.84	233.845	0.5	Gray	Layered	27H-1					
27H-1, 25.5	233.655		34.0	Light gray	Layered	28H-2, 9–21	233.79	233.91	12	White	Layered
27H-2, 29		234.02									
27H-2						35H-2, 70–71	266.11	266.12	1	Light gray	Layered
27H-2						35H-3, 18–24	267.11	267.17	6	Brownish gray	Layered
35H-1, 104–107	272.04	272.07	0.5	Light gray	Patched	35H-3					
39H-2, 43–45	290.97	290.99	1.0	Light gray	Layered	35H-3					
39H-3, 14–20	291.85	291.91	3.0	Gray	Patched	35H-3					
45H-3, 37.6–37.7	321.266	321.263	0.2	Light gray	Layered	47H-1, 23–23.2	320.93	320.932	0.2	Light gray	Layered
45H-4, 39.4–40.5	322.654	322.665	1.1	White	Layered	47H-2, 22–23	322.43	322.44	1	White	Layered
46H-3, 102.8–104	325.508	325.52	1.2	White	Layered	47H-2					
46H-4, 12.6–13.6	326.066	326.076	1.0	White	Layered	47H-2					
						49H-2, 11–12.5	328.76	328.775	1.5	Light gray	Layered
						49H-2, 21–22.5	328.86	328.875	1.5	Light gray	Layered
47H-3, 0–1	328.8	328.81	1.0	Light gray	Layered	49H-2					
49H-2, 86.5–88	338.475	338.49	1.5	Light gray	Layered	51H-1, 90–91	338.7	338.71	1	Light gray	Layered
49H-3, 88.2–91	339.692	339.72	2.8	Light gray	Layered	51H-2, 85–86	340.1	340.11	1	Light gray	Layered
49H-4, 49.2–50	340.802	340.815	0.8	White	Layered	51H-3, 49–59	341.14	341.15	1	White	Layered
49H-4						55H-5, 29–32	358.76	358.79	3	Light gray	Layered
59H-3, 80–81	386.69	386.7	0.5	Gray	Layered						
70H-2, 51–52	437.44	437.45	1.0	Light gray	Layered						

Some thin layers (<0.5 mm) that potentially correlatable between holes are also shown. Tephra layers in same line are thought to be correlative.

Table T4. Microfossil bioevents, Site U1427.

Core, Section, interval (cm)		Event		Age	Depth CSF-A (m)				Depth CCSF-A (m)			
Top	Bottom	type	Bioevents and epoch boundaries	(Ma)	Top	Bottom	Midpoint	±	Top	Bottom	Midpoint	±
346-U1427A-	346-U1427A-											
1H-CC	1H-CC	R	*Larcopyle buetschlii* Zone	0-0.01	1.74	1.74	1.74	0.00	1.80	1.80	1.80	0.00
2H-CC	3H-CC	R	LO *Lychnocanoma sakaii*	0.05	11.29	21.39	16.34	5.05	11.07	21.92	16.50	5.43
4H-CC	5H-CC	F	FO and LO *Globigerinoides ruber* (pink)	0.12–0.40	30.79	39.46	35.13	4.34	31.43	40.30	35.87	4.43
5H-CC	6H-CC	R	LO *Amphimelissa setosa*	0.08	39.46	50.03	44.75	5.29	40.30	50.37	45.33	5.03
6H-4W, 75	6H-6W, 75	CN	FO *Emiliania huxleyi*	0.29	43.91	46.92	45.42	1.51	44.25	47.26	45.75	1.51
8H-7W, 75	8H-CC	CN	LO *Pseudoemiliania lacunosa*	0.44	66.85	68.52	67.69	0.83	68.49	70.16	69.32	0.83
10H-CC	11H-CC	R	LO *Spongodiscus* sp.	0.29	88.07	97.04	92.56	4.49	90.20	100.38	95.29	5.09
28H-CC	29H-CC	F	LO *Neogloboquadrina kagaensis* group	0.70	242.86	246.30	244.58	1.72	257.92	260.88	259.40	1.48
50H-CC	51H-1W, 75	CN	LO *Reticulofenestra asanoi*	0.91	346.82	346.95	346.89	0.06	364.34	364.40	364.37	0.03
67H-CC	68H-CC	CN	FCO *Reticulofenestra asanoi*	1.14	426.62	431.08	428.85	2.23	449.07	453.53	451.30	2.23
78H-CC	79H-CC	F	*Neogloboquadrina pachyderma* (D to S)	1.14–1.24	477.42	481.73	479.58	2.15	499.87	504.18	502.02	2.15
79H-CC	80H-1W, 23	CN	LO *Gephyrocapsa* (>5.5 µm)	1.24	481.73	482.03	481.88	0.15	504.18	504.48	504.33	0.15
80H-2W, 80	80H-3W, 80	CN	LO *Helicosphaera sellii*	1.34	483.09	484.59	483.84	0.75	505.54	507.04	506.29	0.75
83X-CC	84X-CC	F	T *Globorotalia inflata* (#2 bed)	1.24–1.34	500.37	511.75	506.06	5.69	522.82	534.20	528.51	5.69

R = radiolarian, F = foraminifer, CN = calcareous nannofossil. LO = last occurrence, FO = first occurrence, FCO = base common, T = top.

Table T5. Preservation and estimated abundance of calcareous nannofossils, Site U1427. (Continued on next page.)

Core, section, interval (cm)	Top depth CSF-A (m)	Bottom depth CSF-A (m)	Preservation	Abundance	*Braarudosphaera bigelowii*	*Calcidiscus leptoporus*	*Calcidiscus macintyrei*	*Coccolithus pelagicus*	*Coronocyclus nitescens*	*Dictyococcites* spp.	*Emiliania huxleyi*	*Florisphaera profunda*	*Gephyrocapsa caribbeanica*	*Gephyrocapsa margereliii/muellerae*	*Gephyrocapsa oceanica* s.s.	*Gephyrocapsa omega*	*Gephyrocapsa* spp. (>4 µm)	*Gephyrocapsa* spp. large (>5.5 µm)	*Gephyrocapsa* spp. small (<4 µm)	*Helicosphaera carteri*	*Helicosphaera sellii*	*Helicosphaera* spp.	*Pontosphaera japonica*	*Pontosphaera* spp.	*Pseudoemiliania lacunosa*	*Reticulofenestra asanoi*	*Reticulofenestra* small	*Reticulofenestra* spp.	*Rhabdosphaera clavigera*	*Syracosphaera* spp.	*Umbilicosphaera sibogae*
346-U1427A-																														
1H-1-mudline	0.00	0.00	M	F		F		R				C			C		C	C	C											
1H-CC	1.74	1.79	G	C	R						R		R		C			F	F	R										
2H-CC	11.29	11.34	G	R	R						R				R				R											
3H-CC	21.39	21.44	M	F	R						F		R	R	R		R		F											
4H-2, 75	22.06	22.06	M	F	R			R			C			C	R				C											
4H-4, 75	24.76	24.76	M	F	R			R			C			C	F				C											
4H-6, 75	27.25	27.25	M	C				C			F				F				C											
4H-CC	30.79	30.84	G	A				C					R	R	C	F	C	F	A	R										
5H-1, 75	31.05	31.05	M	A				R			F				C				A	R										
5H-3, 30–32	33.53	33.55	M	C				F			F				C		C		A											
5H-6, 75	37.95	37.95	M	A				C			F				A				F										R	
5H-CC	39.46	39.51	G	A				F			F				F	R		R	A	F										R
6H-2, 75	40.90	40.90	G	A											C				A	R										
6H-4, 75	43.91	43.91	M	F							R				C				C											
6H-6, 75	46.92	46.92	P	R				R											R											
6H-CC	50.03	50.08	P	R				R							R				R											
7H-CC	59.12	59.17	M	A	R			F					C	C	R			R	D											
8H-3, 60–62	61.24	61.26	M	C	R			C						F	C		F		C	R				R			A		R		
8H-5, 75	63.84	63.84	M	C				F							F		F		C								C				
8H-7, 75	66.85	66.85	M	C				F						R	F		R		F					R			C				
8H-CC	68.52	68.57	M	C	R	R		F					R	F	C		R	R	A	R					R				R		
9H-CC	78.14	78.19	M	A	R			C				F	F		C		R	R	C	R		R		R	R				R		
10H-CC	88.07	88.12	M	F	R			F					R		R				C						R						
11H-CC	97.04	97.09	G	F				R					R	F	F				C	R					R						
12H-CC	106.71	106.76	G	A				F						F	C				C						F						
13H-CC	115.80	115.85	P	F				F					R		R				C						R						
14H-CC	125.48	125.53	M	C	R								F	C	R				A						R						
15H-CC	135.22	135.27	G	D		F		R					F		F				D	R					R				R		
16H-CC	144.99	145.04	G	A				F					F		R				A						R						
17H-CC	154.10	154.14		B																										
18H-CC	163.91	163.96	P	R															R											
19H-CC	172.88	172.92	M	C	R			R					R		F				D	R					R						
20H-CC	182.39	182.43	M	C				F					F		F				D						R		F	F		R	
21H-CC	191.61	191.67	M	C		R		R				F		R					C						R			C			
22H-CC	201.67	201.72	G	F		R		R							F		F		C	R					R		C	F			
23H-CC	210.68	210.73		B																										
24H-CC	219.75	219.80		B																										
25H-CC	228.67	228.73		B																										
26H-CC	233.80	233.85	P	R				R									F		F											
27H-CC	238.49	238.54	M	C	R			F					R		F				A				R							
28H-CC	242.86	242.91	M	C				F					R		F				A											
29H-CC	246.30	246.35	M	C				F					R		C		F		A						R					
30H-CC	251.82	251.87	M	C	R	R		R							C				C								R	R			
31H-CC	257.18	257.23	P	R		R									R				F											
32H-CC	261.73	261.75	G	C				C							C													R		
33H-CC	266.43	266.46	M	C				R							C				C	R							F	F			
34H-CC	271.50	271.54	M	F	R			R					R		F				R								R				
35H-CC	275.58	275.63	M	F				R					F		C				C								F	R			
36H-CC	280.34	280.38	M	F		R		C							C				C									F			
37H-CC	285.69	285.74	P	R				R					R						R												
38H-CC	290.20	290.25	M	C	R	R		R					R	F					A	R							C	F			
39H-CC	295.11	295.15	G	A	R			C					R	F	R				D	R							D	R			
40H-CC	299.21	299.26	M	F		R		R				F	R	F	F				C	R							C				
41H-CC	304.23	304.28	M	C	R	F		F					F						A								A	F			
42H-CC	308.87	308.92	M	C				F					F		C				C								C				
43H-CC	313.08	313.13	G	D		R		F						C	F		F	F	D	R					R		D	R			
44H-CC	317.91	317.96	P	R									R		R				R												

Table T5 (continued).

Core, section, interval (cm)	Top depth CSF-A (m)	Bottom depth CSF-A (m)	Preservation	Abundance	*Braarudosphaera bigelowii*	*Calcidiscus leptoporus*	*Calcidiscus macintyrei*	*Coccolithus pelagicus*	*Coronocyclus nitescens*	*Dictyococcites* spp.	*Emiliania huxleyi*	*Florisphaera profunda*	*Gephyrocapsa caribbeanica*	*Gephyrocapsa margerelii/muellerae*	*Gephyrocapsa oceanica* s.s.	*Gephyrocapsa omega*	*Gephyrocapsa* spp. (>4 µm)	*Gephyrocapsa* spp. large (>5.5 µm)	*Gephyrocapsa* spp. small (<4 µm)	*Helicosphaera carteri*	*Helicosphaera sellii*	*Helicosphaera* spp.	*Pontosphaera japonica*	*Pontosphaera* spp.	*Pseudoemiliania lacunosa*	*Reticulofenestra asanoi*	*Reticulofenestra* small	*Reticulofenestra* spp.	*Rhabdosphaera clavigera*	*Syracosphaera* spp.	*Umbilicosphaera sibogae*
45H-CC	323.02	323.07	M	R				R					R		F				F						R						
46H-CC	327.95	328.00	P	R				R				F							R												
47H-CC	332.58	332.63	M	R										R	R				F								R				
48H-CC	337.48	337.53	M	F				F							R				F								F				
49H-CC	342.14	342.19	G	C	R			C											A								C				
50H-CC	346.82	346.87	M	C				R					R	F	F				A								C				
51H-1, 75	346.95	346.95	M	A	R	F		F							C				F	F						R	A				
51H-2, 75	347.88	347.88	G	C				R											D							R	C				
51H-3, 75	349.08	349.08	M	C		F		R		R			F						D	R							C	R			
51H-4, 75	350.50	350.50	M	A				F											D							F	C	F			
51H-5, 75	351.52	351.52	M	A		C		R	*						R				D							F	C				
51H-CC	351.68	351.73	M	F		R		F		R		F	F		F				C						F	R		F			
52H-CC	356.03	356.08	M	C				R							F		R		A				R			R	C				
53H-CC	361.02	361.07	G	C				R							R				A							R					
54H-CC	365.70	365.75	G	C	R	R		C											A						R						
55H-CC	370.20	370.25	M	C				F											C					R	R	R					
56H-CC	374.88	374.93	M	F				F											C							R					
57H-CC	379.82	379.88	P	F				F											C							R					
58H-CC	384.71	384.76	M	C				F											C					R		R					
59H-CC	386.70	386.75	M	C				C											C							F					
60H-CC	393.59	393.61	P	C				F											C					R			C				
61H-CC	398.17	398.20	M	C	R			C											C					R		R	C				
62H-CC	402.78	402.81	M	C				C											F						R		R				
63H-CC	407.84	407.89	M	F	R			F							R				C					R		R	F				
64H-CC	412.63	412.68	M	F				F											F							R	C	F			
65H-CC	417.01	417.06	M	A	R			F											A							F	A				
66H-CC	421.22	421.27	M	F	R	R		F											C							F	C	R			
67H-CC	426.62	426.67	G	C				C																	F	F	C	F			
68H-2, 25	426.50	426.50	M	F				R											R						C		F	F			
68H-3, 75	427.58	427.58	M	F		R		F																		R	R	F			
68H-4, 75	428.79	428.79	M	R				R							R				R				R								
68H-5, 45	429.76	429.76	P	R				R		R									R						R		R	R			
68H-CC	431.08	431.13	M	R				R											F								C	R			
69H-CC	435.75	435.80	M	C		F		F											C	R							C	F			
70H-CC	440.21	440.26		B																											
71H-CC	445.47	445.52	P	R				F											R												
72H-CC	449.89	449.94	M	C				F											C								C				
73H-CC	454.27	454.32	M	F	F			C											F								C				
74H-CC	459.40	459.45	M	C		R		C											F						R		A	F			
75H-CC	464.24	464.29	M	C		F		C											F					R		R	A	F			
76H-CC	469.13	469.19	P	F		F		F												R					F	F	F	F			
77H-CC	473.58	473.63	P	R		R		R															R				R	R			
78H-CC	477.42	477.47	M	F	R			R												R			R			R	R	F			
79H-1, 75	478.25	478.25		B																											
79H-CC	481.73	481.78	P	R				R																			R				
80H-1, 23	482.03	482.03	P	R	R			R		R					R		R	R	R						R			R			
80H-2, 80	483.09	483.09	P	R	R			F		F			R		R			R										R			
80H-3, 80	484.59	484.59	M	R				R		R					R			R				R				R	R			
80H-4, 45	485.69	485.69	M	R		R									R			R								R	R			
80H-CC	487.04	487.09	M	F		R		R		R					F			F	R	R							R				
81H-CC	490.38	490.43	P	F		R		R		F					R			R								R	R	R			
82X-CC	491.89	491.94	M	A		R		C					F		C			F	A						F		C	F			
83X-CC	500.37	500.42	P	R				F							F				C								F	R			
84X-CC	511.75	511.80	M	C				C		F			F		F		F		C								A	C			
85X-CC	528.06	528.11	G	C		R	R	F		C					F			F	F			R					C				
86X-CC	535.14	535.19	G	A		R		F		C					C			F	C			R	R		F		C	C			
87X-CC	547.87	547.92	M	C		F		R		C					C				C	R						R	R	C			

* = reworked specimens. Preservation: G = good, M = moderate, P = poor. Abundance: D = dominant, A = abundant, C = common, F = few, R = rare, B = barren. Shaded intervals = barren.

Table T6. Preservation and estimated abundance of radiolarians, Hole U1427A. (Continued on next page.)

Core, section	Top depth CSF-A (m)	Bottom depth CSF-A (m)	Preservation	Abundance	*Amphimelissa setosa*	*Amphirhopalum ypsilon*	*Ceratospyris borealis*	*Cycladophora davisiana*	*Dictyocoryne profunda*	*Dictyocoryne truncatum*	*Didymocyrtis tetrathalamus*	*Euchitonia furcata*	*Hymeniastrum euclidis*	*Larcopyle polyacantha* group	*Lychnocanoma sakaii*	*Octopyle/Tetrapyle* group	*Phortlicium pylonium* group	*Pseudodictyophimus gracilipes*	*Siphocampe arachnea* group	*Spongaster tetras tetras*	*Spongodiscus* sp.	*Stylochlamydium venustum*	*Stylochlamydium bensoni*
346-U1427A-																							
1H-CC	1.74	1.79	G	F				C	F	F	F			A		C							
2H-CC	11.29	11.34	G	R			C	R						F					P			F	
3H-CC	21.39	21.44	G	F			F							C	A							F	
4H-CC	30.79	30.84	G	F										R	A	F							
5H-CC	39.46	39.51	G	F				P	F	F	R		P	R	P	A							
6H-CC	50.03	50.08	M	R	R	P								P	C	F							
7H-CC	59.12	59.17	G	R	R		P							F	F	P							
8H-CC	68.52	68.57	G	R	C									F									
9H-CC	78.14	78.19	G	R	P						R				P	F						P	
10H-CC	88.07	88.12	G	F	R		C			P	P			R		R						A	
11H-CC	97.04	97.09	G	R	C			P	P							F					R		
12H-CC	106.71	106.76	M	F	P		P						P	A		F				P		P	
13H-CC	115.80	115.85	G	F	F		P	F	R		R			F							C	C	
14H-CC	125.48	125.53	G	C	A		A		P	R				F							R	A	
15H-CC	135.22	135.27	G	R			R							C		P	R				P	R	
16H-CC	144.99	145.04	G	F					P		F			A		R	F				P	F	A
17H-CC	154.10	154.14	M	R	P					P				P		P							
18H-CC	163.91	163.96	G	F	F			F								P	P				P	P	
19H-CC	172.88	172.92	G	F	R		F	R						R							A		
20H-CC	182.39	182.43	G	F	R	P			P		F			A		F				P	F		
21H-CC	191.61	191.67	G	R		P				P	P	P		C		P					C		
22H-CC	201.67	201.72	G	F	P	F	P		R	F	F	F	P	C		C				R	F	R	
23H-CC	210.68	210.73	G	R				P			P					R							P
24H-CC	219.75	219.80	G	R		P			P							F							
26H-CC	233.80	233.85	M	R			P									F					F		
27H-CC	238.49	238.54	G	R			F							R		P					C		
29H-CC	246.30	246.35	G	R												P					C		
31H-CC	257.18	257.23	G	R	F											R					F		
33H-CC	266.43	266.46	M	R										F			P				C		
35H-CC	275.58	275.63	M	R												A							
37H-CC	285.69	285.74	M	R			F			P						F					F		
39H-CC	295.11	295.15	G	F			R							F		A					P		
41H-CC	304.23	304.28	G	R					P					C		F				P			
43H-CC	313.08	313.13	G	F				F		R	R					C					C		
45H-CC	323.02	323.07	G	R												P							
46H-CC	327.95	328.00	G	R		P										P							R
47H-CC	332.58	332.63	M	R			P	F								R			P		C		
49H-CC	342.14	342.19	G	R			A							F		F			P		C		
51H-CC	351.68	351.73	G	R				C	R	F	F			C		C					F		
53H-CC	361.02	361.07	G	F										A		F					F		
55H-CC	370.20	370.25	G	F												C							
57H-CC	379.82	379.88	G	F	F	P								R		R					F	P	
59H-CC	386.70	386.75	M	F					P							F					R	C	
61H-CC	398.17	398.20	M	F										C								A	
63H-CC	407.84	407.89	G	F		P	P							C		R					F		
65H-CC	417.01	417.06	G	R			F									F					F		
67H-CC	426.62	426.67	G	C		P			P	P	P			F		C	C				P		
69H-CC	435.75	435.80	M	R						R				P			P						P
71H-CC	445.47	445.52	G	R		P	P		P							F							
73H-CC	454.27	454.32	M	R				P															P
75H-CC	464.24	464.29	G	F										R		F		P					
77H-CC	473.58	473.63	G	F			P				P			P		F		R			R		C
79H-CC	481.73	481.78	M	R	F		C														R		
81H-CC	490.38	490.43	G	C	P		R		R	P	F			F		F	R			P	F	C	C
83X-CC	500.37	500.42	G	R																			A

Table T6 (continued).

Core, section	Top depth CSF-A (m)	Bottom depth CSF-A (m)	Preservation	Abundance	*Amphimelissa setosa*	*Amphirhopalum ypsilon*	*Ceratospyris borealis*	*Cycladophora davisiana*	*Dictyocoryne profunda*	*Dictyocoryne truncatum*	*Didymocyrtis tetrathalamus*	*Euchitonia furcata*	*Hymeniastrum euclidis*	*Larcopyle polyacantha* group	*Lychnocanoma sakaii*	*Octopyle/Tetrapyle* group	*Phorticium pylonium* group	*Pseudodictyophimus gracilipes*	*Siphocampe arachnea* group	*Spongaster tetras tetras*	*Spongodiscus* sp.	*Stylochlamydium venustum*	*Stylochlamydium bensoni*
84X-CC	511.75	511.80	G	C						F	F			F		F				P			C
85X-CC	528.06	528.11	G	C		C			C	C	P			F		F		P			P		C
86X-CC	535.14	535.19	G	C		F			F				R	P		R		P					C
87X-CC	547.87	547.92	G	A		F			C	A	F			F		C				F			A

Preservation: G = good, M = moderate. Abundance: A = abundant, C = common, F = few, R = rare, P = present.

Table T7. Preservation and estimated abundance of diatoms, Hole U1427A. (Continued on next page.)

Core, section	Top depth CSF-A (m)	Bottom depth CSF-A (m)	Preservation	Abundance	*Actinocyclus curvatulus*	*Actinocyclus oculatus*	*Actinoptychus senarius*	Freshwater spp.	*Azpeitia endoi*	*Azpeitia nodulifera*	*Chaetoceros* spp. and similar spores	*Cocconeis scutellum*	*Coscinodiscus marginatus*	*Coscinodiscus oculus-iridis*	*Coscinodiscus radiatus*	*Cyclotella striata*	*Diploneis bombus*	*Neodenticula koizumii*	*Neodenticula seminae*	*Paralia sulcata*	*Shionodiscus oestrupii*	*Stephanopyxis turris*	*Stephanopyxis* spp.	*Thalassionema nitzschioides*	*Thalassiosira antiqua*	*Thalassiosira eccentrica*	*Thalassiosira leptopus*	*Thalassiosira lineata*	*Thalassiosira pacifica*
346-U1427A-																													
1H-CC	1.74	1.79	G	A	R		F			R	R					R	R			A	A			A	R		R	R	
2H-CC	11.29	11.34	G	C	R		F			R	F									A	A			A					
3H-CC	21.39	21.44	G	A	R		F				A					C		R	R	A	R			A	R	R			
4H-CC	30.79	30.84	G	A			C				A					C				A	A			A		F			
5H-CC	39.46	39.51	G	A							A			R		R				A				A		F			
6H-CC	50.03	50.08	M	C				C			C	C					R			A	A			C					
7H-CC	59.12	59.17	G	C			R				A	R			F	A	C			A				A					
8H-CC	68.52	68.57	G	A			R				A	R			R	C				C	A			A					F
9H-CC	78.14	78.19	G	A							C	F			R	C				A	R			A					R
10H-CC	88.07	88.12	G	C							A		F	F		R				A				C					
11H-CC	97.04	97.09	G	C				F			A	R			R	R				A	R			C		R	R		
12H-CC	106.71	106.76	G	A			F						F		R	A				A				A					
13H-CC	115.80	115.85	G	A	R						A				A	F		R	R	A				C		R		R	
14H-CC	125.48	125.53	G	A							C	R								C	C			A					
15H-CC	135.22	135.27	G	A			F				A	R				R		R		A	F			A				R	
16H-CC	144.99	145.04	G	C			R	R			A					A				F				A		R			R
17H-CC	154.10	154.14	G	A				C	F		C				R	C				A	A			A		R		R	
18H-CC	163.91	163.96	G	D			R	C			A	R								A	R			A	R				
19H-CC	172.88	172.92	G	C		F	F	C	R		A	R	R					R		A	F			A		R			
20H-CC	182.39	182.43	G	A				R			C						A		F	A	F			A					
21H-CC	191.61	191.67	G	A	R				F		C				F		C	R	R	C	A	R	R	C			R		
22H-CC	201.67	201.72	G	A			F				A				R		R			A		R		A					
23H-CC	210.68	210.73	G	A			F	C			C						F			A	A			R					
24H-CC	219.75	219.80	G	A			A	R			C	R						R		A	C			C			R		
26H-CC	233.80	233.85	G	A	R		A				A	R		F				R		C	F	R		R		R	R		
27H-CC	238.49	238.54	G	C			A	R			A						F	R		A	F			C	R				
28H-CC	242.86	242.91	G	C			C				A						R	F		C			R	A	R				
29H-CC	246.30	246.35	G	A	R		A				A	R			F		R			A				A		F			
30H-CC	251.82	251.87	G	C			C				A						F			A	R			A					
31H-CC	257.18	257.23	G	C	R			C			C									C	C			C					R
32H-CC	261.73	261.75	G	C			F				A				R		C	R		A	F			A	R	C		R	
33H-CC	266.43	266.46	G	C	R		F				A			R						R	F			C		R			
34H-CC	271.50	271.54	G	C							A									A				A					
35H-CC	275.58	275.63	G	F			F																	C					
36H-CC	280.34	280.38	G	C			R				A			R	R		R			A				C					
37H-CC	285.69	285.74	G	A			C			R	A						C	R	R	A	C	R	F	A				R	
38H-CC	290.20	290.25	G	A			R				A						R			A				C		R			
39H-CC	295.11	295.15	G	A			C				A					R	C			C	F			A					
40H-CC	299.21	299.26	G	A		R	F		R		A				R					A	F			A		R			
41H-CC	304.23	304.28	G	A			C				A			R			R			A			R	A					
42H-CC	308.87	308.92	G	A			A	F	R		A						R		R	A	R			A			R		
43H-CC	313.08	313.13	G	A			A				A						C			A	F			A		R			
44H-CC	317.91	317.96	G	F				F			C							R		F				R					
45H-CC	323.02	323.07	G	C				R			A					R				A									F
46H-CC	327.95	328.00	G	C				C			A						R			A	F			F		R			
47H-CC	332.58	332.63	G	C	R						C					R	R			C	F			R					C
48H-CC	337.48	337.53	G	C							A						R			A	R			C					
49H-CC	342.14	342.19	G	A			R	R			A	R				C				A	R		R	A					
50H-CC	346.82	346.87	G	A			F				A			R						A	R			A		C			
51H-CC	351.68	351.73	G	A			F				A	R				C	C		R	A	R		R	A					
52H-CC	356.03	356.08	G	A			R				A						R			A				A					
53H-CC	361.02	361.07	G	A			C				A				C	C	C		R	A	R		R	A	R				
54H-CC	365.70	365.75	G	A			C	R			A						R			A				F					
55H-CC	370.20	370.25	G	A			C				F					A	R			A	R		F	A					
56H-CC	374.88	374.93	G	A			C				A						R			A	R			F		C			
57H-CC	379.82	379.88	G	C	R		C								R	A		R		A		R		A					
58H-CC	384.71	384.76	C	C			R				A				R	F	C			A	R			A					

Table T7 (continued).

Core, section	Top depth CSF-A (m)	Bottom depth CSF-A (m)	Preservation	Abundance	*Actinocyclus curvatulus*	*Actinocyclus oculatus*	*Actinoptychus senarius*	Freshwater spp.	*Azpeitia endoi*	*Azpeitia nodulifera*	*Chaetoceros* spp. and similar spores	*Cocconeis scutellum*	*Coscinodiscus marginatus*	*Coscinodiscus oculus-iridis*	*Coscinodiscus radiatus*	*Cyclotella striata*	*Diploneis bombus*	*Neodenticula koizumii*	*Neodenticula seminae*	*Paralia sulcata*	*Shionodiscus oestrupii*	*Stephanopyxis turris*	*Stephanopyxis* spp.	*Thalassionema nitzschioides*	*Thalassiosira antiqua*	*Thalassiosira eccentrica*	*Thalassiosira leptopus*	*Thalassiosira lineata*	*Thalassiosira pacifica*
59H-CC	386.70	386.75	G	C			C			A				R	F				A	R	R		R					
60H-CC	393.59	393.61	G	A						A				A	F	F	R		A		R		A					
61H-CC	398.17	398.20	G	F			R			A									C				C					
62H-CC	402.78	402.81	G	F						F				R		R			C				F		R			
63H-CC	407.84	407.89	G	A			A			A					C	R			A				C					
64H-CC	412.63	412.68	G	C			R			C				R		R		R	A		R		A		F			
65H-CC	417.01	417.06	G	A			C			A					R				F				A			R		
66H-CC	421.22	421.27	G	A			C	F		A					F	R			C				A		F			
67H-CC	426.62	426.67	G	D			A	R		A				R	F	R	R		A				A		R			
68H-CC	431.08	431.13	G	D	F		A	R		A						R			A				A			R		
69H-CC	435.75	435.80	G	A	R		A			A							C		C				A	R				
70H-CC	440.21	440.26	G	A			C			A									C				A	R				
71H-CC	445.47	445.52	G	A			C			A		R				F			C				A					
72H-CC	449.89	449.94	G	A			R			A					F		R		A				A					
73H-CC	454.27	454.32	G	A			C			C									C				C					
74H-CC	459.40	459.45	G	A			C			A					R		R		A				A		F			
75H-CC	464.24	464.29	G	D			A								A	F	C		C				A					R
76H-CC	469.13	469.19	G	A			C			A					F		C		A				C		C			
77H-CC	473.58	473.63	G	A			R	F		F					R	F	C		A		R	F	A					
78H-CC	477.42	477.47	G	C			C			C					R	R			A				C					
79H-CC	481.73	481.78		R						A							R						C					
80H-CC	487.04	487.09	G	C			R								R				A			F	A					
81H-CC	490.38	490.43	G	F						A							R						F					
82X-CC	491.89	491.94	G	C				R		A					R		R		A				A		F			
83X-CC	500.37	500.42	G	A			C			A							C		A			R	C					
84X-CC	511.75	511.80	G	A			A	R		A							R		A				F		C	R		
85X-CC	528.06	528.11	G	A			A			R						F			A				F					
86X-CC	535.14	535.19	G	C			A			R				R					C	R			A		R			
87X-CC	547.87	547.92	G	A			A			A							C		A				A					

Preservation: G = good, M = moderate. Abundance: D = dominant, A = abundant, C = common, F = few, R = rare, B = barren.

Table T8. Preservation and estimated abundance of planktonic foraminifers, Site U1427. (Continued on next two pages.)

Core, section	Top depth CSF-A (m)	Bottom depth CSF-A (m)	Preservation	Abundance	% Planktonic foraminifers	*Globigerina bulloides*	*Globigerina bulloides umbilicata*	*Globigerina quinqueloba*	*Globigerina* sp.	*Globigerinita glutinata*	*Globigerinoides ruber* (pink)	*Globigerinoides ruber* (white)	*Globigerinoides* sp.	*Globorotalia inflata*	*Globorotalia menardii*	*Globorotalia praeinflata*	*Globoturborotalita woodi*	*Neogloboquadrina dutertrei*	*Neogloboquadrina humerosa*	*Neogloboquadrina kagaensis* and *Neogloboquadrina inglei*	*Neogloboquadrina pachyderma* (d) and *Neogloboquadrina incompta*	*Neogloboquadrina pachyderma* (s)	*Neogloboquadrina* sp.	*Pulleniatina obliquiloculata*	Total number of planktonic foraminifers	Total planktonic foraminifer/10 cm^3
346-U1427A-																										
1H-CC	1.74	1.79	G	A	43	10		2										1			9	28			50	16.7
2H-CC	11.29	11.34	G	A	65	16		3													4	27			50	16.7
3H-CC	21.39	21.44	G	A	94	19	2	1													2	26			50	0.0
4H-CC	30.79	30.84	G	F	76	1		1														48			50	16.7
5H-CC	39.46	39.51	G	F	64	22					1	1		1				1			3	26			55	18.3

Table T8 (continued). (Continued on next page.)

Core, section	Top depth CSF-A (m)	Bottom depth CSF-A (m)	Preservation	Abundance	% Planktonic foraminifers	*Globigerina bulloides*	*Globigerina bulloides umbilicata*	*Globigerina quinqueloba*	*Globigerina* sp.	*Globigerinita glutinata*	*Globigerinoides ruber* (pink)	*Globigerinoides ruber* (white)	*Globigerinoides* sp.	*Globorotalia inflata*	*Globorotalia menardii*	*Globorotalia praeinflata*	*Globoturborotalita woodi*	*Neogloboquadrina dutertrei*	*Neogloboquadrina humerosa*	*Neogloboquadrina kagaensis* and *Neogloboquadrina inglei*	*Neogloboquadrina pachyderma* (d) and *Neogloboquadrina incompta*	*Neogloboquadrina pachyderma* (s)	*Neogloboquadrina* sp.	*Pulleniatina obliquiloculata*	Total number of planktonic foraminifers	Total planktonic foraminifer/10 cm^3
6H-CC	50.03	50.08	G	F	80	34	3	1													1	11			50	16.7
7H-CC	59.12	59.17	G	A	70			34													1	13			48	16.0
8H-CC	68.52	68.57	M	F	60			16	2									2				33			53	17.7
9H-CC	78.14	78.19	M	F	85	3	1	6		1							2				2	37			52	17.3
10H-CC	88.07	88.12	G	A	70	13		1										2			2	41			59	19.7
11H-CC	97.04	97.09	G	A	88	1		2										2				49			54	18.0
12H-CC	106.71	106.76	G	F	59			2													3	45			50	16.7
13H-CC	115.80	115.85	M	R	40	32	4	4													3	7			50	16.7
14H-CC	125.48	125.53	G	F	20	14															5	31			50	16.7
15H-CC	135.22	135.27	G	A	89	13		1		1											10	76			101	33.7
16H-CC	144.99	145.04	G	F	15	38																11			49	16.3
17H-CC	154.10	154.14	M	F	99	2															3	45			50	16.7
18H-CC	163.91	163.96	M	R	47	21	3	3										2			3	18			50	16.7
19H-CC	172.88	172.92		B	0																	0			0	0.0
20H-CC	182.39	182.43	M	F	80	43	1								1							6		1	52	17.3
21H-CC	191.61	191.67	G	A	80	15				1								2			8	26	1		53	17.7
22H-CC	201.67	201.72	M	F	66	15															2	33			50	16.7
23H-CC	210.68	210.73		B	0																	0			0	0.0
24H-CC	219.75	219.80		B	0																	0			0	0.0
25H-CC	228.67	228.70		B	0																	0			0	0.0
26H-CC	233.80	233.85	G	A	66	24		1													1	24			50	
27H-CC	238.49	238.54	G	A	56	29	3														1	17			50	16.7
28H-CC	242.86	242.91	G	A	86	15															1	34			50	16.7
29H-CC	246.30	246.35	VG	D	79	18	1													1	5	25			50	16.7
30H-CC	251.82	251.87	G	D	74	40	1	1									3			1	6	46			98	32.7
31H-CC	257.18	257.23	G	A	28	29	4														2	15			50	16.7
32H-CC	261.73	261.75	G	D	88	23		7	2	4							3	3		3	1	57			103	34.3
33H-CC	266.43	266.46	G	D	95	21		2		1							8	12		8	3	49	1		105	35.0
34H-CC	271.50	271.54	G	D	94	43	1	5	1	1							4			11	6	34			106	35.3
35H-CC	275.58	275.63	G	D	91															17		34			51	
36H-CC	280.34	280.38	G	D	59	24	1	4										1		1	2	45			78	26.0
37H-CC	285.69	285.74	M	D	55	18												1		3	9	68			99	33.0
38H-CC	290.20	290.25	G	D	88	16	1	6										1		3		24			51	
39H-CC	295.11	295.15	G	D	99	14		1									1			1	6	27			50	16.7
40H-CC	299.21	299.26	G	A	99	7														2	12	32			53	
41H-CC	304.23	304.28	VG	D	99	29		1												2	5	13			50	16.7
42H-CC	308.87	308.92	G	D	83	3											2	1			4	33			43	
43H-CC	313.08	313.13	M	D	79	9		1				1					2				14	26			53	17.7
44H-CC	317.91	317.96	M	A	76	16															12	22			50	
45H-CC	323.02	323.07	G	A	96			21														28			49	16.3
46H-CC	327.95	328.00	M	D	99	13		2												1	6	38			60	
47H-CC	332.58	332.63	M	A	96	30															6	15			51	17.0
48H-CC	337.48	337.53	M	A	65	23	2	3										1		5	6	55			95	31.7
49H-CC	342.14	342.19	M	A	97	22	2	1												3	6	16			50	16.7
50H-CC	346.82	346.87	G	A	63													4		9	5	32			50	
51H-CC	351.68	351.73	G	A	32	15												2		4	9	22			52	17.3
52H-CC	356.03	356.08	G	D	87																	50			50	
53H-CC	361.02	361.07	M	D	72													1			2	48			51	17.0
54H-CC	365.70	365.75	G	A	65	2														12	7	28			49	
55H-CC	370.20	370.25	G	F	70															2		51			53	17.7
56H-CC	374.88	374.93	M	A	59			3												3	1	43			50	
57H-CC	379.82	379.88	G	A	95															4	2	39			45	15.0
58H-CC	384.71	384.76	M	A	90			1									1	4	1	19	3	23			52	
59H-CC	386.70	386.75	M	A	84			2												1	1	47			51	0.0
60H-CC	393.59	393.61	G	D	70	1		3									2				1	45			52	
61H-CC	398.17	398.20	G	D	98	22	4													5	6	13			50	0.0
62H-CC	402.78	402.81	VG	D	64	12														4	2	33			51	

Table T8 (continued).

Core, section	Top depth CSF-A (m)	Bottom depth CSF-A (m)	Preservation	Abundance	% Planktonic foraminifers	*Globigerina bulloides*	*Globigerina bulloides umbilicata*	*Globigerina quinqueloba*	*Globigerina* sp.	*Globigerinita glutinata*	*Globigerinoides ruber* (pink)	*Globigerinoides ruber* (white)	*Globigerinoides* sp.	*Globorotalia inflata*	*Globorotalia menardii*	*Globorotalia praeinflata*	*Globoturborotalita woodi*	*Neogloboquadrina dutertrei*	*Neogloboquadrina humerosa*	*Neogloboquadrina kagaensis* and *Neogloboquadrina inglei*	*Neogloboquadrina pachyderma* (d) and *Neogloboquadrina incompta*	*Neogloboquadrina pachyderma* (s)	*Neogloboquadrina* sp.	*Pulleniatina obliquiloculata*	Total number of planktonic foraminifers	Total planktonic foraminifer/10 cm^3
63H-CC	407.84	407.89	M	F	84	12		1									1			17	7	16			54	0.0
64H-CC	412.63	412.68	M	A	98	1											2			18	6	25			52	
65H-CC	417.01	417.06	G	D	97	1		4												8	22	65			100	0.0
66H-CC	421.22	421.27	M	F	50	2		8												18	68	2			98	0.0
67H-CC	426.62	426.67	M	F	84															1		49			50	0.0
68H-CC	431.08	431.13	G	A	70	19												2			1	71			93	0.0
69H-CC	435.75	435.80	P	R	4	3																45			48	0.0
70H-CC	440.21	440.26	P	R	30			2												2	2	7			13	4.3
71H-CC	445.47	445.52	M	F	60	11														11	4	24			50	16.7
72H-CC	449.89	449.94	M	A	61	24	4	4												17	16	8			73	24.3
73H-CC	454.27	454.32	G	D	73	11	3	2												5	15	17			53	17.7
74H-CC	459.40	459.45	G	B	57	12		2												2	1	33			50	
75H-CC	464.24	464.29	G	A	40	2												1			1	46			50	16.7
76H-CC	469.13	469.19	G	D	42			3													1	46			50	16.7
77H-CC	473.58	473.63	G	A	53	20		1				1								2	5	22			51	17.0
78H-CC	477.42	477.47	G	F	28	14														1	2	30			47	15.7
79H-CC	481.73	481.78	G	A	55	20	4	1									3	2		5	12	5			52	17.3
80H-CC	487.04	487.09	G	R	1	1		1		3		1								7	18	4			35	11.7
81H-CC	490.38	490.43	M	A	28	13		3												5	17	12			50	16.7
82X-CC	491.89	491.94	G	D	37	18						1		2*				1		4	24	1			51	17.0
83X-CC	500.37	500.42	G	F	49	1		1					1							15	28	5			51	17.0
84X-CC	511.75	511.80	P	R	14	14	3	4						2						3	15	9			50	16.7
85X-CC	528.06	528.11	G	R	1	2	1							1		1		1			2	0			8	2.7
86X-CC	535.14	535.19	M	R	27	6		4						6*							5	0			21	7.0
87X-CC	547.87	547.92	M	R	3	2																0			2	0.7

* = *G. inflata* specimens were partly broken. Preservation: VG = very good, G = good, M = moderate, P = poor. Abundance: D = dominant, A = abundant, F = few, R = rare, B = barren. Shaded intervals = barren.

Table T9. Benthic foraminifers, Hole U1427A. This table is available in an **oversized format.**

Table T10. Ostracod abundance, Hole U1427A. (Continued on next two pages.)

Core, section	Top depth CSF-A (m)	Bottom depth CSF-A (m)	Abundance (valves/20 cm^3)
346-U1427A-			
1H, mudline	0.00	0.00	6
1H-CC	1.74	1.79	0
2H-CC	11.29	11.34	13
3H-CC	21.39	21.44	2
4H-CC	30.79	30.84	15
5H-CC	39.46	39.51	9
6H-CC	50.03	50.08	1
7H-CC	59.12	59.17	34
8H-CC	68.52	68.57	3
9H-CC	78.14	78.19	4
10H-CC	88.07	88.12	10
11H-CC	97.04	97.09	3
12H-CC	106.71	106.76	4
13H-CC	115.80	115.85	4

Table T10 (continued). (Continued on next page.)

Core, section	Top depth CSF-A (m)	Bottom depth CSF-A (m)	Abundance (valves/20 cm^3)
14H-CC	125.48	125.53	2
15H-CC	135.22	135.27	
16H-CC	144.99	145.04	15
17H-CC	154.10	154.14	
18H-CC	163.91	163.96	0
19H-CC	172.88	172.92	5
20H-CC	182.39	182.43	7
21H-CC	191.61	191.67	25
22H-CC	201.67	201.72	2
23H-CC	210.68	210.73	0
24H-CC	219.75	219.80	0
25H-CC	228.67	228.73	
26H-CC	233.80	233.85	8
27H-CC	238.49	238.54	24
28H-CC	242.86	242.91	11
29H-CC	246.30	246.35	18
30H-CC	251.82	251.87	13
31H-CC	257.18	257.23	6
32H-CC	261.73	261.75	5
33H-CC	266.43	266.46	13
34H-CC	271.50	271.54	35
35H-CC	275.58	275.63	38
36H-CC	280.34	280.38	5
37H-CC	285.69	285.74	1
38H-CC	290.20	290.25	3
39H-CC	295.11	295.15	8
40H-CC	299.21	299.26	0
41H-CC	304.23	304.28	10
42H-CC	308.87	308.92	0
43H-CC	313.08	313.13	22
44H-CC	317.91	317.96	0
45H-CC	323.02	323.07	0
46H-CC	327.95	328.00	
47H-CC	332.58	332.63	0
48H-CC	337.48	337.53	0
49H-CC	342.14	342.19	9
50H-CC	346.82	346.87	104
51H-CC	351.68	351.73	5
52H-CC	356.03	356.08	9
53H-CC	361.02	361.07	5
54H-CC	365.70	365.75	45
55H-CC	370.20	370.25	1
56H-CC	374.88	374.93	7
57H-CC	379.82	379.88	3
58H-CC	384.71	384.76	81
59H-CC	386.70	386.75	23
60H-CC	393.59	393.61	3
61H-CC	398.17	398.20	18
62H-CC	402.78	402.81	14
63H-CC	407.84	407.89	4
64H-CC	412.63	412.68	13
65H-CC	417.01	417.06	12
66H-CC	421.22	421.27	6
67H-CC	426.62	426.67	1
68H-CC	431.08	431.13	2
69H-CC	435.75	435.80	0
70H-CC	440.21	440.26	0
71H-CC	445.47	445.52	1
72H-CC	449.89	449.94	49
73H-CC	454.27	454.32	14
74H-CC	459.40	459.45	4
75H-CC	464.24	464.29	0
76H-CC	469.13	469.19	0
77H-CC	473.58	473.63	0
78H-CC	477.42	477.47	12
79H-CC	481.73	481.78	3
80H-CC	487.04	487.09	80
81H-CC	490.38	490.43	1

Table T10 (continued).

Core, section	Top depth CSF-A (m)	Bottom depth CSF-A (m)	Abundance (valves/20 cm^3)
82X-CC	491.89	491.94	11
83X-CC	500.37	500.42	0
84X-CC	511.75	511.80	3
85X-CC	528.06	528.11	0
86X-CC	535.14	535.19	0
87X-CC	547.87	547.92	0

Table T11. Calcium carbonate, total carbon (TC), total organic carbon (TOC), and total nitrogen (TN) contents on interstitial water squeeze cake sediment samples, Site U1427.

Core, section, interval (cm)	Top depth CSF-A (m)	Calcium carbonate (wt%)	TC (wt%)	TOC (wt%)	TN (wt%)
346-U1427A-					
1H-2, 65/70	1.56	4.6	2.74	2.20	0.33
2H-1, 145–150	3.25	5.7	2.36	1.68	0.26
2H-4, 145–150	7.75	5.2	1.15	0.53	0.16
3H-1, 145–150	12.75	9.0	2.45	1.37	0.22
3H-4, 143–148	17.16	9.3	2.60	1.49	0.26
4H-2, 145–150	22.76	8.6	1.96	0.92	0.20
4H-5, 132–137	26.45	15.0	3.24	1.45	0.26
5H-1, 145–150	31.75	25.1	5.03	2.02	0.28
6H-2, 146–151	41.61	14.0	4.04	2.36	0.30
7H-2, 141–146	51.37	2.6	0.81	0.50	0.16
8H-2, 139–144	60.59	11.8	2.91	1.50	0.24
9H-2, 137–142	70.19	7.4	1.94	1.05	0.24
12H-1, 145–150	98.25	14.1	3.14	1.45	0.25
15H-2, 140–145	127.14	5.4	1.27	0.62	0.18
18H-2, 145–150	155.70	3.6	1.11	0.69	0.24
21H-2, 140–145	185.20	6.6	1.54	0.76	0.20
22H-4, 150–155	197.65	10.5	2.34	1.08	0.26
24H-1, 140–145	212.20	2.9	0.87	0.52	0.19
28H-1, 123–128	239.33	9.4	1.80	0.67	0.25
34H-2, 121–126	267.90	8.8	2.33	1.28	0.31
41H-2, 86–91	300.71	16.2	3.36	1.42	0.29
47H-2, 95–100	328.70	4.0	1.14	0.66	0.24
52H-1, 140–145	352.30	5.3	1.50	0.86	0.27
60H-2, 121–126	391.08	16.4	3.54	1.57	0.27
66H-1, 108–113	417.78	13.8	3.24	1.59	0.29
72H-2, 125–130	446.50	8.2	2.38	1.39	0.29
79H-1, 140–145	478.90	9.9	1.86	0.68	0.25
85X-2, 138–143	521.56	9.7	2.21	1.05	0.29
87X-1, 140–145	540.30	8.8	2.21	1.15	0.28

Table T12. Interstitial water chemistry, Site U1427. This table is available in an **oversized format.**

Table T13. Headspace (HS) gas concentrations, Site U1427. (Continued on next page.)

Core, section, interval (cm)	Top depth CSF-A (m)	Sample type	Sediment volume (cm^3)	CH_4 (ppmv) NGA-FID measured	Ethane (ppmv) NGA-FID measured	CH_4 (ppmv) NGA-FID normalized	Ethane (ppmv) NGA-FID normalized	C_1/C_2 NGA-FID	Propane + propene (ppmv) NGA-FID	Propane + propene (ppmv) NGA-FID normalized	*iso*-butane (ppmv) NGA-FID	*n*-butane (ppmv) NGA-FID	*iso*-pentane (ppmv) NGA-FID
346-U1427A-													
1H-2, 65–70	1.56	HS	3.0	8.32	0.00	13.87	0.00		0.00	0.00	0.00	0.00	0.00
2H-2, 0–5	3.30	HS	3.0	28.26	0.00	47.10	0.00		0.00	0.00	0.00	0.00	0.00
3H-2, 0–5	12.80	HS	3.0	26,690.76	0.00	44,484.60	0.00		0.00	0.00	0.00	0.00	0.00
4H-3, 0–5	22.81	HS	3.0	16,351.61	1.79	27,252.68	2.98	9,134.98	0.00	0.00	0.00	0.00	0.00
5H-2, 0–5	31.80	HS	2.5	1,964.79	2.52	3,929.58	5.04	779.68	0.00	0.00	0.00	0.00	0.00
6H-3, 0–5	41.66	HS	3.0	3,932.13	3.55	6,553.55	5.92	1,107.64	0.00	0.00	0.00	0.00	0.00
7H-3, 0–5	51.47	HS	3.0	3,189.52	2.00	5,315.87	3.33	1,594.76	0.00	0.00	0.00	0.00	0.00
8H-3, 0–5	60.64	HS	3.0	1,190.80	0.00	1,984.67	0.00		0.00	0.00	0.00	0.00	0.00
9H-3, 0–5	70.24	HS	3.0	5,400.87	3.85	9,001.45	6.42	1,402.82	0.00	0.00	0.00	0.00	0.00
10H-3, 0–5	79.81	HS	2.6	1,194.32	0.00	2,296.77	0.00		0.00	0.00	0.00	0.00	0.00
11H-2, 0–5	88.78	HS	3.4	3,199.23	2.33	4,704.75	3.43	1,373.06	0.00	0.00	0.00	0.00	0.00
12H-2, 0–5	98.30	HS	4.0	3,427.89	2.81	4,284.86	3.51	1,219.89	0.00	0.00	0.00	0.00	0.00
13H-2, 0–5	107.81	HS	4.0	1,311.21	0.00	1,639.01	0.00		0.00	0.00	0.00	0.00	0.00
14H-2, 0–5	117.26	HS	3.6	7,681.57	0.00	10,668.85	0.00		0.00	0.00	0.00	0.00	0.00
15H-3, 0–5	127.19	HS	4.0	1,683.55	0.00	2,104.44	0.00		0.00	0.00	0.00	0.00	0.00
16H-2, 0–5	135.16	HS	3.6	2,003.04	0.00	2,782.00	0.00		0.00	0.00	0.00	0.00	0.00
17H-3, 0–5	145.62	HS	3.6	4,410.96	3.26	6,126.33	4.53	1,353.06	0.00	0.00	0.00	0.00	0.00
18H-3, 0–5	155.75	HS	3.0	822.34	0.00	1,370.57	0.00		0.00	0.00	0.00	0.00	0.00
19H-2, 0–5	164.81	HS	4.0	1,293.93	0.00	1,617.41	0.00		0.00	0.00	0.00	0.00	0.00
20H-2, 0–5	174.22	HS	3.4	1,633.13	0.00	2,401.66	0.00		0.00	0.00	0.00	0.00	0.00
21H-3, 0–5	185.30	HS	3.6	1,000.25	0.00	1,389.24	0.00		0.00	0.00	0.00	0.00	0.00
22H-2, 0–5	193.20	HS	3.6	1,150.79	0.00	1,598.32	0.00		0.00	0.00	0.00	0.00	0.00
23H-2, 0–5	202.81	HS	3.6	1,244.04	0.00	1,727.83	0.00		0.00	0.00	0.00	0.00	0.00
24H-2, 0–5	212.30	HS	3.6	868.03	0.00	1,205.60	0.00		0.00	0.00	0.00	0.00	0.00
25H-3, 0–5	222.36	HS	3.6	575.28	0.00	799.00	0.00		0.00	0.00	0.00	0.00	0.00
26H-3, 0–5	230.46	HS	3.4	987.16	0.00	1,451.71	0.00		0.00	0.00	0.00	0.00	0.00
27H-3, 0–5	234.86	HS	3.0	586.39	0.00	977.32	0.00		0.00	0.00	0.00	0.00	0.00
28H-2, 0–5	239.46	HS	3.2	511.87	0.00	799.80	0.00		0.00	0.00	0.00	0.00	0.00
29H-2, 0–5	244.05	HS	3.0	1,328.63	0.00	2,214.38	0.00		0.00	0.00	0.00	0.00	0.00
30H-2, 0–5	248.73	HS	3.6	1,452.85	1.42	2,017.85	1.97	1,023.13	0.00	0.00	0.00	0.00	0.00
31H-2, 0–5	252.58	HS	3.8	1,375.13	0.00	1,809.38	0.00		0.00	0.00	0.00	0.00	0.57
32H-3, 0–5	258.62	HS	4.0	696.24	0.00	870.30	0.00		0.00	0.00	0.00	0.00	0.00
33H-3, 0–5	263.26	HS	3.6	2,026.48	1.69	2,814.56	2.35	1,199.10	0.00	0.00	0.00	0.00	1.05
34H-3, 0–5	268.00	HS	2.0	827.03	0.00	2,067.58	0.00		0.00	0.00	0.00	0.00	0.00
35H-2, 0–5	272.50	HS	3.0	797.19	0.00	1,328.65	0.00		0.00	0.00	0.00	0.00	0.85
36H-2, 0–5	277.17	HS	2.0	250.55	0.00	626.38	0.00		0.00	0.00	0.00	0.00	0.00
37H-3, 0–5	282.14	HS	3.0	930.51	0.00	1,550.85	0.00		0.00	0.00	0.00	0.00	0.00
38H-3, 0–5	286.79	HS	3.0	516.68	0.00	861.13	0.00		0.00	0.00	0.00	0.00	0.00
39H-3, 0–5	291.71	HS	3.2	740.22	0.00	1,156.59	0.00		0.00	0.00	0.00	0.00	0.00
40H-2, 0–5	295.66	HS	3.0	964.68	0.00	1,607.80	0.00		0.00	0.00	0.00	0.00	0.68
41H-3, 0–5	300.81	HS	3.0	803.94	0.00	1,339.90	0.00		0.00	0.00	0.00	0.00	0.00
42H-3, 0–5	305.50	HS	3.5	945.74	0.00	1,351.06	0.00		0.00	0.00	0.00	0.00	0.00
43H-2, 0–5	309.85	HS	2.5	846.13	0.00	1,692.26	0.00		0.00	0.00	0.00	0.00	0.00
44H-3, 0–5	314.83	HS	3.0	671.33	0.00	1,118.88	0.00		0.00	0.00	0.00	0.00	0.00
45H-2, 0–5	319.41	HS	3.0	616.84	0.00	1,028.07	0.00		0.00	0.00	0.00	0.00	0.00
46H-3, 0–5	324.48	HS	3.0	642.62	0.00	1,071.03	0.00		0.00	0.00	0.00	0.00	0.00
47H-3, 0–5	328.80	HS	3.0	473.99	0.00	789.98	0.00		0.00	0.00	0.00	0.00	0.00

Table T13 (continued).

Core, section, interval (cm)	Top depth CSF-A (m)	Sample type	Sediment volume (cm^3)	CH_4 (ppmv) NGA-FID measured	Ethane (ppmv) NGA-FID measured	CH_4 (ppmv) NGA-FID normalized	Ethane (ppmv) NGA-FID normalized	C_1/C_2 NGA-FID	Propane + propene (ppmv) NGA-FID	Propane + propene (ppmv) NGA-FID normalized	*iso*-butane (ppmv) NGA-FID	*n*-butane (ppmv) NGA-FID	*iso*-pentane (ppmv) NGA-FID
48H-3, 0–5	333.86	HS	3.8	928.59	0.00	1,221.83	0.00		0.00	0.00	0.00	0.00	0.00
49H-3, 0–5	338.81	HS	3.0	963.19	1.39	1,605.32	2.32	692.94	0.00	0.00	0.00	0.00	0.00
50H-3, 0–5	343.84	HS	3.0	587.61	0.00	979.35	0.00		0.00	0.00	0.00	0.00	0.00
51H-3, 0–5	348.33	HS	3.0	789.25	0.00	1,315.42	0.00		0.00	0.00	0.00	0.00	0.00
52H-2, 0–5	352.40	HS	3.3	408.25	0.00	618.56	0.00		0.00	0.00	0.00	0.00	0.00
53H-3, 0–5	357.76	HS	3.0	1,083.26	1.80	1,805.43	3.00	601.81	2.41	4.02	0.00	0.00	1.37
54H-3, 0–5	362.49	HS	3.0	443.84	0.00	739.73	0.00		0.00	0.00	0.00	0.00	0.00
55H-3, 0–5	367.08	HS	3.0	382.46	0.00	637.43	0.00		0.00	0.00	0.00	0.00	0.00
57H-3, 0–5	376.48	HS	3.0	743.72	0.00	1,239.53	0.00		0.00	0.00	0.00	0.00	0.58
59H-2, 0–5	385.09	HS	3.0	824.12	0.00	1,373.53	0.00		0.00	0.00	0.00	0.00	0.00
61H-2, 0–5	394.70	HS	3.0	635.14	0.00	1,058.57	0.00		1.84	3.07	0.00	0.00	0.00
63H-3, 0–5	404.25	HS	3.4	1,509.12	2.50	2,219.29	3.68	603.65	3.00	4.41	0.00	0.00	0.66
65H-2, 0–5	413.45	HS	3.4	541.83	1.64	796.81	2.41	330.38	2.53	3.72	0.00	0.00	0.00
67H-3, 0–5	423.20	HS	3.0	949.69	2.00	1,582.82	3.33	474.85	3.53	5.88	0.78	0.00	1.30
69H-2, 0–5	432.20	HS	3.0	707.80	1.70	1,179.67	2.83	416.35	3.45	5.75	0.81	0.00	1.26
71H-3, 0–5	441.91	HS	3.0	298.13	0.00	496.88	0.00		0.00	0.00	0.00	0.00	0.00
73H-2, 0–5	451.01	HS	3.6	391.52	0.00	543.78	0.00		2.69	3.74	0.00	0.00	0.71
75H-3, 0–5	461.26	HS	2.8	669.09	1.50	1,194.80	2.68	446.06	2.18	3.89	0.00	0.00	1.32
76H-3, 0–5	465.92	HS	3.0	484.01	0.00	806.68	0.00		0.00	0.00	0.00	0.00	0.00
77H-2, 0–5	469.76	HS	4.1	1,221.98	3.04	1,490.22	3.71	401.97	3.94	4.80	1.03	0.00	2.25
79H-2, 0–5	479.00	HS	3.4	2,234.86	4.36	3,286.56	6.41	512.58	2.88	4.24	0.00	0.00	0.66
81H-2, 0–5	488.00	HS	3.0	1,086.79	2.67	1,811.32	4.45	407.04	2.71	4.52	0.00	0.00	0.61
82X-1, 111–116	491.51	HS	3.6	910.87	4.13	1,265.10	5.74	220.55	7.38	10.25	1.51	0.00	1.27
84X-2, 0–5	511.10	HS	4.2	441.12	0.00	525.14	0.00		4.30	5.12	1.24	0.00	0.98
85X-3, 0–5	521.66	HS	4.5	523.64	2.71	581.82	3.01	193.23	7.38	8.20	1.48	0.00	1.08
86X-2, 0–5	530.70	HS	3.5	766.95	3.09	1,095.64	4.41	248.20	9.15	13.07	1.79	0.92	1.34
87X-2, 0–5	540.40	HS	3.0	1,396.56	5.54	2,327.60	9.23	252.09	14.23	23.72	2.37	1.29	1.76
346-U1427C-													
1H-1, 145–150	1.45	HS	4.0	8.79	0.00	10.99	0.00		0.00	0.00	0.00	0.00	0.00
1H-2, 145–150	2.95	HS	4.0	22.12	0.00	27.65	0.00		0.00	0.00	0.00	0.00	0.00
1H-3, 145–150	4.45	HS	4.0	175.66	0.00	219.58	0.00		0.00	0.00	0.00	0.00	0.00
1H-4, 145–150	5.95	HS	4.0	6,113.45	3.82	7,641.81	4.78	1,600.38	0.00	0.00	0.00	0.00	0.00
1H-5, 121–126	7.21	HS	4.0	11,068.09	0.00	13,835.11	0.00		0.00	0.00	0.00	0.00	0.00
2H-1, 146–151	9.46	HS	4.0	20,920.00	0.00	26,150.00	0.00		0.00	0.00	0.00	0.00	0.00
2H-2, 147–152	10.98	HS	4.0	15,306.55	0.00	19,133.19	0.00		0.00	0.00	0.00	0.00	0.00
2H-3, 146–151	12.49	HS	4.0	14,756.02	0.00	18,445.03	0.00		0.00	0.00	0.00	0.00	0.00
2H-4, 148–153	14.02	HS	4.0	12,607.00	0.00	15,758.75	0.00		0.00	0.00	0.00	0.00	0.00
2H-5, 148–153	15.55	HS	4.0	17,763.66	0.00	22,204.58	0.00		0.00	0.00	0.00	0.00	0.00
2H-6, 147–152	17.07	HS	4.0	9,589.07	5.67	11,986.34	7.09	1,691.19	0.00	0.00	0.00	0.00	0.00
2H-7, 72–77	17.84	HS	4.0	7,824.71	0.00	9,780.89	0.00		0.00	0.00	0.00	0.00	0.00

NGA = natural gas analyzer (C_1–C_7), FID = flame ionization detector.

Table T14. Color measurements (absorbance) of interstitial waters, Site U1427.

Core, section, interval (cm)	Top depth CSF-A (m)	Sample	Alkalinity (mM)	Absorbance 375 nm		Absorbance 325 nm		Absorbance 277 nm	
				B1	B2/3	B1	B2/3	B1	B2/3
346-U1427A-									
1H-1, 0	0.00	ML	2.45		0.003		0.004		0.122
1H-2, 65–70	1.56	IW-Sq	15.92	0.076	0.078	0.184	0.183	2.455	2.542
2H-1, 145–150	3.25	IW-Sq	34.16	0.191	0.106	0.423	0.521	3.878	10.530
2H-4, 145–150	7.75	IW-Sq	56.73		0.198		0.541		4.125
3H-1, 145–150	12.75	IW-Sq	70.90		0.383		0.883		5.050
3H-4, 143–148	17.16	IW-Sq	80.74	0.276	0.271	0.773	0.927	4.201	6.897
4H-2, 145–150	22.76	IW-Sq	91.99		0.303		0.882		6.289
4H-5, 132–137	26.45	IW-Sq	99.54	0.330	0.317	0.955	0.927	4.192	6.897
5H-1, 145–150	31.75	IW-Sq	101.95		0.354		1.047		7.549
6H-2, 146–151	41.61	IW-Sq	112.53		0.302		0.914		7.448
7H-2, 141–146	51.37	IW-Sq	112.09						
8H-2, 139–144	60.59	IW-Sq	116.50		0.344		1.040		8.771
9H-2, 137–142	70.19	IW-Sq	121.17		0.363		1.144		9.299
12H-1, 145–150	98.25	IW-Sq	114.48	0.450		1.234		4.334	
15H-2, 140–145	127.14	IW-Sq	117.07		0.329		1.052		9.863
18H-2, 145–150	155.70	IW-Sq	118.49		0.429		1.162		10.121
21H-2, 140–145	185.20	IW-Sq	123.30						
22H-4, 150–155	197.65	IW-Sq	125.05		0.288		0.993		10.072
24H-1, 140–145	212.20	IW-Sq	127.16		0.263		0.938		9.890
28H-1, 123–128	239.33	IW-Sq	129.47	0.294	0.301	1.057	1.066	4.214	10.575
34H-2, 121–126	267.90	IW-Sq	127.66	0.303		1.124		4.207	
41H-2, 86–91	300.71	IW-Sq	130.87	0.260	0.256	0.965	0.960	4.233	10.460
47H-2, 95–100	328.70	IW-Sq	132.17		0.238		0.910		10.389
52H-1, 140–145	352.30	IW-Sq	132.27		0.245		0.963		10.600
60H-2, 121–126	391.08	IW-Sq	112.82		0.180		0.726		9.964
60H-2, 121–126	391.08	IW-Sq	109.18						
66H-1, 108–113	417.78	IW-Sq			0.187		0.812		10.496
72H-2, 125–130	446.50	IW-Sq	97.37		0.167		0.746		10.306
79H-1, 140–145	478.90	IW-Sq	91.88	0.132	0.125	0.618	0.616	4.141	10.046
85X-2, 138–143	521.56	IW-Sq	71.40		0.126		0.574		10.029
87X-1, 140–145	540.30	IW-Sq	79.14						
346-U1427B-									
1H-1, 0	0.00	IW-Rh	2.43						
1H-1, 10–11	0.10	IW-Rh	3.42		0.032		0.067		0.275
1H-1, 30–31	0.30	IW-Rh	4.38		0.018		0.034		0.251
1H-1, 50–51	0.50	IW-Rh	6.01						
1H-1, 80–81	0.80	IW-Rh	8.50		0.032		0.074		0.754
1H-1, 120–121	1.20	IW-Rh	11.79		0.044		0.116		1.254
1H-2, 30–31	1.80	IW-Rh	17.34		0.072		0.189		2.638
1H-2, 80–81	2.30	IW-Rh	21.34						
1H-2, 120–121	2.70	IW-Rh	25.80		0.119		0.280		4.433
1H-3, 30–31	3.30	IW-Rh	32.05		0.130		0.338		5.394
1H-3, 80–81	3.80	IW-Rh	36.45		0.140		0.377		6.798
1H-4, 30–31	4.30	IW-Rh	41.30		0.158		0.422		7.059
2H-1, 30–31	5.10	IW-Rh	47.59		0.167		0.455		7.487
2H-1, 80–81	5.60	IW-Rh	48.34						
2H-1, 120–121	6.00	IW-Rh	49.10						
2H-2, 30–31	6.60	IW-Rh	52.71						
2H-2, 80–81	7.10	IW-Rh	54.47		0.167		0.498		6.479
2H-2, 120–121	7.50	IW-Rh	55.38		0.185		0.524		6.155
2H-3, 40–41	8.20	IW-Rh	57.32		0.197		0.551		5.815
2H-3, 100–101	8.80	IW-Rh	59.27		0.192		0.560		5.447

ML = mudline, IW-Sq = interstitial water from whole-round squeezing, IW-Rh = interstitial water from Rhizons. Samples were examined in three batches over 14 days after drilling to evaluate precision in absorbance measurements with regard to time and dilution. Batch 1 comprises undiluted samples examined 3–4 days after recovery. Batches 2 and 3 are samples diluted 2:1 with deionized water and examined 11–14 days after recovery. Measured absorbance values for Batches 2 and 3 (combined) have been multiplied by 3. However, there is a problem with such treatment concerning measurements at 277 nm. The scaling of absorbance measurements for interstitial water samples at Site U1427 is nonlinear at this wavelength, perhaps because undiluted samples have a strong golden color.

Table T15. Vacutainer (VAC) gas concentrations, Site U1427.

Hole, core, section, interval (cm)	Top depth CSF-A (m)	Sample type	Methane (ppmv) GC3	Ethane (ppmv) GC3	Propene (ppmv) GC3	Propane (ppmv) GC3
346-U1427A-						
8H-4, 85–86	62.83	VAC	898,090.2	79.28	0	0
9H-5, 9–10	72.94	VAC	906,277.21	79.41	0	0
10H-4, 5–6	81.13	VAC	871,317.38	75.08	5.69	6.21
12H-4, 16–17	101.2	VAC	881,335.01	74.12	0	8.08
15H-5, 15–16	129.93	VAC	844,419.77	57.26	0	12.29
21H-2, 130–131	185.1	VAC	850,044.09	47.53	0	16.92

Table T16. FlexIT tool core orientation data, Hole U1427A.

Core	Orientation angle (°)	Orientation standard (°)
346-U1427A-		
2H	175.779	0.585
3H	9.001	0.751
4H	7.346	0.210
5H	324.140	0.478
6H	330.550	0.373
7H	49.604	0.414
8H	263.164	0.223
9H	273.729	0.863
10H	326.908	0.373
11H	211.051	0.806
12H	127.230	0.237
13H	64.160	0.453
14H	309.144	1.820
15H	277.678	0.934
16H	106.511	0.672
17H	213.591	0.592
18H	109.161	0.549
19H	78.473	1.968
20H	111.198	0.312
21H	102.533	0.779
22H	271.274	0.539
23H	207.136	0.240
24H	47.355	1.445
25H	281.913	1.052

Table T17. Core disturbance intervals, Site U1427. (Continued on next six pages.)

Core, section, interval (cm)	Comments on disturbance	Drilling disturbance intensity
346-U1427A-		
1H-1, 0–140	Soupy	
2H-2, 35–85	Mixed	
2H-6, 19–20	Gas expansion	
2H-6, 65–71	Gas expansion	
2H-6, 92–115	Gas expansion	
2H-7, 0–31	Ash and mixed sediments	
2H-CC, 0–20		Slight
3H-3, 54–55	Crack	
3H-3, 69–70	Gas expansion	
3H-3, 90–120	Gas expansion	
3H-3, 128–141	Gas expansion	
3H-4, 49–50	Crack	
3H-4, 125–128	Gas expansion	
3H-5, 40–51	Gas expansion	
3H-5, 80–85	Gas expansion	
3H-6, 100–112	Gas expansion	
3H-6, 119–121	Crack	
3H-6, 125–126	Crack	
3H-6, 135–150	Gas expansion	
4H-1, 0–10	Disturbed	Slight
4H-1, 22–31	Disturbed	
4H-1, 39–45	Disturbed	
4H-5, 74–76	Crack	
4H-6, 32–35	Crack	
4H-6, 69–71	Crack	
4H-6, 115–116	Crack	
4H-7, 0–35	Crack	
4H-7, 65–95	Crack	
4H-7, 105–107	Crack	
4H-CC, 0–32		Slight
5H-2, 0–33	Gas expansion	
5H-4, 60–61	Crack	
5H-6, 20–32	Crack	
5H-6, 65–80	Gas expansion	
5H-CC, 0–19		Slight
6H-1, 0–35		Slight to moderate
6H-2, 0–12	Disturbed	Slight
6H-2, 72–75	Void	
6H-5, 120–150	Nodule and gas expansion	Moderate to high
6H-6, 25–43	Gas expansion	
6H-6, 115–150	Gas expansion	
7H-1, 0–66	Gas expansion	Slight
7H-2, 55–61	Gas expansion	
7H-2, 75–79	Void	
7H-5, 28–31	Crack	
7H-7, 55–56	Crack	
7H-7, 105–106	Crack	
7H-8, 0–15	Gas expansion	
7H-8, 50–74	Gas expansion	Slight
8H-1, 0–40	Gas expansion and disturbed	Moderate
8H-2, 44–45	Crack	
8H-3, 43–60	Gas expansion	
8H-5, 24–27	Void	
8H-5, 80–110	Gas expansion	Slight
8H-6, 37–45	Gas expansion	Slight
8H-6, 115–145	Gas expansion	
8H-7, 0–15	Gas expansion	
8H-7, 95–101	Void	
8H-7, 135–149	Gas expansion	
8H-CC, 0–8	Gas expansion	Moderate
8H-CC, 8–32		Slight
9H-1, 0–52	Gas expansion	Moderate
9H-4, 60–67	Gas expansion	
9H-4, 80–87	Gas expansion	
9H-4, 0–136	Gas expansion	Moderate
9H-4, 120–124	Gas expansion	
9H-6, 20–22	Crack	
9H-6, 43–46	Crack	
9H-6, 55–58	Crack	
9H-6, 75–82	Crack	
9H-7, 9–10	Crack	
9H-8, 14–15	Crack	
9H-8, 40–43	Crack	
10H-1, 0–20	Gas expansion	High
10H-1, 30–51	Gas expansion	
10H-2, 0–27	Gas expansion	Moderate
10H-2, 70–71	Crack	
10H-3, 34–37	Void	
10H-3, 75–93	Gas expansion	
10H-4, 85–86	Crack	
10H-5, 104–108	Void	
10H-7, 49–51	Crack	
10H-7, 68–71	Crack	
10H-7, 100–116	Void	
11H-1, 0–20	Gas expansion	Slight
11H-3, 57–70	Gas expansion	Slight
11H-3, 75–95	Ash and mixed sediments	Slight
11H-4, 110–121	Gas expansion	
11H-5, 111–115	Gas expansion	
11H-6, 44–47	Void	
11H-7, 9–15	Gas expansion	
12H-1, 0–10	Gas expansion	Moderate
12H-2, 59–63	Void	
12H-3, 61–71	Void	
12H-4, 23–63	Gas expansion and void	
12H-7, 22–37	Void	
13H-1, 137–151	Gas expansion	Moderate
13H-2, 67–73.5	Void	
13H-3, 15–29	Gas expansion	Moderate
13H-4, 41–44	Void	
13H-6, 87–92	Void	
14H-1, 0–44	Disturbed	
14H-2, 0–10	Ash and mixed sediments	
14H-2, 44–45	Crack	
14H-2, 110–115	Crack	
14H-3, 10–13	Crack	
14H-3, 143–150	Void	
14H-4, 122–136	Void	
14H-5, 80–102	Gas expansion	
14H-6, 10–30	Gas expansion	
14H-6, 45–53	Gas expansion	
14H-6, 75–80	Gas expansion	
15H-1, 15–22	Gas expansion	Moderate
15H-1, 28–43	Gas expansion	
15H-3, 59–65	Void	
15H-3, 65–75	Gas expansion	
15H-6, 14–16	Crack	
15H-6, 35–65	Crack	
15H-7, 90–150	Gas expansion	
15H-8, 68–77	Void	
16H-1, 0–15	Gas expansion	
16H-4, 117–124	Void	
16H-5, 105–130	Gas expansion	
16H-5, 130–151	Void	
16H-6, 60–85	Gas expansions	
16H-7, 147–150	Void	
16H-8, 92–106	Void	
17H-1, 9–15	Gas expansion	
17H-2, 75–80	Gas expansion	
17H-3, 145–150	Void	
17H-4, 40–45	Gas expansion	
17H-4, 62–71	Gas expansion	
17H-5, 40–43	Gas expansion	
17H-6, 130–150	Gas expansion	
18H-2, 75–87	Gas expansion	
18H-2, 87–97	Void	
18H-2, 140–150	Void	

Table T17 (continued). (Continued on next page.)

Core, section, interval (cm)	Comments on disturbance	Drilling disturbance intensity
18H-3, 0–12	Gas expansion	
18H-3, 40–47	Gas expansion	
18H-3, 50–60	Void	
18H-3, 60–73	Gas expansion	
18H-3, 108–113	Void	
18H-3, 125–127	Crack	
18H-4, 35–69	Gas expansion	
18H-4, 69–82	Void	
18H-4, 94–102	Gas expansion	
18H-8, 50–72	Less sediments	
19H-4, 147–150	Void	
19H-6, 131–137	Void	
20H-1, 0–3	Void	
20H-1, 72–77	Void	
20H-2, 70–72	Crack	
20H-3, 60–84	Gas expansion	Slight
20H-CC, 0–17		Slight to moderate
21H-2, 102–110	Gas expansion	
21H-2, 110–118	Void	
21H-4, 122–126	Ash and crack	
21H-7, 48–67		Slight
22H-1, 139–140	Void	
22H-3, 97–100	Void	
22H-3, 85–96	Gas expansion	
22H-5, 77–78	Crack	Slight
22H-6, 98–110	Gas expansion	
22H-CC, 0–31	Gas expansion	Moderate
23H-2, 0–5	Gas expansion	Slight
23H-3, 53–62	Pumice layer	
23H-6, 50–56	Gas expansion	
23H-6, 95–102	Gas expansion	
23H-7, 23–50	Mixed with ash	
24H-1, 95–117	Ash, mixed sediments, and gas expansion	
24H-2, 133–145	Gas expansion	
25H-1, 40–74	Gas expansion	Slight
25H-2, 83–90	Gas expansion	
25H-3, 83–120	Gas expansion	Slight
25H-4, 39–41	Crack	
25H-4, 57–63	Gas expansion	
25H-4, 105–106	Gas expansion	
25H-5, 110–117	Gas expansion	Moderate
25H-6, 15–141	Ash and washed out	Moderate
25H-7, 0–51	Washed out	Moderate
26H-1, 0–31	Gas expansion, extruded on rig floor	Slight
26H-1, 26–31	Void	
26H-2, 78–79	Crack	
26H-3, 49–84	Gas expansion	Slight
26H-3, 84–96	Void	
26H-5, 30–46	Gas expansion	
26H-CC, 0–30	Gas expansion	Slight
27H-1, 0–15	Gas expansion	Slight
27H-2, 0–95	Ash and mixed sediments	
27H-3, 48–132	Gas expansion	Slight
27H-3, 77–84	Void	
28H-1, 0–35	Mousselike	Slight
28H-2, 30–45	Fault	
28H-2, 100–125	Gas expansion	Slight
28H-2, 140–150	Gas expansion	
28H-CC, 0–31		Slight
29H-1, 0–29	Gas expansion	Slight
29H-CC, 0–30		Slight
30H-1, 0–27	Gas expansion	Slight
30H-CC, 0–14		Slight
31H-1, 0–38	Gas expansion and disturbed	Slight
31H-2, 60–65	Gas expansion	Moderate
31H-2, 76–78	Gas expansion	Moderate
31H-2, 90–95	Void	
31H-3, 45–60	Gas expansion	Slight
31H-3, 61–62	Void	
31H-4, 40–41	Gas expansion	Moderate
31H-4, 39–40	Crack	
31H-4, 95–105	Crack	
31H-CC, 0–20		Slight
32H-1, 0–37	Extruded on rig floor, disturbed	Slight to moderate
32H-2, 76–79	Void	
32H-2, 70–95	Gas expansion	
32H-3, 23–25	Gas expansion	Slight
32H-3, 78–79	Void	
32H-4, 80–85	Gas expansion	
32H-4, 79–84	Gas expansion	Slight
33H-1, 0–26	Extruded on rig floor, disturbed	
33H-2, 66–75	Void	
33H-3, 36.5–39	Void	
33H-4, 88–92	Crack	
33H-4, 99–104	Void	
34H-1, 23–37	Disturbed	
34H-2, 60–83	Void	
34H-2, 83–100	Gas expansion	
34H-3, 59–67	Void	
34H-3, 50–115	Gas expansion and tilted	
35H-1, 0–8	Gas expansion	Slight
35H-1, 13–17	Void	
36H-1, 0–147	Gas expansion	Moderate
36H-1, 62–117	Gas expansion	
36H-1, 62–68	Void	
36H-1, 109–115	Void	
36H-2, 25–100	Gas expansion	Moderate
36H-3, 52–56	Void	
36H-3, 69–75	Void	
36H-4, 17–42	Gas expansion	Moderate
36H-4, 30–34	Void	
37H-1, 0–20	Gas expansion, extruded on rig floor	High
37H-1, 60–83	Gas expansion, extruded on rig floor	
37H-2, 20–60	Gas expansion	
37H-3, 66–75	Void	
37H-4, 20–60	Gas expansion	
37H-5, 0–30	Gas expansion	
38H-1, 0–84	Gas expansion, extruded on rig floor	Moderate
38H-3, 93–108	Void	
38H-4, 53–59	Void	
38H-5, 54–58	Void	
39H-1, 8–11	Gas expansion	
39H-1, 23–25	Gas expansion	
39H-1, 37–42	Gas expansion	
39H-3, 43–91	Gas expansion	
39H-3, 52–56	Void	
39H-3, 69–75	Void	
39H-4, 58–70	Gas expansion	Moderate
39H-5, 20–60	Gas expansion	
40H-1, 0–30	Gas expansion	Moderate
40H-1, 83–91	Gas expansion	
40H-2, 30–35	Gas expansion	
40H-2, 61–65	Void	
40H-2, 75–85	Gas expansion	
41H-1, 0–65	Gas expansion, extruded on rig floor	
41H-2, 40–60	Gas expansion	
41H-2, 50–55	Void	
41H-2, 0–53	Gas expansion	
41H-4, 100–125	Gas expansion	
41H-4, 108–111	Void	
41H-5, 56–62	Void	
42H-1, 0–66	Gas expansion, extruded on rig floor	Moderate
42H-2, 40–80	Gas expansion	

Table T17 (continued). (Continued on next page.)

Core, section, interval (cm)	Comments on disturbance	Drilling disturbance intensity
42H-2, 65–69	Void	
42H-3, 26–55	Gas expansion	Moderate
42H-3, 90–130	Gas expansion	
43H-3, 0–22	Gas expansion	
43H-4, 28–37	Void	
44H-1, 0–60	Gas expansion, extruded on rig floor	High
44H-3, 0–99	Gas expansion	Moderate
44H-4, 0–20	Gas expansion	
44H-4, 105–112	Void	
44H-5, 23–30	Void and gas expansion	
45H-2, 45–95	Void and gas expansion	
46H-1, 0–42	Gas expansion, extruded on rig floor	Moderate
46H-2, 86–105	Void	
46H-3, 38–42	Gas expansion	
46H-5, 22–31	Disturbed	
46H-5, 50–57	Disturbed	
47H-1, 0–35	Gas expansion, extruded on rig floor	Moderate
47H-2, 60–70	Gas expansion	
48H-1, 0–15	Gas expansion, extruded on rig floor	Moderate
48H-1, 30–55	Gas expansion	
48H-2, 30–73	Void and gas expansion	
48H-2, 85–95	Gas expansion	
48H-3, 59–65	Void	
48H-5, 35–36	Crack	
49H-1, 0–81	Gas expansion, extruded on rig floor	Moderate
49H-2, 63–80	Void and gas expansion	
49H-3, 103–115	Gas expansion	
49H-5, 15–16	Crack	
50H-1, 0–59	Gas expansion, extruded on rig floor	Moderate
50H-1, 82–112	Void	
50H-3, 60–67	Void	
51H-1, 0–35	Gas expansion	
51H-1, 55–93	Gas expansion	Moderate to high
51H-2, 43–93	Gas expansion	High
51H-2, 107–120	Void	
51H-3, 24–42	Gas expansion	High
51H-3, 42–46	Void	
51H-3, 46–53	Gas expansion	
51H-3, 85–104	Gas expansion	Moderate
51H-3, 104–112	Void	
51H-3, 112–125	Gas expansion	Moderate
52H-1, 94–108	Void and gas expansion	
52H-2, 112–113	Crack	
52H-CC, 0–24		Slight
53H-1, 0–9	Gas expansion	Moderate
53H-1, 40–71	Gas expansion	
53H-1, 71–76	Void	
53H-2, 45–61	Void	
53H-2, 61–90	Gas expansion	Moderate to high
53H-3, 46–54	Void	
53H-3, 54–72	Gas expansion	Moderate to high
53H-4, 44–45	Crack	Slight
53H-CC, 0–18	Gas expansion	Moderate to high
54H-1, 0–10	Gas expansion, extruded on rig floor	Moderate to high
54H-1, 55–85	Gas expansion	
54H-2, 55–74	Gas expansion	High
54H-2, 86–108	Void	
54H-3, 43–46	Void	
54H-3, 78–90	Gas expansion	Moderate
55H-1, 0–60	Gas expansion	Moderate
55H-2, 40–47	Gas expansion	
55H-2, 47–52	Void	
55H-2, 95–101	Gas expansion	Moderate
55H-2, 141–147	Void	
55H-3, 68–80	Void	
55H-5, 40–55	Gas expansion	
55H-5, 70–82	Void	
55H-CC, 0–24		Slight
56H-2, 85–101	Void	
56H-3, 50–63	Gas expansion	Moderate
56H-3, 80–85	Gas expansion	
56H-3, 93–128	Gas expansion	Moderate
56H-5, 30–34	Void	
56H-5, 34–45	Gas expansion	
56H-CC, 0–31		Slight to moderate
57H-1, 0–93	Gas expansion, extruded on rig floor	Slight
57H-2, 36–52	Gas expansion	Slight
57H-2, 52–65	Void	
57H-2, 65–94	Gas expansion	Slight
57H-3, 33–49	Gas expansion	Moderate to high
57H-3, 49–59	Void	
57H-3, 59–75	Gas expansion	High
57H-CC, 0–22		Slight
58H-1, 28–87	Gas expansion	Moderate
58H-2, 33–98	Gas expansion	High
58H-2, 98–120	Void	
58H-2, 120–123	Gas expansion	Slight
58H-3, 30–64	Gas expansion	Slight
58H-3, 64–75	Void	
58H-CC, 0–17		Slight
59H-1, 41–58	Gas expansion	Slight to moderate
59H-1, 40–60	Gas expansion	
59H-1, 58–72	Void	
59H-1, 72–91	Gas expansion	Moderate
59H-2, 48–52	Gas expansion	Slight
59H-2, 52–57	Void	
60H-1, 13–87	Gas expansion	High
60H-1, 87–91	Void	
60H-1, 91–132	Gas expansion	High
60H-1, 132–137	Void	
60H-2, 100–120	Disturbed	
60H-3, 29–62	Gas expansion	High
60H-3, 62–114	Gas expansion	Slight
60H-4, 36–60	Gas expansion	Slight to moderate
61H-2, 0–22	Gas expansion	Slight to moderate
61H-4, 67–71		Slight
61H-CC, 0–12		Slight to moderate
62H-1, 0–87	Gas expansion	Moderate to high
62H-1, 87–92	Void	
62H-2, 54–56	Crack	High
62H-4, 40–45	Gas expansion	Slight
62H-4, 45–49	Void	
62H-4, 49–54	Gas expansion	Slight
62H-5, 55–57	Crack	Slight
63H-1, 0–41	Gas expansion	Moderate to high
63H-1, 41–45	Void	
63H-2, 39–48	Gas expansion	Slight to moderate
63H-2, 48–73	Void	
63H-2, 73–76	Gas expansion	Slight to moderate
63H-3, 0–151	Gas expansion	Moderate
63H-3, 58–66	Void	
63H-5, 74–78	Gas expansion	
63H-CC, 0–21		Slight
64H-1, 0–76	Gas expansion	Slight to moderate
64H-2, 67–80	Gas expansion	Moderate
64H-2, 80–85	Void	
64H-2, 102–109	Void	
64H-2, 110–120	Gas expansion	Moderate
64H-3, 27–38	Gas expansion	Slight to moderate
64H-3, 100–112	Gas expansion	Slight to moderate
64H-5, 40–50	Gas expansion	Moderate to high
64H-CC, 0–24		Slight
65H-1, 66–74	Void	

Table T17 (continued). (Continued on next page.)

Core, section, interval (cm)	Comments on disturbance	Drilling disturbance intensity
65H-2, 50–56	Gas expansion	
65H-2, 57–65	Void	
65H-2, 66–76	Gas expansion	
65H-4, 69–72	Void	
65H-CC, 0–18		Moderate
66H-1, 35–39	Void	
66H-3, 34–36	Void	
66H-4, 54–60	Gas expansion	Slight
66H-CC, 30–37	Gas expansion	Slight to moderate
67H-2, 49–58	Gas expansion	
67H-2, 59–73	Void	
67H-2, 73–77	Void	
67H-3, 25–27	Void	
67H-3, 27–31	Gas expansion	
67H-3, 93–100	Void	
67H-4, 60–72	Gas expansion	
67H-4, 72–75	Void	
67H-4, 76–83	Gas expansion	
67H-5, 36–45	Gas expansion	
67H-5, 46–49	Gas expansion	
68H-3, 43–54	Void and gas expansion	
68H-4, 37–47	Void and gas expansion	
69H-1, 110–124	Void and gas expansion	
69H-2, 110–122	Gas expansion	
71H-1, 0–37	Gas expansion, extruded on rig floor	
71H-2, 69–111	Gas expansion	
71H-3, 78–82	Gas expansion	
71H-5, 15–25	Gas expansion	
72H-2, 56–74	Void	
72H-3, 20–31	Void and gas expansion	
72H-4, 93–101	Void and gas expansion	
73H-1, 76–86	Void	
73H-2, 97–101	Void	
73H-3, 70–73	Void	
73H-4, 21–42	Void and gas expansion	
74H-1, 0–25	Gas expansion, extruded on rig floor	
74H-1, 47–79	Gas expansion, extruded on rig floor	
74H-2, 38–78	Gas expansion	
74H-3, 36–46	Gas expansion	
74H-5, 62–65	Void	
75H-1, 0–94	Gas expansion, extruded on rig floor	Moderate
75H-2, 65–83	Void	
75H-3, 109–127	Gas expansion	
75H-4, 63–67	Void	
76H	Gas expansion	Moderate
76H-1, 0–70	Gas expansion, extruded on rig floor	Moderate
76H-2, 32–105	Gas expansion	
76H-2, 105–122	Void	
76H-3, 107–129	Gas expansion	
76H-4, 70–110	Void and gas expansion	
77H-1, 64–104	Void and gas expansion	
77H-2, 141–154	Disturbed	
78H-2, 135–150	Suck in?	
78H-3, 0–85	Suck in	
78H-4, 0–47	Suck in	
79H-3, 50–58	Void	
79H-3, 59–105	Gas expansion and soupy ash	
80H-1, 0–49	Gas expansion, extruded on rig floor	
80H-2, 40–77	Void and gas expansion	
80H-3, 49–136	Gas expansion	
80H-4, 90–94	Void	
81H-1, 129–136	Mixed sediments	
82X	Biscuit	High
83X	Biscuit	High
84X-1, 0–130	Inter-mud of biscuit	High
84X-2, 0–58	Inter-mud of biscuit	
85X-1, 0–68	Inter-mud of biscuit	
85X-2, 13–15	Inter-mud of biscuit	High
85X-2, 37–43	Inter-mud of biscuit	
85X-2, 100–106	Inter-mud of biscuit	
85X-3, 24–27	Inter-mud of biscuit	
85X-3, 36–44	Inter-mud of biscuit	
85X-3, 50–54	Inter-mud of biscuit	
85X-3, 98–150	Inter-mud of biscuit	
85X-4, 9–10	Inter-mud of biscuit	
85X-4, 20–40	Inter-mud of biscuit	
85X-5, 0–19	Inter-mud of biscuit	
85X-6, 0–89	Tilted and inter-mud biscuit	
85X-6, 0–57	Inter-mud of biscuit	
86X-1, 0–150	Biscuit	High
86X-2, 0–150	Biscuit	Severe
86X-3, 0–134	Biscuit	Severe
86X-4, 23–28	Inter-mud of biscuit	Severe
86X-4, 48–80	Inter-mud of biscuit	
86X-4, 94–133	Inter-mud of biscuit	
86X-CC, 0–31	Biscuit	Severe
87X-1, 0–150	Biscuit, too disturbed	High
87X-2, 0–146	Biscuit, too disturbed	
87X-3, 0–84	Biscuit, too disturbed	
87X-3, 97–134	Biscuit, too disturbed	
87X-3, 145–150	Biscuit, too disturbed	
87X-4, 35–63	Biscuit, too disturbed	
87X-4, 80–145	Biscuit, too disturbed	
87X-5, 0–100	Biscuit, too disturbed	
87X-6, 0–44	Gas expansion, extruded on rig floor	
87X-7, 0–113	Gas expansion, extruded on rig floor	
346-U1427B-		
1H-1, 0–10	Soupy	
1H-CC, 0–26		Slight
2H-6, 0–30	Gas expansion	
2H-CC, 0–17		Slight
3H-6, 73–76	Crack	
3H-6, 110–130	Gas expansion	Slight
3H-7, 0–81	Gas expansion	Slight
3H-CC, 0–30		Slight to moderate
4H-1, 65–140	Extruded on rig floor, disturbed, gas expansion	Slight
4H-5, 90–115	Gas expansion	
4H-6, 50–60	Gas expansion	Slight
4H-6, 90–120	Gas expansion	
4H-7, 0–40	Gas expansion	Slight
4H-CC, 0–28		Moderate
5H-1, 74–79	Gas expansion	Slight to moderate
5H-2, 133–145	Gas expansion	
5H-3, 95–105	Gas expansion	
5H-5, 50–110	Gas expansion	
5H-6, 59–66	Gas expansion	
5H-6, 87–127	Gas expansion	
5H-CC, 0–28		Slight
6H-1, 105–145	Gas expansion	
6H-4, 50–75	Gas expansion	
6H-5, 13–26	Gas expansion	
6H-5, 40–110	Gas expansion	
6H-6, 60–80	Gas expansion	
6H-6, 87–120	Gas expansion	
6H-4, 53–76		Slight
6H-5, 0–150	Gas expansion	Slight
6H-6, 59–147	Gas expansion	Slight to moderate
6H-CC, 0–39		Slight
8H-1, 0–28	Extruded on rig floor, disturbed	
8H-1, 10–12	Gas expansion	Slight
8H-1, 25–29	Gas expansion	Slight

Table T17 (continued). (Continued on next page.)

Core, section, interval (cm)	Comments on disturbance	Drilling disturbance intensity
8H-3, 0–30	Gas expansion	Slight
8H-6, 90–110	Gas expansion	
8H-6, 130–140	Gas expansion	
8H-7, 25–33	Disturbed	
8H-8, 20–22	Crack	
8H-CC, 0–33		Slight
9H-1	Extruded on rig floor, disturbed	Slight to moderate
9H-2, 0–3	Gas expansion	Slight
9H-5, 23–26	Gas expansion	Slight to moderate
9H-8, 25–62	Gas expansion	Slight
9H-8, 62–65	Void	
9H-8, 94–96	Void	
9H-CC, 0–32		Slight
10H-1, 0–60	Extruded on rig floor, disturbed gas expansion	Slight
10H-2, 70–130	Gas expansion	Slight
10H-5, 64–66	Crack	
10H-5, 81–86	Void	
10H-6, 110–135	Gas expansion	
10H-8, 10–15	Gas expansion	
10H-8, 38–45	Gas expansion	
10H-CC, 0–32		Moderate
11H-1, 0–70	Extruded on rig floor, disturbed	Slight
11H-1, 21–23	Void	
11H-4, 0–20	Gas expansion	
11H-7, 60–80	Gas expansion	
11H-8, 25–45	Gas expansion	
11H-CC, 0–44		Slight
12H-1, 0–72	Extruded on rig floor, disturbed	Slight to moderate
12H-3, 81–83	Void	
12H-8, 25–45	Gas expansion	
14H-1, 56–74	Gas expansion	Slight
14H-1, 74–82	Void	
14H-2, 68–125	Gas expansion	Slight
14H-4, 90–146	Gas expansion	Slight
14H-7, 34–41	Void	
14H-7, 41–48	Gas expansion	Slight to moderate
14H-CC, 0–44		Slight
15H-1, 0–74	Extruded on rig floor, disturbed	
15H-2, 0–136	Gas expansion	Slight to moderate
15H-3, 85–97	Gas expansion	Slight to moderate
15H-5, 65–72	Void	
15H-6, 36–46	Ash	
15H-7, 20–21	Crack	
16H-1, 0–59	Extruded on rig floor, disturbed	
16H-4, 75–95	Gas expansion	
16H-5, 40–72	Gas expansion and void	
17H-1, 81–110	Gas expansion	
17H-1, 98–106	Void	
17H-1, 132–150	Gas expansion	
17H-3, 68–82	Gas expansion	
17H-6, 100–150	Ash mixed	
18H-1, 0–58	Extruded on rig floor, disturbed, gas expansion	Slight to moderate
18H-3, 62–100	Gas expansion	
18H-4, 85–95	Gas expansion	
20H-1, 0–81	Extruded on rig floor, disturbed	
20H-1, 30–34	Extruded on rig floor, disturbed	
20H-1, 55–67	Gas expansion	
20H-2, 60–66	Gas expansion	
20H-2, 66–71	Void	
20H-3, 59–61	Gas expansion	
20H-3, 66–75	Void	
20H-3, 75–81	Gas expansion	
20H-6, 133–137	Ash	
20H-7, 45–52	Gas expansion	
20H-8, 20–35	Gas expansion	
21H-1, 0–20	Extruded on rig floor, disturbed, gas expansion	Slight to moderate
21H-3, 88–90	Void	
21H-7, 100–120	Gas expansion	
22H-1, 0–20	Gas expansion	Moderate
22H-2, 85–87	Void	
22H-7, 11.5–16	Void	
23H-1, 44–46	Crack	
23H-1, 60–76	Gas expansion	
23H-1, 90–150	Gas expansion	
23H-6, 24–33	Void	
23H-6, 33–65	Gas expansion	
24H-1, 0–67	Gas expansion	Moderate
24H-2, 46–62	Gas expansion	
24H-2, 88–96	Gas expansion	
24H-2, 97–105	Void	
24H-3, 67–71	Void	
24H-3, 70–80	Gas expansion	
24H-8, 0–15	sandy	
25H-2, 0–25		High
25H-3, 26–86		Moderate to high
25H-5, 115–120	Gas expansion	
26H-1, 0–110		Moderate to high
26H-2, 73–76	Gas expansion	
26H-4, 68–100	Gas expansion	Slight
26H-5, 62–72	Gas expansion and void	
26H-8, 25–73	Soupy ash	
27H-1, 116–125	Ash	
27H-4, 34–36	Crack	
27H-5, 0–40	Gas expansion	
27H-5, 40–50	Void	
28H-2, 0–149	Suck in	
28H-3, 0–130	Suck in	
29H-1, 0–35	Crack	High
29H-5, 29–55	Gas expansion	
29H-5, 75–86	Void	
30H-1, 85–102	Gas expansion	
30H-2, 0–12	Crack	
30H-4, 0–30	Disturbed	
31H-1, 0–27	Extruded on rig floor, gas expansion	Slight
31H-2, 53–67	Void	
31H-2, 67–110	Gas expansion	High
31H-3, 31–78	Gas expansion	High
31H-3, 78–88	Void	
31H-3, 88–106	Gas expansion	High
31H-4, 104–107	Void	
31H-CC, 0–24		Slight
32H-1, 0–15	Gas expansion	Slight
32H-1, 83–87	Void	
32H-1, 87–95	Gas expansion	
32H-1, 117–120	Void	
32H-4, 40–55	Gas expansion	
32H-4, 55–62	Void	
32H-CC, 0–27		Slight
33H-3, 0–17	Gas expansion	Slight
33H-CC, 0–57		Slight
34H-1, 0–89	Extruded on rig floor, disturbed, gas expansion	Slight to moderate
34H-2, 54–59	Gas expansion	
34H-3, 55–66	Void	
34H-3, 94–113	Gas expansion	Moderate
34H-4, 7–8	Crack	High
34H-4, 54–61	Void	
34H-5, 18–22	Crack	High
34H-5, 40–43	Gas expansion	Moderate
34H-5, 43–46	Void	
34H-CC, 0–39		Slight to moderate
35H-1, 88–105	Gas expansion	
35H-2, 0–15	Gas expansion	
35H-3, 20–46	Disturbed	
35H-3, 46–47	Void	
35H-3, 108–112	Void	

Table T17 (continued). (Continued on next page.)

Core, section, interval (cm)	Comments on disturbance	Drilling disturbance intensity
35H-4, 65–68	Void	
35H-CC, 0–31		Moderate
36H-1, 0–95	Gas expansion	Moderate
36H-3, 63.5–70	Void	
36H-3, 82–94	Gas expansion	Moderate to high
36H-3, 94–105	Void	
36H-4, 88–99	Void	
36H-CC, 0–32		Slight
37H-3, 115–150	Washed	High
37H-4, 0–18	Washed	High
37H-6, 33–44	Gas expansion and void	
37H-CC, 0–22		Slight
39H-1, 0–23	Gas expansion	Slight
39H-2, 40–60	Gas expansion and void	
39H-3, 32–35	Void	
39H-4, 75–78	Gas expansion	
39H-CC, 0–40		Slight
40H-4, 18–38	Gas expansion	Slight to moderate
40H-4, 38–47	Void	
40H-CC, 0–38		Slight to moderate
41H-1, 0–12	Extruded on rig floor, disturbed	
41H-2, 65–75	Gas expansion	Slight
41H-2, 75–85	Void	
41H-5, 36–37	Void	
41H-CC, 0–50		Slight
42H-1, 0–41	Extruded on rig floor, disturbed, gas expansion	Moderate
42H-2, 53–66	Gas expansion	Slight to moderate
42H-2, 66–89	Void	
42H-2, 89–138	Gas expansion	Slight to moderate
42H-3, 33–44	Gas expansion	Slight to moderate
42H-3, 44–50	Void	
42H-3, 50–58	Gas expansion	Slight
42H-3, 128–130	Void	
42H-4, 89–93	Void	
43H-1, 75–89	Gas expansion	Moderate to high
43H-1, 89–94	Void	
43H-1, 118–134	Gas expansion	High
43H-1, 134–137	Void	
43H-1, 137–151	Gas expansion	High
43H-2, 0–3	Void	
43H-2, 22–26	Crack	High
43H-2, 98–101	Crack	High
43H-3, 28–33	Gas expansion	Slight to moderate
43H-3, 110–120	Gas expansion	
43H-3, 120–147	Void	
43H-CC, 0–53		Slight to moderate
44H-1, 0–20	Gas expansion	
44H-1, 40–77	Extruded on rig floor, disturbed, gas expansion	Moderate
44H-3, 60–65	Gas expansion	
44H-3, 65–69	Void	
44H-3, 69–76	Gas expansion	Slight to moderate
44H-CC, 0–29		Slight
45H-1, 0–53	Extruded on rig floor, disturbed, gas expansion	High
45H-2, 70–81	Gas expansion	Moderate to high
45H-2, 94–101	Gas expansion	
45H-2, 114–116	Gas expansion	
45H-2, 133–148	Void	
45H-3, 48–51	Gas expansion	Moderate
45H-4, 20–22	Gas expansion	
45H-CC, 0–28		Slight
46H-1, 0–41	Extruded on rig floor, disturbed	
46H-2, 35–40	Gas expansion	
46H-2, 70–80	Gas expansion	
46H-2, 101–107	Void	
46H-3, 40–61	Gas expansion	
46H-3, 61–75	Void	
46H-3, 85–91	Gas expansion	
46H-3, 112–115	Void	
46H-4, 95–111	Gas expansion	
47H-1, 68–71	Gas expansion	
47H-1, 83–86	Gas expansion	
47H-1, 86–95	Void	
47H-1, 95–107	Gas expansion	
47H-3, 93–108	Gas expansion	
48H-1, 0–40	Soupy	
49H-1, 0–23	Extruded on rig floor	
49H-2, 52–56	Gas expansion	
49H-2, 56–64	Void	
49H-2, 96–101	Void	
50H-1, 0–55	Extruded on rig floor	
50H-2, 55–63	Gas expansion	
50H-1, 64–76	Void	
50H-1, 76–125	Gas expansion	
50H-5, 16–20	Gas expansion	
50H-5, 25–27	Gas expansion	
51H-1, 0–25	Gas expansion	
51H-1, 90–94	Gas expansion	
51H-1, 94–104	Void	
51H-1, 104–111	Gas expansion	
52H-1, 0–46	Extruded on rig floor	
52H-2, 94–102	Void	
52H-3, 70–112	Gas expansion and void	
52H-4, 67–73	Void	
52H-4, 73–90	Gas expansion	
54H-1, 0–51	Extruded on rig floor	
54H-1, 24–30	Void	
54H-2, 40–77	Gas expansion and void	
54H-2, 95–111	Gas expansion and void	
55H-1, 0–48	Extruded on rig floor	
55H-2, 50–100	Gas expansion and void	
55H-3, 42–68	Gas expansion and void	
56H-1, 0–61	Extruded on rig floor, gas expansion	Moderate
56H-2, 84–126	Gas expansion and void	
56H-3, 50–95	Gas expansion and void	
57H-1, 0–20	Extruded on rig floor	
57H-3, 60–85	Gas expansion and void	
57H-4, 24–40	Gas expansion and void	
58H-1, 45–79	Extruded on rig floor	
58H-2, 48–84	Gas expansion	
58H-2, 90–107	Void	
58H-2, 118–123	Gas expansion	
58H-3, 38–63	Gas expansion	
58H-3, 63–76	Void	
58H-3, 76–115	Gas expansion	
59H-1, 0–121	Extruded on rig floor, gas expansion	Moderate to high
59H-3, 30–47	Ash mixed	
59H-3, 74–77	Void	
60H-1, 0–45	Extruded on rig floor, disturbed	
60H-2, 45–90	Gas expansion	
60H-3, 60–72	Gas expansion	
61H-1, 0–12	Ash mixed?	
61H-1, 139–146	Void	
61H-2, 144–147	Void	
61H-3, 35–39	Void	
62H-2, 43–63	Gas expansion	
62H-2, 63–80	Void	
62H-2, 80–89	Void	
62H-3, 67–75	Void	
64H-1, 0–63	Extruded on rig floor, disturbed, gas expansion	Moderate
64H-2, 44–49	Void	
64H-2, 49–52	Gas expansion	Moderate
64H-3, 45–57	Gas expansion and void	
64H-3, 53–57	Gas expansion	Moderate

Table T17 (continued).

Core, section, interval (cm)	Comments on disturbance	Drilling disturbance intensity
64H-4, 140–142	Void	
64H-5, 23–39	Gas expansion	
64H-CC, 0–29		Slight
65H-1, 0–75	Extruded on rig floor, disturbed, gas expansion	Moderate
65H-2, 67–78	Gas expansion	Moderate
65H-3, 63–85	Gas expansion	Moderate to high
65H-3, 85–87	Void	
65H-3, 87–100	Gas expansion	Slight
65H-4, 24–54	Gas expansion	
65H-4, 54–57	Void	
65H-4, 57–83	Gas expansion	
65H-CC, 0–28		Slight

Table T18. NRM inclination, declination, and intensity data after 20 mT peak field AF demagnetization, Site U1427.

Core, section, interval (cm)	Depth CSF-A (m)	Inclination (°)	Declination (°)	FlexIT-corrected declination (°)	Intensity (A/m)
346-U1427A-					
1H-1	0				
1H-1, 5	0.05				
1H-1, 10	0.1				
1H-1, 15	0.15				
1H-1, 20	0.2				
1H-1, 25	0.25				
1H-1, 30	0.3				
1H-1, 35	0.35				
1H-1, 40	0.4				
1H-1, 45	0.45				
1H-1, 50	0.5				
1H-1, 55	0.55				
1H-1, 60	0.6				
1H-1, 65	0.65				
1H-1, 70	0.7				
1H-1, 75	0.75				
1H-1, 80	0.8				
1H-1, 85	0.85				
1H-1, 90	0.9				
1H-2, 0	0.91				
1H-2, 5	0.96				
1H-2, 10	1.01				
1H-2, 15	1.06	61.2	292.9		0.00467
1H-2, 20	1.11	61.7	294.7		0.00488
1H-2, 25	1.16	63.7	297.5		0.00487
1H-2, 30	1.21	65.1	297		0.00511
1H-2, 35	1.26	62.9	292.5		0.00545
1H-2, 40	1.31	62.2	297.6		0.00561
1H-2, 45	1.36	59.1	296.7		0.00587
1H-2, 50	1.41	62.4	295		0.00525
1H-2, 55	1.46	61.8	294.3		0.00489
1H-2, 60	1.51				
1H-2, 65	1.56				
1H-2, 70	1.61				
2H-1	1.8				
2H-1, 5	1.85				
2H-1, 10	1.9				
2H-1, 15	1.95	70.4	190.5	6.28	0.00874
2H-1, 20	2	69.1	178.6	354.38	0.00907
2H-1, 25	2.05	65.6	188.8	4.58	0.00934
2H-1, 30	2.1	64.2	200.6	16.38	0.00974
2H-1, 35	2.15	63.5	206.1	21.88	0.010215
2H-1, 40	2.2	62.6	198.6	14.38	0.010379
2H-1, 45	2.25	62.3	195.2	10.98	0.010207
2H-1, 50	2.3	63.5	193.2	8.98	0.00949
2H-1, 55	2.35	62.9	191	6.78	0.00951
2H-1, 60	2.4	61.6	194.3	10.08	0.0094
2H-1, 65	2.45	61.8	195.6	11.38	0.00907
2H-1, 70	2.5	61.5	193	8.78	0.0088
2H-1, 75	2.55	61.7	194.2	9.98	0.00837
2H-1, 80	2.6	63.5	196.5	12.28	0.00765
2H-1, 85	2.65	62.3	193.1	8.88	0.00736
2H-1, 90	2.7	60.9	194.3	10.08	0.00661
2H-1, 95	2.75	60.9	193.1	8.88	0.00596
2H-1, 100	2.8	63.2	190.9	6.68	0.00542
2H-1, 100	2.85	61.3	193.2	8.98	0.00543
2H-1, 100	2.9	60	190.9	6.68	0.00528

Blank cells indicate depth levels where data were either not available (i.e., FlexIT-corrected declination data for nonoriented cores) or removed because of disturbance, voids, or measurement edge effects. Only a portion of this table appears here. The complete table is available in **ASCII.**

Table T19. Polarity boundaries, Site U1427.

Core, section, interval (cm)		Polarity boundary	Age (Ma)	Depth CSF-A (m)				Depth CCSF-D (m)			
Top	Bottom			Top	Bottom	Midpoint	±	Top	Bottom	Midpoint	±
346-U1427A-39H-4, ~30	346-U1427A-40H-3, ~15	(B) C1n (Brunhes/Matuyama)	0.781	293.3	297.3	295.3	2.00	307.123	311.707	309.707	2.00
346-U1427B-4H-6, ~140	346-U1427B-5H-1, ~140	(B) C1n (Brunhes/Matuyama)	0.781	292.7	294.7	293.7	1.00	307.212	309.212	308.212	1.00

B = bottom.

Table T20. Results from APCT-3 temperature profiles, Site U1427.

Hole, core	Minimum temperature at mudline (°C)	Average temperature at mudline (°C)	Depth CSF-A (m)	In situ temperature (°C)	Thermal resistance (m^2K/W)
346-					
U1427C-3H	8.67	8.92	27.0	3.13	26.56
U1427A-4H	6.79	6.90	30.3	3.07	30.21
U1427C-5H	6.44	10.58	46.0	4.36	45.17
U1427A-7H	7.43	7.52	58.8	5.27	58.45
U1427A-10H	7.69	7.69	87.3	7.13	86.54
U1427A-13H	6.85	6.87	115.8	9.10	114.47
Average:	7.31	8.08			

In situ temperatures were determined using TP-Fit software by Martin Heesemann. Thermal resistance was calculated from thermal conductivity data (see **"Physical properties"**) corrected for in situ conditions (see **"Downhole measurements"** in the "Methods" chapter [Tada et al., 2015b]).

Table T21. Vertical offsets applied to cores in order to align a specific feature in adjacent cores, Site U1427. This table is available in an **oversized format.**

Table T22. Splice intervals, Site U1427. (Continued on next two pages.)

Hole, core, section	Depth in section (cm)	Depth CSF-A (m)	Depth CCSF-D (m)	Hole, core, section	Depth in section (cm)	Depth CSF-A (m)	Depth CCSF-D (m)
346-				346-			
U1427C-1H-1	0	0.00	0.00	U1427C-1H-5	115	7.15	7.15
U1427B-2H-2	106	7.32	7.15	U1427B-2H-5	149	12.29	12.13
U1427C-2H-3	55	11.58	12.13	U1427C-2H-6	23	15.83	16.38
U1427B-3H-1	122	15.52	16.38	U1427B-3H-5	27	20.52	21.38
U1427C-3H-3	327	20.69	21.38	U1427C-3H-6	133	26.25	26.95
U1427B-4H-2	128	26.48	26.95	U1427B-4H-5	80	30.48	30.95
U1427C-4H-3	50	29.31	30.95	U1427C-4H-6	109	34.26	35.89
U1427B-5H-2	71	35.32	35.89	U1427B-5H-5	148	40.43	41.00
U1427C-5H-2	126	39.19	41.00	U1427C-5H-6	136	44.50	46.31
U1427B-6H-2	97	45.27	46.31	U1427B-6H-5	139	50.03	51.07
U1427C-6H-3	75	49.26	51.07	U1427C-6H-6	118	53.41	55.22
U1427B-8H-2	48	54.30	55.22	U1427B-8H-6	29	59.96	60.87
U1427C-7H-3	120	59.06	60.87	U1427C-7H-7	106	64.13	65.95
U1427B-9H-2	84	63.86	65.95	U1427B-9H-5	140	68.33	70.42
U1427C-8H-4	23	69.24	70.42	U1427C-8H-7	54	74.03	75.21
U1427B-10H-2	116	74.06	75.21	U1427B-10H-6	103	79.85	81.00
U1427C-9H-3	84	78.27	81.00	U1427C-9H-6	115	82.57	85.30
U1427B-11H-2	21	82.71	85.30	U1427B-11H-5	55	87.08	89.67
U1427C-10H-2	88	86.38	89.67	U1427C-10H-6	103	92.12	95.41
U1427B-12H-2	24	92.26	95.41	U1427B-12H-7	87	99.98	103.13
U1427C-12H-1	50	98.70	103.13	U1427C-12H-5	73	104.87	109.30
U1427B-14H-3	5	104.54	109.30	U1427B-14H-6	96	109.87	114.63
U1427C-13H-3	88	111.44	114.63	U1427C-13H-6	58	115.46	118.65
U1427B-15H-4	98	115.69	118.65	U1427B-15H-8	50	120.52	123.48
U1427C-14H-2	77	118.62	123.48	U1427C-14H-5	71	122.82	127.68
U1427B-16H-4	44	124.70	127.68	U1427B-16H-7	56	129.21	132.20
U1427C-15H-1	63	127.33	132.20	U1427C-15H-5	129	133.44	138.31
U1427B-17H-3	111	134.19	138.31	U1427B-17H-7	15	139.12	143.24
U1427C-16H-2	50	137.42	143.24	U1427C-16H-5	77	142.06	147.87
U1427B-18H-3	68	142.49	147.87	U1427B-18H-7	78	148.25	153.64
U1427C-17H-2	81	146.90	153.64	U1427C-17H-6	23	152.18	158.91
U1427B-19H-2	139	152.19	158.91	U1427B-19H-6	72	157.37	164.09
U1427C-18H-1	80	156.00	164.09	U1427C-18H-4	143	160.95	169.04
U1427B-20H-3	107	161.93	169.04	U1427B-20H-7	125	168.01	175.11
U1427C-19H-2	6	166.22	175.11	U1427C-19H-5	150	172.02	180.91
U1427B-21H-4	107	172.60	180.91	U1427B-21H-8	20	177.49	185.80
U1427C-20H-2	24	175.94	185.80	U1427C-20H-4	126	179.98	189.84
U1427B-22H-3	5	180.59	189.84	U1427B-22H-6	149	186.61	195.85
U1427C-21H-2	4	184.78	195.85	U1427C-21H-4	135	188.91	199.98

Table T22 (continued). (Continued on next page.)

Hole, core, section	Depth in section (cm)	Depth CSF-A (m)	Depth CCSF-D (m)	Hole, core, section	Depth in section (cm)	Depth CSF-A (m)	Depth CCSF-D (m)
U1427B-23H-3	76	191.02	199.98	U1427B-23H-7	61	196.43	205.40
U1427C-22H-1	113	194.33	205.40	U1427C-22H-6	17	200.51	211.58
U1427B-24H-5	15	201.68	211.58	U1427B-24H-7	74	205.28	215.18
U1427C-23H-1	95	203.65	215.18	U1427C-23H-6	6	210.14	221.67
U1427B-25H-3	95	210.27	221.67	U1427B-25H-6	70	214.55	225.95
U1427C-24H-2	15	212.50	225.95	U1427C-24H-5	102	217.84	231.29
U1427B-26H-4	110	219.70	231.29	U1427B-26H-6	91	222.26	233.85
U1427C-25H-1	59	221.09	233.85	U1427C-25H-3	74	223.65	236.42
U1427A-25H-4	15	223.96	236.42	U1427A-25H-5	121	226.52	238.98
U1427C-26H-2	85	225.44	238.98	U1427C-26H-4	21	227.46	241.00
U1427B-27H-2	128	227.50	241.00	U1427B-27H-4	107	230.30	243.80
U1427C-27H-2	73	230.03	243.80	U1427C-27H-5	48	233.42	247.18
U1427A-27H-1	6	233.46	247.18	U1427A-27H-4	150	237.86	251.58
U1427C-29H-2	91	239.57	251.58	U1427C-29H-5	14	242.78	254.80
U1427B-30H-1	22	240.72	254.80	U1427B-30H-3	59	243.87	257.95
U1427A-29H-1	57	243.37	257.95	U1427A-29H-3	40	245.95	260.53
U1427C-31H-2	7	248.11	260.53	U1427C-31H-5	33	252.69	265.11
U1427B-32H-1	42	250.32	265.11	U1427B-32H-3	4	252.83	267.62
U1427C-32H-2	137	254.20	267.62	U1427C-32H-4	102	256.71	270.13
U1427B-33H-1	74	255.34	270.13	U1427B-33H-4	50	258.39	273.18
U1427C-33H-2	10	257.98	273.18	U1427C-33H-3	102	260.24	275.44
U1427B-34H-2	70	260.89	275.44	U1427B-34H-4	58	263.40	277.95
U1427C-34H-2	131	263.46	277.95	U1427C-34H-4	51	265.46	279.95
U1427B-35H-1	139	265.39	279.95	U1427B-35H-4	52	268.57	283.13
U1427C-35H-1	52	267.02	283.13	U1427C-35H-3	35	269.64	285.75
U1427B-36H-3	48	271.43	285.75	U1427B-36H-4	81	273.08	287.40
U1427C-36H-1	31	271.51	287.40	U1427C-36H-4	46	274.95	290.84
U1427B-37H-2	93	275.83	290.84	U1427B-37H-6	76	281.68	296.69
U1427C-38H-2	16	280.97	296.69	U1427C-38H-3	95	283.06	298.78
U1427B-39H-3	12	284.89	298.78	U1427B-39H-4	84	287.08	300.96
U1427C-39H-2	26	286.28	300.96	U1427C-39H-4	32	288.66	303.35
U1427B-40H-2	8	289.41	303.35	U1427B-40H-4	28	291.97	305.91
U1427C-40H-2	60	291.06	305.91	U1427C-40H-4	104	294.18	309.04
U1427B-41H-3	52	294.52	309.04	U1427B-41H-5	18	296.05	310.56
U1427C-41H-1	36	295.06	310.56	U1427C-41H-4	65	298.64	314.15
U1427B-42H-3	70	299.81	314.15	U1427B-42H-4	31	300.72	315.05
U1427C-42H-1	73	300.13	315.05	U1427C-42H-3	94	303.13	318.05
U1427B-43H-1	121	303.11	318.05	U1427B-43H-3	97	305.89	320.84
U1427C-43H-1	27	304.37	320.84	U1427C-43H-4	8	307.75	324.22
U1427B-44H-2	107	308.44	324.22	U1427B-44H-4	62	310.38	326.16
U1427C-44H-1	96	309.76	326.16	U1427C-44H-3	48	312.23	328.63
U1427B-45H-2	99	312.82	328.63	U1427B-45H-5	50	316.10	331.91
U1427C-45H-2	103	315.04	331.91	U1427C-45H-5	19	318.54	335.41
U1427B-46H-3	83	318.67	335.41	U1427B-46H-4	70	320.05	336.79
U1427C-46H-1	85	319.05	336.79	U1427C-46H-3	73	321.31	339.05
U1427B-47H-1	114	321.84	339.05	U1427B-47H-3	45	324.09	341.29
U1427C-47H-2	8	323.56	341.29	U1427C-47H-5	4	327.55	345.28
U1427B-49H-2	9	328.74	345.28	U1427B-49H-3	83	330.98	347.52
U1427C-48H-2	79	329.59	347.52	U1427C-48H-4	52	332.25	350.18
U1427B-50H-1	29	333.39	350.18	U1427B-50H-4	22	336.84	353.64
U1427C-49H-3	93	335.08	353.64	U1427C-49H-4	94	336.56	355.12
U1427B-51H-1	30	338.10	355.12	U1427B-51H-2	133	340.58	357.61
U1427C-50H-2	60	339.06	357.61	U1427C-50H-4	58	341.75	360.29
U1427B-52H-1	5	342.55	360.29	U1427B-52H-3	4	344.51	362.25
U1427C-51H-2	0	342.98	362.25	U1427C-51H-3	65	345.06	364.33
U1427A-51H-1	68	346.88	364.33	U1427A-51H-5	32	351.09	368.54
U1427B-54H-2	129	351.01	368.54	U1427B-54H-4	90	353.50	371.03
U1427A-52H-2	29	352.69	371.03	U1427A-52H-3	114	355.04	373.38
U1427B-55H-2	86	355.24	373.38	U1427B-55H-4	129	358.42	376.56
U1427A-53H-3	69	358.45	376.56	U1427A-53H-4	104	360.17	378.27
U1427B-56H-2	36	359.57	378.27	U1427B-56H-4	91	363.13	381.83
U1427A-54H-2	120	362.35	381.83	U1427A-54H-4	30	363.99	383.48
U1427B-57H-1	3	364.13	383.48	U1427B-57H-3	122	366.82	386.16
U1427A-55H-2	84	366.44	386.16	U1427A-55H-5	31	369.50	389.22
U1427B-58H-2	18	368.99	389.22	U1427B-58H-4	90	372.38	392.62
U1427A-56H-3	14	371.68	392.62	U1427A-56H-5	15	374.18	395.12
U1427B-59H-2	116	375.07	395.12	U1427B-59H-4	55	377.19	397.24
U1427A-57H-2	85	376.18	397.24	U1427A-57H-4	70	378.68	399.74
U1427B-60H-2	90	378.76	399.74	U1427B-60H-4	8	382.02	403.00
U1427A-58H-2	132	381.29	403.00	U1427A-58H-3	3	382.85	404.56

Table T22 (continued).

Hole, core, section	Depth in section (cm)	Depth CSF-A (m)	Depth CCSF-D (m)	Hole, core, section	Depth in section (cm)	Depth CSF-A (m)	Depth CCSF-D (m)
U1427B-61H-2	16	383.73	404.56	U1427B-61H-4	34	386.50	407.34
U1427A-59H-1	18	383.98	407.34	U1427A-59H-3	42	386.31	409.67
U1427B-62H-1	81	387.61	409.67	U1427B-62H-3	138	390.21	412.27
U1427A-60H-2	18	390.05	412.27	U1427A-60H-3	140	392.58	414.79
U1427B-63H-1	71	392.21	414.79	U1427B-63H-3	17	394.67	417.26
U1427A-61H-2	25	394.95	417.26	U1427A-61H-4	15	397.52	419.82
U1427B-64H-2	118	398.01	419.82	U1427B-64H-4	81	399.92	421.74
U1427A-62H-2	48	399.30	421.74	U1427A-62H-5	33	402.18	424.61
U1427B-65H-2	29	401.94	424.61	U1427B-65H-4	91	404.88	427.56
U1427A-63H-3	86	405.11	427.56	U1427A-63H-CC	21	425.05	430.34

Table T23. Constrained tie points for depth-age relationship, Site U1427.

Selected ties for depth-age lines	Event type	Bioevents and epoch boundaries	Depth CCSF-A (m)	Depth range (±)	Age (Ma)	Age range (±)	Sedimentation rate (m/m.y.)
Top			*0.00*		*0.000*		
	R	*Larcopyle buetschlii* Zone	1.80	0.00	0.005	0.005	264.0
	R	LO *Lychnocanoma sakai*	16.50	5.43	0.050	0.000	
	PF	FO and LO *Globigerinoides ruber* (pink)	35.87	4.44	0.260	0.140	
	R	LO *Amphimelissa setosa*	45.34	5.04	0.080	0.000	
	CN	FO *Emiliania huxleyi*	45.76	1.51	0.290	0.000	
	CN	LO *Pseudoemiliania lacunosa*	69.33	0.83	0.440	0.000	
	R	LO *Spongodiscus* sp.	95.29	5.09	0.290	0.000	
Unit A1/A2			*132.09*		*0.500*		
	PF	LO *Neogloboquadrina kagaensis* group	259.40	1.48	0.700	0.000	630.1
Paleomag	PM	Bottom of C1n (Brunhes/Matuyama)	*308.96*	0.75	*0.781*	0.000	
	CN	LO *Reticulofenestra asanoi*	364.37	0.03	0.910	0.000	423.4
	CN	Bc *Reticulofenestra asanoi*	451.30	2.23	1.140	0.000	
	PF	*Neogloboquadrina pachyderma* (D to S)	502.03	2.15	1.190	0.050	
	CN	LO *Gephyrocapsa* (>5.5 µm)	504.33	0.15	1.240	0.000	
	CN	LO *Helicosphaera sellii*	506.29	0.75	1.340	0.000	
	PF	T *Globorotalia inflata* (No. 2 bed)	528.51	5.69	1.290	0.050	
Bottom			*571.05*		*1.400*		

R = radiolarian, PF = planktonic foraminifer, CN = calcareous nannofossil, PM = paleomagnetism. LO = last occurrence, FO = first occurrence, Bc = base of common occurrence, T = top. D to S = dextral to sinistral coiling change.